A Precision Measurement of the B_s Lifetime
in $p\bar{p}$ Collisions at $\sqrt{s} = 1.96$ TeV
Using Partially and Fully Reconstructed Modes

by

Amanda Jean Deisher

B.A. (University of Montana, Missoula) 2002
B.A. (University of Montana, Missoula) 2002
M.A. (University of California, Berkeley) 2004

A dissertation submitted in partial satisfaction of the

requirements for the degree of

Doctor of Philosophy

in

Physics

in the

Graduate Division

of the

University of California, Berkeley

Committee in Charge:
Professor Marjorie Shapiro, Chair
Professor Robert Jacobsen
Professor Stephen Derenzo

Fall 2008

The dissertation of Amanda Jean Deisher is approved:

Chair	Date

	Date

	Date

University of California, Berkeley

Abstract

A Precision Measurement of the B_s Lifetime

in $p\bar{p}$ Collisions at $\sqrt{s} = 1.96$ TeV

Using Partially and Fully Reconstructed Modes

by

Amanda Jean Deisher

Doctor of Philosophy in Physics

University of California, Berkeley

Professor Marjorie Shapiro, Chair

We present a measurement of the B_s lifetime in fully and partially reconstructed $B_s \to D_s(\phi\pi)X$ decays in $\sim$1.3 fb^{-1} of $p\bar{p}$ collisions at $\sqrt{s} = 1.96$ TeV collected by the CDF II detector at the Fermilab Tevatron. We measure $c\tau(B_s) = 455.0 \pm 12.2$ (stat.)±8.2 (syst.) μm. The ratio of this result and the world average B^0 lifetime yields $\tau(B_s)/\tau(B^0) = 0.99 \pm 0.03$, which is in agreement with recent theoretical predictions.

Chair   Date

To my parents.

Contents

List of Figures

List of Tables

Acknowledgements

The first acknowledge should go to the other members of the LBL B group, with whose collaboration, in its various forms, have contributed to the completion of this analysis. As an advisor This analysis was performed in close collabor Marjorie for guidance, and help refocusing on the big picture. Also getting her hands dirty in the analysis details and the processing of many files.Actively processing files. All while fufilling her many other obligations Alex for long conversation while I was fleshing out technical details, sage advice, after-hours grad student support. Fitter initially developed by Hung-Chung and expanded by Johannes; they completed many mass and de/dx studies that helped us understand the sample composition. Share samples. Use their fitter macros.

The remainder of the CDF group at LBNL for many helpful and informative interactions. Amy, Beate, Bob, Carl, Charles, Erik, Greg, Henri, Jason, Jeremy, John, Juerg, Laurent, Lina, Maurice, Paul, Ramon, Tony, Weiming, Young-Kee

Italian collaborators, Donatella, Giuseppe, Simone.

Conveners: Cheng-Ju, Manfred, Giovanni Subconveners: Sinead, Diego, Guillelmo, Gavril Godparents: Pat, Enrique, Simone professors on my committee for all guidance seeing this analysis through and writing it up.

CDF collaboration ATLAS postdoc for getting me started on hardware. Aldo and the rest of the LBL ATLAS group

I've learned much from conversations and collaborations with the Johns Hopkins folks (Petar, Mat, Reid, and Satyajit) working on the parallel Λ_b lifetime analysis.

Thank you to my officemates (past and present), Hung-Chung, Joe, Johannes, John, and Paul, (honorary Tommy) for many discussions, technical consultations, ROOT tips, and diversions. Hung-Chung in particular has been an invaluable sounding board during the analysis process.

Anne, Donna, and Anytra for administrative and moral support.

Thank you to my parents and sisters for your unconditional love and support; its constancy has carried me through grad school. Mom, your care packages, letters, and phone conversations have meant more that I can say.

On the homefront, Ginny, Kristin, Yukiko, Heidi, Isabel, and Elena have been the best housemates one could hope for.

Much needed sail therapy during my time in Berkeley was provided by the crews of Ex Indigo, Tupelo Honey, and pHat Jack. I am grateful for the time on the water and the shared knowledge and friendships.

Chapter 1

Introduction

To first order, the decay widths of hadrons containing a b quark are equal to the decay width of the b quark itself, with the lighter quarks in the hadrons mere spectators to the b's decay. If one looks to higher orders, one sees that the spectator quarks have active roles in the time evolution and decay of b hadrons. Theorists predict and experimentalists observe that the flavor of the light quark does affect the decay width of a b hadron and induces a lifetime hierarchy, $\tau(B_c) < \tau(\Lambda_b) < \tau(B_s) \cong \tau(B^0) < \tau(B^+)$. In addition to a qualitative ranking, theorist also provide quantitative predictions (with theoretical uncertainties) for the ratios of lifetimes. Experimental results are in excellent agreement with predictions for $\tau(B^+)/\tau(B^0)$, with experimental uncertainties a factor of two smaller than theoretical uncertainties. The lifetimes of the B_s, B_c, and Λ_b, however, require additional experimental input before a definitive statement about agreement can be made. We choose to focus on a precision measurement of the B_s lifetime, and we will use the world average of the B^0 lifetime to calculate the ratio $\tau(B_s)/\tau(B^0)$.

The Tevatron at Fermilab provides an excellent environment for the study of heavy flavor hadrons, as it is currently the only facility in the world capable of producing all standard model varieties of b hadrons. For the analysis described here, we study hadronic decays of $B_s \rightarrow D_s^-(\phi\pi^-)\pi^+$ recorded by the Collider Detector at Fermilab (CDF II). Although B_s decays with a lepton daughter particle have a signature that is easy to trigger on, the uncertainty on the momentum carried out of the system by the neutrino makes a precision measurement of the lifetime difficult. To trigger on fully hadronic decays, we take advantage of the long lifetime of the B_s and the fact that it can travel a measurable distance from its production point before decaying. By looking for events with two tracks that do not point back to the beamspot, we can collect a large sample of B_s mesons with high purity. Since our event selection explicitly excludes b hadrons that decay near their production points, we do not expect to see decay times of B_s mesons distributed according to an exponential decay curve. We rely on simulations to model the effects of our trigger selection, so we can parameterize their sculpting of the proper time distribution.

In order to improve on the precision of previous measurements of the B_s lifetime

at CDF II, we need to both obtain a larger sample of B_s decays and maintain control of the systematic uncertainties associated with any innovations in our fit procedure. One way to increase the sample size is to increase the length of data taking. We can also double the number of events available for analysis by including hadronic B_s decays "partially reconstructed" as containing a $D_s^-(\phi\pi^-)\pi^+$, meaning there are additional tracks from the B_s decay that are not used to determine the reconstructed mass or momentum of the B_s. Since the lifetime of a particular B_s meson is determined by dividing the distance it traveled by its speed, we need to account for the missing momentum in the partially reconstructed decays, and we again rely on simulation to model this distribution.

As with any analysis, it is essential to test and refine the lifetime fit procedure to gain confidence in its performance. To guard against biasing our B_s lifetime measurement, we first study three control samples: $B^0 \to D^-(K^+\pi^-\pi^-)\pi^+$, $B^0 \to D^{*-}[\overline{D}^0(K^+\pi^-)\pi^-]\pi^+$, and $B^+ \to \overline{D}^0(K^+\pi^-)\pi^+$. We also keep the signal results blinded until after the systematic uncertainties have been assessed.

The organization of this thesis is as follows:

Chapter 2 presents a brief overview of the standard model picture of the B_s and $\bar{B}_s$ states and their evolution as a function of time. We also discuss the theory of heavy flavor hadron decay and compare theoretical predictions of the ratios of b hadron lifetimes to previous experimental results.

The experimental apparatus that makes this analysis possible, the Fermilab accelerator complex and the Collider Detector at Fermilab (CDF II), are described in Chapter 3. The trigger strategy for selecting hadronic decays is also discussed.

The analysis strategy is outlined in Chapter 4.

The reconstruction of B mesons in the triggered events and further analysis selection requirements are discussed in Chapter 5. Also included is a brief description of the samples of b hadron decays simulated for this analysis, the Monte Carlo.

A general description of the mass fits is found in Chapter 6. The lifetime fits are described in Chapter 7. Because the components in the mass fit are not identical to the components in the lifetime fit, Chapter 8 explains how the outputs of a mass fit

are translated into lifetime fit inputs.

The mass fit and lifetime fit results of the $B^0 \to D^{*-}[\overline{D}^0(K^+\pi^-)\pi^-]\pi^+$, $B^0 \to D^-(K^+\pi^-\pi^-)\pi^+$, and $B^+ \to \overline{D}^0(K^+\pi^-)\pi^+$ control sample analyses are given in Chapter 9. A study of the systematic uncertainties in the $B^0 \to D^-\pi^+$ lifetime measurement is also included. The results for the $B_s \to D_s^-(\phi\pi^-)\pi^+$ signal sample are presented in Chapter 10 with a discussion of systematic uncertainties. The conclusions are given in Chapter 11.

There have been numerous studies over the course of this analysis to test the lifetime fit procedure. We present a selection of the most important studies in three appendices.

The most crucial assumption in this analysis is that we can model the effect of the displaced-track trigger on the distribution of the B_s decay length. In Appendix A we present a study performed on a $J/\psi \to \mu^+\mu^-$ sample collected by an unbiased di-muon trigger. Applying the displaced-track trigger selection to both data and Monte Carlo, we compare trigger efficiencies and parameterize the level of agreement between the two. This parameterization is used to set a systematic uncertainty in the B_s lifetime measurement.

Before moving to the B_s sample, much time and effort went into understanding the control samples. The $B^0 \to D^-\pi^+$ sample, with its large background level, was particularly challenging. Appendix B documents several studies of the effects of changing the selection criteria (to eliminate background, even at the expense of signal) and fit configurations (to test our assumptions of background content).

In Appendix C we discuss various cross-checks that were performed on the B_s sample before the results were unblinded. After these final studies, we opened the box confidently.

Chapter 2

Theoretical Overview

In this chapter we discuss the theoretical basis for this measurement. Section 2.1 contains a general discussion of the theory of heavy flavor hadron decay, with emphasis on the diagrams in b hadron decays that interfere with each other. A statement of the current level of agreement between theoretical predictions and experimental measurements of lifetime ratios is found in Sec. 2.2. In Sec. 2.3 we discuss the time evolution of the B_s system, the mass and flavor eigenstates, and what lifetime we are actually measuring in this experiment.

2.1 Heavy Flavor Hadron Decay

In this section, we generally follow the presentation of Ref. [1].

For hadrons with a heavy quark such as the b or c, the decay of the hadron H_Q is dominated by the weak decay of the heavy quark Q, and to first order, the lighter quark(s) in the hadron can be considered a spectator to the decay. In the absence of spectator effects, the lifetimes of the H_Q would be equal. Experimentally, we see large deviations of an order of magnitude from equality for H_c lifetimes with, for example, $\tau(D^{\pm}) = 1.040 \pm 0.007$ ps and $\tau(\Omega_c) = 0.069 \pm 0.012$ [2]. For the heavier b quark ($m_b \sim 3m_c$), the differences are smaller and it has been observed that

$$\tau(B_c) < \tau(\Lambda_b) < \tau(B_s) \cong \tau(B^0) < \tau(B^+)$$

Beyond a qualitative description of the expected (and observed) H_b lifetime hierarchy, theoretical tools such as Operator Product Expansion (OPE) [3] can be used to provide quantitative predictions for H_b lifetimes.

The decay width of a heavy hadron can be related to the imaginary part of its forward scattering amplitude. For the weak decay width we have [4]

$$\Gamma(H_Q \to f) = \langle H_Q | L_{eff} | H_Q \rangle$$

where

$$L_{eff} = i\text{Im} \int d^4x \left\{ L_W(x) L_W^{\dagger}(0) \right\}_T,$$

6

is the integral of the time ordered product of the parton level weak Lagrangian. Employing OPE and considering just the first three terms of the expansion we find

$$
\begin{aligned}
\Gamma(H_q \to f) &= \frac{G_F^2 m_Q^5}{192\pi^3} |V_{CKM}|^2 \left[c_3^f \langle H_Q | \bar{Q}Q | H_Q \rangle + c_5^f \frac{\langle H_Q | \bar{Q} i\sigma \cdot GQ | H_Q \rangle}{m_Q^2} \right. \\
&\quad \left. + \sum_i c_{6,i}^f \frac{\langle H_Q | (\bar{Q}\Gamma_i q)(\bar{q}\Gamma_i Q) | H_Q \rangle}{m_Q^3} + O(1/m_Q^4) \right]
\end{aligned}
\tag{2.1}
$$

where V_{CKM} are the appropriate CKM parameters, G is the gluon field, q are the light quarks, and the Γ_i describe the spin and color structure of the quark interactions. The coefficients c_i^f are calculable with perturbative QCD.

The first term in Eqn. 2.1 simply represents the heavy quark decay, with no consideration of the gluon field or other quarks in the hadron. As $m_Q \to \infty$, the other terms are suppressed by multiple factors of $(1/m_Q)$, and we asymptotically approach the spectator model of heavy hadron decay. The second term in Eqn. 2.1 describes the interaction of Q and the gluon field in the hadron. It partially responsible for the difference in lifetimes between mesons and baryons of the same flavor. The third term represents the involvement of the light quarks in the decay. These spectator effects can be grouped into two categories: Pauli interference (PI) and weak scattering (WS). In PI, one of the quarks from the b decay is identical to another light quark in the hadron. An example of this is shown in Fig. 2.1, where a B^+ decays to $D^0\pi^+$ by emitting a W externally or internally. In general, the interference can be either constructive or destructive; in the B^+ case it is destructive. Such interference is not possible in the $B^0 \to D^-\pi^+$ decay, as shown in Fig 2.2, contributing to $\tau(B^0) < \tau(B^+)$. In WS, the heavy and light quarks can annihilate or there can be a W from the decay of Q that scatters off a light quark. A diagram of a WS process that shortens the Λ_b lifetime is shown in Fig. 2.3.
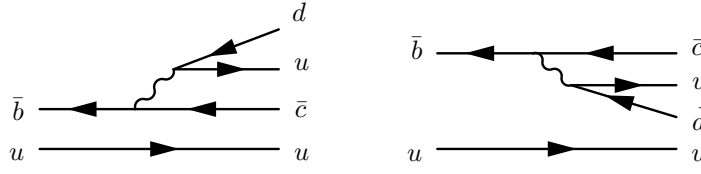
Figure 2.1: Pauli interference contributes to the $B^+ \to D^0\pi^+$ decays, since one of the quarks from the b decay is identical to the light quark in the meson.
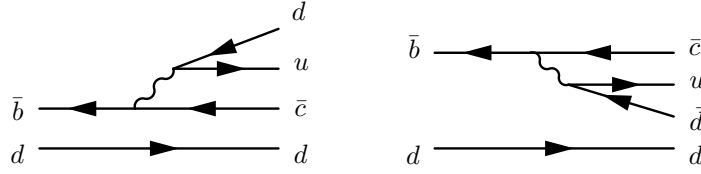
Figure 2.2: There is no Pauli interference in $B^0 \to D^-\pi^+$ decays, since an internally emitted W leads to a $D^0\pi^0$ final state.
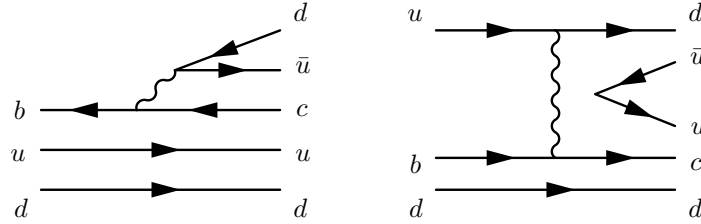
Figure 2.3: Weak Scattering in a $\Lambda_b \to \Lambda_c^+\pi^-$ decay.

2.2 Theoretical Predictions and Experimental Status

A useful figure of merit for comparisons between theoretical predictions of b hadron lifetimes and experimental results is their agreement on the ratios of lifetimes, usually presented with $\tau(B^0)$ as the denominator. In the calculation of the ratios, some of the theoretical uncertainties (*e.g.* CKM parameter uncertainties) cancel, and theorists and experimentalists can begin to approach similar precision. A summary of theoretical predictions and the experimental world averages of the ratios of b hadron lifetimes as of 2007 [5] can be seen in Tab. 2.1.

	Theory	Experiment
$\tau(B_s)/\tau(B^0)$	1.00 ± 0.01	0.939 ± 0.021
$\tau(B^+)/\tau(B^0)$	1.06 ± 0.02	1.071 ± 0.009
$\tau(\Lambda_b)/\tau(B^0)$	0.90 ± 0.04	0.921 ± 0.036

Table 2.1: Summary of theoretical predictions and the world average measurements of the ratios of b hadron lifetimes as of 2007 [5, 6, 7].

Good agreement between theory and experiment for $\tau(B^+)/\tau(B^0)$ and $\tau(\Lambda_b)/\tau(B^0)$ already exists, and the experimental uncertainties are smaller than the theoretical uncertainties at this point. There is 2-3 σ difference in the $\tau(B_s)/\tau(B^0)$ values, and the burden is on the experimentalists to decrease their uncertainty and see if the discrepancy remains. The lifetime of the B^0 has already been well measured; the goal of this analysis is to measure $\tau(B_s)$ with high precision.

2.3   Standard Model Overview of the B_s System

In order to be specific about what we mean by the B_s lifetime, we briefly review the composition and time evolution of the B_s system. We follow the general outline of the discussion in Ref. [8].

The B_s meson is composed of a $\overline{b}$ antiquark and s quark; the $\overline{B}_s$ contains a b and $\overline{s}$. Over time, these states evolve according to the Schrödinger equation

$$i\frac{d}{dt}\left|\begin{array}{c} B_s(t) \\ \overline{B}_s(t) \end{array}\right\rangle = \left(M - i\frac{\Gamma}{2}\right)\left|\begin{array}{c} B_s(t) \\ \overline{B}_s(t) \end{array}\right\rangle. \tag{2.2}$$

CPT invariance requires $M_{11} = M_{22}$ and $\Gamma_{11} = \Gamma_{22}$. The off-diagonal elements of the M and Γ matrices are non-zero due to B_s-$\overline{B}_s$ mixing (shown in Fig. 2.4) and the existence of final states that are accessible to both mesons.

The matrices can be diagonalized, and the result is a mass eigenbasis with the heavy B_s^H and light B_s^L. The mass eigenstates can be expressed in the flavor basis
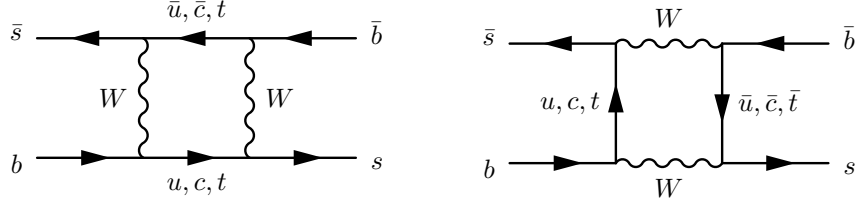
Figure 2.4: B_s-$\overline{B}_s$ mixing is allowed through the Standard Model box diagrams.

as

$$\left|B_s^L\right\rangle = p\left|B_s\right\rangle + q\left|\overline{B}_s\right\rangle$$
$$\left|B_s^H\right\rangle = p\left|B_s\right\rangle - q\left|\overline{B}_s\right\rangle \tag{2.3}$$

with $|p|^2 + |q|^2 = 1$. The mass eigenstates then evolve over time without mixing according to

$$\left|B_s^H(t)\right\rangle = e^{-(iM_H + \Gamma_H/2)}\left|B_s^H\right\rangle$$
$$\left|B_s^L(t)\right\rangle = e^{-(iM_L + \Gamma_L/2)}\left|B_s^L\right\rangle, \tag{2.4}$$

where Γ_H and Γ_L are the heavy and light eigenstates' decay widths. The mass difference and width difference are defined as

$$\Delta m_s \equiv M_H - M_L, \quad \Delta\Gamma_s \equiv \Gamma_L - \Gamma_H \tag{2.5}$$

so Δm_s and $\Delta\Gamma_s$ are both positive. The mass and width of the B_s in the flavor basis can be expressed as

$$m(B_s) = \frac{M_H + M_L}{2} = M_{11}, \quad \Gamma(B_s) = \frac{\Gamma_H + \Gamma_L}{2} = \Gamma_{11}$$

Note $\tau(B_s) = 1/\Gamma(B_s)$, $\tau(B_s^L) = 1/\Gamma_L$, and $\tau(B_s^H) = 1/\Gamma_H$. To calculate decay rates, we would ultimately like to express the time evolution of $|B_s(t)\rangle$ as a function of $|B_s\rangle$ and $\left|\overline{B}_s\right\rangle$. As a first step, we combine Eqns. 2.4 and 2.3 and find

$$|B_s(t)\rangle = \frac{1}{2p}\left[e^{-(iM_H + \Gamma_H/2)}\left|B_s^H\right\rangle + e^{-(iM_L + \Gamma_L/2)}\left|B_s^L\right\rangle\right]$$
$$\left|\overline{B}_s(t)\right\rangle = \frac{1}{2q}\left[e^{-(iM_H + \Gamma_H/2)}\left|B_s^H\right\rangle - e^{-(iM_L + \Gamma_L/2)}\left|B_s^L\right\rangle\right]. \tag{2.6}$$

10

Again employing Eqn. 2.3 and combining terms, the time evolution can be expressed as

$$
\begin{aligned}
|B_s(t)\rangle &= g_+(t)\,|B_s\rangle + \frac{q}{p}g_-(t)\,\big|\overline{B}_s\big\rangle \\
\big|\overline{B}_s(t)\big\rangle &= \frac{p}{g}g_-(t)\,|B_s\rangle + g_+(t)\,\big|\overline{B}_s\big\rangle
\end{aligned}
\tag{2.7}
$$

with

$$
\begin{aligned}
g_+(t) &= e^{-imt}e^{-i\Gamma t/2}\left[\cosh\frac{\Delta\Gamma t}{4}\cos\frac{\Delta m t}{2} - i\sinh\frac{\Delta\Gamma t}{4}\sin\frac{\Delta m t}{2}\right] \\
g_-(t) &= e^{-imt}e^{-i\Gamma t/2}\left[-\sinh\frac{\Delta\Gamma t}{4}\cos\frac{\Delta m t}{2} + i\cosh\frac{\Delta\Gamma t}{4}\sin\frac{\Delta m t}{2}\right], \tag{2.8}
\end{aligned}
$$

so a B_s meson at production ($t = 0$) will never be purely B_s for $t > 0$. In the analysis described here, we do not differentiate between B_s and $\overline{B}_s$ at production. Instead we measure the decay rate to a final state f. Assuming B_s and $\overline{B}_s$ are produced in equal quantities, the decay rate we will measure is

$$
\begin{aligned}
\Gamma[f,t] &= \Gamma\left(B_s^0(t)\to f\right) + \Gamma\left(\overline{B}_s^0(t)\to f\right) \\
&= N_f|A_f|^2\left(1 + |\lambda_f|^2\right)e^{-\Gamma t}\left[\cosh\frac{\Delta\Gamma t}{2} - \frac{2\mathrm{Re}\lambda_f}{1 + |\lambda_f|^2}\sinh\frac{\Delta\Gamma t}{2}\right] + O(a)
\end{aligned}
\tag{2.9}
$$

where N_f is a time-independent normalization factor, A_f is the decay amplitude $\langle f|B_s^0\rangle$ (likewise $\bar{A}_f = \langle f|\overline{B}_s^0\rangle$), $\lambda_f = \frac{q}{p}\frac{\bar{A}_f}{A_f}$, and $a = \mathrm{Im}\frac{\Gamma_{12}}{M_{12}}$

By choosing a flavor decay mode, a mode where the flavor of the B_s at decay can be determined from its decay products, the expression in Eqn. 2.9 is considerably simplified. In our case we reconstruct $B_s \to D_s^-\pi^+$ decays (note $\overline{B}_s^0$ does not decay to $D_s^-\pi^+$, but rather $D_s^+\pi^-$), so $\bar{A}_f$ and consequently λ_f are zero. Eqn. 2.9 can then be written as

$$
\begin{aligned}
\Gamma[f,t] &= N_f|A_f|^2 e^{-i\Gamma t}\cosh\frac{\Delta\Gamma t}{2} \\
&= N_f|A_f|^2 e^{-\Gamma t}\frac{1}{2}\left[e^{\frac{\Delta\Gamma t}{2}} + e^{-\frac{\Delta\Gamma t}{2}}\right] \\
&= N_f|A_f|^2\frac{1}{2}\left[e^{-\Gamma t + \frac{\Delta\Gamma t}{2}} + e^{-\Gamma t - \frac{\Delta\Gamma t}{2}}\right] \\
&= N_f|A_f|^2\frac{1}{2}\left[e^{-\Gamma_H t} + e^{-\Gamma_L t}\right]
\end{aligned}
\tag{2.10}
$$

11

which is equivalent to saying there is an equal mixture of $B_{s,H}$ and $B_{s,L}$ at production. If the decay rate in Eqn. 2.10 is integrated over time, one does not expect equal parts $B_{s,H}$ and $B_{s,L}$ since the shorter-lived $B_{s,L}$ will decay more quickly. The fraction of $B_{s,H}$ will be

$$f_H = \frac{1/\Gamma_H}{1/\Gamma_H + 1/\Gamma_L} = \frac{\Gamma_L}{\Gamma_H + \Gamma_L} = \frac{\Gamma_L}{2\Gamma}. \tag{2.11}$$

The fraction of $B_{s,L}$ will be

$$f_L = \frac{1/\Gamma_L}{1/\Gamma_H + 1/\Gamma_L} = \frac{\Gamma_H}{\Gamma_H + \Gamma_L} = \frac{\Gamma_H}{2\Gamma}. \tag{2.12}$$

The mean B_s lifetime measured in fit with a single exponential to a flavor-specific sample will be

$$
\begin{aligned}
\tau_m(B_s) &= f_L \cdot \tau_L + f_H \cdot \tau_H \\
&= \frac{1}{\Gamma} \cdot \frac{1 + \frac{1}{4}\left(\frac{\Delta\Gamma}{\Gamma}\right)^2}{1 - \frac{1}{4}\left(\frac{\Delta\Gamma}{\Gamma}\right)^2}
\end{aligned}
\tag{2.13}
$$

Note that $\tau_m(B_s) \neq 1/\Gamma$ and also $\tau_m(B_s) \neq (\tau_H + \tau_L)/2$, since

$$
\begin{aligned}
\frac{1}{2}(\tau_H + \tau_L) &= \frac{1}{2}\left(\frac{1}{\Gamma_H} + \frac{1}{\Gamma_H}\right) \\
&= \frac{1}{2}\left(\frac{1}{\Gamma - \frac{1}{2}\Delta\Gamma} + \frac{1}{\Gamma + \frac{1}{2}\Delta\Gamma}\right) \\
&= \frac{1}{\Gamma} \cdot \frac{1}{1 - \frac{1}{4}\left(\frac{\Delta\Gamma}{\Gamma}\right)^2}
\end{aligned}
\tag{2.14}
$$

12

Chapter 3

Experimental Apparatus

The data for this measurement come from $p\overline{p}$ collisions at $\sqrt{s} = 1.96$ TeV collected by the CDF II detector at the Fermilab Tevatron. The analysis is based on an integrated luminosity of $\sim$1.3 fb^{-1} collected between February 2002 and November 2006. This chapter briefly describes the accelerator complex and the detector components crucial for the B_s lifetime measurement.

3.1 The Fermilab Accelerator System

The Fermilab accelerator system is a complex network of accelerators that provides high intensity particle beams for multiple high energy physics experiments. The b hadrons for this analysis were collected by the CDF II detector at a $p\overline{p}$ collision point on the Tevatron. The following sections briefly summarize the acceleration chain for protons and anti-protons [9]. A schematic of the accelerator system is found in Fig. 3.1.
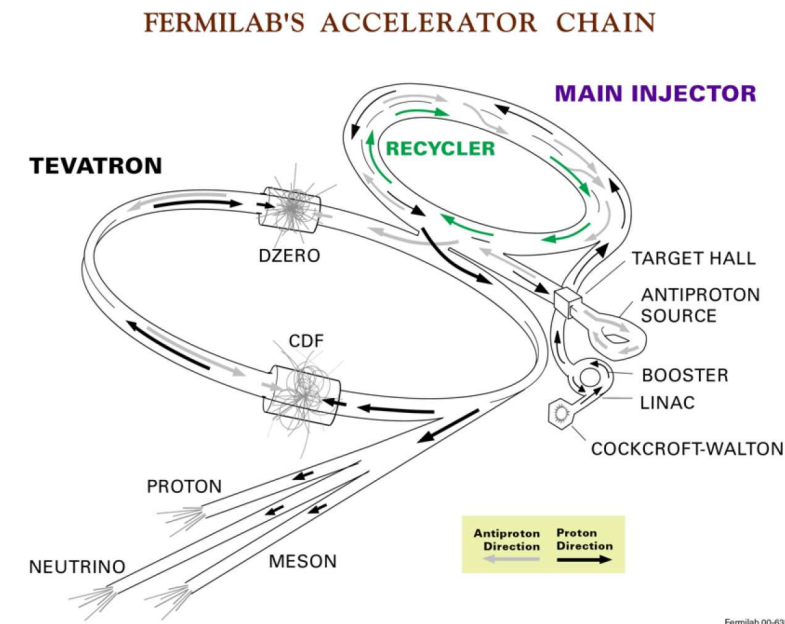
Figure 3.1: Schematic of the Fermilab accelerator system.

3.1.1 Proton Source

The proton source consists of three main components: the pre-accelerator, a linear accelerator (the Linac), and the Booster. The pre-accelerator is a Cockcroft-Walton type device that accelerates negatively charged hydrogen gas (H^-) to an energy of 750 keV. The Linac accepts the H^- ions and further accelerates them to 400 MeV using 12 radio-frequency (RF) cavities. The electrons are then stripped from the H^- ions, and the remaining protons are injected into the Booster, a synchrotron accelerator with a 75 meter radius. The 18 RF cavities of the Booster accelerate the protons to 8 GeV.

3.1.2 Main Injector

The main injector is a circular synchrotron. Its 18 RF cavities accelerate the 8 GeV protons from the Booster to either 120 GeV or 150 GeV. The 150 GeV protons are ready for injection into the main collider ring, the Tevatron. The 120 GeV protons are sent to the anti-proton source for $\bar{p}$ production. The Main Injector also accepts 8 GeV anti-protons from the recycler and accelerates them to 150 GeV so they are ready for injection into the Tevatron.

3.1.3 Anti-Proton Source

The anti-proton source consists of three main components: the target, the De-buncher, and the Accumulator. Anti-protons are generated when 120 GeV protons from the Main Injector are directed towards a nickel target. Anti-protons with an energy of 8 GeV are separated from the other particles produced in the proton-target collisions using magnets. The anti-protons then enter the Debuncher, a synchrotron in the shape of a rounded triangle with mean radius 90 m. The anti-protons are cooled to reduce the momentum spread but are kept at an energy of 8 GeV. They then enter the Accumulator, a triangular shaped synchrotron of radius 75m that shares the same tunnel as the Debuncher, for storage and further cooling.

3.1.4 Recyler

The Recycler is a synchrotron located in the same tunnel as the Main Injector. It accepts 8 GeV anti-protons from the Accumulator and further cools the beam with stochastic and electron cooling. The anti-protons remain at 8 GeV in the Recycler until they are needed for injection into the Tevatron. At that point they are extracted to the Main Injector, accelerated to 150 GeV, and injected into the Tevatron.

3.1.5 Tevatron

The Tevatron is the final destination for the p and $\bar{p}$ that collide at center-of-mass energy $\sqrt{s} = 1.96$ TeV. It is a synchrotron of radius 1 km with 8 accelerating RF cavities. In preparation for a physics run, 36 group of 150 GeV protons are injected into the Tevatron from the Main Injector. The protons circulate clockwise (when viewed from above). After the protons are fully loaded into stable orbits, anti-protons with energy 150 GeV are injected from the Recycler. The anti-protons circulate in the same beampipe, utilizing the same magnets, but in the counter-clockwise direction. The protons and anti-protons are then accelerated to 980 GeV and the beams are made to pass through each other every 396 ns at two interaction points. At one of these locations, the Collider Detector at Fermilab (CDF) II is constructed so the products of the collisions can be observed.

3.2 The Collider Detector at Fermilab (CDF) II

The Collider Detector at Fermilab is a multi-purpose detector constructed with roughly cylindrical symmetry around a $p\bar{p}$ interaction point at the Fermilab Tevatron [10]. It consists of an inner tracking volume immersed in a 1.4 T solenoidal magnetic field, electromagnetic and hadronic calorimeters located outside the solenoid, and muon drift chambers at large radii. A diagram of the detector is shown in Figure 3.2.

Before further describing the detector components, a short description of the
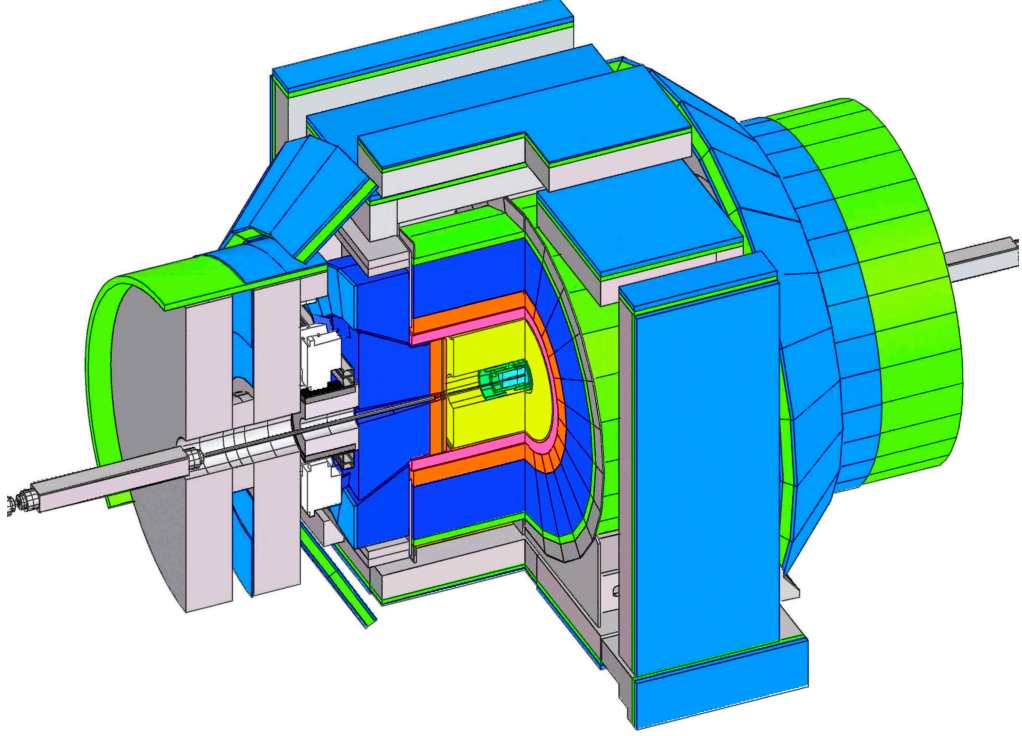
Figure 3.2: View of CDF II detector with one quarter of the detector cutaway.

CDF II coordinate system is necessary. In Cartesian coordinates, the $+z$ axis is defined as the proton direction (east), the $+x$ axis is radially outward (north), and the $+y$ axis is up at the interaction point $(x = 0, y = 0, z = 0)$. The radial distance from the beamline is called r. The azimuthal angle ϕ is measured from the $+x$ axis with $\phi = 90$ degrees along the $+y$ axis, as expected. The plane transverse to the beam direction can be equivalently referred to as the $x - y$ plane or the $r - \phi$ plane. The polar angle θ is measured from the $+z$ axis $(\theta = 0)$, so the transverse momentum of a particle is $p_T = p \sin \theta$. Instead of θ, we often refer to a pseudo-rapidity variable η defined as $\eta = \ln \tan(\theta/2)$.

The inner tracking volume consists of a multi-component silicon-strip detector and a wire drift chamber which provide precise measurements of location and curvature of the tracks left by charged particles. It is the ability to resolve the B_s production and decay positions and to precisely determine the momentum of the B_S decay products that makes this lifetime measurement possible. A cutaway view of
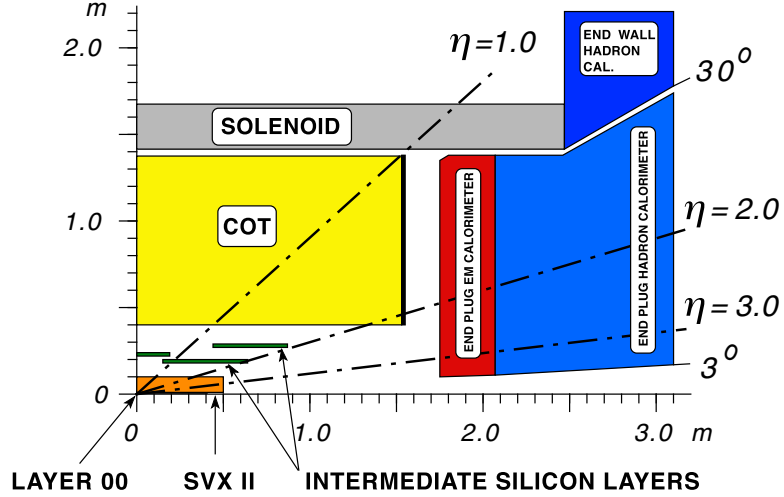
Figure 3.3: Cutaway view of one quarter of the CDF II inner detector

the inner detector is shown in Figure 3.3. The silicon detector and drift chamber are further discussed in Sections 3.2.1 and 3.2.2, respectively. The calorimeters and muon chambers were not directly used in this measurement. These systems are discussed in greater detail elsewhere [10].

The three-level trigger system employed by CDF to select events is discussed in Section 3.2.3.

3.2.1 Silicon Detector

The silicon detector is comprised of three sub-detectors. In order of increasing radius, they are Layer 00 (L00), the SVX II, and the intermediate silicon layers (ISL). An $r - z$ view of the three components is shown in Figure 3.6.

L00 is the innermost component of the silicon detector [11]. It consists of single-sided silicon microstrip detectors mounted directly on the beampipe. Twelve azimuthal wedges, a combination of 6 narrow wedges at $r = 1.35$ cm and 6 wider wedges at $r = 1.62$ cm, provide full coverage in ϕ [12]. L00 was added to the silicon configuration to mitigate the effect on track resolution of the SVXII electronics being present in the active volume of the detector. The arrangement of 12 azimuthal wedges of L00 can be seen in Figure 3.5.

18
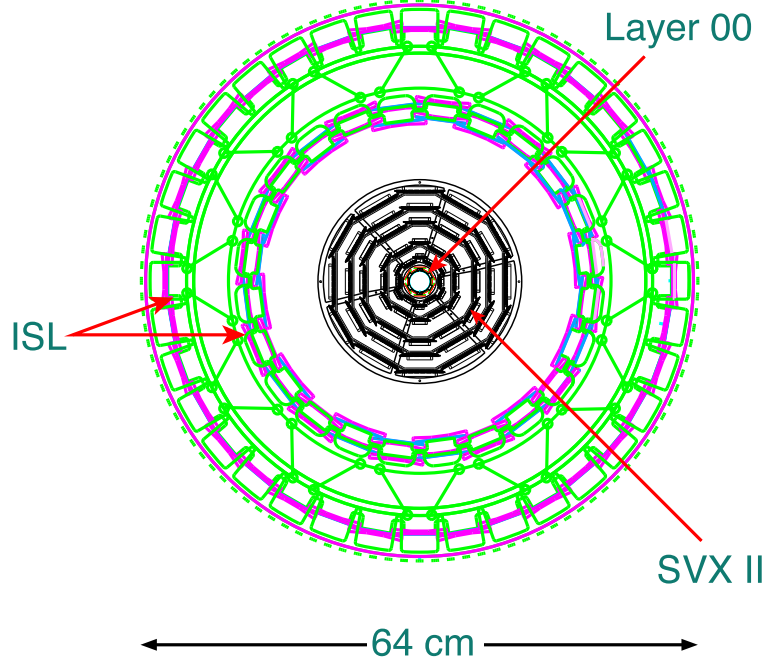
Figure 3.4: Endview of the three components that make up the silicon detector. The support structure is included.

The SVX II consists of 5 layers of double-sided silicon microstrip detectors between $r =$2.4 cm and $r = 10.6$ cm [10]. Each layer is a cylindrical shell made up of 12 azimuthal wedges. Along the z direction, SVX II is divided into three identical barrels. Five layer coverage is provided up to $\eta < 2.0$. The position of the SVX II relative to the other components of the silicon detector can be seen in Figures 3.4-3.6. The double-sided detectors all have a ϕ side, meaning the microstrips are arranged parallel to the z axis so the ϕ of the particle track can be determined. The second side of the detectors provides z information about a track's position with either 90° or small angle stereo sensors. The stereo angle pattern for the five layers is 90°, 90°, $-1.2°$, 90°, and $+1.2°$ [11].

ISL consists of five barrels in the region $r \in [20, 29]$ cm. There is one central barrel and an inner and outer barrel pair in the forward and backward regions. The $r - z$ position of the ISL is shown in Figure 3.6. The ISL also uses double-sided sensors. One side has ϕ sensors, and the other has 1.2° stereo sensors [13].
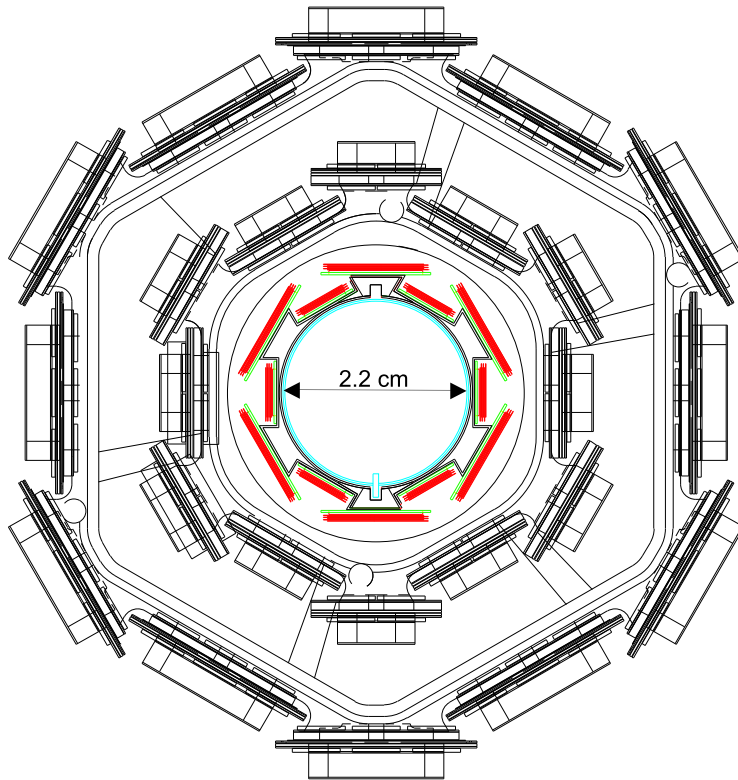
Figure 3.5: Endview the innermost layers of the silicon detector: SVX II and L00
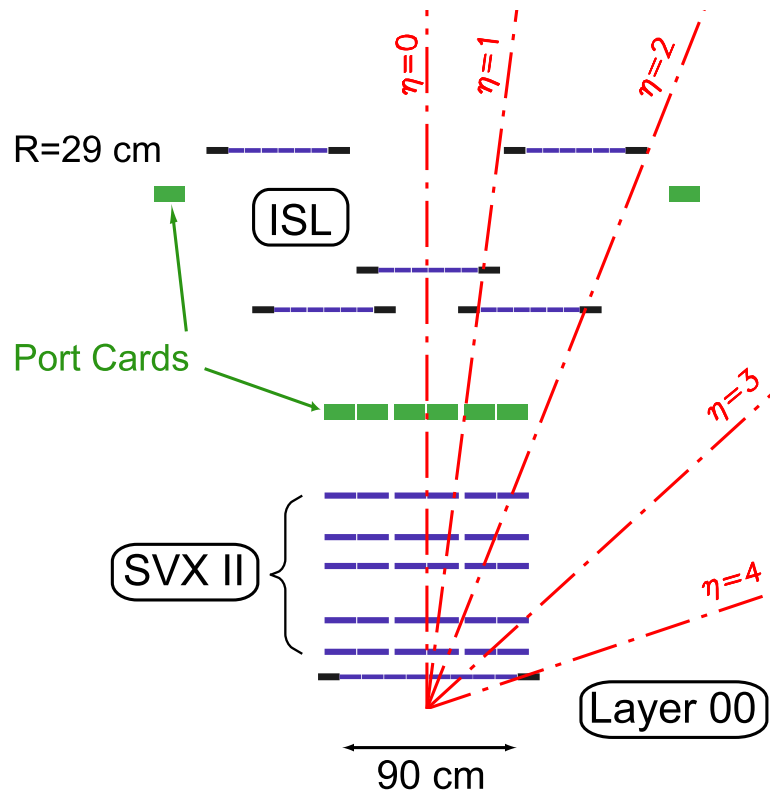
Figure 3.6: Sideview of half of the silicon detector. The z coordinate is compressed.

3.2.2 Central Outer Tracker

The central outer tracker (COT) is an open-cell cylindrical drift chamber that provides charged particle tracking up to $|\eta| < 1$. The COT is located outside the silicon detector, but inside the time-of-flight scintillators and the solenoid. Its active volume covers $r \in [43.4, 132.3]$ cm and $|z| < 155$ cm. The COT contains over 30,000 sense wires in 96 layers, grouped into eight super layers (the layers are in the r direction). Half of the super layers are axial, extending from endplate to endplate with no change in r or ϕ positions of the wires. The other half provide small angle stereo ($\pm$ 2 °) information. Tracks reconstructed from COT hits have excellent p_T resolution ($(\sigma(p_T)/p_T = 0.17\% p_T$ [GeV/c]$^{-1}$) [14] but less precise z information. The sense wires are 40 μm gold-plated tungsten with 7.112 mm spacing. The gas mixture in the COT is 50% argon, 50% ethane.

3.2.3 Trigger System

The total hadronic cross-section at the Tevatron is 75 mb, resulting in an event rate of 75 MHz at an instantaneous luminosity of 1.0e32 cm^{-2} s^{-1}. It is neither possible, nor desirable, to record the full detector read-out for each of these events. The rate at which events can be written to tape is $\sim$100 Hz. As not all events are equally interesting from a physics standpoint, a strategy where events are randomly selected would not be the most effective way to collect data for this or most any other analysis. Instead we make decisions in real time using information about the each event. To this end, CDF employs a three-level trigger system with more information available for the decision at each level.

Overview

Level 1 of the trigger consists of three parallel hardware processing streams. One path identifies calorimeter objects such as electrons and jets with energy deposited in the electromagnetic and hadronic calorimeters, respectively. A second path identifies muons from deposits in the muon chambers. A third set of dedicated hardware called

the extremely fast tracker (XFT) identifies tracks in the COT by comparing COT hits to predetermined hit patterns [15]. The XFT has a high efficiency for track finding with good momentum resolution ($\sigma(p_T)/p_T < 2\% p_T$ $[\text{GeV}/c]^{-1}$) and ϕ resolution at the origin ($\delta\phi < 8$ mrad). The minimum p_T for an XFT triggerable track is 1.5 GeV/c. Level 1 decisions are made based on the number of objects and calculated global calorimeter energy quantities. The accept rate is $\sim$20 kHz.

Level 2 of the trigger uses a combination of dedicated hardware and processors to select events. There are two main pieces of dedicated hardware. The first performs cluster finding by merging hits in neighboring calorimeter towers. The second set of hardware, the silicon vertex trigger (SVT), searches for tracks with displaced vertices [16]. The SVT takes XFT tracks, extrapolates them into the silicon detector, and attaches silicon hits. A SVT track must have coincidence with a XFT track and hits in 4 out of the 5 SVX layers. A SVT track has transverse impact parameter (the distance of closest approach to the primary vertex) resolution of 35 μm (50 μm convoluted with the beamspot). Output from the level 2 dedicated hardware, level 1, and additional electromagnetic shower information are used by the level 2 processors to decide which events are passed on to level 3. The level 2 accept rate is $\sim$300 Hz.

At level 3, approximately 300 commercial dual processor PC's use the full detector information to perform full three dimensional track reconstruction. Additional cuts may be imposed at this level to bring the rate down to $\sim$100 Hz.

Triggering on Hadronic B Decays

In hadronic B decays we are left with a handful of tracks with an energy of a few GeV and no lepton to easily trigger on. It is a signature that, to first approximation, is hard to distinguish from the other 75 million events produced every second. However, b hadrons are unique in that they have a relatively long lifetime and travel a measurable distance from their production points before they decay. The SVT is designed to find tracks that do not point back to the beamspot. By requiring a pair of SVT tracks with an intersection displaced from the primary vertex, we are able to collect a large sample of hadronic B's with excellent purity.

The CDF collaboration has several trigger paths in place that require a track pair with an intersection displaced from the primary vertex. The most inclusive two-track trigger is dubbed "Scenario Low" as it has the lowest minimum momentum requirement for the tracks. At high instantaneous luminosities, Scenario Low has a large cross-section, so triggers with tougher selection criteria, called Scenario A and Scenario C, were developed to replace Scenario Low. Even with the tighter selection, the rates for Scenario A and Scenario C have also been unacceptably large at high luminosities. Rather than remove the triggers, the triggers are often prescaled, meaning that some fraction of the events that pass the trigger are still rejected, so the overall rate remains acceptable.

The cuts for the two-track triggers are tabulated in Tab. 3.1, but we summarize the general two-track trigger strategy here. At level 1, patterns of hits in the COT are identified as tracks by the XFT. At level 2, the SVT associates a set of SVX hits with the XFT tracks and calculates the track parameters. We further require a pair of charged particles from a single event to each have a transverse momentum $p_T \geq 2$ GeV/c and impact parameter d_0, a particle's distance of closest approach to the beamline measured in the transverse plane, satisfy 120 μm$< d_0 <$1 mm. The opening angle between the particles' trajectories ($\Delta\phi$ in the $r - \phi$ plane transverse to the beam direction) must be between 2° and 90°, and their intersection must be 200 μm transverse to the $\overline{p}p$-interaction point. Track reconstruction is performed at level 3, and the level 1 and 2 cuts are confirmed.

These trigger level cuts preferentially select longer lived particles, shaping the proper time distribution. Thus the exponential distribution of lifetimes no longer extends down to $ct = 0$. Instead there is a "trigger turn-on" in the distribution. Our treatment of this turn-on and the ability of our simulations to model it correctly will be discussed in greater detail in Chap. 7

		Scen Low	Scen A	Scen C
Level 1	Single Track			
	•No. of XFT layers	4	4	4
	•XFT p_T (GeV/c)	2.04	2.04	2.46
	Track Pair			
	•p_T scalar sum (GeV/c)	0	5.5	6.5
	•Charge Product ($q_1 \cdot q_2$)		-1	-1
	•$\Delta\phi_{\min}$	0	0	0
	•$\Delta\phi_{\max}$	90°	135°	135°
Level 2	Single Track			
	•SVT χ^2	15	25	25
	•SVT d_0 min (μm)	120	120	120
	•SVT d_0 max (μm)	1000	1000	1000
	•SVT p_T (GeV/c)	2.0	2.0	2.5
	•SVT L_{xy} min (μm)	200	200	200
	Track Pair			
	•p_T scalar sum (GeV/c)	0	5.5	6.5
	•Charge Product ($q_1 \cdot q_2$)		-1	-1
	•$\Delta\phi_{\min}$	2°	2°	2°
	•$\Delta\phi_{\max}$	90°	90°	90°

Table 3.1: The three trigger scenarios have slightly different requirements for single tracks and track pairs. This table list the level 1 XFT requirements and level 2 SVT requirements.

Chapter 4

Analysis Strategy Overview

For the analysis described here, we study hadronic decays of $B_s \rightarrow D_s^-(\phi\pi^-)\pi^+$ recorded by CDF II. To trigger on fully hadronic decays, we take advantage of the long lifetime of the B_s and the fact that it can travel a measurable distance from its production point before decaying. By looking for events with two tracks that do not point back to the beamspot, we can collect a large sample of B_s mesons with high purity.

Since our trigger selection explicitly excludes b hadrons that decay near their production points (they are difficult to distinguish in from background coming from the interaction point), we do not expect to see decay times of B_s mesons distributed according to an exponential decay. Instead we see a "trigger turn-on" effect that we can parameterize in the proper time probability distribution function (PDF) as a multiplicative term. This term we call the "efficiency curve." This technique was proposed by others in the CDF collaboration [20] and has been used in, perhaps most notably, in the recent CDF B_s mixing analysis [21]. An illustration of the trigger turn-on is found is Fig. 4.1.

(a) Before Trigger

(b) After Trigger
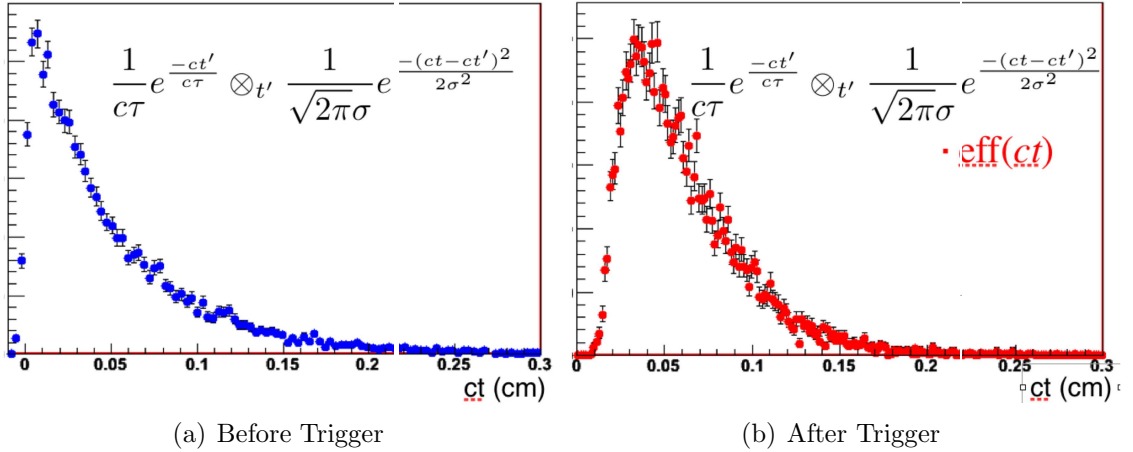
Figure 4.1: The left plot shows the expected shape of the proper time distribution of a B meson: an exponential smeared by a Gaussian. The right plot illustrates what happens to the distribution when we require the events to pass the two-track trigger. Both distributions are generated from functions.

The selection criteria affect each B_s decay mode differently due to their different event topologies, so we assign each major B_s decay mode a separate efficiency curve.

27

(B_s modes with few events are grouped together into a "remainder" PDF with a shared efficiency curve.) The parameters of each of the efficiency curves are found in fits to realistic B_s Monte Carlo samples that have undergone detector and trigger simulation, where the lifetime used for generation is already known and fixed in the fit. The efficiency curve parameters are then fixed in the fit to data, and the lifetime of the B_s is the only variable allowed to float.

A salient feature of this analysis is the treatment of B_s mesons that are partially reconstructed as $D_s^- \pi^+$ as signal events that contribute to the lifetime measurement. One such decay is the $B_s \to D_s^- \rho^+$ with $\rho^+ \to \pi^+ \pi^0$ where the π^0 is not reconstructed. These partially reconstructed decays contain real B_s's, but in order to include them we have to correct the lifetime for the momentum carried away by the missing particles. This is done with a "K factor" distribution convoluted in the PDFs of these modes. Each partially reconstructed mode has its own K factor distribution taken from a Monte Carlo sample where the true momenta of the missing particles are known. A precise definition of the K factor and details about how it is included in the PDFs are found in Sec. 7.2. Since the inclusion of partially reconstructed modes in a hadronic lifetime measurement is an innovation for this analysis, we perform separate lifetime fits for the fully reconstructed (FR) and partially reconstructed (PR) regions as a cross-check before the final fit to events in the combined FR+PR region.

Since we rely heavily on simulations to get the proper time distributions of our signal, we take care to check that the simulation reproduces the data well. As one point of comparison, we plot the distributions of the kinematic variables used to select events for background-subtracted data and simulation (shown in Chapter 7). In Chapter 7 we also describe the reweighting procedure used to bring Monte Carlo back into agreement with data in two variables where there is a disagreement (B_s p_T and trigger category). Additional verification that the two-track trigger emulator applied to Monte Carlo performs the same as the real trigger is provided in Appendix A where we study a $J/\psi \to \mu^+ \mu^-$ sample collected with an unbiased di-muon trigger.

Before performing a fit to the proper time distribution of the B_s data sample,

we first determine the sample composition in a separate fit to the mass distribution of the sample. The different signal and background components have very distinct mass profiles, so the extra information contained in the mass variable is valuable. The fractions of events in the various modes are then fixed in the final fit to the proper time distribution of the sample. The mass PDFs for the signal components are derived from realistic Monte Carlo, and an example of the mass distributions of various B_s decays reconstructed as $B_s \to D_s^-(\phi\pi^-)\pi^+$ is shown in Fig. 4.2. We must also account for non-B_s backgrounds in the sample, and we describe the parameterization of the background PDFs in Chapter 6. A plot of B_s data with mass fit results showing the signal sitting on top of background components is shown in Fig. 4.3.
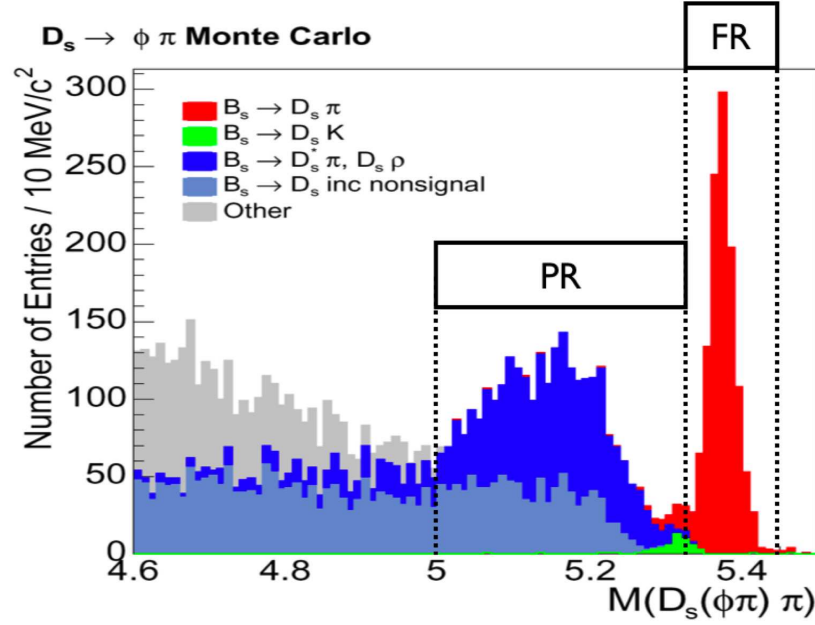
Figure 4.2: Invariant mass distribution of the B_s candidates from $B_s \to D_s X$ Monte Carlo reconstructed as $B_s \to D_s^-\pi^+$. These components are easier to distinguish when looking at their mass distributions than their proper time distributions. The fully reconstructed (FR) and partially reconstructed (PR) regions are also shown.
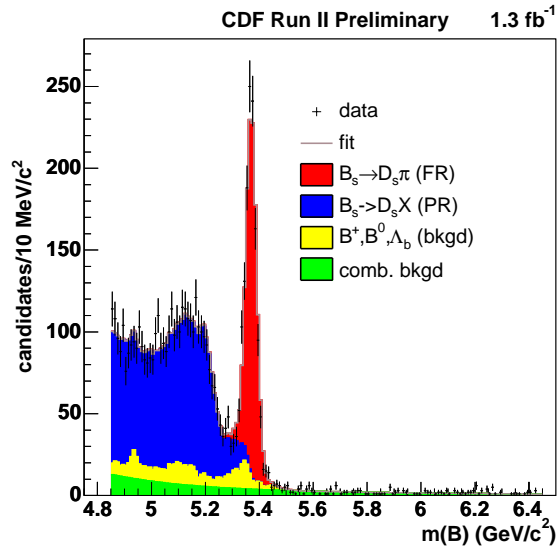
Figure 4.3: $B_s \rightarrow D_s^- \pi^+$ data with mass fit results showing the signal sitting on top of B^+, B^0, Λ_b, and combinatorial background components.

To estimate most systematic uncertainties we use a "toy Monte Carlo" method. For example, if we want to test the effect of increasing the background fraction (determined from the mass fit) in the lifetime fit within its uncertainties, we generate 1000 datasets with larger background fractions and fit the datasets with the default configuration. The toy MC dataset is very simple, in that we only generate a proper time for each event; our toy datasets do not include the mass or any other kinematic variable. To generate the 1000 toy Monte Carlo datasets we throw dice at the proper time PDFs for the various decay modes and backgrounds according to the fraction of events that we expect of each type. The systematic uncertainty is the mean of the 1000 fitter biases $(\tau(\text{generation}) - \tau(\text{fit}))$.

To guard against biasing our $B_s \rightarrow D_s^-(\phi\pi^-)\pi^+$ lifetime measurement when studying the fitter performance, we used three control samples for our initial studies.

- $\boldsymbol{B^0 \rightarrow D^{*-}[\overline{D}^0(K^+\pi^-)\pi^-]\pi^+}$ This mode has four decay products like the B_s mode we are interested in. It has $\sim$4000 events in the fully reconstructed peak and very little background (2.5% in the FR+PR regions).

- $\boldsymbol{B^0 \rightarrow D^-(K^+\pi^-\pi^-)\pi^+}$ This is also a four-body decay. The high statistics ($\sim$18000 events in the $D\pi$ peak) were extremely useful in the tests, but the background rates of 12% in the FR+PR regions provided additional challenges. The B_s sample only has 6% background, but the variations seen when changing the $B^0 \rightarrow D^-\pi^+$ background treatment (described in App. B) informed our assessment of the background systematic uncertainty and prompted us to tighten our cuts.

- $\boldsymbol{B^+ \rightarrow \overline{D}^0(K^+\pi^-)\pi^+}$ Although this is a three-body decay, we included this high statistics ($\sim$20000 events in the $D\pi$ peak) sample as an additional cross-check with a moderate level of background (4.4% in the FR+PR region).

Since the lifetimes of the B^+ and B^0 have already been well-measured elsewhere, it is useful to compare our results to the world averages.

As an additional layer of security, we also keep the B_s results blinded until after the systematic uncertainties have been assessed. Although the statistical uncertainty

31

returned by the blinded fitter is accurate, the results displayed on the screen are offset by an unknown quantity. This blinding is performed using RooFit tools [22].

Chapter 5

Event Reconstruction and Selection

The data events in this analysis must satisfy selection requirements at three stages to be included: trigger selection, candidate reconstruction, and candidate selection.

In its primary role the trigger ensures that events that may be interesting for an analysis are identified in real time and saved for later, more thorough review. As all-hadronic decays of B mesons do not have what one would consider to be easy-to-trigger-on or especially clean signatures (such as muons or large energy deposits in the calorimeter), special hardware was developed to take advantage of the long lifetime of the B mesons. The displaced track trigger system was discussed in Sec. 3.2.3.

In Sec. 5.1 we discuss how B meson candidates are reconstructed in events that pass the trigger criteria. Sec. 5.2 describes additional quality requirements the reconstructed candidates must pass to be included in this analysis.

As an additional tool for understanding the data, we need to study events with b hadrons where we know what the decay products and their kinematic quantities actually are. This is accomplished by modeling b hadron production and decay and simulating the detector and trigger response to the decay products. The Monte Carlo simulation generated for this analysis are discussed further in Sec. 5.3.

5.1 Candidate Reconstruction

After events of interest have been selected by the two-track trigger and permanently recorded, we attempt to reconstruct $B_s \to D_s^-(\phi\pi^-)\pi^+$, $B^0 \to D^-(K^+\pi^-\pi^-)\pi^+$, $B^0 \to D^{*-}[\overline{D}^0(K^+\pi^-)\pi^-]\pi^+$, and $B^+ \to \overline{D}^0(K^+\pi^-)\pi^+$ decays from tracks in the events. We call a collection of tracks consistent with a B meson decay a "B candidate."

The B meson candidates are reconstructed from tracks with $p_T > 350$ MeV/c and at least five hits each in at least two axial and two stereo COT super layers. The tracks must also have $|\eta| < 2.0$ and at least three silicon hits (a requirement that is dropped for the pion from the $D^* \to D^0\pi$ decay).

The first task in the reconstruction is to form a D candidate ($D^- \to K^+\pi^-\pi^-$, $\overline{D}^0 \to K^+\pi^-$, or $D_s^- \to \phi(K^+K^-)\pi^-$) with at least one of the tracks matched to a

SVT track. A loose cut on the reconstructed invariant mass of the D is applied at this point. For the D^0 and D^+, the window is [1.81, 1.92] GeV/c^2. For the D_s, the window is [1.91, 2.03] GeV/c^2. The D candidate must also be separated from the interaction point by 200 μm, measured in the transverse plane. This last requirement removes a significant fraction of the combinatorial background.

Next a B candidate is formed by adding one track (two in the case of the $B^0 \rightarrow D^{*-}\pi^+$) to the D candidate. We require the reconstructed B meet the following criteria:

- reconstructed invariant mass of the B in [4.65, 6.5] GeV/c^2,

- p_T of the B greater than 5.5 GeV/c,

- impact parameter of the B with respect to the beamline less than 100 μm

- transverse component of the B decay length greater than 300 μm, and

- χ^2 of the vertex fit less than 30.

We also require that two tracks in the B candidate satisfy the loosest two-track trigger requirement. Further trigger validation is done later. We permit multiple B candidates in the same event.

5.2 Candidate Selection

To further separate B mesons from backgrounds with similar topologies, we cut on the following variables:

- $\chi^2_{xy}(B)$: a goodness-of-fit quantity for the B candidate vertex using only the track parameters of the transverse plane

- prob($\chi^2_{xy}(B)/1.7$,n(dof)): the probability of the fit for the B candidate vertex using only the track parameters of the transverse plane to have a the resulting χ^2 for its given degrees of freedom. The χ^2 is scaled down by 1.7 to make

the probability distribution flat. The need for this rescaling indicated that the uncertainties returned from the track fit were underestimated.

- $\chi^2_{xy}(D)$: a goodness-of-fit quantity for the D candidate vertex using only the track parameters of the transverse plane

- $L_{xy}(B)$: the decay length of the B candidate projected along its transverse momentum. The decay length is measured from the event-by-event determined primary vertex. This primary vertex position is determined from the other tracks in the event (after removing the B candidate's tracks).

- $L_{xy}(B)/\sigma_{L_{xy}}(B)$: the transverse decay length significance

- $L_{xy}(B \to D)$: the transverse distance between the B and D decay points

- $d_0(B)$: the transverse impact parameter of the B, its distance of closest approach to the event-by-event determined primary vertex

- $z_0(B)/\sigma_{z_0(B)}$: the significance of the longitudinal impact parameter of the B, its distance of closest approach to the event-by-event determined primary vertex

- p_{T_B}: the transverse momentum of the B

- $p_T(\pi_B)$: the transverse momentum of the π from the B

- $\Delta R(D, \pi_B)$: the angular separation between the D and the π from the B, where $\Delta R = \sqrt{(\Delta \eta)^2 + (\Delta \phi)^2}$

- iso(B) $(\Delta R < 1)$: the isolation of the B, defined as $p_T(B)$ divided by the scalar sum of the transverse momenta of all the tracks in a cone of $\Delta R < 1$ around the B.

- $m(D)$: the reconstructed invariant mass of the D

- $m(\phi)$: the reconstructed invariant mass of the ϕ in the $B_s \to D_s^-(\phi\pi^-)\pi^+$ sample

- $m(K\pi\pi) - m(K\pi)$: a D^* veto. A D^* candidate is constructed by taking the D_s^- or D^- daughter tracks and assigning the pion mass to the like-signed particles and the kaon mass to the oppositely signed one. We then check that the mass difference between the D^* and a possible D^0 candidate, $\Delta m = m(K^+\pi^-\pi^-) - m(K^+\pi^-)$ is not consistent with the pion mass.

- $m(K, \pi \mapsto p, \pi)$: a Λ_c veto. A Λ_c^+ is candidate is constructed by assigning the proton mass to the pion that is the opposite charge of the kaon. We then check that the invariant mass is not consistent with the Λ_c mass.

- SVT trigger confirmation: require that the candidate (not just the event) contains two tracks that satisfy the level-2 Scenario Low, Scenario A, or Scenario C trigger requirements.

The combination of cuts used for the individual control sample lifetime analyses are listed in Tab. 5.1. The cuts used for the $B_s \to D_s^-\pi^+$ analysis are listed in Tab. 5.2

Plots of the reconstructed candidate masses for the data events that satisfy the selection criteria can be found in Fig. 5.1.

(a) $B^0 \to D^{*-}[\overline{D}^0(K^+\pi^-)\pi^-]\pi^+$ candidates

(b) $B^+ \to \overline{D}^0(K^+\pi^-)\pi^+$ candidates

(c) $B^0 \to D^-(K^+\pi^-\pi^-)\pi^+$ candidates

(d) $B_s \to D_s^-(\phi\pi^-)\pi^+$ candidates
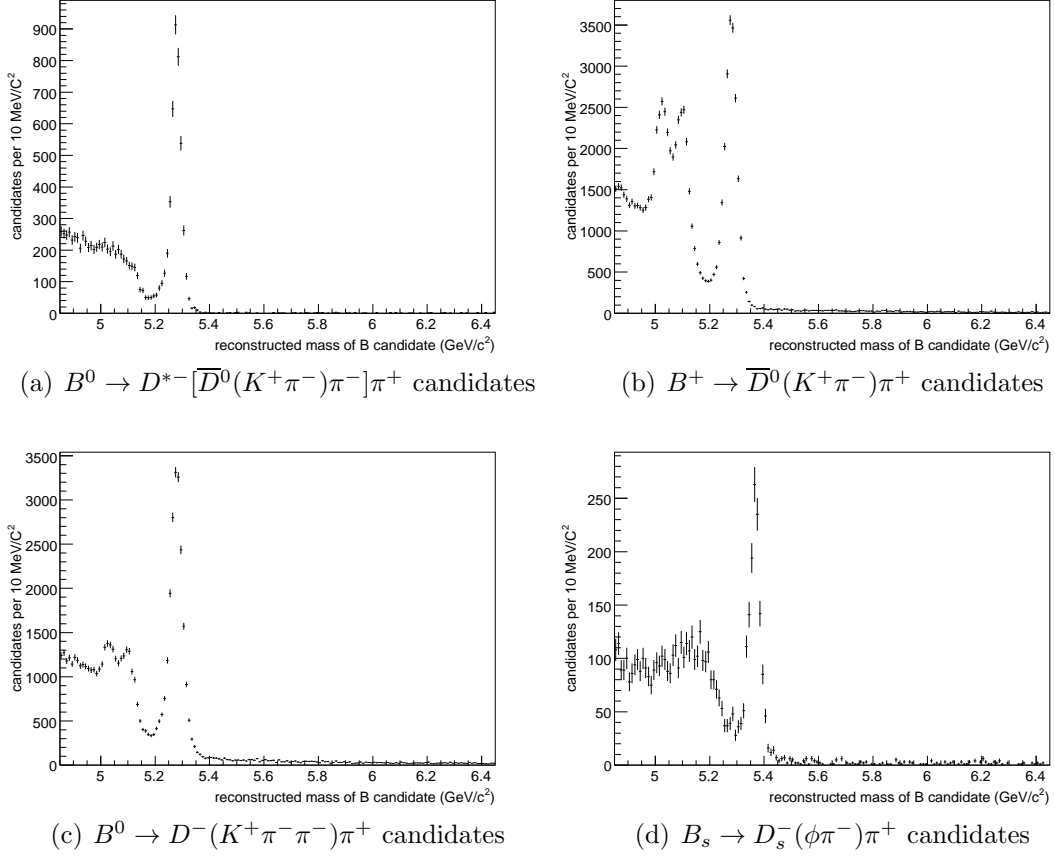
Figure 5.1: Plot of the reconstructed B candidate masses for the signal sample and three control samples after selection criteria are applied.

	$B^0 \to D^-\pi^+$	$B^+ \to \overline{D}^0\pi^+$	$B^0 \to D^{*-}\pi^+$
$\chi^2_{xy}(B)$	< 10	< 10	
$\mathrm{prob}(\chi^2_{xy}(B)/1.7, n(\mathrm{dof}))$			> 0.001
$\chi^2_{xy}(D)$	< 15	< 15	
$L_{xy}(B)$ (μm)	> 450	> 450	
$L_{xy}(B)/\sigma_{L_{xy}}(B)$	> 5	> 5	> 8
$L_{xy}(B \leftarrow D)$	> 0	> 0	
$L_{xy}(B \leftarrow D)/\sigma_{L_{xy}}(B \leftarrow D)$			> -2
$|d_0(B)|$ (μm)	< 60	< 60	
$|d_0(B)/\sigma_{d_0}(B)|$			< 3
$p_T(B)$ (GeV/c)	> 5.5	> 5.5	
$p_T(\pi_B)$ (GeV/c)	> 1.0	> 1.0	> 2.0
$\Delta R(D, \pi_B)$	< 1.5	< 1.5	
$|z_0(B)/\sigma_{z_0}(B)|$	< 3	< 3	< 3
iso(B) ($\Delta R < 1$)	> 0.5	> 0.5	> 0.5
$|m(D^+) - 1869.4|$ (MeV/c^2)	< 20		
$|m(D^0) - 1864.6|$ (MeV/c^2)		< 20	< 20
$m(D^{*+}) - m(D^0)$ (MeV/c^2)			$144 < \Delta m < 165$
π_B SVT match distance			< 25
π_B SVT χ^2			< 15
π_B SVT p_T (GeV/c)			> 2
$|m(K, \pi \mapsto p, \pi) - 2285|$ (MeV/c^2)	> 250	> 250	
$m(K\pi\pi) - m(K\pi)$ (MeV/c^2)	$\Delta m > 180$	$\Delta m > 180$	
Good run list	B_s mixing version 17	B_s mixing version 17	B_s mixing version 17
SVT trigger confirmation	$\checkmark$	$\checkmark$	$\checkmark$

Table 5.1: Final cuts used to select candidates for the $B^0 \to D^-\pi^+$, $B^+ \to \overline{D}^0\pi^+$, and $B^0 \to D^{*-}\pi^+$ control samples. See the text for definitions of the variable.

	$B_s \to D_s^- (\phi \pi^-) \pi^+$
$\chi^2_{xy}(B)$	< 10
$\chi^2_{xy}(D)$	< 15
$L_{xy}(B)$ (μm)	> 450
$L_{xy}(B)/\sigma_{L_{xy}}(B)$	> 5
$L_{xy}(B \leftarrow D)$	> 0
$|d_0(B)|$ (μm)	< 60
$p_T(B)$ (GeV/c)	> 5.5
$p_T(\pi_B)$ (GeV/c)	> 1.0
$\Delta R(D, \pi_B)$	< 1.5
$|z_0(B)/\sigma_{z_0}(B)|$	< 3
iso(B) ($\Delta R < 1$)	> 0.5
$m(D_s)$ (MeV/c^2)	$|m - 1968.3| < 12$
$m(\phi)$ (MeV/c^2)	$1013 < m < 1028$
$m(K\pi\pi) - m(K\pi)$ (MeV/c^2)	$\Delta m > 180$
Good run list	B_s mixing version 17
SVT trigger confirmation	$\checkmark$

Table 5.2: Final cuts used to select candidates for the $B_s \to D_s^- \pi^+$ signal sample.

5.3 Monte Carlo Samples

Realistic Monte Carlo simulations of b hadron decays are essential for the mass and lifetime fits performed in these analyses. The decay modes generated for each analysis are listed in Tab. 5.3. The b hadron in each Monte Carlo event is generated with `Bgenerator` [17], a code package that can generate and fragment a b quark. The b hadrons are then decayed by `EvtGen` [18], which handles complex sequential decays. `EvtGen` allows the user to set the branching ratios for the decay modes and the hadron lifetimes. The daughter particles are then passed through a `Geant-3` [19] simulation of the CDF II detector and an emulation of the trigger.

The Monte Carlo candidates have to satisfy the same candidate selection requirements as the data candidates with only a few exceptions. Because the simulations do not start with more than one b hadron per event, the iso(B) requirement is trivial. We also do not attempt to model $z_0(B)$ or its significance, so this cut is not applied to Monte Carlo.

In Chapters 6 and 7, we discuss how well Monte Carlo reproduces the data.

Channels			Sample name
		$\overline{B}^0 \to D^+\pi^-$ fit	
$\overline{B}^0$	$\to$	$D^+\pi^-(n\gamma)$	b0dkpp
$\overline{B}^0/B^0$	$\to$	D^+X	z35ba0
B^-/B^+	$\to$	D^+X	bdpkpx
B_s	$\to$	$D_s^-(\phi\pi^-)X$	mcbh03
		$\overline{B}^0 \to D^{*+}\pi^-$ fit	
$\overline{B}^0$	$\to$	$D^{*+}\pi^-(n\gamma)$	b0dspp
$\overline{B}^0/B^0$	$\to$	$D^0\pi^+X$	z35b90
B^-/B^+	$\to$	$D^0\pi^+X$	bd0kpx
		$B^+ \to \overline{D}^0\pi^+$ fit	
B^-	$\to$	$D^0\pi^-(n\gamma)$	bd0kpp
$\overline{B}^0/B^0$	$\to$	$D^0\pi^+X$	z35b90
B^-/B^+	$\to$	$D^0\pi^+X$	bd0kpx
		$B_s \to D_s^-\pi^+$ fit	
$\overline{B}_s^0$	$\to$	$D_s^+(\phi\pi)\pi^-(n\gamma)$	bsdspi
$\overline{B}_s^0/B_s^0$	$\to$	$D_s^+(\phi\pi^+)X$	mcbh03
$\overline{B}^0/B^0$	$\to$	D^+X	z35ba0
B^-/B^+	$\to$	D^+X	bdpkpx
$\overline{B}^0$	$\to D_s^{(*)+}(\phi\pi(\gamma/\pi^0))X$		b0dssx
Λ_b	$\to$	$\Lambda_c(pK^-\pi^+)X$	jlcbg0

Table 5.3: Monte Carlo samples used in this analysis. The samples are available in SAM or in the process of being copied to SAM.

Chapter 6

Mass Fit Description

We determine the composition of the sample from a fit to the invariant mass distribution of the B_s candidates. The fractions of events in each mode are then fixed inputs into the later fit for $\tau(B_s)$.

The mass fit code used here was originally developed for parallel $DK/D\pi$ branching ratio analyses for the B^0, B^+, and B_s [23, 24, 25]. The fitter, the fitter validation, and the results for the B_s branching ratio analysis in particular are described in greater detail in Ref. [26].

6.1 Likelihood Formulation

The mass fit is a maximum likelihood fit to the invariant masses of the candidates reconstructed as $D_s\pi$. The likelihood can be extended or non-extended. The extended and unextended fits should yield equivalent results, and both were implemented to verify the performance of the fitter. In the extended case, the likelihood is written as

$$L(\mu_1, \ldots, \mu_M) = \frac{\exp(-\sum_j \mu_j)}{N!} \prod_{i=1}^{N} \sum_{j=1}^{M} \mu_j\, p_j(m_i) \tag{6.1}$$

where the μ_j, the number of events in the jth component of the fit, are the only variables allowed to float. $\prod_{i=1}^{N}$ is the product over the N candidates in the sample. $\sum_{j=1}^{M}$ is the sum over the M components (signal and background). We will discuss later the form of the mass PDFs for each component, $p_j(m_i)$. In the unextended case, we fit for the fraction of events in each mode, f_j. The likelihood is as follows:

$$L(f_1, \ldots, f_{M-1}) = \prod_{i=1}^{N} \sum_{j=1}^{M} f_j\, p_j(m_i), \quad \text{where } f_M = 1 - \sum_{j=1}^{M-1} f_j \tag{6.2}$$

There are many options that are available for the fit, and different combinations are chosen for each control sample and the signal sample. We list various options below.

- The fitter can use histograms as the mass PDFs or functional forms. The shape of a background template, for example, is an exponential plus a constant. These shape parameters can be allowed to vary, although after the auxiliary fits to

the background samples, we keep them fixed for all final fits described in this note.

- The absolute normalization of a component can be fixed.

- The relative normalization of two components can be fixed or constrained assuming Gaussian errors.

6.2   Mass Fit Components

The choice of fit components is channel-dependent. In all cases, these components can be characterized as coming from one of three possible sources: single B, fake D + track, and real D + track. As an example, we present the templates for the $B_s \to D_s^- \pi^+$ mass fit as we discuss each type.

6.2.1   Single B

Single B candidates are composed entirely of tracks from a single b hadron. If the tracks come from a B_s, these modes are considered to be "signal." We also have "background" single B candidates where all the tracks come from a B^+, B^0, or Λ_b hadron.

The mass PDFs $p_j(m_i)$ for signal components come from B_s Monte Carlo samples, where we know which decay modes are actually being reconstructed as $D_s\pi$. Since these samples have several times the statistics of data, we choose to use histograms instead of functional forms for these PDFs. This technique has the advantage that it properly accounts for non-Gaussian tails and difficult to parameterize kinematic edges. The number of single-B components varies for each channel. In the B_s case, we separate out the following B_s modes:

- $B_s \to D_s\pi$

- $B_s \to D_s\pi(n\gamma)$

- $B_s \to D_sK$

45

- $B_s \to D_s \rho$

- $B_s \to D_s^* \pi$

- $B_s \to D_s^{(*)} K^{(*)}$

- $B_s \to D_s^{(*)} eX$

- $B_s \to D_s^{(*)} X$ (everything else B_s).

How these modes are normalized relative to each other is detailed in Table 10.5 A subset of the mass templates for these B_s decay modes reconstructed as $B_s \to D_s^-(\phi\pi^-)\pi^+$ are shown in Fig. 6.1.
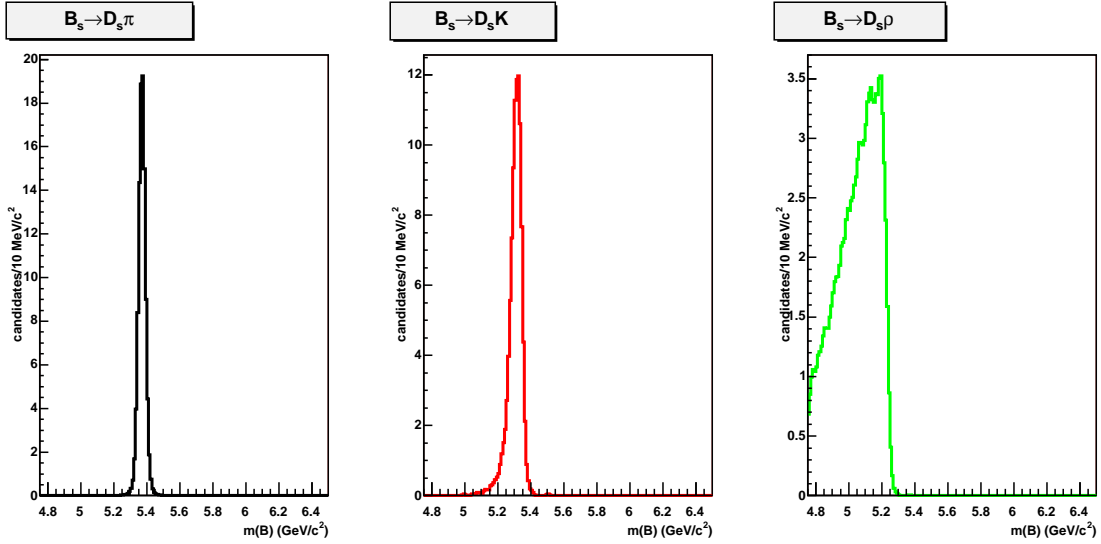
Figure 6.1: The mass templates for a subset of B_s decay modes. From left to right: $B_s \to D_s\pi$, $B_s \to D_sK$, and $B_s \to D_s\rho$.

For the background B^+, B^0, and Λ_b decays that we reconstruct as $D_s\pi$, we can still use high statistics b hadron Monte Carlo to derive the $p_j(m_i)$ for these modes. For the B_s mass fit, we separate out the following single B backgrounds:

- $B^0 \to D_s^{(*)} K$

- $B^0 \to D_s^{(*)} \pi$

46

- $\Lambda_b \to \Lambda_c X$

- $B^0/B^+ \to D^+ X$.

In order to get a good mass fit, our mass PDFs need to reproduce the resolution of the mass peaks, and we must ensure there is no systematic shift. We apply two adjustments to the mass PDFs from MC to bring them into better agreement with data. A small difference between the magnetic field in CDF II and the field used in the simulation caused a small shift in the reconstructed masses of the D's and B's. To correct for this effect, the MC mass templates are scaled by 1.0002482. The mass resolution of the Monte Carlo is also slightly better than in data. To correct for this effect, the MC mass templates are convoluted with a Gaussian of width 6.43 MeV/c^2. Further comparisons between data and Monte Carlo are discussed in Chap. 7, as they are most relevant to the lifetime PDFs.

6.2.2 Fake D + Track

The fake-D + track component is a background that can still include tracks from b hadron decays, but the distribution of the masses of the tracks reconstructed as D_s's in these candidates does not peak at the D_s mass. The mass template for these events comes from the D_s sidebands. An illustration of the D_s peak and D_s sideband regions is shown in the left plot of Fig. 6.2.

We could simply use the reconstructed "B_s" mass of candidates in the D_s sidebands as the mass PDF, but we find that there is some real D_s contamination in this sample. The D_s sidebands are close enough to the D_s peak that there is some leakage from single-B events with poor mass resolution. This leakage must be subtracted out in an auxiliary fit. The right plot of Fig. 6.2 shows the reconstructed "B_s" mass of the fake-D + track candidates. Superimposed on the data plot is the result of a fit with two components (1) a histogram for the real D_s leakage taken from single-B Monte Carlo and (2) an exponential plus a constant that we consider the true fake-D + track $p_j(m_i)$. When this fake-D +track PDF is used in the final mass fit, we fix its normalization by extrapolating the D_s sidebands into the D_s signal region.

(a) Sample D_s peak on top of flat fake D_s background

(b) D_s sideband with signal leakage
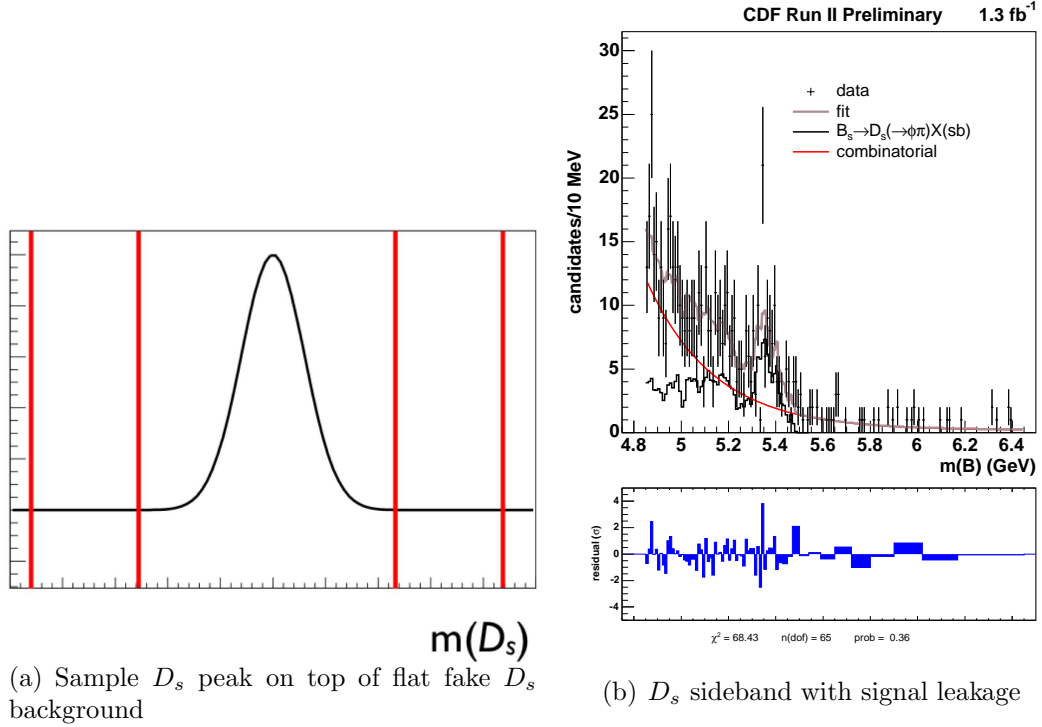
Figure 6.2: The left plot is an illustration of the D_s sideband region when the D_s mass of a candidate is plotted. The right plot is the reconstructed "B" mass of these fake-D + track candidates, and the B_s signal leakage is clearly visible. We use the function fit to this histogram as the mass PDF for the fake-D + track component.

6.2.3 Real D + Track

The real-D + track component is a background consisting of a real D_s, either promptly produced in the beamspot or from a b hadron decay, plus a track from the underlying event or other the b hadron. We take the mass PDF for these events from the D_s peak of events reconstructed as the wrong-sign (WS) combination $D_s^- \pi^-$, which we do not expect to come from a real physics source. Sideband subtraction in the D_s mass is performed to isolate the real D_s's. The invariant mass of the $D_s \pi$ is then fit with an exponential plus a constant in the restricted region [5.00, 6.45] GeV/c^2. Below 5.00 GeV/c^2 partially reconstructed single-B modes contaminate the WS distribution. The normalization of the real-D + track component is allowed to float in the final mass fit, but the shape parameters are fixed. The real-D + track shape for the $D_s^- \pi^-$ is shown in Fig. 6.3 with a visual explanation of sideband

48
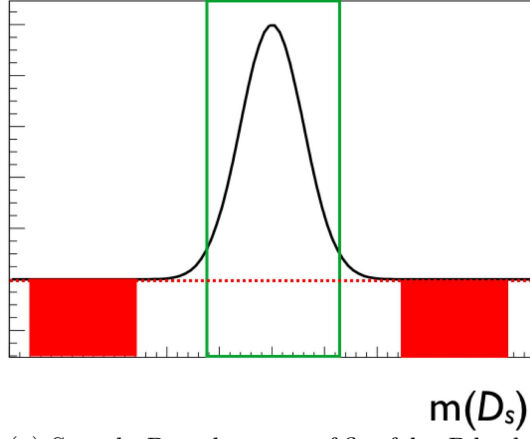
subtraction.

(a) Sample D peak on top of flat fake-D background
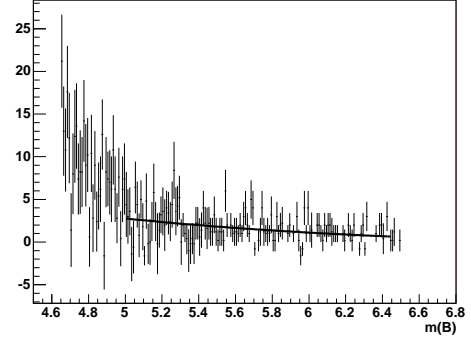
(b) Sideband subtracted WS

Figure 6.3: The left plot is an illustration of the D peak and D sideband regions when the D mass of a candidate is plotted. The right plot is $D_s^- \pi^-$ invariant mass distribution after sideband subtraction in the D_s mass has been performed. We use the function fit to this histogram as the mass PDF for the real-D + track component.

Chapter 7

Lifetime Fit Description

The lifetimes of the B mesons are determined from unbinned maximum likelihood fits with separate probability distribution functions for the fully reconstructed (FR) modes, partially reconstructed (PR) modes, and the backgrounds. Only the FR and PR PDFs depend on τ_B, the B lifetime. The likelihood can be written as

$$\mathcal{L} = \prod_{i=1}^{N_{\text{events}}} \left[f_{\text{FR}} P_{\text{FR}}(ct_i) + \sum_{j=1}^{m} f_{\text{PR},j} P_{\text{PR},j}(ct_i) + \sum_{k=1}^{n} f_{\text{Bkgd},k} P_{\text{Bkgd},k}(ct_i) \right] \qquad (7.1)$$

where m is the number of PR modes and n the number of backgrounds.

The fractions f_{FR}, $f_{\text{PR},j}$, and $f_{\text{Bkgd},k}$ are determined from a mass fit and are fixed in the lifetime fit. The mass fit procedure is described in Chap. 6. We assess a systematic uncertainty for using fixed fraction f_{Bkgd}, which will be discussed later. The fractions satisfy the condition

$$f_{\text{FR}} + \sum_{j=1}^{m} f_{\text{PR},j} + \sum_{k=1}^{n} f_{\text{Bkgd},k} = 1$$

The functional forms for P_{FR}, P_{PR}, and P_{Bkgd} are discussed in Section 7.2.

The lifetime fit is performed in three B mass regions, the third region being the union of the first two. The fully reconstructed (FR) region contains the bulk of the DK and $D\pi$ peaks. The partially reconstructed (PR) region consists mostly of $D\rho$ and $D^*\pi$ and has a larger background fraction. The FR and PR regions are fit separately to check for agreement. The third fit is to the union of the FR and PR regions. This last fit properly propagates the errors from the FR and PR regions, and its result is the final value we quote.

7.1 Lifetime Fit Components

As in the mass fit, the choice of lifetime fit components is channel dependent. How each component is treated depends on its decay structure and whether it can provide information about the B lifetime. Each of the components fits into one of three categories of proper time PDFs. We list the categories below.

- **Fully Reconstructed:** The only mode fully reconstructed in each analysis is the $D\pi$. The fully reconstructed mode has been the main focus of the previous

hadronic lifetime analyses, as there are no uncertainties associated with tracks missing from the reconstruction. The shape parameters of this PDF come from an auxiliary fit to a Monte Carlo sample where the lifetime used for generation is known. All the parameters for the PDF except the lifetime of the B meson are then fixed for the final fit to data. The partially reconstructed, PHOTOS-modeled $D\pi(n\gamma)$ decays are grouped with the FR $D\pi$ for this analysis. This simplification will be considered as a possible source of systematic uncertainty.

- **Partially Reconstructed:** As they also come from the B meson of interest, the DK, $D\rho$, $D^*\pi$, and other partially reconstructed modes can contribute to the B lifetime measurement. Since the partially reconstructed candidates are missing tracks after reconstruction, a multiplicative correction factor K to the decay length is needed. See Section 7.2.1 for a complete definition of the K factor. The distributions of the K factors for these modes are taken from Monte Carlo and folded into the PR PDFs. Strictly speaking, the DK mode is not a partially reconstructed mode, but a mode with a single mis-identified track (we call the K a π during reconstruction). However, we choose to group it with the PR modes, since it also requires a K factor. Similar to the FR PDF, the shape parameters of the PR PDFs come from auxiliary fits to Monte Carlo samples where the lifetime used for generation is known. All the parameters for the PDFs except the lifetime of the B meson are then fixed for the final fit to data.

    In the B^0 case, the B^+ PR decays also contribute to the lifetime measurement with the lifetime ratio $\tau(B^+)/\tau(B^0)$ fixed to the PDG value 1.071 [5]. Likewise the PR B^0s contribute to the B^+ lifetime measurement.

- **Background:** The backgrounds can either come from b hadrons of other flavors for which we have Monte Carlo or be combinatorial in nature. The latter are combinations of tracks from various sources (*e.g.*, the other b hadron and the underlying event) which pass our reconstruction cuts without coming from a single, easily modeled physics source. In the mass fit, the combinatorial

backgrounds are grouped into real D + track and fake D + track events. For the lifetime fit, there are two proxies that are available.

- The B upper sideband, taken from the m_B interval [5.7, 6.4] GeV/c^2, contains a mixture of real and fake D's. The fractions of each are determined by counting the number of events in the D-peak and D-sideband regions and extrapolating the sideband region under the peak.

- The D sidebands in the fully and partially reconstructed regions contain fake D's. However, there is some leakage from poorly measured signal events as well. The leakage fraction is determined in an auxiliary fit as described in Chap. 6.

Since neither background proxy is 100% real or fake D, we must use the mass fit fractions as inputs to calculate the fractions of B upper sideband and D sideband needed for the lifetime fit. The calculation also involves an adjustment of the signal fractions. A discussion of the calculation is presented in Chap. 8 along with a numerical example.

The background PDFs come from fits to Monte Carlo samples (for single-B backgrounds) or to the background proxies discussed above (for fake D and real D not coming from a single B meson). All the background parameters are fixed in the final lifetime fit.

7.2 Functional Forms of Probability Distribution Functions

7.2.1 Definition of Variables

With perfect knowledge of the decay of a B meson, the true proper decay length ct' could be easily calculated as

$$ct' = \frac{L'_{xy} \cdot m'_B}{p'_{T_B}} \qquad (7.2)$$

53

where p'_{T_B} is the transverse momentum of the B, L'_{xy} the decay length projected along the direction of p'_{T_B}, and m'_B the B mass. The prime indicates that the symbol represents the true value of the quantity, not the measured value.

In our experimental situation, we define the reconstructed proper decay length ct of a fully reconstructed B meson as

$$ct \equiv \frac{L_{xy} \cdot m_B^{rec}}{p_{T_B}} \qquad (7.3)$$

Note that the reconstructed mass of the B meson in the event m_B^{rec} is used instead of the world average B mass.

A salient feature of this analysis is the treatment of partially reconstructed B mesons as signal events that contribute to the lifetime measurement. Since in the partially reconstructed cases L_{xy}, m_B^{rec}, and $p_T(B)$ are extracted from candidates that are missing tracks after reconstruction or have the wrong mass assignment for a track, a multiplicative correction factor K to the decay length is needed. The distribution of the K factor is taken from Monte Carlo, where we have the advantage of knowing what type of B was produced and its daughter particles' true properties before detector simulation (we will call this the MCTRUTH). The K factor should only correct for the track dropped during reconstruction and not include any of the uncertainties introduced by detector simulation. For each Monte Carlo event, one can construct a "partially reconstructed MCTRUTH candidate" by the following procedure:

1. For each track in the reconstructed candidate, find a MCTRUTH particle match.

2. Check that no MCTRUTH particle has been matched to more than one reconstructed track.

3. Construct a four-momentum vector for each reconstructed track using the three-momentum of the MCTRUTH particle and the default mass assumption of reconstruction. For example, if a MCTRUTH kaon was reconstructed

as a pion, use the kaon's true three-momentum and the pion mass hypothesis to fill the four-momentum vector.

4. Create the four-momentum vector of the partially reconstructed MCTRUTH candidate by summing the vectors created in step 3.

By constructing the ratio of the true decay length of the B meson to the decay length that would be calculated from the partially reconstructed MCTRUTH candidate (using the four-momentum from the above procedure and the true B-decay vertex position), we can quantify the effect of missing tracks and misassigned masses. K is then given as

$$
\begin{aligned}
K &= \frac{ct'}{ct_{\mathrm{MCTRUTH}}(\mathrm{PR})} \\
&= \frac{L'_{xy}}{L_{xy}(\mathrm{PR})} \cdot \frac{p_T(\mathrm{PR})}{p'_T} \cdot \frac{m'_B}{m_{rec}(\mathrm{PR})} \\
&= \frac{1}{\cos\theta_{\mathrm{PR}}} \cdot \frac{p_T(\mathrm{PR})}{p'_T} \cdot \frac{m'_B}{m_{rec}(\mathrm{PR})},
\end{aligned}
\tag{7.4}
$$

where θ_{PR} is the angle in the $x - y$ plane between the transverse momenta of the fully and partially reconstructed B's. Note that although the position of the B-decay vertex is the same in both candidates, the decay length projected along the transverse momentum changes by a factor of $\cos\theta_{PR}$. The primes again denote Monte Carlo truth. "PR" denotes that a quantity is calculated from the partially reconstructed MCTRUTH candidate. The K factor distributions from Monte Carlo are shown in Figures 7.1-7.4.

7.2.2   PDF for Fully Reconstructed Decays

With perfect knowledge of decays of particles with lifetime τ, the distribution of the true decay lengths ct' would be described by an exponential decay model. The PDF is given by the following equation:

$$
P_{\mathrm{FR}}(ct') = \frac{1}{c\tau} e^{\frac{-ct'}{c\tau}}
\tag{7.5}
$$

55
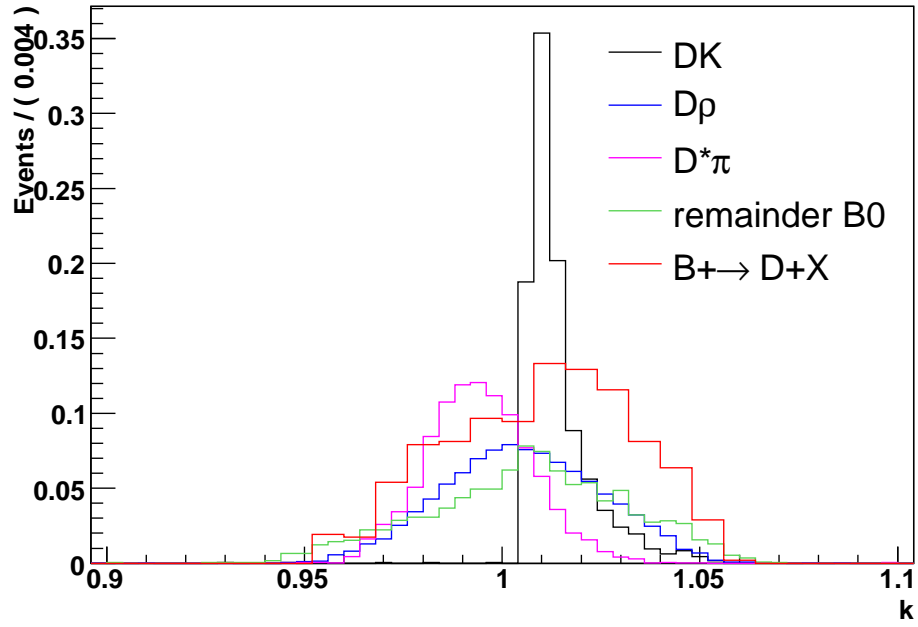
Figure 7.1: K factor distributions for the modes partially reconstructed as $B^0 \to D^-(K^+\pi^-\pi^-)\pi^+$. The remainder piece encompasses all $B^0 \to D^-\pi^+X$ modes that are not $D^-\pi^+$, D^-K^+, $D^{*-}\pi^+$, or $D^-\rho^+$
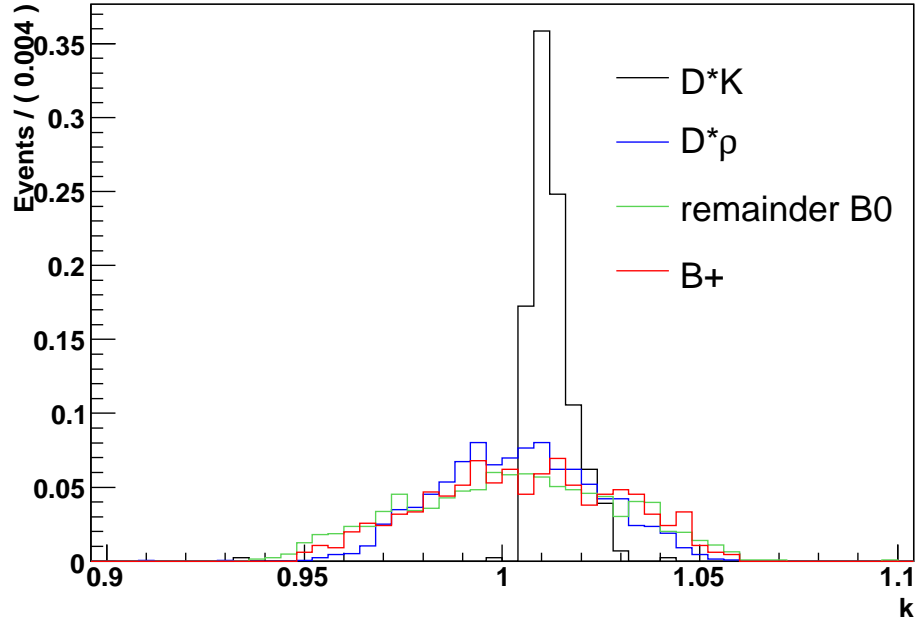
Figure 7.2: K factor distributions for the modes partially reconstructed as $B^0 \to D^{*-}[\overline{D}^0(K^+\pi^-)\pi^-]\pi^+$.
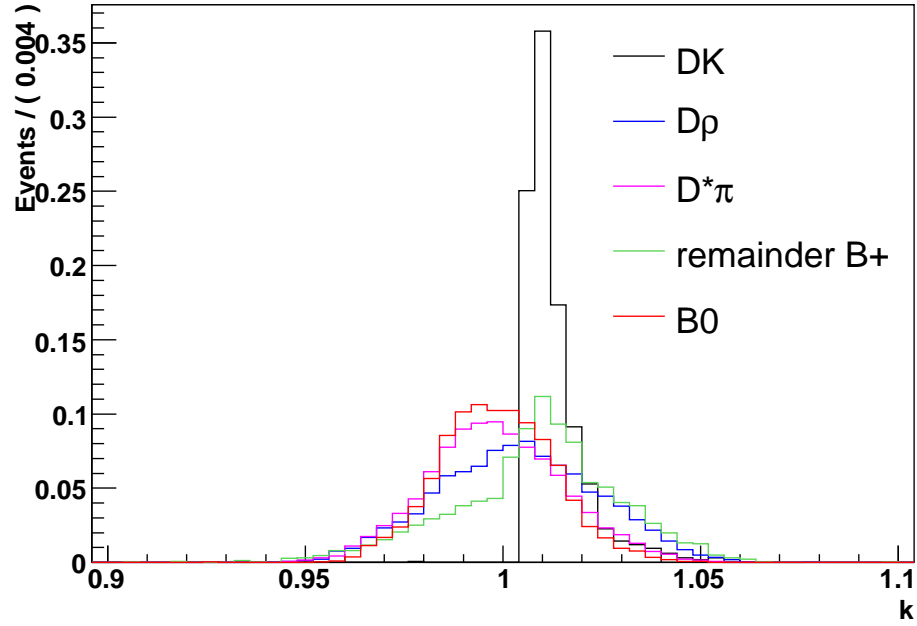
Figure 7.3: K factor distributions for the modes partially reconstructed as $B^+ \to \overline{D}^0(K^+\pi^-)\pi^+$.
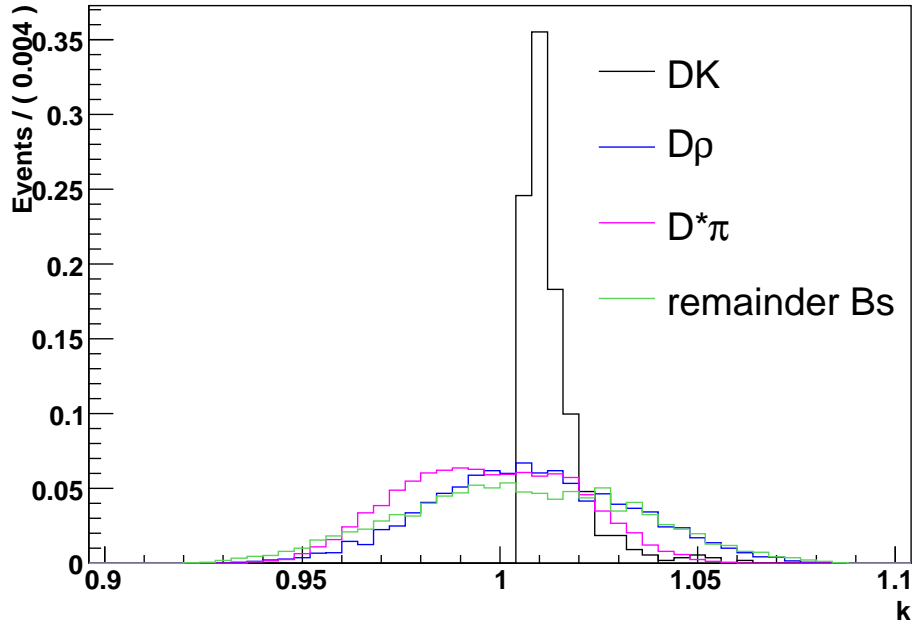
Figure 7.4: K factor distributions for the modes partially reconstructed as $B_s \to D_s^-(\phi\pi^-)\pi^+$. The remainder piece encompasses all $B_s \to D_s^-(\phi\pi^-)\pi^+X$ modes that are not $D_s^-\pi^+$, $D_s^-K^+$, $D_s^{*-}\pi^+$, or $D_s^-\rho^+$

Experimentally, we find a measured decay length ct that has been smeared by the detector resolution σ. This gives

$$P_{\text{FR}}(ct) = \frac{1}{c\tau} e^{\frac{-ct'}{c\tau}} \otimes_{t'} \frac{1}{\sqrt{2\pi}\sigma} e^{\frac{-(ct-ct')^2}{2\sigma^2}} \tag{7.6}$$

where $\otimes_{t'}$ is the convolution over the true decay time variable t'.

In this analysis the decay length distribution is also sculpted by the trigger selection and analysis cuts. These enter the PDF as a function of the measured decay length, called the efficiency curve $\text{eff}(ct)$. The parameterization of the efficiency curve will be discussed in Section 7.2.5.

$$P_{\text{FR}}(ct) = \left[\frac{1}{c\tau} e^{\frac{-ct'}{c\tau}} \otimes_{t'} \frac{1}{\sqrt{2\pi}\sigma} e^{\frac{-(ct-ct')^2}{2\sigma^2}} \right] \cdot \text{eff}(ct) \tag{7.7}$$

A more detailed discussion of the fit for the parameters of this function follows in Section 7.3. In brief, we determine a σ and the efficiency curve parameters for each mode separately by fitting Monte Carlo where the τ used for generation is known and fixed in the preliminary fit. The efficiency curve parameters and σ are then fixed in the fit to the data. The only free parameter in the unbinned likelihood fit to the data is the lifetime of the B meson being measured. Note that although σ is intended to be a detector resolution, it floats along with the efficiency curve parameters during the fits to the Monte Carlo. During this process it becomes correlated with the other parameters describing the overall PDF shape and loses some of its physical meaning.

Although we have been cavalier about writing the above expression without explicit normalization, it should be done at least once. The following normalization condition applies:

$$\int P(ct) \, \mathrm{d}ct \;=\; 1 \tag{7.8}$$

Equation (7.7) should then be written as

$$P_{\text{FR}}(ct) = \frac{\left[\frac{1}{c\tau} e^{\frac{-ct'}{c\tau}} \otimes_{t'} \frac{1}{\sqrt{2\pi}\sigma} e^{\frac{-(ct-ct')^2}{2(\sigma)^2}} \right] \cdot \text{eff}(ct)}{\int \left[\frac{1}{c\tau} e^{\frac{-ct'}{c\tau}} \otimes_{t'} \frac{1}{\sqrt{2\pi}\sigma} e^{\frac{-(ct-ct')^2}{2(\sigma)^2}} \right] \cdot \text{eff}(ct) \, \mathrm{d}ct} \tag{7.9}$$

but we will not explicitly write the normalization again; it is implied.

7.2.3 PDF for Partially Reconstructed Decays

For the partially reconstructed case the distribution of K factors must be folded in as well.

$$P_{\text{PR}}(ct) = \left[\frac{1}{c\tau} e^{\frac{-ct'}{c\tau}} \otimes_{t'} \frac{1}{\sqrt{2\pi}K\sigma} e^{\frac{-(K \cdot ct - ct')^2}{2K^2\sigma^2}} \otimes_K p(K) \right] \cdot \text{eff}(ct) \qquad (7.10)$$

Consider the $B^0 \to D^-\pi^+$ sample. This analysis uses a FR PDF for the $D\pi$ signal. The DK, $D^*\pi$, and $D\rho$ modes are also treated as signal, using separate PR PDFs with separate K factor distributions, σ's, and efficiency curves for each mode. The remaining B^0 decay modes also contribute to the $c\tau$ measurement, but they are grouped together with a collective K factor distribution, σ, and efficiency curve into a single PR PDF. The $B^+ \to D^+\pi^-X$ decays are treated as a single partially reconstructed mode with the lifetime ratio $\tau(B^+)/\tau(B^0)$ fixed to the PDG value 1.071 [5]. In this way they also contribute to the measurement of $\tau(B^0)$.

7.2.4 PDF for Background Events

The functional form of the background PDFs is the same as the FR PDF. One should note, however, that the decay constant of the exponential, τ_{Bkgd}, has little physical meaning for some backgrounds, since the background may not come from a single physics source (such as a decaying B meson) and may be a mixture of real D's and fake D's plus a track. Because τ_{Bkgd} is degenerate with other lifetime-like parameters in the efficiency curve, we fix it at 500 μm with no detrimental effect on the fit quality.

$$P_{\text{Bkgd}}(ct) = \left[\frac{1}{c\tau_{\text{Bkgd}}} e^{\frac{-ct'}{c\tau_{\text{Bkgd}}}} \otimes_{t'} \frac{1}{\sqrt{2\pi}\sigma_{\text{Bkgd}}} e^{\frac{-(ct - ct')^2}{2\sigma_{\text{Bkgd}}^2}} \right] \cdot \text{eff}(ct) \qquad (7.11)$$

Although its name suggests otherwise, $\text{eff}(ct)$ for the real D and fake D backgrounds is not actually an efficiency curve. Efficiency curves parameterize the effect of the trigger and analysis cuts on the shape of the measured ct distribution for signal events. Since we do not have background Monte Carlo and can not tell how the trigger selections and analysis cuts affect the background shape, the best we can do is

to choose a sample to serve as a proxy for the background and use its ct distribution as the background PDF. We choose to parameterize the shape of the background instead of using a histogram, and a natural choice for the parameterization is a functional form similar to those used for the fully and partially reconstructed modes. Again, eff(ct) for the background PDF does not have the same physical significance.

7.2.5 Efficiency Curve Parameterization

The efficiency curves describing the sculpting of the decay length distribution due to trigger and analysis cuts are parameterized the same way as in the previous hadronic B lifetime analysis [20].

$$\text{eff}(ct) = \begin{cases} 0 & \text{if } ct \leq \beta_i \\ \sum_{i=1}^{3} N_i \cdot (ct - \beta_i)^2 \cdot e^{\frac{-ct}{\tau_i}} & \text{if } ct > \beta_i \end{cases} \tag{7.12}$$

Since the total PDF must be normalized to one, the efficiency curve actually only contributes 8 additional parameters to the PDF: β_1, β_2, β_3, τ_1, τ_2, τ_3, N_2/N_1, and N_3/N_1.

The parameters of the efficiency curves for the FR and PR modes and single-B backgrounds (e.g., B_s in the $B^0 \to D^- \pi^+$) are derived from unbinned likelihood fits to the Monte Carlo with τ_B set to the lifetime used for the Monte Carlo generation. For some fits to low statistics Monte Carlo, fewer than eight parameters are needed for a good fit (high χ^2 probability), and N_3 and possibly N_2 may be set to zero.

After the efficiency curve parameters are found in fits to the reweighted Monte Carlo (with τ_B set to the generator lifetime), they are fixed for the fit to the data. The only free parameter in the unbinned likelihood fit to the data is the lifetime of the meson being measured.

7.3 Data and Monte Carlo Agreement

7.3.1 Reweighting in $p_T(B)$ and Trigger Category

The data collected differs from the Monte Carlo in both its momentum spectrum and its trigger mix. To prevent the trigger rate from exceeding the processing limits of the system, CDF prescales some triggers when the instantaneous luminosity is high and removes the prescales as more bandwidth becomes available. A prescale factor of two means that only 50% of the events that satisfy a trigger's requirements are passed to the next level; the rest are vetoed. Since our Monte Carlo does not match the prescale pattern for the full dataset, the mixture of events that pass Scenario Low, Scenario A, and Scenario C does not match either. A different prescale pattern for triggers with various momentum thresholds also contributes to the B momentum spectrum disagreement between data and Monte Carlo. To correct for these effects, the Monte Carlo is reweighted in two dimensions: p_T of the reconstructed B and fraction of events in a given trigger category. The three trigger categories are as follows:

- Scenario C

- Scenario A, not Scenario C

- Scenario Low, not Scenario A, not Scenario C

An event must have both the L2 bit and SVT confirmation of the trigger to be sorted into a given trigger category.

The fractions of the events found in the three categories in data, Monte Carlo, and Monte Carlo after 2-D reweighting to the full sample are listed in Tab. 7.1 for the $B^0 \to D^- \pi^+$ sample, Tab. 7.2 for the $B^0 \to D^{*-} \pi^+$ sample, Tab. 7.3 for the $B^+ \to \overline{D}^0 \pi^+$ sample, and Tab. 7.4 for the $B_s \to D_s^- \pi^+$ sample. The effect of 2-D reweighting on the p_T spectrum of the B is shown in Fig. 7.5 for the exclusive $B^0 \to D^- \pi^+$ Monte Carlo, Fig. 7.6 for the exclusive $B^0 \to D^{*-} \pi^+$ Monte Carlo, Fig. 7.7 for the exclusive $B^+ \to \overline{D}^0 \pi^+$ Monte Carlo, and Fig. 7.8 for the exclusive $B_s \to D_s^- \pi^+$ Monte Carlo.

Reweighting in both dimensions is performed simultaneously for the $B^0 \to D^- \pi^+$ and $B^+ \to \overline{D}^0 \pi^+$ samples. Because the statistics of the $B^0 \to D^{*-} \pi^+$ and $B_s \to D_s^- \pi^+$ data are not sufficient, the reweighting is performed in two steps:

1. A ratio of the data in the B-peak region p_T histogram to the $B \to D\pi$ exclusive Monte Carlo p_T histogram is constructed. This ratio histogram is used to perform the momentum reweighting separately for each mode in the $B \to D\pi$ Monte Carlo samples.

2. A ratio of the data in the B-peak region trigger category histogram to the $B \to D\pi$ exclusive Monte Carlo trigger category histogram is constructed. This ratio histogram is then used to perform the trigger category reweighting for the $B \to D\pi$ Monte Carlo samples that result from step 1.

Sample	Scenario Low ($\neg$A and $\neg$C)	Scenario A ($\neg$C)	Scenario C
Monte Carlo Before 2D Reweighting			
$D^-\pi^+$	36.6	23.1	40.3
D^-K^+	37.5	22.4	40.1
$D^{*-}\pi^+$	37.6	23.2	39.2
$D^-\rho^+$	37.6	23.2	39.2
B^0 remainder	39.1	23.1	37.8
B^+	39.0	23.7	37.3
B_s	16.8	27.3	55.9
Data			
`xbhd0d+xbhd0h+xbhd0i`	21.1	40.0	45.0
Monte Carlo after 2D Reweighting `xbhd0d+xbhd0h+xbhd0i`			
$D^-\pi^+$	20.0	34.8	45.2
D^-K^+	19.9	33.8	46.3
$D^{*-}\pi^+$	20.4	34.8	44.8
$D^-\rho^+$	20.8	34.2	45.1
B^0 remainder	21.7	34.3	44.0
B^+	21.5	35.8	42.7
B_s	8.2	33.7	58.2

Table 7.1: Percentage of events in three trigger categories for Monte Carlo and data reconstructed as $B^0 \to D^-\pi^+$. Although three separate 2-D reweightings were performed for subsets of the full run range, only the percentages for the MC reweighted to match the full data sample are listed in the table. The three categories are constructed to be mutually exclusive: Scenario C, Scenario A$\neg$C, and Scenario Low$\neg$A$\neg$C.

Sample	Scenario Low ($\neg$A and $\neg$C)	Scenario A ($\neg$C)	Scenario C
Monte Carlo Before 2D Reweighting			
$D^{*-}\pi^+$	43.5	15.0	41.5
$D^{*-}K^+$	43.5	15.4	41.0
$D^{*-}\rho^+$	44.6	14.8	40.6
B^0 remainder	45.3	15.5	39.2
B^+	45.1	15.0	39.9
Data			
xbhd0d+xbhd0h+xbhd0i	26.0	25.7	48.3
Monte Carlo after 2D Reweighting			
$D^{*-}\pi^+$	24.7	25.0	50.3
$D^{*-}K^+$	25.7	26.0	48.3
$D^{*-}\rho^+$	26.0	24.4	49.6
B^0 remainder	25.4	25.8	48.7
B^+	26.2	25.0	48.7

Table 7.2: Percentage of events in three trigger categories for Monte Carlo and data reconstructed as $B^0 \to D^{*-}[\overline{D}^0(K^+\pi^-)\pi^-]\pi^+$.

Sample	Scenario Low ($\neg$A and $\neg$C)	Scenario A ($\neg$C)	Scenario C
Monte Carlo Before 2D Reweighting			
$D^0\pi^+$	39.4	18.0	42.6
D^0K^+	39.9	17.6	42.5
$D^*\pi^+$	40.1	18.7	41.2
$D^0\rho^+$	39.8	19.1	41.1
B^+ remainder	41.0	19.4	39.6
B^0	41.2	19.1	39.7
Data			
xbhd0d+xbhd0h+xbhd0i	22.6	29.5	47.8
Monte Carlo after 2D Reweighting			
$D^0\pi^+$	22.1	29.8	48.1
D^0K^+	22.3	29.2	48.5
$D^*\pi^+$	22.6	30.4	47.0
$D^0\rho^+$	22.3	31.1	46.6
B^+ remainder	23.4	30.9	45.7
B^0	23.3	31.3	45.4

Table 7.3: Percentage of events in three trigger categories for Monte Carlo and data reconstructed as $B^+ \to \overline{D}^0(K^+\pi^-)\pi^+$.

Sample	Scenario Low ($\neg A$ and $\neg C$)	Scenario A ($\neg C$)	Scenario C
Monte Carlo Before 2D Reweighting			
$D_s^- \pi^+$	28.2	27.5	44.3
$D_s^- K^+$	27.0	29.5	43.5
$D_s^{*-} \pi^+$	28.9	28.1	43.0
$D_s^- \rho^+$	31.1	28.0	40.9
B_s remainder	31.5	27.7	40.8
Data			
`xbhd0d+xbhd0h+xbhd0i`	13.9	36.8	49.3
Monte Carlo after 2D Reweighting			
$D_s^- \pi^+$	13.4	34.8	51.8
$D_s^- K^+$	12.2	36.6	51.2
$D_s^{*-} \pi^+$	14.0	35.8	50.3
$D_s^- \rho^+$	15.3	35.8	48.9
B_s remainder	15.0	34.4	50.6

Table 7.4: Percentage of events in three trigger categories for Monte Carlo and data reconstructed as $B_s \to D_s^-(\phi\pi^-)\pi^+$
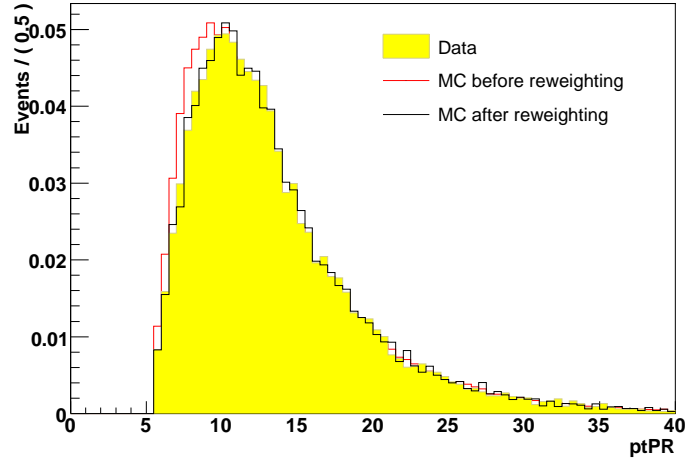
Figure 7.5: Effect of 2-D reweighting on the p_T spectrum of the exclusive $B^0 \to D^- \pi^+$ sample.
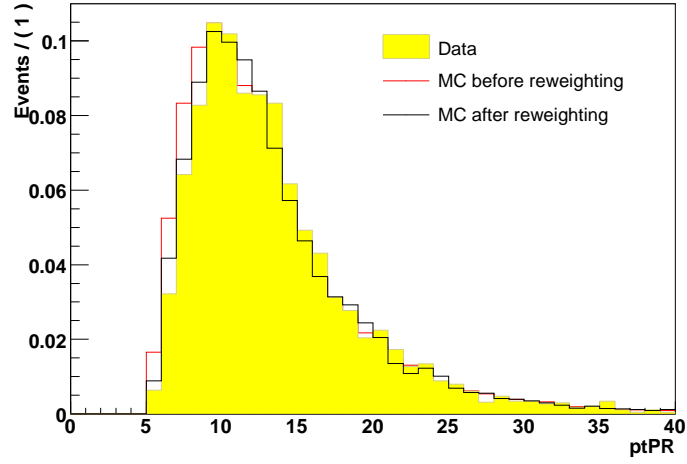
Figure 7.6: Effect of reweighting on the p_T spectrum of the exclusive $B^0 \to D^{*-}\pi^+$ sample. The p_T and trigger category reweightings are performed sequentially.
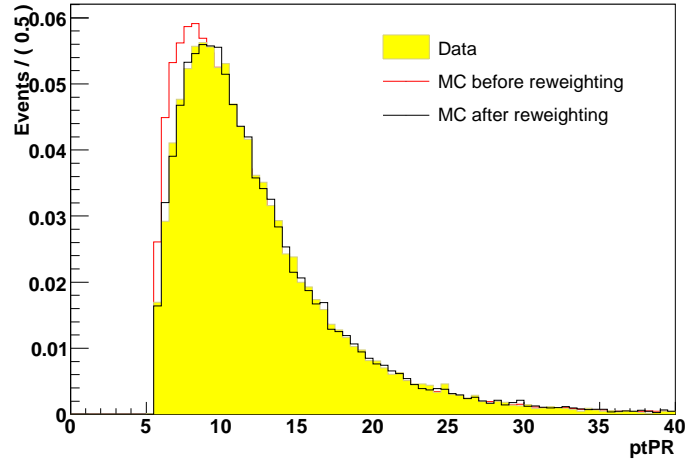
Figure 7.7: Effect of 2-D reweighting on the p_T spectrum of the exclusive $B^+ \to \overline{D}^0\pi^+$ sample.
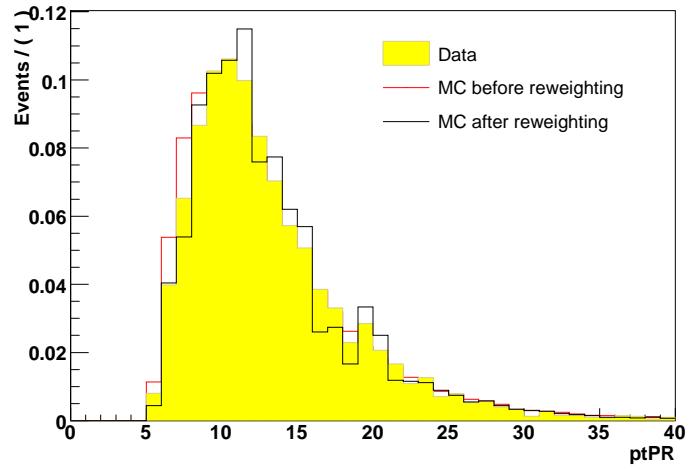
Figure 7.8: Effect of reweighting on the p_T spectrum of the exclusive $B_s \rightarrow D_s^-(\phi\pi^-)\pi^+$ sample. The p_T and trigger category reweightings are performed sequentially.

7.3.2 Monte Carlo Validation

After the reweighting the Monte Carlo, we check that its agreement with data in several key variables is adequate. Overlaid plots can be found in Figs. 7.9, 7.10, and 7.11.
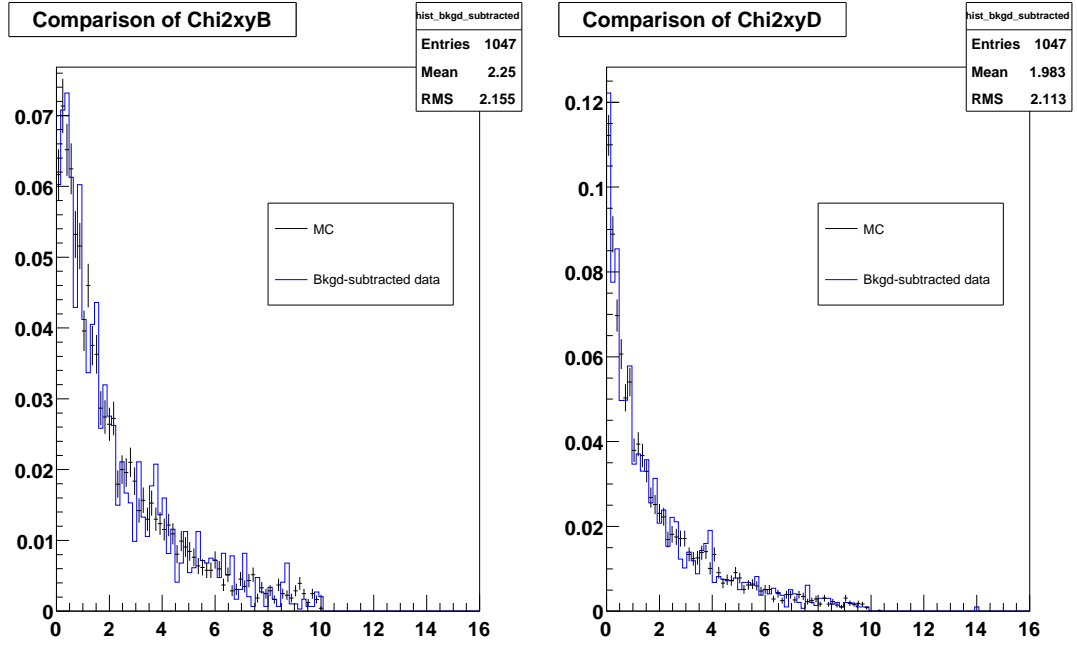
(a) χ^2 of the fit to the B vertex

(b) χ^2 of the fit to the D vertex
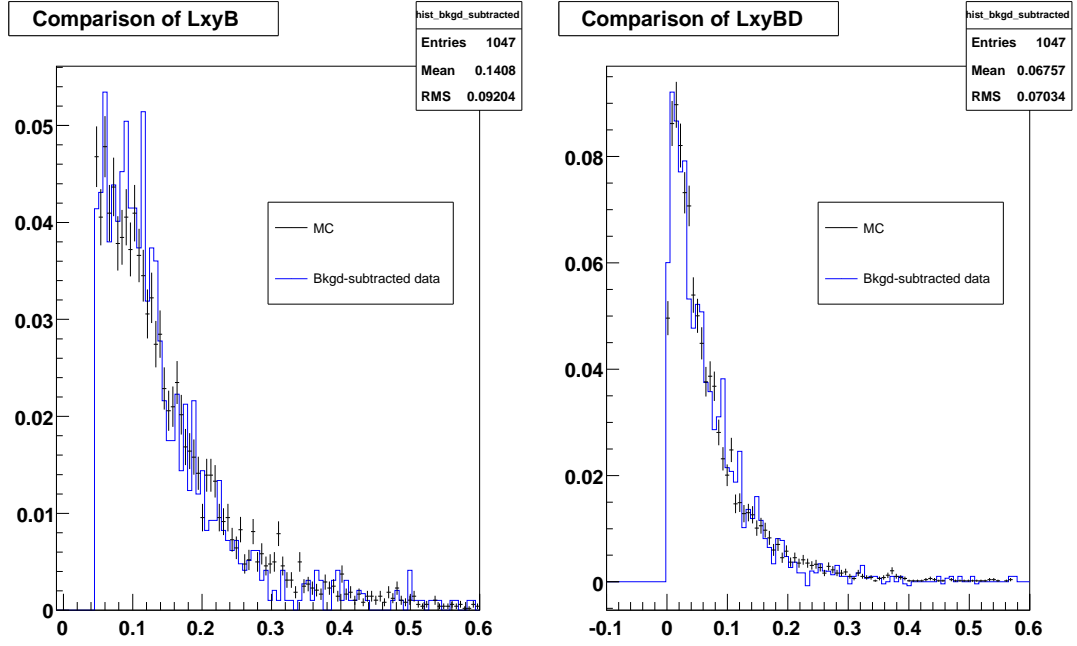
(c) $L_{xy}(B)$ (cm)

(d) $L_{xy}(B \leftarrow D)$ (cm)

Figure 7.9: Comparison between $B_s \rightarrow D_s^-(\phi\pi^-)\pi^+$ simulation and data
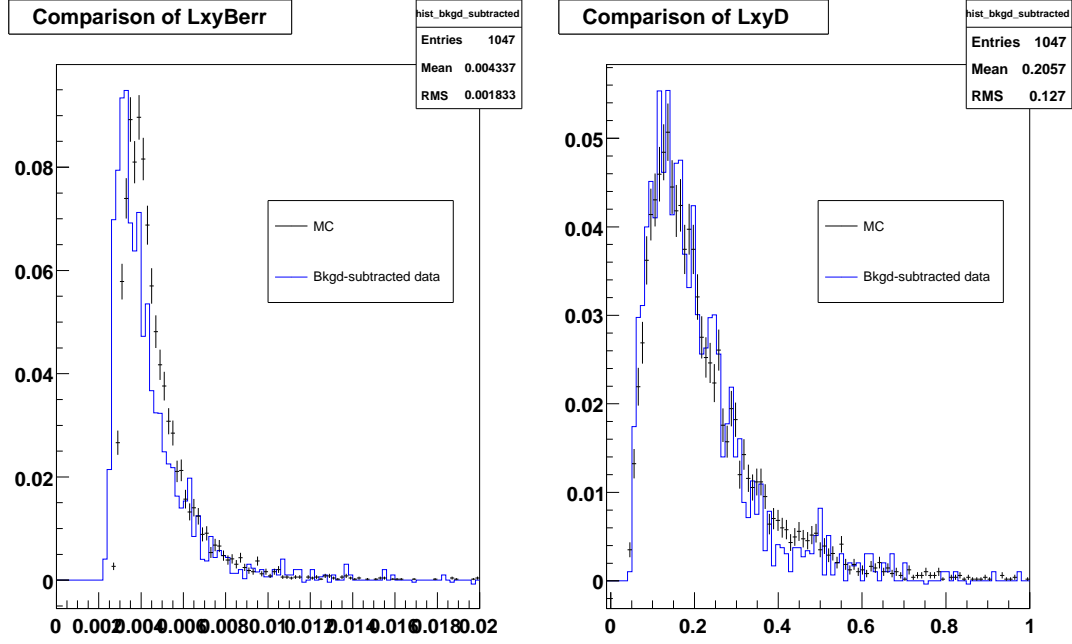
(a) $\sigma(L_{xy}(B))$ (cm)

(b) $L_{xy}(D)$ (cm)
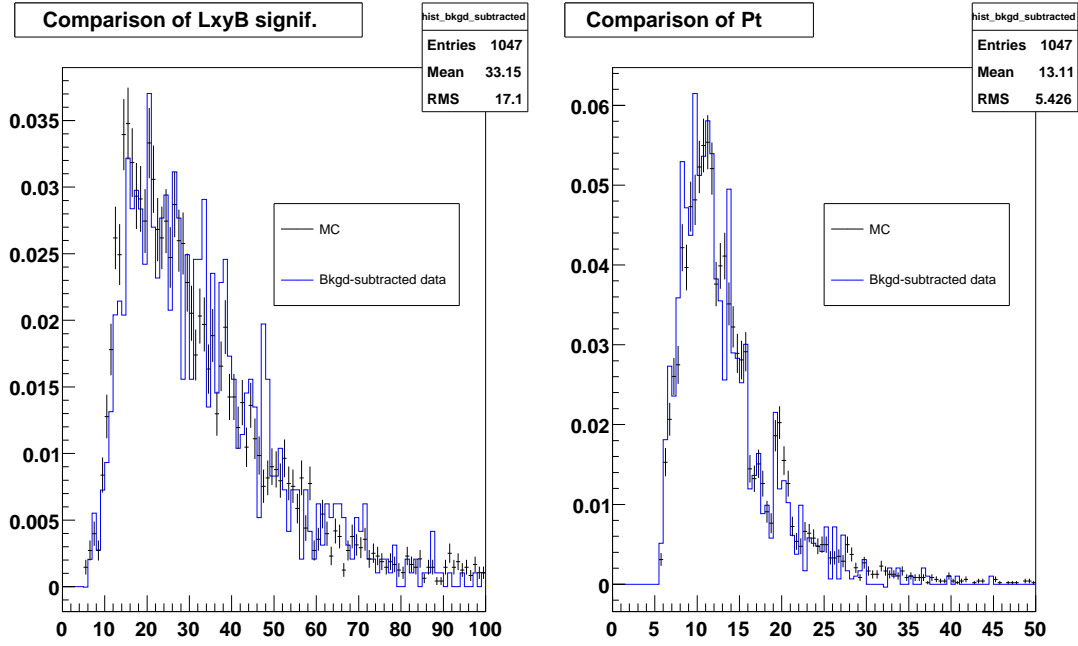
(c) $L_{xy}(B)/\sigma_{L_{xy}}(B)$

(d) $p_T(B)$ (GeV/c)

Figure 7.10: Comparison between $B_s \to D_s^-(\phi\pi^-)\pi^+$ simulation and data
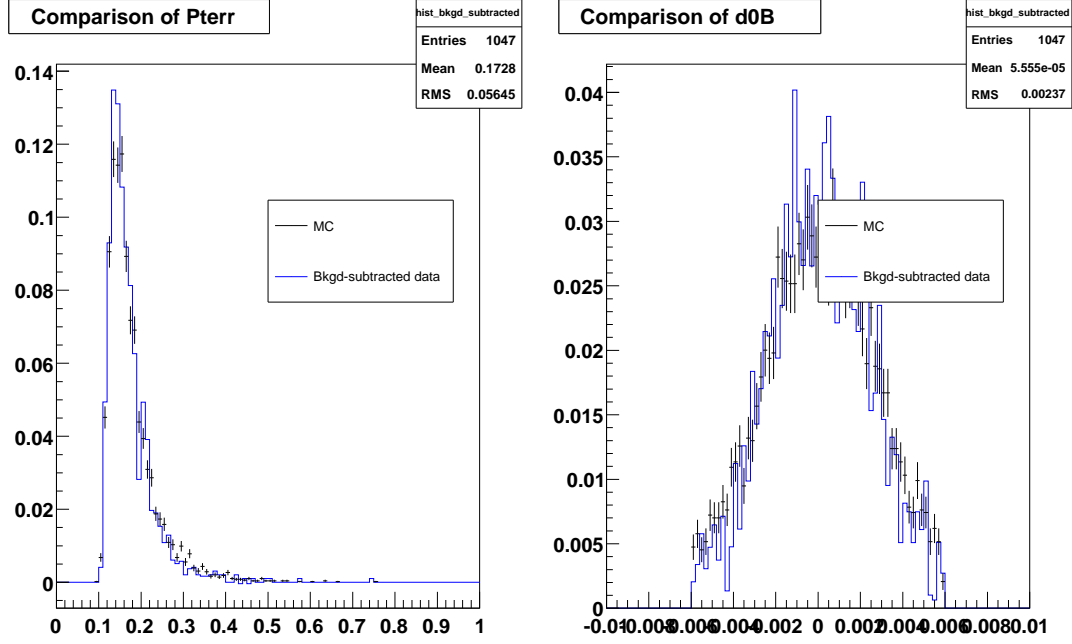
(a) $\sigma(p_T(B))$ (GeV/c)

(b) $d_0(B)$ (cm)
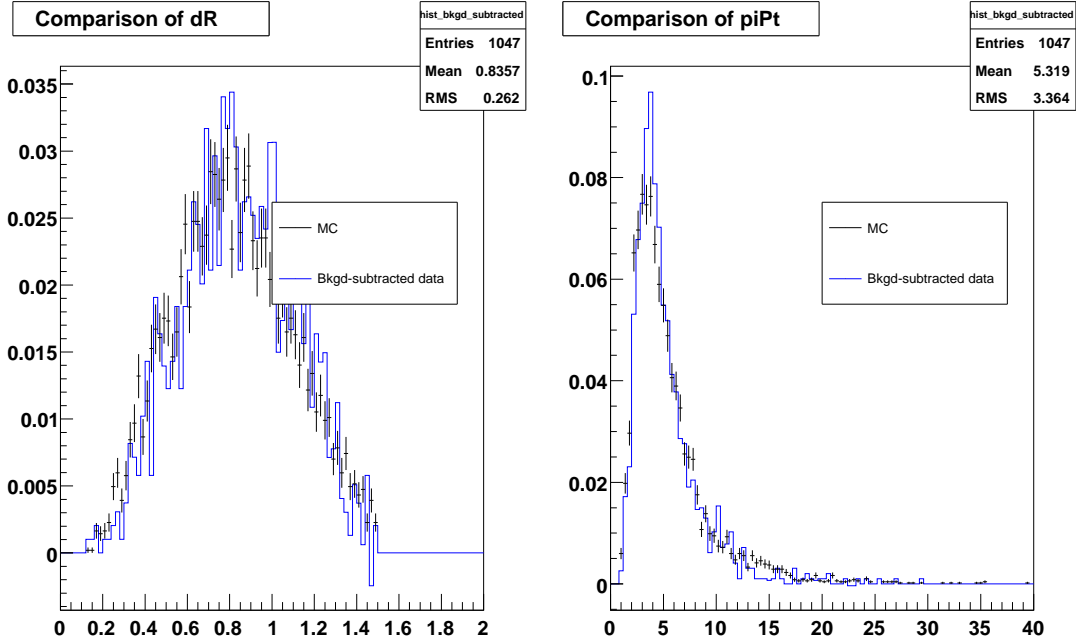
(c) $\Delta R(D, \pi_B)$ (radians)

(d) $p_T(\pi_B)$ (GeV/c)

Figure 7.11: Comparison between $B_s \rightarrow D_s^-(\phi\pi^-)\pi^+$ simulation and data

7.4 Fitter Validation

7.4.1 Normalization Check

The unbinned likelihood fits used in this analysis are implemented within the RooFit framework. To ensure the evaluation of the likelihood is performed as efficiently and accurately as possible, analytical forms for the ct integration of Equation (7.7) and Equation (7.10) are used. The results of the analytical form have been compared against a high precision numerical integration assuming different values of τ. The analytical form assumes an upper ct value of 4000 μm. The τ scan was performed in 100 steps from 200 to 2000 μm. The other parameters of the PDF were set to the following: $\sigma = 50$ μm, $\beta_1 = 0.001$ cm, $\tau_1 = 0.02$ cm, $N_2/N_1 = N_3/N_1 = 0$ The agreement was found to be better than 1 part in 10^{11}. Figure 7.12 shows the ratio of the analytical to the numerical forms.

7.4.2 Toy Monte Carlo Tests of the Fitters

Toy Monte Carlo studies of 1000 pseudo-experiments each are performed to test the fitter for a bias in the returned value of the lifetime or a mis-estimation of the errors. These studies use fractions of events in each mode typical for the FR+PR region To make the toy MC as realistic as possible the efficiency curves used for generation and fitting are from the fits to the respective data samples. The numbers of events per experiment are Poisson distributed around the number of events in the combined FR+PR region. The PDFs and fractions used for fitting the toy Monte Carlo data are the same as those used for its generation. The $B^0 \to D^{*-}[\overline{D}^0(K^+\pi^-)\pi^-]\pi^+$ and $B^+ \to \overline{D}^0(K^+\pi^-)\pi^+$ toy MC tests were performed with $c\tau(\text{gen})$ equal to 464 μm and 496 μm, respectively. These were the lifetimes used in the original `Bgen` Monte Carlo. For the $B^0 \to D^-(K^+\pi^-\pi^-)\pi^+$ and $B_s \to D_s^-(\phi\pi^-)\pi^+$ toy MC tests, five studies were performed for each mode with different $c\tau(\text{gen})$. The toy Monte Carlo results are shown in Tab. 7.5. In all tests the pull histogram means are consistent with zero, and the widths are consistent with one.
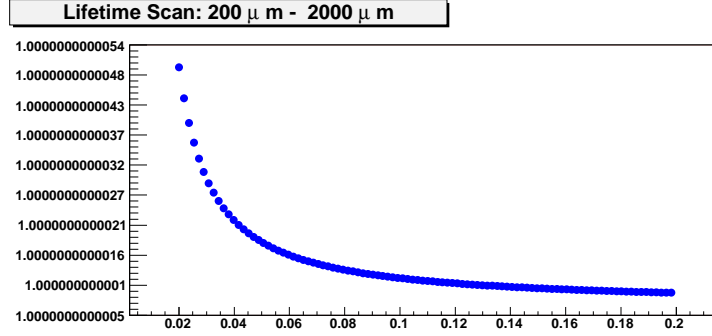
(a) Validation of P_{FR} normalization
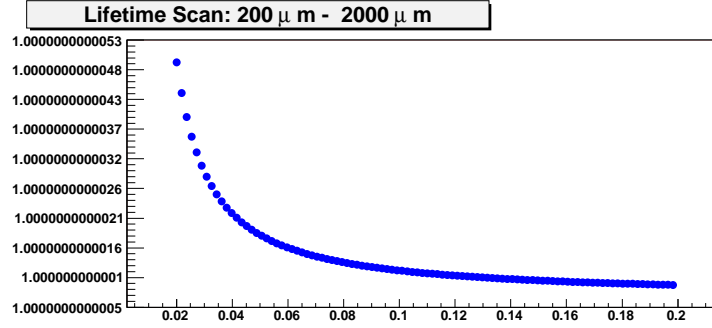
(b) Validation of P_{PR} normalization

Figure 7.12: Validation of the analytical form for integral of the FR and PR PDFs. The ratio of results from the analytic integration used by the fitter to the numeric integration for $c\tau_B$ values from 200 to 2000 μm. The FR (top) and PR (bottom) fitters were both tested. The agreement was found to be better than 1 part in 10^{11}.

Sample	$c\tau$(gen) (μm)	Pull Width (σ)	Pull Mean (σ)	Mean Bias (μm)
$B^0 \to D^{*-}\pi^+$	464	1.001 $\pm$ 0.022	0.026 $\pm$ 0.032	0.418 $\pm$ 0.313
$B^+ \to \overline{D}^0\pi^+$	496	0.987 $\pm$ 0.022	-0.030 $\pm$ 0.031	-0.084 $\pm$ 0.106
	420	1.024 $\pm$ 0.023	-0.003 $\pm$ 0.033	0.009 $\pm$ 0.124
	440	1.005 $\pm$ 0.023	-0.008 $\pm$ 0.032	-0.015 $\pm$ 0.114
$B^0 \to D^-\pi^+$	460	1.007 $\pm$ 0.023	0.014 $\pm$ 0.032	0.077 $\pm$ 0.120
	480	1.051 $\pm$ 0.024	0.023 $\pm$ 0.034	0.123 $\pm$ 0.136
	500	1.004 $\pm$ 0.024	-0.024 $\pm$ 0.034	-0.080 $\pm$ 0.142
	400	1.022 $\pm$ 0.023	0.072 $\pm$ 0.033	0.962 $\pm$ 0.339
	420	1.012 $\pm$ 0.023	0.043 $\pm$ 0.032	0.694 $\pm$ 0.352
$B_s \to D_s^-\pi^+$	440	0.964 $\pm$ 0.022	0.016 $\pm$ 0.031	0.338 $\pm$ 0.359
	460	0.989 $\pm$ 0.022	-0.005 $\pm$ 0.031	0.145 $\pm$ 0.386
	480	0.957 $\pm$ 0.022	-0.011 $\pm$ 0.031	0.006 $\pm$ 0.406

Table 7.5: Results of toy Monte Carlo experiments to test the fitter for biases and non-unit pulls. The 1000 pseudo experiments for each $c\tau$ tested were generated with the default configuration. The number of events for each experiment was Poisson distributed around the number of events in the FR+PR regions in the respective data samples. The fractions of events in each mode and the PDFs used for the generation were the same as those used for fitting. The pull is defined as $(c\tau_{\text{returned}} - c\tau_{\text{gen}})/\sigma_{\text{returned}}$ and is measured in units σ. Gaussian curves were fit to the pull and bias $(c\tau_{\text{returned}} - c\tau_{\text{gen}})$ histograms; the widths and means of the Gaussian curves are quoted in the table.

7.4.3 Real Monte Carlo Test of the Fitter

It is also essential to show that the procedure for extracting the lifetime PDF parameters yields results independent of the true $c\tau$ used to generate the `Bgen` Monte Carlo. To test for dependence in fully and partially reconstructed modes we generate $B_s \to D_s^- \pi^+$ and $B_s \to D_s^- \rho^+$ Monte Carlo samples with full simulation with the true $c\tau(B_s)$ set to 400 μm and 480 μm. We then fit these samples with the default PDFs were derived from fits to Monte Carlo generated with $c\tau(B_s) = 438$ μm. The results are summarized in Tab. 7.6 and are consistent with no dependence on the generator lifetime.

Sample	$c\tau$(True MC) (μm)	$c\tau$ (Returned) (μm)
$B_s \to D_s^- \pi^+$	400	396.8 ± 3.6
$B_s \to D_s^- \rho^+$	400	402.1 ± 4.9
$B_s \to D_s^- \pi^+$	480	488.3 ± 4.7
$B_s \to D_s^- \rho^+$	480	484.0 ± 6.1

Table 7.6: Results of default fit configuration on $B_s \to D_s^- \pi^+$ and $B_s \to D_s^- \rho^+$ Monte Carlo samples with full simulation generated with the true $c\tau(B_s)$ set to 400 μm and 480 μm.

Chapter 8

Translating Mass Fit Results to Lifetime Fit Inputs

The mass fit considers two sources of combinatorial background: real D + track and fake D + track. The real-D component comes from an auxiliary fit to the sideband-subtracted WS. The fake-D component comes from an auxiliary fit to D-signal-leakage-subtracted D sideband. Ideally, the lifetime fit would draw the background PDFs from the same two samples, so the fractions returned by the mass fit can be input into the lifetime fit unchanged. However, due to the limited statistics in our background samples, the sideband subtraction and leakage subtraction of proper time distributions both lead to negative bins as shown for the $B^0 \rightarrow D^- \pi^+$ case in Fig. 8.1 and for the $B_s \rightarrow D_s^- \pi^+$ case in Fig. 8.2.

To avoid negative values for the background PDFs, we are compelled to employ a rotation or change of basis to the fractions returned by the mass fit. We have two background proxies available, neither of which are 100% real D or 100% fake D:

- The B upper sideband, taken from the m_B interval [5.7, 6.4] GeV/c^2, contains a mixture of real and fake D's. The fractions of each are determined by counting the number of events in the D-peak and D-sideband regions and extrapolating.

- The D sidebands in the fully and partially reconstructed regions contain fake D's. There is some leakage from the D signal as well, and the fraction is determined in an auxiliary fit as described in Chap. 6.

It will take some combination of these two proxies (plus some adjustment of the signal fraction to account for the D leakage) to properly model the background contributions. The details of the calculation are shown below in Sec. 8.1. A sample numerical example is given in Sec. 8.2.
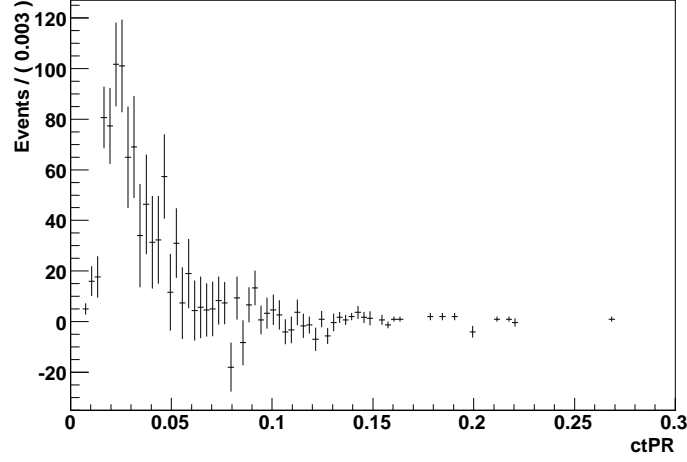
(a) *ct* distribution of SBS Wrong-sign ($D^-\pi^-$)
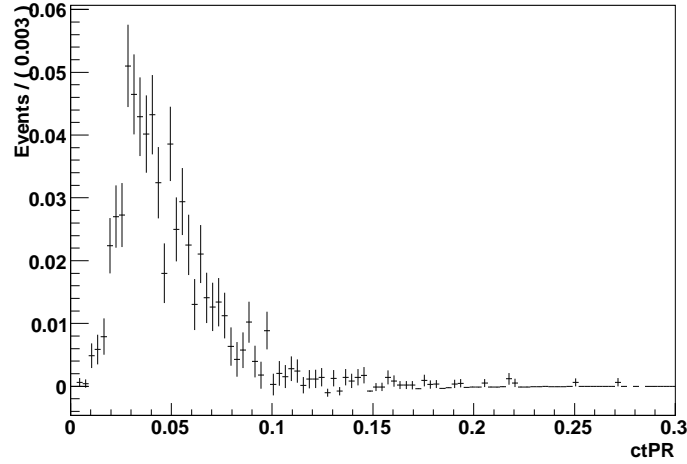
(b) *ct* distribution of leakage subtracted D sidebands

Figure 8.1: *ct* distributions of background samples used in the $B^0 \to D^-\pi^+$ mass fit. The negative bins make these histograms ineligible for use in the lifetime fit.
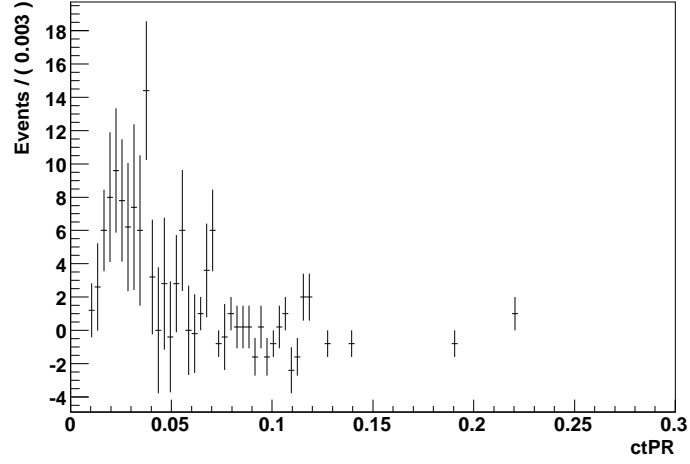
(a) ct distribution of SBS Wrong-sign $D_s^- \pi^-$
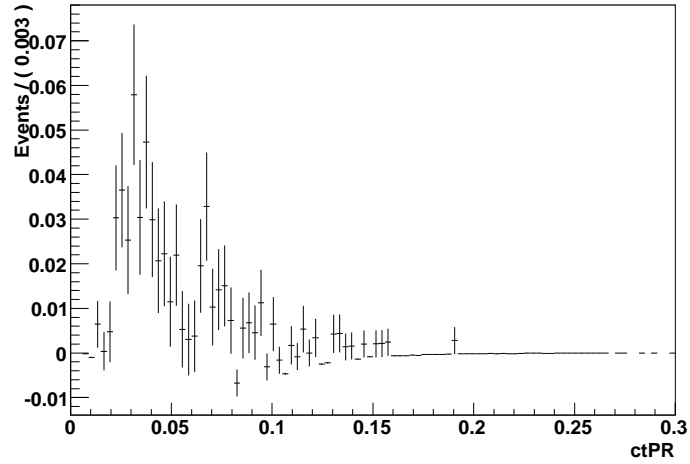
(b) ct distribution of leakage subtracted D_s sidebands

Figure 8.2: ct distributions of background samples used in the $B_s \rightarrow D_s^- \pi^+$ mass fit. The negative bins make these histograms ineligible for use in the lifetime fit.

8.1 Details of the Calculation

What we know:

- f_{Fake-D}, f_{Real-D}, f_{sig} from the mass fit ($f_F + f_R + f_{sig} = 1$)

- p_R = fraction of B upper sideband that is real D

- p_F = fraction of B upper sideband that is fake D ($p_R + p_F = 1$)

- p_{leak} = fraction of D sidebands that is signal leakage

What we want:

- F_{upper}, $F_{sideband}$, F_{sig} to use in the lifetime fit ($F_{upper} + F_{side} + F_{sig} = 1$)

First we calculate the fraction of events in the lifetime fit that will come from a PDF based on the B upper sideband

$$
\begin{aligned}
f_R &= F_{upper} \cdot p_R \\
F_{upper} &= \frac{f_R}{p_R}
\end{aligned}
$$

We can almost solve for the fraction of events in the lifetime fit that will come from our signal PDF

$$
\begin{aligned}
f_{sig} &= F_{side} \cdot p_{leak} + F_{sig} \\
F_{sig} &= f_{sig} - F_{side} \cdot p_{leak}
\end{aligned}
$$

Substituting we find

$$
\begin{aligned}
F_{upper} + F_{side} + F_{sig} &= 1 \\
\frac{f_R}{p_R} + F_{side} + f_{sig} - F_{side} \cdot p_{leak} &= 1
\end{aligned}
$$

$$
F_{side} = \frac{1 - \frac{f_R}{p_R} - f_{sig}}{1 - p_{leak}} = \frac{f_F + f_R - \frac{f_R}{p_R}}{1 - p_{leak}}
$$

8.2 Numerical Example

The effect of this rotation is easier to see if one examines a numerical example. Suppose we had a mass fit to a simple sample that returned $f_{D\pi} = 90\%$, $f_{Fake-D} = 5\%$, and $f_{Real-D} = 5\%$. Let us also assume the fraction of $D\pi$ leakage in the D sidebands is $p_{leak} = 50\%$ and the fraction of the B upper sideband that is real D is $p_R = 70\%$. This is all information we need to solve for the fractions we will use in the lifetime fit:F_{upper}, $F_{sideband}$, $F_{D\pi}$.

The B upper sideband is the only source of real D's, so we will consider F_{upper} first. In order to get 5% real D's in the lifetime fit, F_{upper} must be 7.1%. We know that 5% (70% of 7.1%) is real D, and the remaining 2.1% is fake D.

Since the B upper sideband is already contributing 2.1% toward the 5% fake D required by the mass fit, the D sidebands only need to contribute an additional 2.9%. To achieve this, the lifetime fit will need $F_{sideband} = 5.8\%$. We know the 5.8% is actually 2.9% fake D and 2.9% $D\pi$ leakage.

Since the D sidebands are contributing 2.9% $D\pi$ to the fit, albeit in a way that is independent of the parameter $c\tau_B$, we will need to set $F_{D\pi} = 87.1\%$ instead of 90%. We will loose a bit of statistical power, but neglecting the D leakage in the calculation is not only incorrect, it also leads to large changes in the lifetime fit result.

The inputs and outputs of this sample calculation are summarized in Table 8.1.

Mass Fit Output	value	Lifetime Fit Input	value
$f_{D\pi}$	90%	$F_{D\pi}$	87.1%
f_{Real-D}	5%	F_{upper}	7.1%
f_{Fake-D}	5%	real D	5.0%
p_{leak}	50%	fake D	2.1%
p_R	70%	$F_{sideband}$	5.8%
		fake D	2.9%
		$D\pi$	2.9%

Table 8.1: Summary of inputs and outputs of a simple numerical example to convert the fractions returned by the mass fit $(f_{D\pi}, f_{Fake-D}, f_{Real-D}, p_{leak}, f_{Real-D})$ into fractions usable by the lifetime fit$(F_{upper}, F_{sideband}, F_{D\pi})$.

Chapter 9

Control Sample Results

In this chapter we present the results of the control sample analyses. As in the signal sample, there were two sequential fits performed for each control sample. The first fit is to the invariant mass distribution of the candidates, and it is used to determine the fractions of events in the background and signal modes that will be inputs to the second fit. The second fit is to the proper time distribution of the sample. The only variable that is able to float in the second fit is the lifetime of the B meson.

As discussed in Chapters 6 and 7, there are auxiliary fits to determine the background PDFs for the mass fit and the efficiency curve shapes for the lifetime fit. The results of these fits for the individual control samples are also given.

The $B^0 \to D^{*-}\pi^+$ fits are described in Sec. 9.1, the $B^+ \to \overline{D}^0\pi^+$ fits are described in Sec. 9.2, and the $B^0 \to D^-\pi^+$ fits are described in Sec. 9.3.

9.1 $\quad B^0 \to D^{*-}[\overline{D}^0(K^+\pi^-)\pi^-]\pi^+$

9.1.1 Mass Fit Results

Before the final fit to the invariant mass distribution of $B^0 \to D^{*-}[\overline{D}^0(K^+\pi^-)\pi^-]\pi^+$ candidates, an auxiliary fit is performed to determine the shape of the background PDF that will be used.

Auxiliary Fit

The selection requirement on the D^{*+}-D^0 mass difference does an excellent job of eliminating background, but it also makes it difficult to find a suitable background proxy. Instead we fit an exponential plus a constant to $B^0 \to D^-\pi^+$ candidates in the D sidebands and import the function to the $B^0 \to D^{*-}\pi^+$ final mass fit. The same PDF is used in the final $B^0 \to D^-\pi^+$ mass fit. The auxiliary fit is shown in Fig. 9.22.

Final Mass Fit

The mass fit for the $B^0 \to D^{*-}[\overline{D}^0(K^+\pi^-)\pi^-]\pi^+$ candidates is non-extended. There are no constraints to relative branching ratios applied. The shape of the background PDF from the auxiliary fit is fixed, but its normalization is allowed to float. The configuration of the mass fitter is summarized in Table 9.4.

A plot of the mass fit of the data sample is found in Figure 9.1. The results of the fit in the full mass range [4.85, 6.45] GeV/c^2 are shown in Table 9.5. The fractions of the events found in each decay mode in the FR region ($m(B^0) \in [5.17, 5.35]$ GeV/c^2), the PR region ($m(B^0) \in [5.00, 5.17]$ GeV/c^2), and the combined FR+PR region are listed separately in the upper portion of Tab. 9.6.

9.1.2   Lifetime Fit Results

The final fit to the proper time distribution of the $B^0 \to D^{*-}[\overline{D}^0(K^+\pi^-)\pi^-]\pi^+$ candidates requires two types of inputs: the fractions of events in each mode and the shape parameters of their PDFs. The fractions are derived from the mass fit results. The final fractions used by the lifetime fit are shown in the lower portion of Table 9.6. The shape parameters are derived from auxiliary fits performed for each mode. We discuss the results of these fits in greater detail below.

Auxiliary Lifetime Fits

The shape parameters of the PDFs for the fully and partially reconstructed B^0 modes are determined in fits to Monte Carlo samples that have been reweighted in trigger category and $p_T(B^0)$. Since the lifetime used for generation is known, it can be fixed in the auxiliary fits for the parameters that describe the effects of detector smearing and selection requirements on the proper time distribution. In the final fit to data, the shape parameters are fixed, and the lifetime of the B^0 is the only variable allowed to float. The results of these auxiliary fits are shown in Figs. 9.2-9.5 and summarized in Tab. 9.3.

We also treat $B^- \to D^0\pi^- X$ events as signal events by fixing the lifetime ratio

$\tau(B^+)/\tau(B^0)$ to the PDG value 1.071 [5]. Like the B^0 modes, shape parameters for the $B^- \to D^0\pi^- X$ PDF come from a fit to a Monte Carlo sample where the lifetime used for generation is known. The result of this auxiliary fit is shown in Fig. 9.6 and summarized in Tab. 9.3.

For the background PDF, we fit for the shape parameters of one background sample. Since the background does not depend on $\tau(B^0)$, all the background shape parameters are frozen in the final fit. The combinatorial background is modeled by a PDF fit to the B^0 upper sideband ($m_B \in [5.7,\ 6.4]$ GeV/c^2). Since τ_{Bkgd} in this fit is degenerate with other shape parameters and has little physical meaning, we fix it to 500 μm. The results of the background auxiliary fit is shown in Figs. 9.7 and summarized in Tab. 9.3.

Final Lifetime Fit

A lifetime of $c\tau_{B^0} = 452.1 \pm 9.5$(stat.) μm is obtained from the full fit to the combined FR and PR regions. The results of the lifetime fit are separated by mass region in Table 9.7. The fit results are plotted in Figures 9.8 and 9.9. The results for the FR region (442.8 ± 12.5 μm) and PR region (466.4 ± 14.7 μm) are both within 1.3σ of the world average $c\tau(B^0) = 458.7 \pm 2.7$ μm [2], and they disagree with each other by 1.2σ.

9.2 $\quad B^+ \to \overline{D}^0(K^+\pi^-)\pi^+$

9.2.1 Mass Fit Results

Before the final fit to the invariant mass distribution of $B^+ \to \overline{D}^0(K^+\pi^-)\pi^+$ candidates, two auxiliary fits are performed to determine the shapes of the background PDFs that will be used.

Auxiliary Mass Fits

The first auxiliary fit is a fit to the invariant mass distribution of the candidates in the D^0 sidebands, those candidates that satisfy $m(D^0) \in [1.820, 1.835] \cup [1.895, 1.910]$ GeV/c^2, to determine the fake D + track shape. The fake D + track shape is assumed to be an exponential on top of a flat line. Since there are some real D's that leak into the D sidebands, the fit to the invariant mass of the candidates in the sidebands includes a histogram PDF taken from the D sidebands of B^+ Monte Carlo. Its normalization floats along with the normalization and shape parameters of the fake D + track PDF. The results of the fake-D + track fit are shown in Fig. 9.10.

Since the $B^+ \to \overline{D}^0 \pi^+$ does not have an associated "wrong-sign" sample, we turn to the $D^- \pi^-$ wrong-sign sample to derive the shape for the real-D + track PDF. The second auxiliary fit is to the invariant mass distribution of the $D^- \pi^-$ sample The sample is first sideband subtracted in the D mass, so that only real D's remain. The real D + track shape is also assumed to be an exponential on top of a flat line. The results of the real-D + track fit are shown in Fig. 9.23.

Final Mass Fit

The final mass fit for the $B^+ \to \overline{D}^0 (K^+ \pi^-) \pi^+$ candidates is extended. There are no constraints applied to relative branching ratios. The normalization of the fake-D component is fixed by extrapolating the D sidebands into the D signal region. The shape of the real-D + track background PDF is fixed, but its normalization is allowed to float. The configuration of the mass fitter is summarized in Table 9.10.

A plot of the mass fit of the full data sample is found in Figure 9.11. The results of the fit in the full mass range [4.85, 6.45] GeV/c^2 are shown in Table 9.11. The fractions of the events found in each decay mode in the FR region ($m(B^+) \in [5.17, 5.35]$ GeV/c^2), the PR region ($m(B^+) \in [5.00, 5.17]$ GeV/c^2), and the combined FR+PR region are listed separately in the upper portion of Table 9.12.

9.2.2 Lifetime Fit Results

The final fit to the proper time distribution of the $B^+ \to \overline{D}^0(K^+\pi^-)\pi^+$ candidates requires two types of inputs: the fractions of events in each mode and the shape parameters of their PDFs. The fractions are derived from the mass fit results. Since the backgrounds in the mass fit are not grouped in the same categories as in the lifetime fit, some translation (described in Chap. 8) is required. The final fractions used by the lifetime fit are shown in the lower portion of Table 9.12. The shape parameters are derived from auxiliary fits performed for each mode. We discuss the results of these fits in greater detail below.

Auxiliary Lifetime Fits

The shape parameters of the PDFs for the fully and partially reconstructed B^+ modes are determined in fits to Monte Carlo samples that have been reweighted in trigger category and $p_T(B^+)$. Since the lifetime used for generation is known, it can be fixed in the auxiliary fits for the parameters that describe the effects of detector smearing and selection requirements on the proper time distribution. In the final fit to data, the shape parameters are fixed, and the lifetime of the B^+ is the only variable allowed to float. The results of these auxiliary fits are shown in Figs. 9.12-9.16 and summarized in Tab. 9.8.

We also treat $B^0 \to D^0\pi^+X$ events as signal events by fixing the lifetime ratio $\tau(B^+)/\tau(B^0)$ to the PDG value 1.071 [5]. Like the B^+ modes, shape parameters for the $B^0 \to D^0\pi^+X$ PDF come from a fit to a Monte Carlo sample where the lifetime used for generation is known. The result of this auxiliary fit is shown in Fig. 9.17 and summarized in Tab. 9.8.

For the background PDFs, we fit for the shape parameters of two background samples. Since the backgrounds do not depend on $\tau(B_s)$, all the background shape parameters are frozen in the final fit. The backgrounds included in this fit are the D^0 sidebands, and the B^+ upper sideband ($m_B \in [5.7, 6.4]$ GeV/c^2). Since τ_{Bkgd} in these fits is degenerate with other shape parameters and has little physical meaning, we fix

it to 500 μm. The results of the background auxiliary fits are shown in Figs. 9.18-9.19 and summarized in Tab. 9.9.

Final Lifetime Fit

A lifetime of $c\tau_{B^+} = 487.8 \pm 3.3$(stat.) μm is obtained from the full fit to the combined FR and PR regions. The results of the lifetime fit are separated by mass region in Table 9.13. The fit results are plotted in Figures 9.20 and 9.21. The results for the FR region (492.9 ± 5.2 μm) and PR region (484.1 ± 4.4 μm) are both within 1.3σ of the world average $c\tau(B^0) = 491.1 \pm 3.3$ μm [2], and they disagree with each other by 1.3σ.

9.3 $B^0 \rightarrow D^-(K^+\pi^-\pi^-)\pi^+$

9.3.1 Mass Fit Results

Before the final fit to the invariant mass distribution of $B^0 \rightarrow D^-\pi^+$ candidates, two auxiliary fits are performed to determine the shapes of the background PDFs that will be used.

Auxiliary Mass Fits

The first auxiliary fit is a fit to the invariant mass distribution of the candidates in the D sidebands, those candidate that satisfy $m(D) \in [1.825, 1.840] \cup [1.900, 1.915]$ GeV/c^2, to determine the fake D + track shape. The fake D + track shape is assumed to be an exponential on top of a flat line. Since there are some real D's that leak into the D sidebands, the fit to the invariant mass of the candidates in the sidebands includes a histogram PDF taken from the D sidebands of B^0 Monte Carlo. Its normalization floats along with the normalization and shape parameters of the fake D + track PDF. The results of the fake-D + track fit are shown in Fig. 9.22.

The second auxiliary fit is to the invariant mass distribution of the $D^-\pi^-$ sample, also called the wrong-sign (WS) sample, to determine the real D + track shape. The

sample is first sideband subtracted in the D mass, so that only real D's remain. The real D + track shape is also assumed to be an exponential on top of a flat line. The results of the real-D + track fit are shown in Fig. 9.23.

9.3.2 Final Mass Fit

The mass fit for the $B^0 \to D^-(K^+\pi^-\pi^-)\pi^+$ candidates is extended. The $DK/D\pi$, $D\rho/D\pi$, and $D^*\pi/D\pi$ fractions are constrained to values calculated using PDG results. The normalization of the fake-D component is fixed by extrapolating the D sidebands into the D signal region. The shape of the real-D + track background PDF is fixed, but its normalization is allowed to float. The configuration of the mass fitter is summarized in Table 9.16.

A plot of the mass fit of the data sample is found in Figure 9.24. The results of the fit in the full mass range [4.85, 6.45] GeV/c^2 are shown in Table 9.17. The fractions of the events found in each decay mode in the FR region ($m(B^0) \in$ [5.15, 5.35] GeV/c^2), the PR region ($m(B^0) \in$ [5.00, 5.15] GeV/c^2), and the combined FR+PR region are listed separately in the upper portion of Table 9.18.

9.3.3 Lifetime Fit Results

The final fit to the proper time distribution of the $B^0 \to D^-(K^+\pi^-\pi^-)\pi^+$ candidates requires two types of inputs: the fractions of events in each mode and the shape parameters of their PDFs. The fractions are derived from the mass fit results. Since the backgrounds in the mass fit are not grouped in the same categories as in the lifetime fit, some translation (described in Chap. 8) is required. The final fractions used by the lifetime fit are shown in the lower portion of Table 9.18. The shape parameters are derived from auxiliary fits performed for each mode. We discuss the results of these fits in greater detail below.

Auxiliary Lifetime Fits

The shape parameters of the PDFs for the fully and partially reconstructed B^0 modes are determined in fits to Monte Carlo samples that have been reweighted in trigger category and $p_T(B^0)$. Since the lifetime used for generation is known, it can be fixed in the auxiliary fits for the parameters that describe the effects of detector smearing and selection requirements on the proper time distribution. In the final fit to data, the shape parameters are fixed, and the lifetime of the B^0 is the only variable allowed to float. The results of these auxiliary fits are shown in Figs. 9.25-9.29 and summarized in Tab. 9.14.

For the background PDFs, we fit for the shape parameters of several background samples. Since the backgrounds do not depend on $\tau(B^0)$, all the background shape parameters are frozen in the final fit. The backgrounds included in this fit are $B^- \to D^- X$ (reconstructed as $D^- \pi^+$), $B_s \to D_s X$ (reconstructed as $D^- \pi^+$), the D sidebands, and the B upper sideband ($m_B \in [5.7, 6.4]$ GeV$/c^2$). Since τ_{Bkgd} in these fits is degenerate with other shape parameters and has little physical meaning, we fix it to 500 μm. The results of the background auxiliary fits are shown in Figs. 9.30-9.33 and summarized in Tab. 9.15.

Final Lifetime Fit

A lifetime of $c\tau_{B^0} = 449.9 \pm 3.6$(stat) μm is obtained from the full fit. The results of the lifetime fit are separated by mass region in Table 9.19. The fit results are plotted in Figures 9.34 and 9.35. The results for the FR region (448.7 ± 4.6 μm) and PR region (452.5 ± 5.8 μm) are both within 2σ of the world average $c\tau(B^0) = 458.7 \pm 2.7$ μm [2], and they disagree with each other by 0.6σ. The 2σ discrepancy is further discussed in Appendix B.

9.4 Systematic Uncertainties for the $B^0 \to D^- \pi^+$

The $B^0 \to D^- \pi^+$ sample was a challenging control sample, largely due to the level of background. To better understand the fitter and the sample, we varied

selection requirements, background treatments, and fit procedures. Some of these explorations are further explained in Appendix B. Because we were able to see large variations in the returned lifetime between fit configurations that were equally physically motivated, we decided to check if the systematic uncertainty, as estimated by a procedure we would eventually apply to our signal sample, would be sufficient to cover these variations. To this end we estimated all the systematic uncertainties for the $B^0 \to D^-(K^+\pi^-\pi^-)\pi^+$ channel using a toy Monte Carlo technique.

For each systematic uncertainty, 1000 pseudo-experiments are generated with the number of events Poisson-distributed around 39600 (the number of events in the combined fully and partially reconstructed regions). Each set of experiments is generated with a non-standard configuration of the fitter (the one exception is a bootstrapped Monte Carlo described in Sec. 9.4.5); the particular variations are described in detail in the following sections. The model used to fit the the pseudo-experiments is the same as was used for the $B^0 \to D^-\pi^+$ full data sample fit. The mean biases ($c\tau_{\text{returned}} - c\tau_{\text{gen}}$) returned from the toy Monte Carlo are used to set the size of the systematic uncertainties. Where $\pm 1\sigma$ variations are considered, the larger returned bias is used to set the final systematic. The results of all the toy Monte Carlo studies, including those that probe greater than 1σ variations, are summarized in Table 9.1. Table 9.2 contains the final list of systematic uncertainties for this lifetime measurement.

9.4.1 Background Model Choice and Fractions

In the default model, the B upper sideband ($m_B \in [5.7, 6.4]$ GeV/c^2) and the D sideband in the FR + PR regions ($m_B \in [5.00, 5.35]$ GeV/c^2) are combined to form the mixture of real D's and fake D's measured by the mass fit. There are several inputs that go into determining the fractions of the B upper sideband and the D sideband (see Chap. 8). The uncertainties on these inputs translate into a systematic uncertainty on the final lifetime measurement. We also perform an extreme test (greater than 1σ variation) where we generate with only one type of background and fit with the default model. The biases returned from the toy Monte

Carlo studies are listed below.

The following two situations in which only one background is used for generation are extreme deviations from the default model. These studies probe the size of the largest possible deviation from the default fit, and a 1σ variation will be well within the bounds established by these two situations.

- We use a background PDF from the B upper sideband only for generation and fit with the default model. The returned bias is -15.3 μm.

- We use a background PDF from the D sideband only for generation and fit with the default model. The returned bias is 15.9 μm.

The following situations are more consistent with $\pm 1\sigma$ variations. The four sources of systematics will be added in quadrature to determine the final systematic for the background fraction.

- The fraction of the B upper sideband that is real D is determined by extrapolating the D sidebands in the B upper sideband under the D peak. The value used in the default fit is 70%. Varying this fraction by +2% and -2% for generation returns biases of 0.4 μm and -0.5 μm, respectively.

- The fraction of the D sidebands in the FR+PR region that is D-signal leakage is determined by an auxiliary fit to the B mass shape of the D sidebands. The value used in the default fit is 30.6%. Varying this fraction by +2.5% and -2.5% for generation returns biases of -0.5 μm and 0.4 μm, respectively.

- The mass fit measures the fraction of real-D events in the FR+PR region to be 4.4%. Varying this fraction by +0.7% and -0.7% for generation returns biases of -2.6 μm and 2.6 μm, respectively.

- The mass fit measures the fraction of fake-D events in the FR+PR region to be 7.9%. Varying this fraction by +0.2% and -0.2% for generation returns biases of -0.5 μm and 0.5 μm, respectively.

Combining the above errors in quadrature, we find a 2.8 μm uncertainty.

Further studies have indicated that a systematic uncertainty should be assessed for the "choice of background model" in addition to the "background fraction" systematics that have already been discussed in this section. The systematic is estimated using the following procedure:

1. We perform a mass fit to the full sample using a flat (constant in B mass) real-D shape and the fake-D shape from the auxiliary D-sideband fit. The normalizations of both the real-D and fake-D shapes are allowed to float, but their shapes are fixed.

2. We generate toy Monte Carlo for the FR+PR region using the new fractions from Step 1 and fit the toy Monte Carlo samples with the default fractions.

3. Since this variation is believed to be greater than 1σ and is not completely isolated from the "background fraction" systematics above, we take half the size of the observed toy Monte Carlo bias as the systematic.

Since the returned bias is 10.5μm, the systematic for background modeling is estimated to be 5.2μm. The combined uncertainty from both the choice of background model and the background fraction is then $2.8 \oplus 5.2 = 5.9$ μm.

9.4.2 Fixed Single-B Background $c\tau$

The PDF for the B_s background comes from a fit to a Monte Carlo sample generated with $c\tau = 438\mu$m. In the fit for the efficiency curve parameters, $c\tau_{B_s}$ is set to 438 μm. If the lifetime used by the Monte Carlo generator is different from the true B_s lifetime, this would then affect the B^0 lifetime measurement. To estimate the size of this effect, we generate toy MC with $c\tau_{B_s}$ set to $438 - 15 = 423\mu$m. We repeat the toy Monte Carlo study with $c\tau_{B_s}$ set to $438 + 15 = 453\mu$m. The returned biases for these -1σ and $+1\sigma$ variations are -0.5 μm and 0.5 μm, respectively.

9.4.3 Effect of Reweighting for p_T and Trigger Category

Due to the finite statistics of data and Monte Carlo, there is a possibility that a bias is introduced when the Monte Carlo samples are reweighted to match the data p_T and trigger category distributions. The procedure for the reweighting is described in Sec. 7.3. To estimate the systematic uncertainty associated with reweighting to a histogram, we use a functional form fit to the histogram instead. We choose to fit the $p_T(B)$ histogram with a first degree polynomial. The efficiency curves derived from Monte Carlo reweighted to the function are then used for generation of toy Monte Carlo. The toy Monte Carlo is fit with the default model. The mean bias is -2.6 μm.

For an extreme test (much larger than a 1σ variation) to probe the importance of reweighting, we also generate with curves fit to unreweighted Monte Carlo. The returned bias is 8.1 μm.

9.4.4 Lifetime Contribution of the Radiative Tail

In the default configuration, we do not currently separate the radiative tail (modeled by PHOTOS [27]) from the $D^-\pi^+$ Monte Carlo before fitting for the P_{FR} efficiency curve parameters. For the mass fit, the PHOTOS tail is treated separately, and its size is allowed to float.

Here we estimate the systematic uncertainty associated with (1) treating the $D\pi(n\gamma)$ as a single, fully reconstructed mode and (2) not constraining the size of the PHOTOS tail using the returned mass fit errors. When deriving efficiency curves we treat the PHOTOS tail as a PR mode and the non-PHOTOS peak as a FR mode. We use these separate efficiency curves for generation and at the same time vary the relative fraction of PHOTOS to non-PHOTOS events. We perform two toy Monte Carlo studies: one with the fraction varied up by 1 σ, the other with the fraction varied down by 1 σ. Since the statistics of the PHOTOS component is low, the divided $D\pi$ sample is not reweighted. We then fit with the default model with one modification: the combined $D\pi$ (PHOTOS + non-PHOTOS) template is

also derived from unreweighted Monte Carlo. The mean biases are -0.6 and 0.5μm, respectively.

9.4.5 Efficiency Curve Parameterization

To test whether a PDF adequately describes a Monte Carlo ct distribution, one would ideally fit for the efficiency curve parameters on one MC sample and then freeze the parameters and fit for the lifetime on 1000 other realistic samples. Since we do not have the extra realistic MC samples, we "make" 1000 samples from the one we have by bootstrapping.

For example, we know the final B^0 data has (according to the mass fit) 16857 $D\pi$ events in the FR+PR region. We generate the $D\pi$ part of a bootstrapped Monte Carlo as follows:

1. The number of $D\pi$ events for a particular bootstrapped sample is *Poisson* distributed around 16857.

2. To get the first event, we generate a random number N between 0 and 20053 (the number of events in the original MC sample) and get the ct from the N-th event.

3. To get the second event, we generate another random number between 0 and 20053 and grab the ct from that event. The same event can be chosen twice; not all events have to be chosen.

4. This process continues until the target number of $D\pi$ events is reached.

The process is repeated for all the individual modes, including the real-D, fake-D, and single-B backgrounds, until a complete sample is generated. For the fake-D and real-D backgrounds we bootstrap off the D sideband and B upper sideband data samples. The complete bootstrapped sample is then fit with the default PDFs.

After generating and fitting 1000 bootstrapped samples, we find the mean bias is -0.2 μm.

9.4.6 Additional Systematics

We assess 1.0 μm uncertainty for the impact parameter correlation. For the uncertainty due to the internal alignment of the detector, we assess a value of 2.4 μm. Both values are taken from the previous hadronic lifetime analysis [20].

In the $B_s \to D_s^- \pi^+$ signal sample we assess an additional systematic for the modeling of the two-track triggers, as is discussed in detail in Sec. 10.3.6. Although we did not include this systematic in the initial $B^0 \to D^- \pi^+$ systematic studies, we expect that an uncertainty of a similar size would be assessed here.

9.5   Control Sample Summary

We perform lifetime measurements of the three B^0 and B^+ control samples using $\sim$1.3 fb^{-1} of data in the fully and partially reconstructed modes of $B^0 \to D^-(K^+\pi^-\pi^-)\pi^+$, $B^+ \to \overline{D}^0(K^+\pi^-)\pi^+$, and $B^0 \to D^{*-}[\overline{D}^0(K^+\pi^-)\pi^-]\pi^+$. We measure

$$c\tau(B^0 \to D^-(K^+\pi^-\pi^-)\pi^+) = 449.9 \pm 3.6(\text{stat.}) \pm 7.0(\text{syst.}) \ \mu\text{m}$$

$$c\tau(B^0 \to D^{*-}[\overline{D}^0(K^+\pi^-)\pi^-]\pi^+) = 452.1 \pm 9.5(\text{stat.}) \ \mu\text{m}$$

$$c\tau(B^+ \to \overline{D}^0(K^+\pi^-)\pi^+) = 487.8 \pm 3.3(\text{stat.}) \ \mu\text{m}$$

The results for $B^0 \to D^{*-}[\overline{D}^0(K^+\pi^-)\pi^-]\pi^+$ and $B^+ \to \overline{D}^0(K^+\pi^-)\pi^+$ are consistent within statistical errors with the PDG values $c\tau(B^0) = 458.7 \pm 2.7$ and $c\tau(B^+) = 491.1 \pm 3.3$ [2]. The larger background sample $B^0 \to D^-(K^+\pi^-\pi^-)\pi^+$ has additional large systematics associated with the background modeling, but its result is consistent with the PDG value if the systematics are included.

	Pull Width (σ)	Pull Mean (σ)	Mean Bias (μm)
Single background proxy choice			
a) B upper sideband only	1.027±0.025	-4.187±0.035	-15.313±0.123
b) D sideband only	0.955±0.023	4.053±0.032	15.913±0.131
Background rotation inputs			
a) Real D % upper SB = 68%	1.030±0.025	-0.148±0.035	-0.530±0.132
b) Real D % upper SB = 72%	0.990±0.023	0.091±0.033	0.350±0.124
c) D leakage in D SB = 28.1%	1.035±0.024	0.099±0.034	0.404±0.127
d) D leakage in D SB = 33.1%	1.044±0.024	-0.139±0.034	-0.513±0.129
Real D background fraction			
$+1\sigma$	1.041±0.023	-0.687±0.033	-2.554±0.124
-1σ	0.999±0.023	0.681±0.033	2.610±0.126
Fake D background fraction			
$+1\sigma$	0.964±0.022	-0.143±0.031	-0.542±0.117
-1σ	0.976±0.023	0.126±0.033	0.494±0.125
Alternate Background Model	0.979±0.022	2.697±0.031	10.473±0.123
Fixed $c\tau(B_s)$			
$+15\mu$m	0.997±0.023	0.115±0.032	0.454±0.122
-15μm	1.006±0.022	-0.135±0.032	-0.489±0.121
Reweighting for p_T and trigger			
no reweight	0.922±0.023	2.094±0.033	8.099±0.130
reweight with function	1.036±0.024	-0.693±0.033	-2.601±0.124
Contribution of radiative tail			
$+1\sigma$	1.006±0.028	0.147±0.040	0.570±0.153
-1σ	1.018±0.025	0.114±0.036	0.484±0.137
Efficiency curve parameterization	1.044±0.024	-0.055±0.034	-0.201±0.129

Table 9.1: Summary of toy Monte Carlo studies with the $B^0 \rightarrow D^-\pi^+$ fitter. Note that some of these toy Monte Carlo studies test variations that are greater than 1σ. See text for full explanation. The pull is defined as $(c\tau_{\text{returned}} - c\tau_{\text{gen}})/\sigma_{\text{returned}}$ and is measured in units σ. Gaussian curves were fit to the pull and bias $(c\tau_{\text{returned}} - c\tau_{\text{gen}})$ histograms; the widths and means of the Gaussian curves are quoted in the table.

Description	Value (μm)
Background modeling and fractions	5.9
Fixed single-B background ct	0.5
Reweighting for p_T and trigger	2.6
Lifetime contribution of radiative tail	0.6
Efficiency curve parameterization	0.2
Impact parameter correlation	1.0
Alignment + others	2.4
TOTAL	7.0

Table 9.2: Final systematics for $B^0 \to D^-\pi^+$ fit. The total is calculated assuming the individual contributions are uncorrelated. In the $B_s \to D_s^-\pi^+$ signal sample we assess an additional systematic for the modeling of the two-track triggers, as is discussed in detail in Sec. 10.3.6. Although we did not include this source in the $B^0 \to D^-\pi^+$ systematic studies, we expect that an uncertainty of a similar size would be appropriate.

Table 9.3: Parameters of PDFs for $B^0 \to D^{*-}[\overline{D}^0(K^+\pi^-)\pi^-]\pi^+$

	$D\pi$	DK	$D\rho$	B^0 other	B^+	Bkgd- RS upper
N_1	1.000000	1.000000	1.000000	1.000000	1.000000	1.00000e+00
β_1	0.005424	0.004356	0.006871	0.007855	0.005416	4.53650e-03
τ_1	0.063950	0.025657	0.027937	0.026872	0.025751	6.41113e-03
N_2	1194.314		21.28838	4.272259		
β_2	0.009604		0.010642	0.007922		
τ_2	0.007660		0.006602	0.009909		
N_3	68.32172					
β_3	0.005356					
τ_3	0.025055					
τ	τ_{B^0}	τ_{B^0}	τ_{B^0}	τ_{B^0}	$\tau_{B^0}*1.071$	0.0500(fixed)
σ	0.030000	0.008053	0.006004	0.003845	0.009185	6.50063e-03
χ^2	104.7	27.0	16.2	51.4	26.5	1.00
ndf	$120-9$	$25-3$	$36-6$	$67-6$	$29-3$	$3-3$
$prob$	0.65	0.21	0.98	0.81	0.43	

Table 9.4: Fit components for $B^0 \to D^{*-}\pi^+$ mass fits.

Decay modes	Mass pdf	Configuration
	$B^0 \to D^{*-}[\overline{D}^0(K^+\pi^-)\pi^-]\pi^+$ fit	
$D^{*+}\pi^-$	MC	norm floating
$D^{*+}K^-$	MC	$D^*K/D^*\pi$ constrained to PDG
$D^{*+}\rho^-$	MC	norm floating
$D^{*+}\pi^-(n\gamma)$	MC	norm floating
remainder	MC	norm floating
combinatorial	$B^0 \to D^-\pi^+$ leakage-subtraced D SB	norm floating

Decay modes	Number of events	Fraction of total
$D*^+\pi^-$	3850.53	0.359425 ± 0.004965
$D*^+K^-$	326.07	0.030437 ± 0.001617
$D*^+\rho^-$	2803.92	0.261731 ± 0.013956
$D*^+\pi^-(n\gamma)$	316.76	0.029568 ± 0.005309
remainder	2982.32	0.278383 ± 0.013788
combinatorial	433.40	0.040455 ± 0.004352

Table 9.5: Results of the mass fit for $B^0 \to D^{*-}\pi^+$ in terms of the number of events in the region [4.85, 6.45] GeV/c^2. Since the fit is non-extended, the errors on the fractions are quoted.

Fractions returned by mass fit			
	FR	PR	FR + PR
$D^{*-}\pi^+$	0.906343	0.039813	0.577138
$D^{*-}K^+$	0.067040	0.010752	0.045655
$D^{*-}\rho^+$	0.001543	0.564460	0.215400
B^0 remainder	0.006425	0.221380	0.088090
B^+	0.003561	0.122680	0.048816
Bkgd - real D	0.015088	0.040915	0.024901
Fractions used by lifetime fit			
	FR	PR	FR + PR
$D^{*-}\pi^+$	0.906343	0.039813	0.577138
$D^{*-}K^+$	0.067040	0.010752	0.045655
$D^{*-}\rho^+$	0.001543	0.564460	0.215400
B^0 remainder	0.006425	0.221380	0.088090
B^+	0.003561	0.122680	0.048816
Bkgd - RS upper	0.015088	0.040915	0.024901

Table 9.6: Fractions of each mode reconstructed as $B^0 \to D^{*-}[\overline{D}^0(K^+\pi^-)\pi^-]\pi^+$ found in the three mass regions of the full data sample. The fully reconstructed (FR) region includes all events with $m_B \in [5.17, 5.35]$ GeV/c^2. The partially reconstructed (PR) region includes all events with $m_B \in [5.00, 5.17]$ GeV/c^2. The combined (FR+PR) region includes all events with $m_B \in [5.00, 5.35]$ GeV/c^2

FR	$\tau_{B^0}(\mu\mathrm{m})$	442.8 ± 12.5
	χ^2/ndf	$85.8/(90\text{-}1)$
	prob	57.6%
PR	$\tau_{B^0}(\mu\mathrm{m})$	466.5 ± 14.7
	χ^2/ndf	$89.9/(82\text{-}1)$
	prob	23.3%
FR + PR	$\tau_{B^0}(\mu\mathrm{m})$	452.1 ± 9.5
	χ^2/ndf	$106.8/(97\text{-}1)$
	prob	21.2%

Table 9.7: Results of $B^0 \to D^{*-}[\overline{D}^0(K^+\pi^-)\pi^-]\pi^+$ lifetime fit: The lifetime fit is performed in three mass regions. The fully reconstructed (FR) region includes all events with $m_B \in [5.17, 5.35]$ GeV/c^2. The partially reconstructed (PR) region includes all events with $m_B \in [5.00, 5.17]$ GeV/c^2. The combined (FR+PR) region includes all events with $m_B \in [5.00, 5.35]$ GeV/c^2.
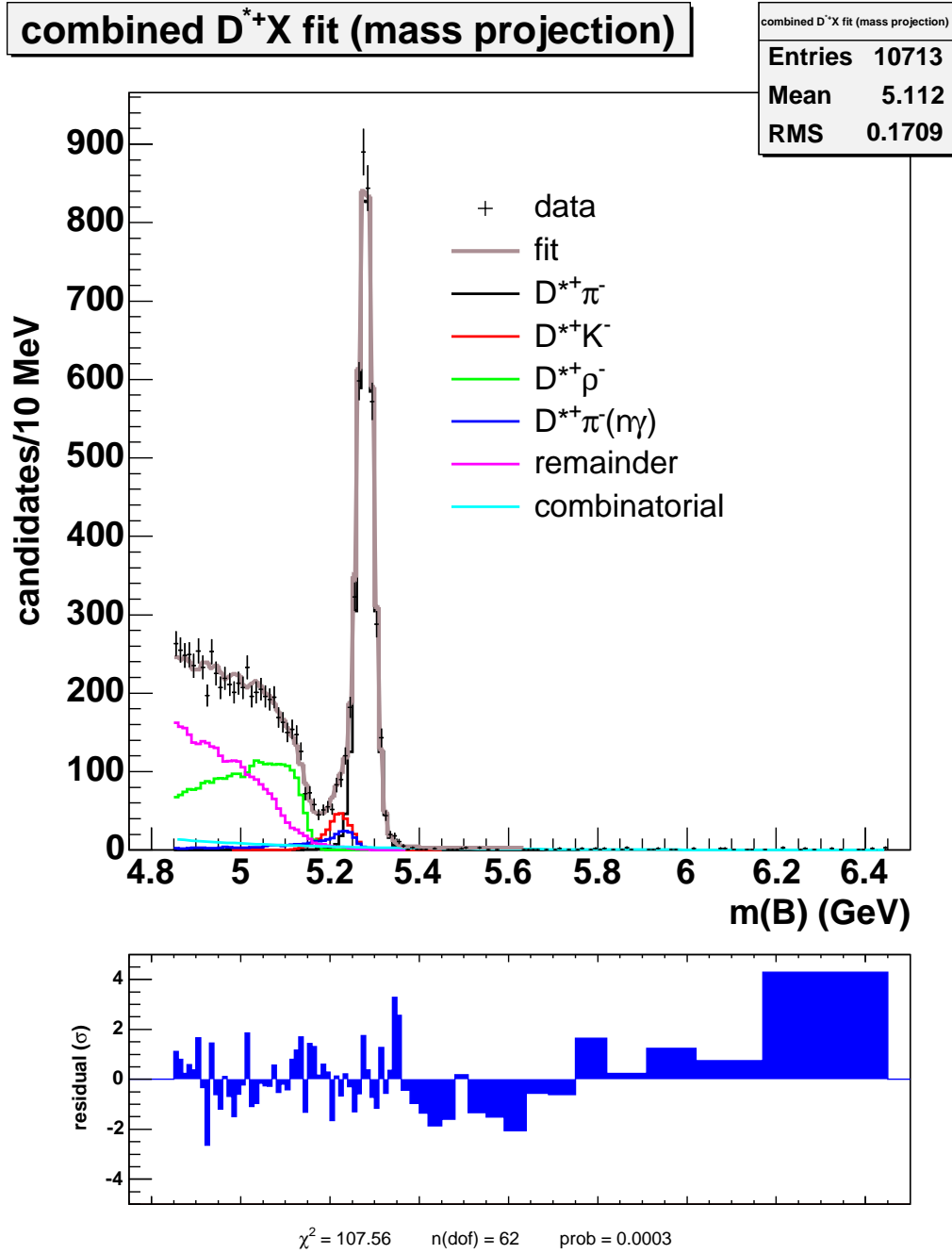
Figure 9.1: Mass fit of events reconstructed as $B^0 \to D^{*-}\pi^+$ in full 1.3 fb^{-1}.
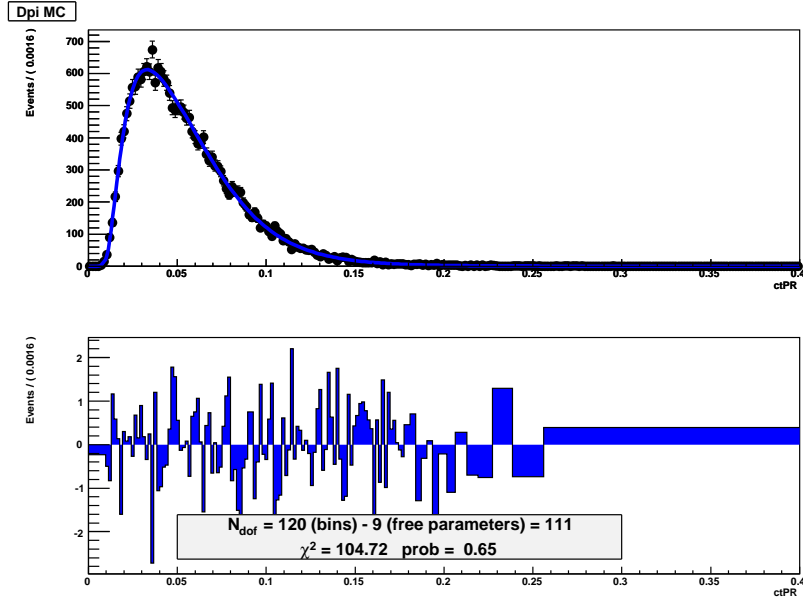
Figure 9.2: PDF fit to Monte Carlo for $B^0 \to D^{*-}\pi^+$ reconstructed as $B^0 \to D^{*-}\pi^+$.
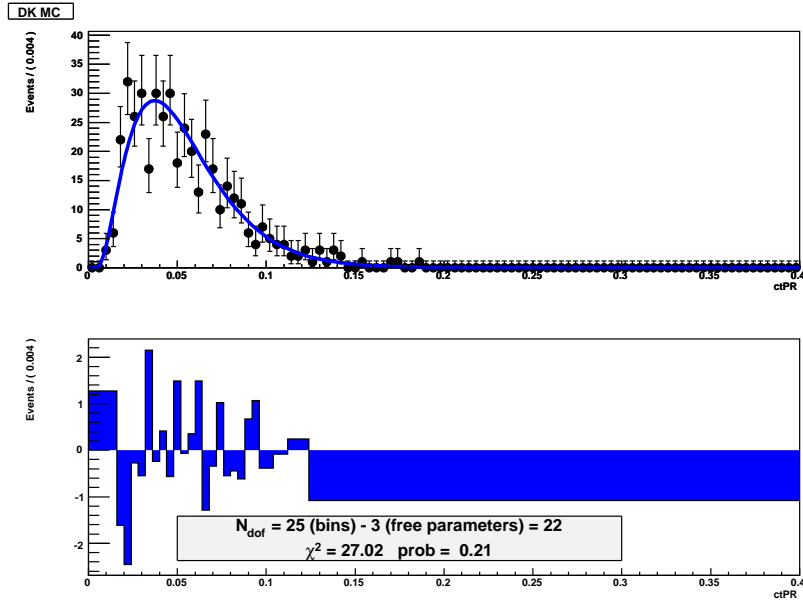
Figure 9.3: PDF fit to Monte Carlo for $B^0 \to D^{*-}K^+$ reconstructed as $B^0 \to D^{*-}\pi^+$.

106
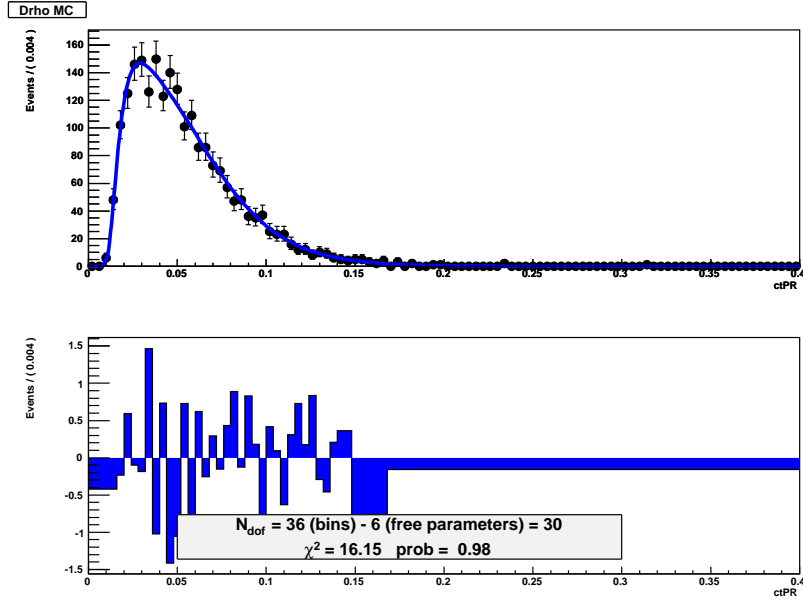
Figure 9.4: PDF fit to Monte Carlo for $B^0 \to D^{*-}\rho^+$ reconstructed as $B^0 \to D^{*-}\pi^+$.
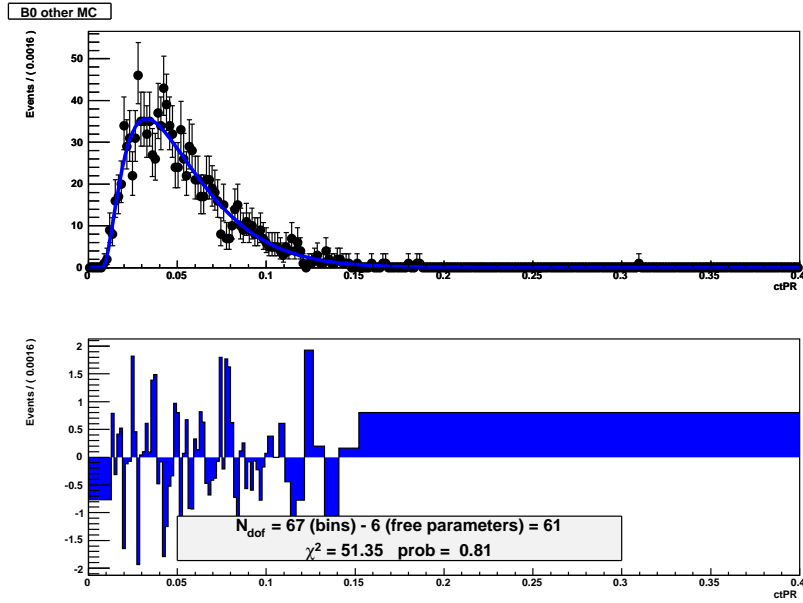
Figure 9.5: PDF fit to Monte Carlo for the remaining $B^0 \to D\pi X$ reconstructed as $B^0 \to D^{*-}\pi^+$.
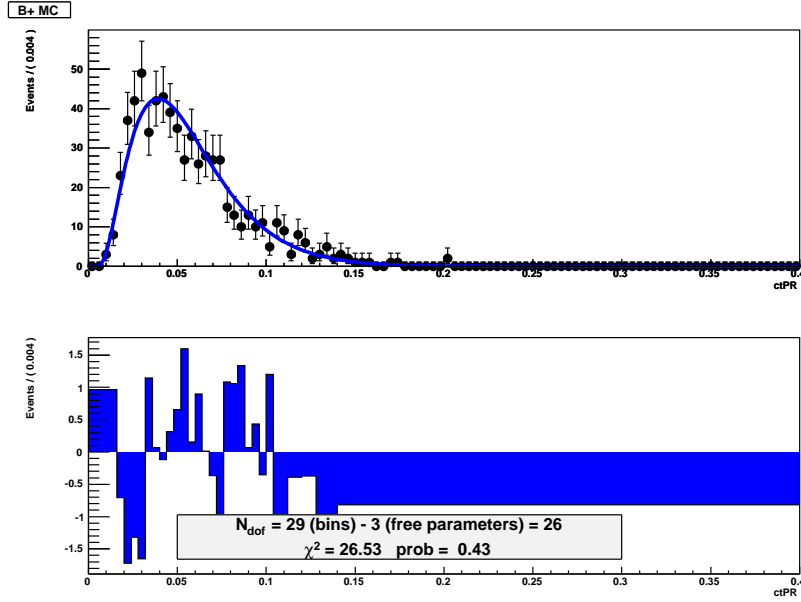
Figure 9.6: PDF fit to Monte Carlo for $B^+ \rightarrow D^{*-}\pi^+ X$ reconstructed as $B^0 \rightarrow D^{*-}\pi^+$.
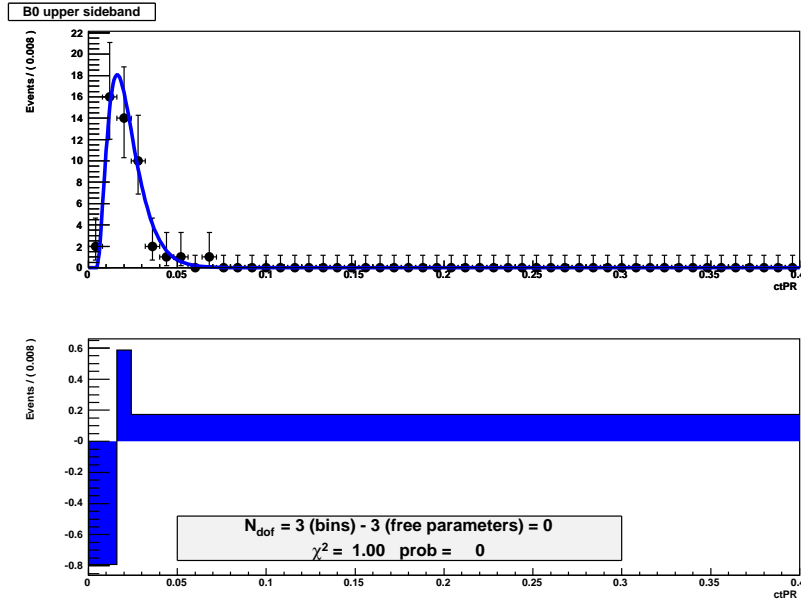
Figure 9.7: Background model for $B^0 \rightarrow D^{*-}\pi^+$ from the upper sideband data with $m_B \in [5.7, 6.4]$ GeV/c^2.
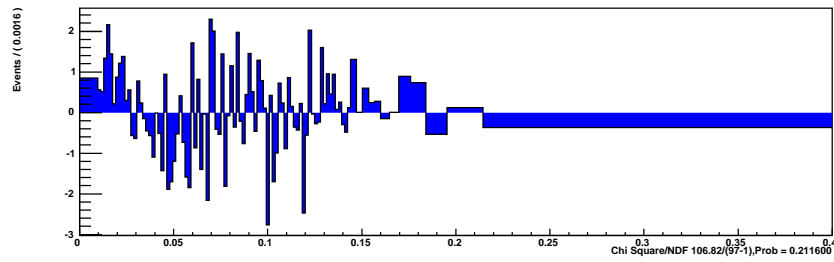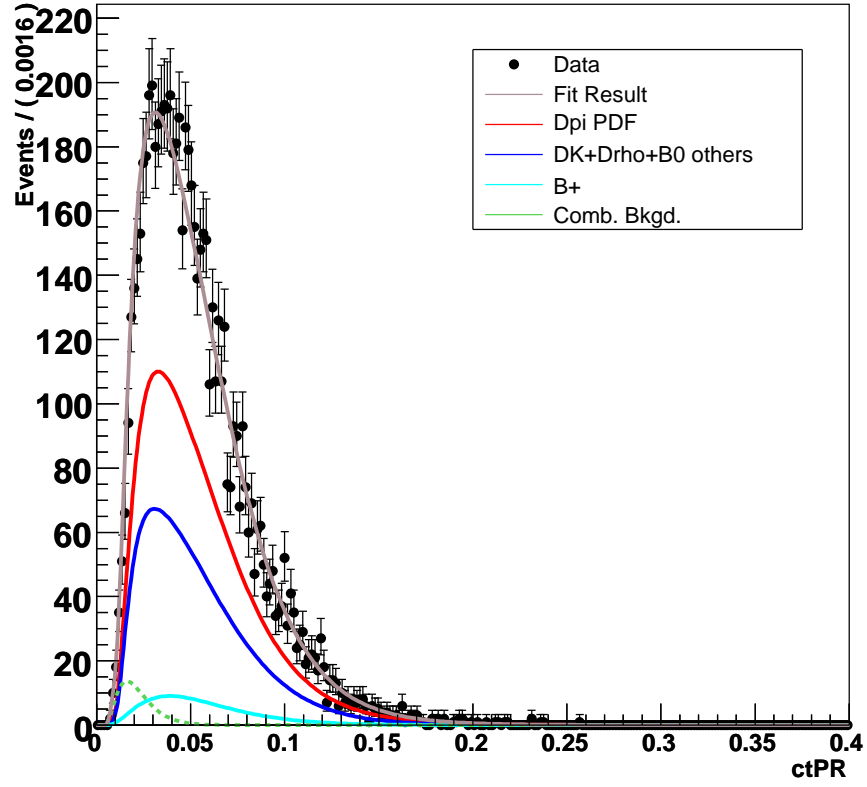
Figure 9.8: ct projection of the lifetime fit to events reconstructed as $B^0 \to D^{*-}\pi^+$ in the combined FR+PR region.
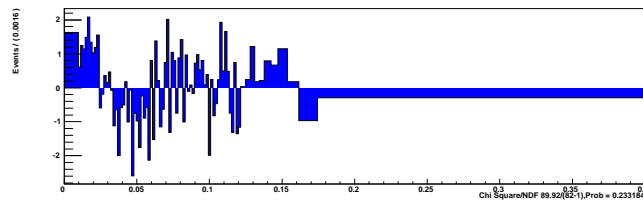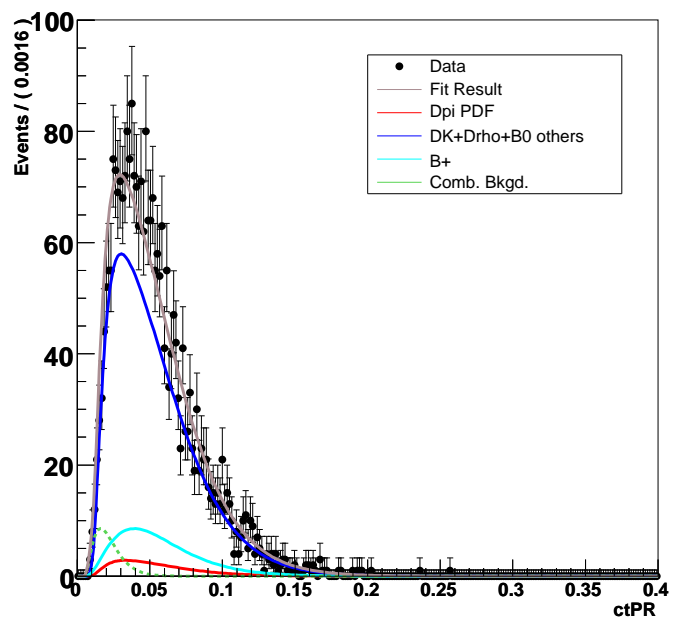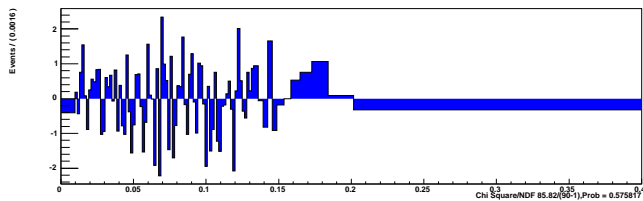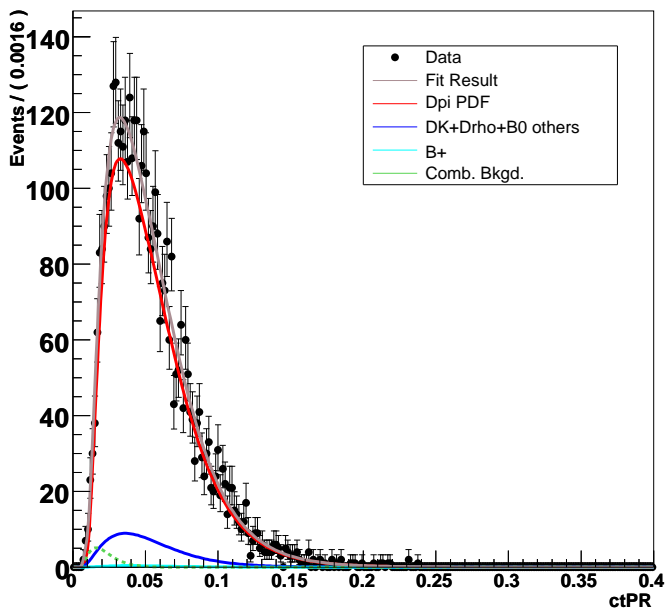
Figure 9.9: ct projection of the lifetime fits to events reconstructed as $B^0 \to D^{*-}\pi^+$ in the separate FR and PR mass regions.

(a) Fully Reconstructed Region

(b) Partially Reconstructed Region

	$D\pi$	DK	$D*\pi$	$D\rho$	B^+ other	B^0
N_1	1.000000	1.000000	1.000000	1.000000	1.000000	1.000000
β_1	0.011989	0.008035	0.009321	0.007965	0.007977	0.011833
τ_1	0.018576	0.020845	0.021501	0.019166	0.015092	0.018463
N_2	0.136279	0.071719	0.126840	0.219871	0.341764	0.146446
β_2	0.004876	0.012797	0.003983	0.012834	0.008071	0.004552
τ_2	0.039427	0.048238	0.041435	0.036876	0.032639	0.038671
τ	τ_{B^+}	τ_{B^+}	τ_{B^+}	τ_{B^+}	τ_{B^+}	$\tau_{B^+}/1.071$
σ	0.011394	0.018738	0.013979	0.014851	0.019760	0.011942
χ^2	145.6	23.2	131.1	48.3	63.9	80.6
ndf	$135-6$	$39-6$	$123-6$	$51-6$	$87-6$	$87-6$
$prob$	0.15	0.90	0.18	0.34	0.92	0.49

Table 9.8: Parameters of single-B PDFs for $B^+ \to \overline{D}^0\pi^+$

	upper sideband (RS)	D sideband (FR)	D sideband (PR)	D sideband (PR+FR)
N_1	1.00000e+00	1.00000e+00	1.00000e+00	1.00000e+00
β_1	6.26723e-03	5.93353e-03	8.72384e-03	7.09737e-03
τ_1	9.53452e-03	1.87127e-02	1.81567e-02	1.90889e-02
N_2	3.02077e-03	6.00924e-02	3.83645e-02	4.31642e-02
β_2	5.00000e-04	1.16690e-02	1.04528e-02	1.11136e-02
τ_2	4.13602e-02	4.32962e-02	4.07443e-02	4.34388e-02
τ_{Bkgd}	0.0500(fixed)			
σ_{Bkgd}	1.50679e-02	1.99999e-02	7.57711e-03	1.44205e-02
χ^2	21.9	16.3	24.7	23.5
ndf	$16-6$	$19-6$	$18-6$	$21-6$
$prob$	0.016	0.23	0.025	0.075

Table 9.9: Parameters of background PDFs for $B^+ \to \overline{D}^0\pi^+$

Table 9.10: Fit components for $B^+ \to \overline{D}^0 \pi^+$ mass fits.

Decay modes	Mass pdf	Configuration
$B^+ \to \overline{D}^0 \pi^+$ fit		
$B^- \to D^0 \pi^-$	MC	norm floating
$B^- \to D^0 \pi^- (n\gamma)$	MC	norm floating
$B^- \to D^0 K^-$	MC	norm floating
$B^-/\bar{B}^0 \to D^{*0/+}\pi^-$	MC	norm floating
$B^- \to D^{*0}K^-$	MC	norm floating
$B^- \to D^0 \rho^-$	MC	norm floating
$B^-/\bar{B}^0 \to D^0 X$(remainder)	MC	norm floating
Fake $D+$ track	leakage subtracted D^0 sideband	norm fixed
Real $D+$ track	SBS $D^+\pi^+$ WS [5.00, 6.45] GeV/c^2	norm floating

Decay modes	Number of events	Fraction of total
$B^- \to D^0\pi^-$	18957.71 ± 149.69	0.242328
$B^- \to D^0\pi^-(n\gamma)$	641.41 ± 513.50	0.008199
$B^- \to D^0K^-$	1892.94 ± 319.62	0.024197
$B^-/\bar{B}^0 \to D^{*0/+}\pi^-$	23109.90 ± 594.31	0.295404
$B^- \to D^{*0}K^-$	1300.77 ± 503.34	0.016627
$B^- \to D^0\rho^-$	11551.20 ± 1297.80	0.147654
$B^-/\bar{B}^0 \to D^0X(\text{remainder})$	13825.02 ± 464.23	0.176719
Fake $D+$ track	3998.36	0.051109
Real $D+$ track	2954.17 ± 93.08	0.037762

Table 9.11: Results of the mass fit for $B^+ \to \overline{D}^0\pi^+$ in terms of the number of events in the region [4.85, 6.45] GeV/c^2. Since the fit is extended, the errors on the numbers of events are quoted. The normalization of the fake D component was fixed in the fit.

Fractions returned by mass fit			
	FR	PR	FR + PR
$D^0\pi^+$	0.841751	0.007888	0.035739
D^0K^+	0.074570	0.005910	0.034688
$D^*\pi^+$	0.031567	0.463037	0.282234
$D^0\rho^+$	0.002702	0.205484	0.120490
B^+ remainder	0.004166	0.064067	0.038881
B^0	0.000454	0.209771	0.122075
Bkgd - real D	0.018532	0.013835	0.015804
Bkgd - fake D	0.026258	0.030008	0.028436
Real D in upper sideband	0.63		
D leakage	0.498849	0.451383	0.470783
Fractions used by lifetime fit			
	FR	PR	FR + PR
$D^0\pi^+$	0.826447	0.007896	0.348871
D^0K^+	0.074570	0.005910	0.034688
$D^*\pi^+$	0.031567	0.445030	0.273710
$D^0\rho^+$	0.002702	0.205480	0.120490
B^+ remainder	0.004166	0.064067	0.038881
B^0	0.000454	0.209770	0.122080
Bkgd - D SB	0.030678	0.039887	0.036194
Bkgd - upper SB	0.029416	0.021960	0.025086

Table 9.12: Fractions of each mode reconstructed as $B^+ \to \overline{D}^0\pi^+$ found in the three mass regions of the full data sample. The fully reconstructed (FR) region includes all events with $m_B \in [5.17, 5.35]$ GeV/c^2. The partially reconstructed (PR) region includes all events with $m_B \in [5.00, 5.17]$ GeV/c^2. The combined (FR+PR) region includes all events with $m_B \in [5.00, 5.35]$ GeV/c^2.

FR	$\tau_{B^+}(\mu\text{m})$	492.9 ± 5.2
	χ^2/ndf	137.1/(129-1)
	prob	27.5%
PR	$\tau_{B^+}(\mu\text{m})$	484.1 ± 4.4
	χ^2/ndf	151.8/(131-1)
	prob	9.2%
FR + PR	$\tau_{B^+}(\mu\text{m})$	487.8 ± 3.3
	χ^2/ndf	170.4/(142-1)
	prob	4.6%

Table 9.13: Results of $B^+ \rightarrow \overline{D}^0\pi^+$ lifetime fit: The lifetime fit is performed in three mass regions. The fully reconstructed (FR) region includes all events with $m_B \in [5.17, 5.35]$ GeV/c^2. The partially reconstructed (PR) region includes all events with $m_B \in [5.00, 5.17]$ GeV/c^2. The combined (FR+PR) region includes all events with $m_B \in [5.00, 5.35]$ GeV/c^2.
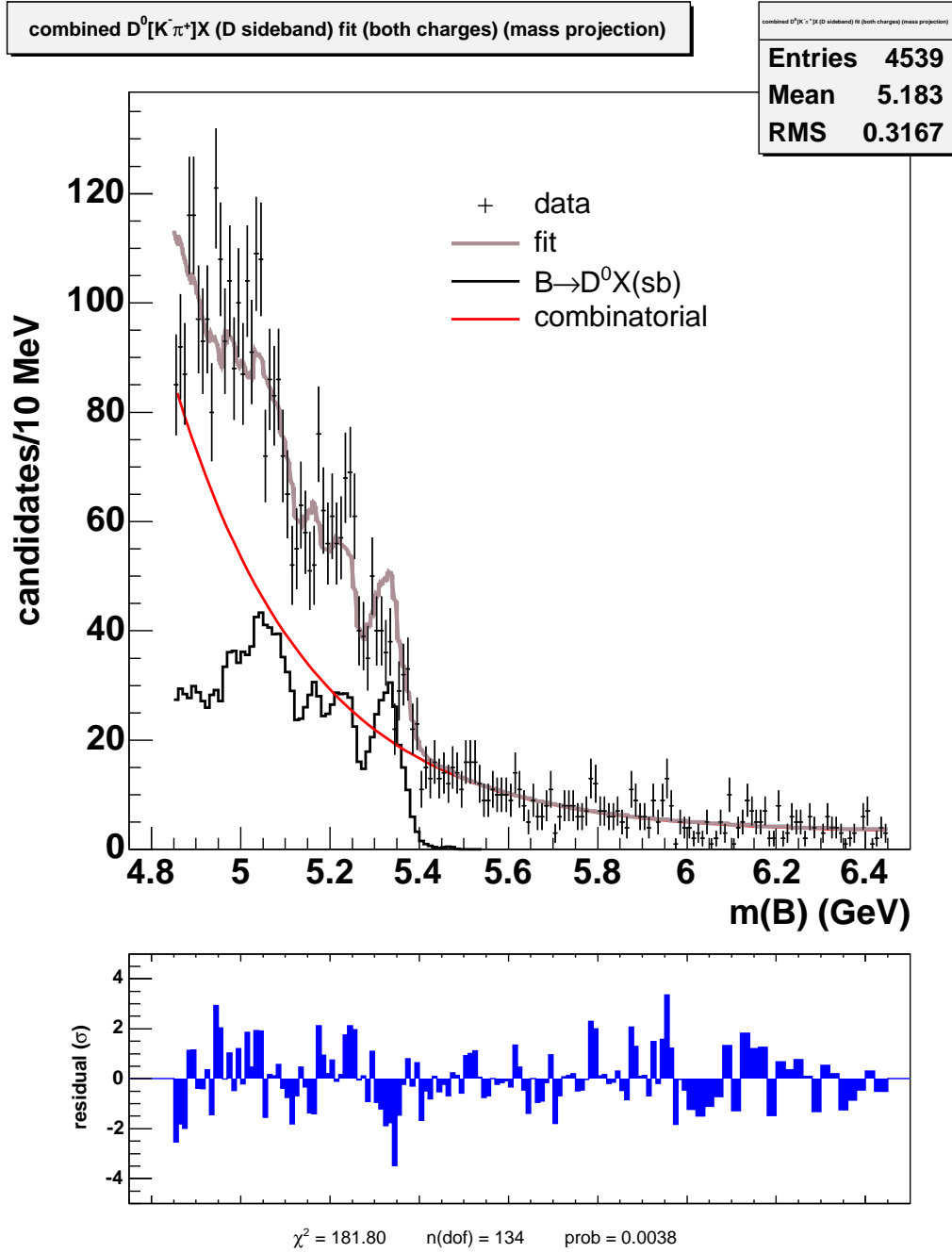
Figure 9.10: This auxiliary fit to the D sidebands with D leakage subtracted is used to determine the shape of the fake-D component for the mass fit. These events are reconstructed as $B^+ \to \overline{D}^0 \pi^+$ in full 1.3 fb^{-1}.
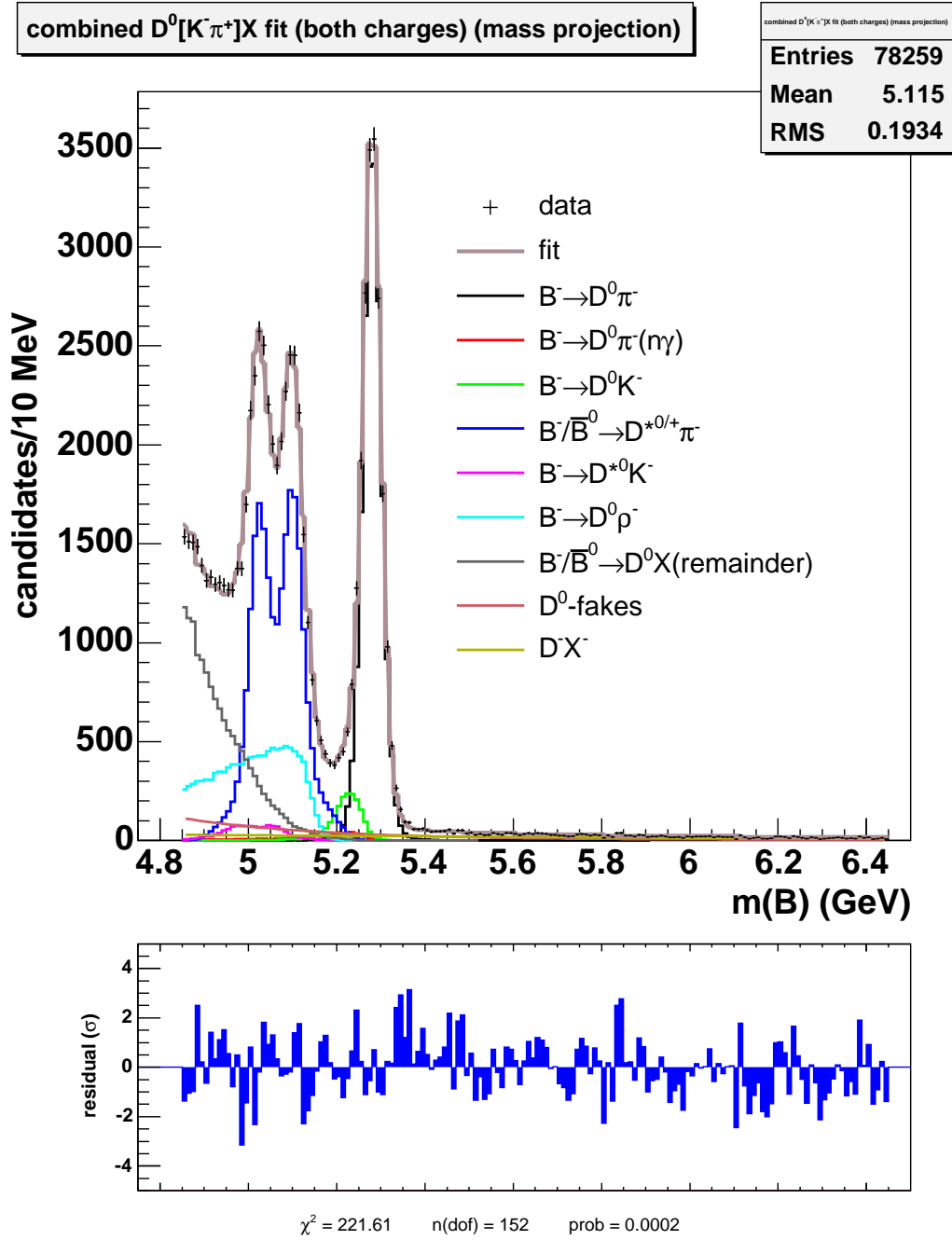
Figure 9.11: Mass fit of events reconstructed as $B^+ \to \overline{D}^0 \pi^+$ in full 1.3 fb^{-1}.
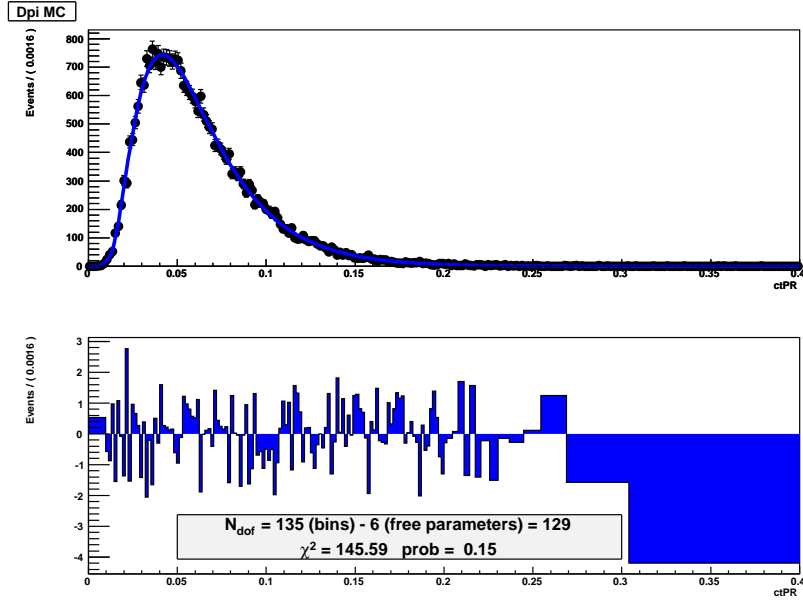
Figure 9.12: PDF fit to Monte Carlo for $B^+ \to \overline{D}^0 \pi^+$ reconstructed as $B^+ \to \overline{D}^0 \pi^+$.
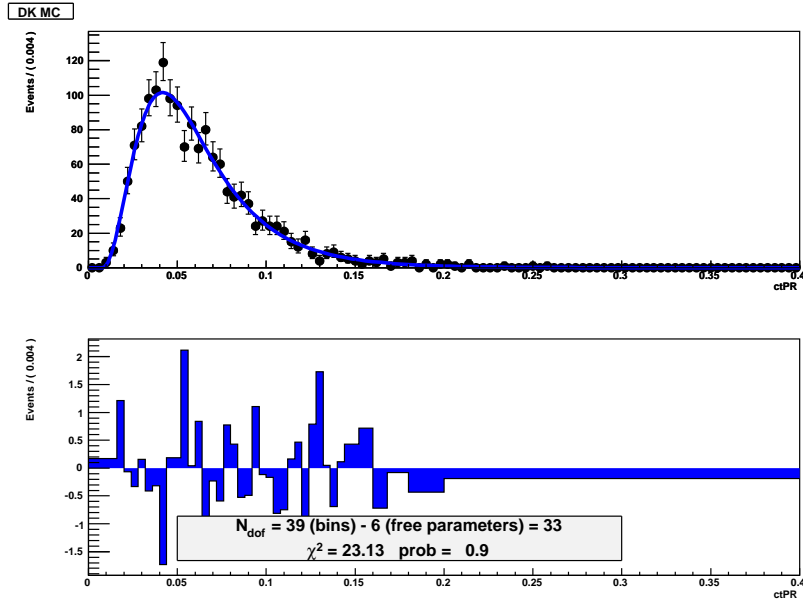
Figure 9.13: PDF fit to Monte Carlo for $B^+ \to \overline{D}^0 K^+$ reconstructed as $B^+ \to \overline{D}^0 \pi^+$.
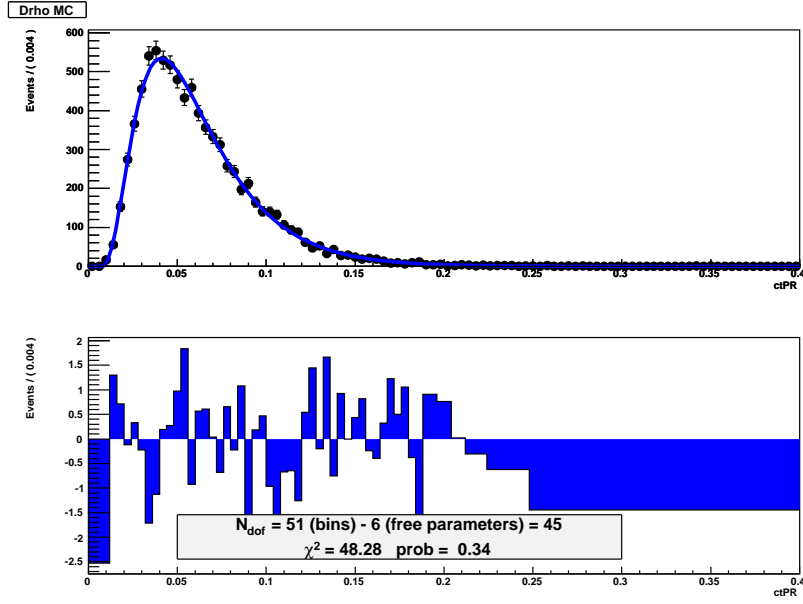
Figure 9.14: PDF fit to Monte Carlo for $B^+ \to \overline{D}^0 \rho^+$ reconstructed as $B^+ \to \overline{D}^0 \pi^+$.
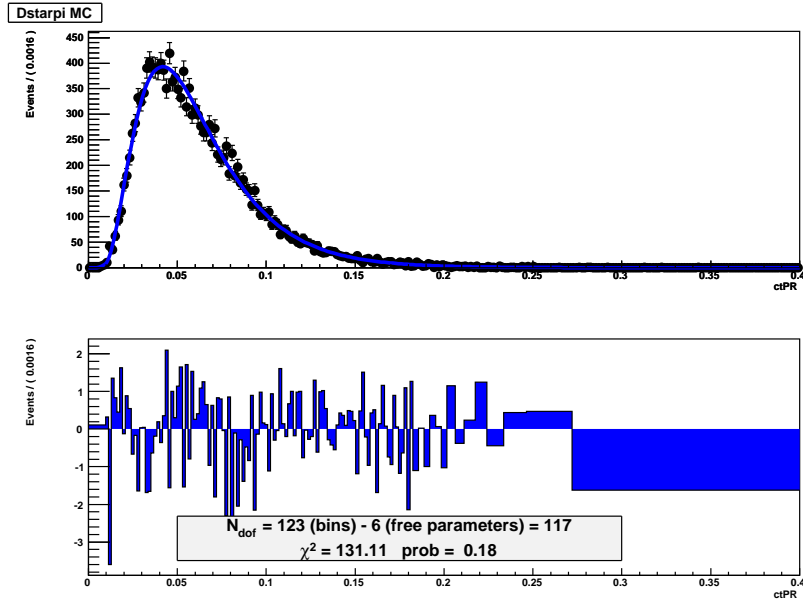
Figure 9.15: PDF fit to Monte Carlo for $B^+ \to D^* \pi^+$ reconstructed as $B^+ \to \overline{D}^0 \pi^+$.

119
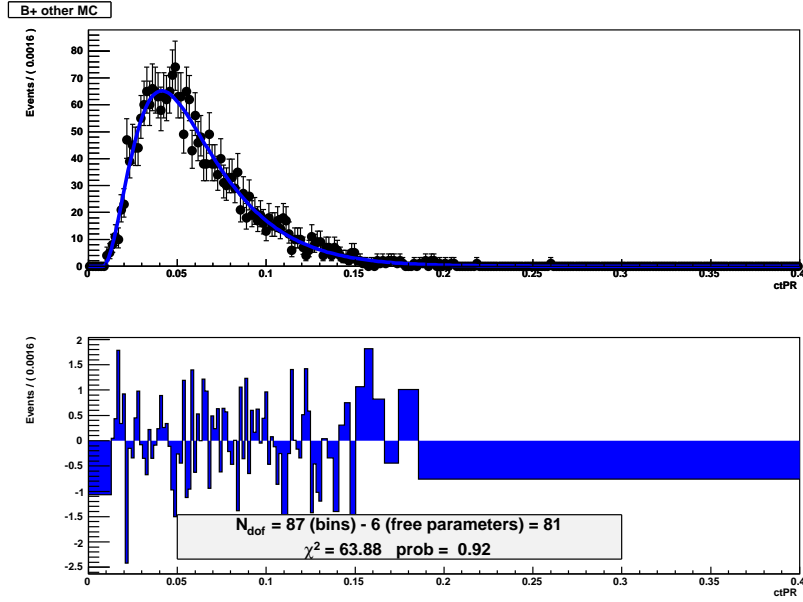
Figure 9.16: PDF fit to Monte Carlo for the remaining $B^+ \to D\pi X$ reconstructed as $B^+ \to \overline{D}^0\pi^+$.
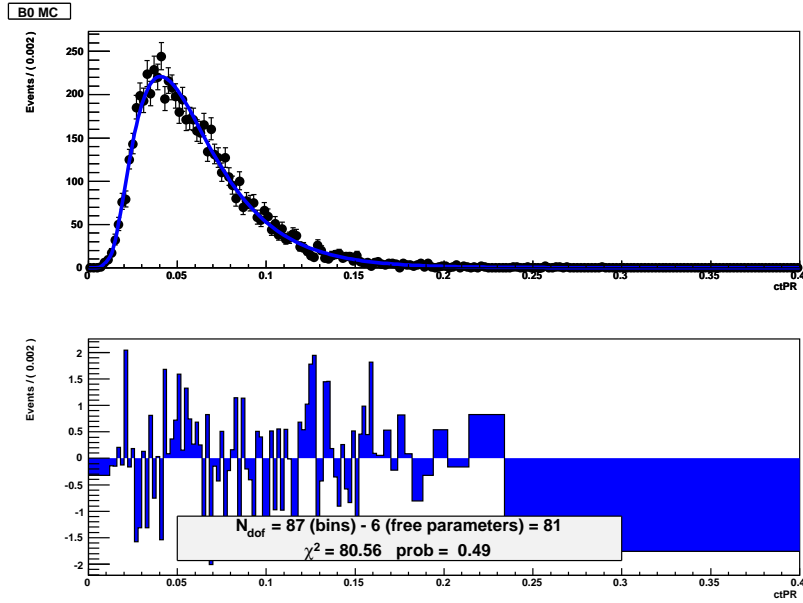
Figure 9.17: PDF fit to Monte Carlo for $B^0 \to \overline{D}^0\pi^+ X$ reconstructed as $B^+ \to \overline{D}^0\pi^+$.
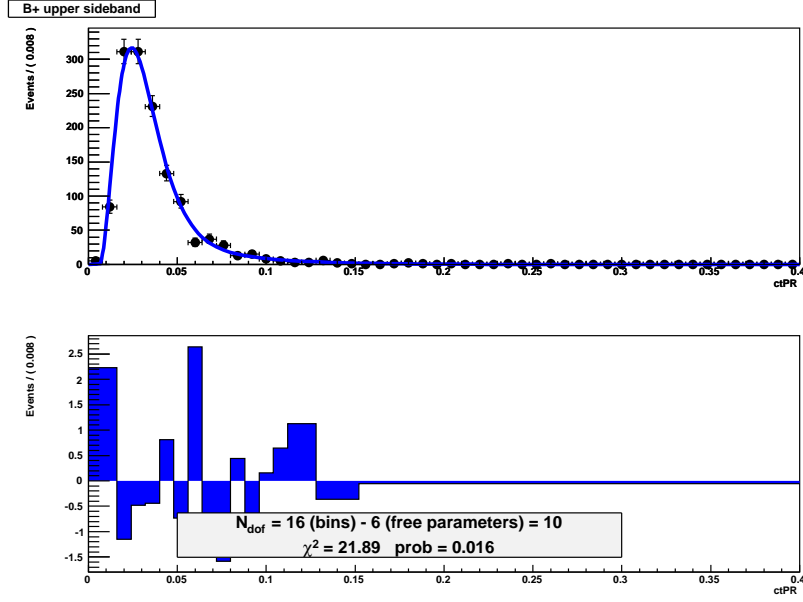
Figure 9.18: Background model for $B^+ \to \overline{D}^0\pi^+$ from the upper sideband data with $m_B \in [5.7,\ 6.4]$ GeV/c^2.
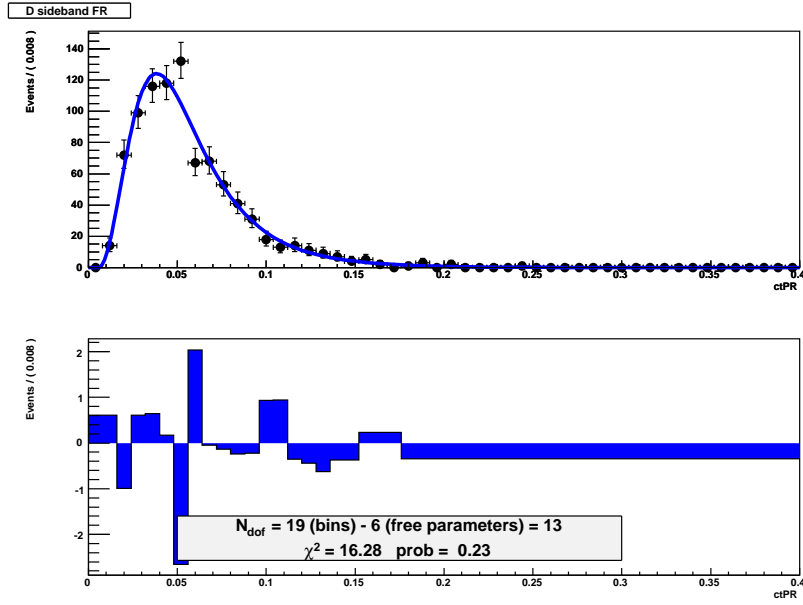
Figure 9.19: Background model for $B^+ \to \overline{D}^0\pi^+$ from the D sideband in the FR region ($m_B \in [5.17,\ 5.35]$ GeV/c^2).
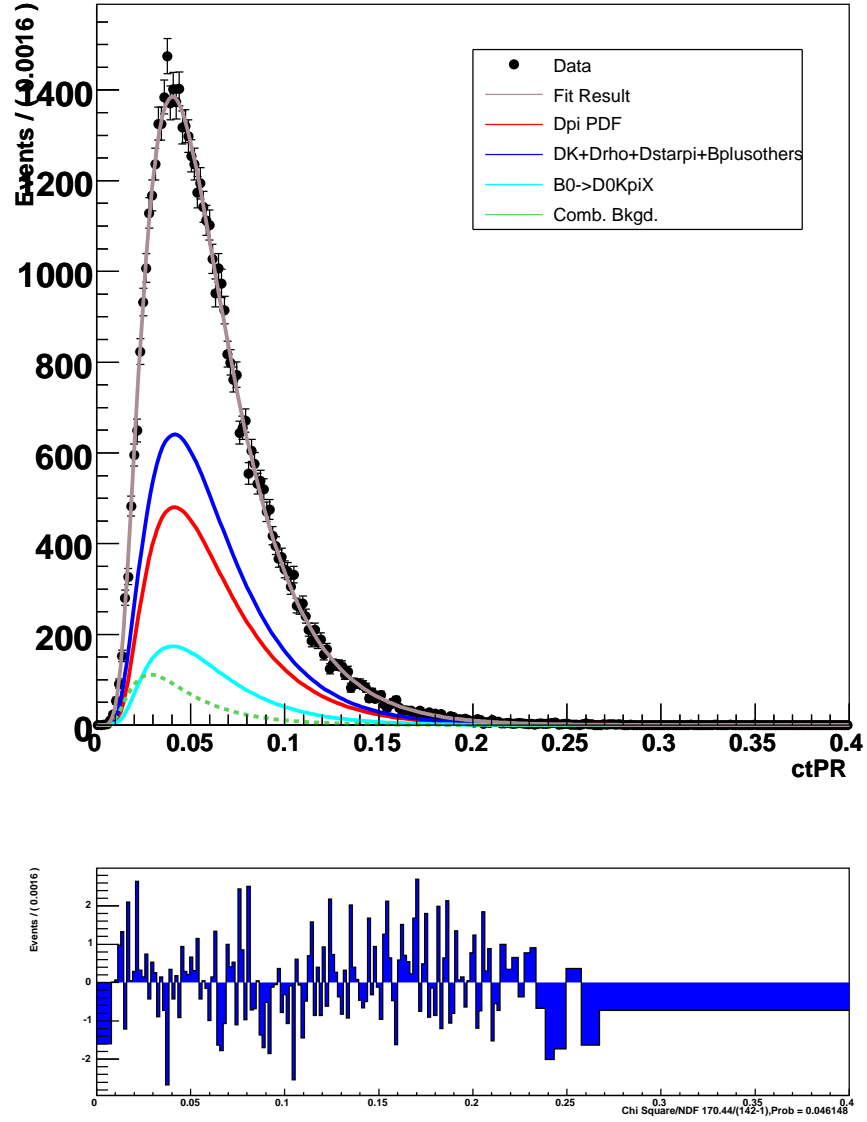
Figure 9.20: ct projection of the lifetime fit to events reconstructed as $B^+ \to \overline{D}^0 \pi^+$ in the combined FR+PR region.
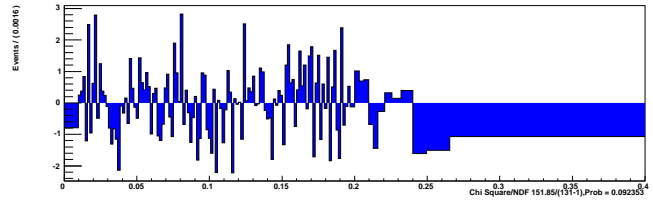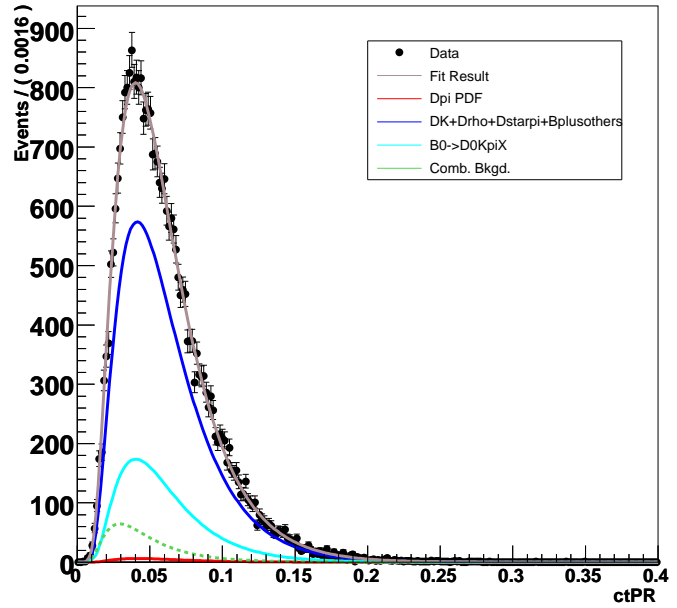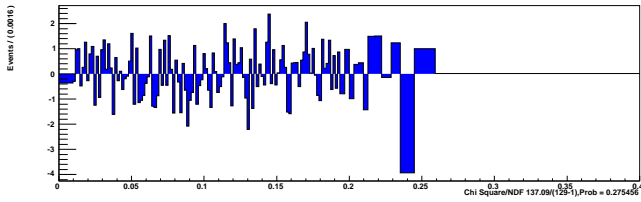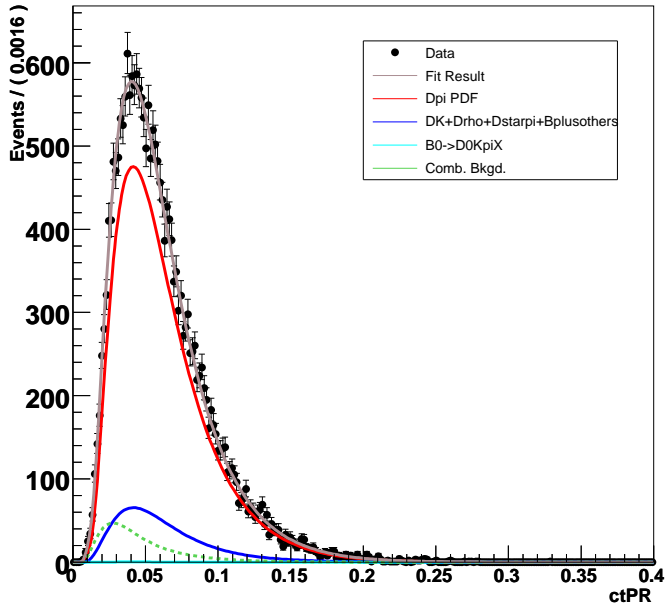
(a) Fully Reconstructed Region (b) Partially Reconstructed Region

Figure 9.21: ct projection of the lifetime fits to events reconstructed as $B^+ \to \overline{D}^0 \pi^+$ in the separate FR and PR mass regions.

123

Table 9.14: Parameters of single-B PDFs for $B^0 \to D^- \pi^+$

	$D\pi$	DK	$D * \pi$	$D\rho$	B^0 other	B^+	B_s
N_1	1.000000	1.000000	1.000000	1.000000	1.000000	1.000000	1.000000
β_1	0.005810	0.005241	0.004896	0.005780	0.008893	0.008586	0.006886
τ_1	0.035427	0.031127	0.054741	0.035570	0.013523	0.026426	0.032589
N_2	6.823687	19.91008	41.48383	7.810262	0.290113		6.137812
β_2	0.012712	0.015577	0.009970	0.011033	0.014274		0.014003
τ_2	0.016614	0.009335	0.021861	0.016978	0.028596		0.018364
τ	τ_{B^0}	τ_{B^0}	τ_{B^0}	τ_{B^0}	τ_{B^0}	$1.071 * \tau_{B^0}$	0.0438
$\sigma_B kgd$	0.010477	0.018277	0.003869	0.013966	0.015495	0.008819	0.009851
χ^2	148.0	76.7	91.0	117.6	92.2	18.1	48.7
ndf	$133 - 6$	$83 - 6$	$108 - 6$	$117 - 6$	$86 - 6$	$17 - 3$	$48 - 6$
$prob$	9.9%	48.8%	77.5%	31.6%	16.6%	20.2%	22.3%

	upper sideband (RS)	D sideband (FR)	D sideband (PR)	D sideband (PR+FR)
N_1	1.00000e+00	1.00000e+00	1.00000e+00	1.00000e+00
β_1	6.59798e-03	1.42067e-02	9.79457e-03	8.86191e-03
τ_1	8.03205e-03	1.17988e-02	1.20750e-02	1.46575e-02
N_2	6.76764e-03	2.64435e-02	8.14559e-02	3.80440e-02
β_2	5.00000e-04	1.71102e-03	3.16404e-03	7.38573e-04
τ_2	2.54327e-02	3.41265e-02	2.71697e-02	3.58094e-02
τ_{Bkgd}	0.0500(fixed)			
σ_{Bkgd}	1.44604e-02	6.21212e-03	1.94647e-02	1.74907e-02
χ^2	17.4	13.9	32.4	30.4
ndf	$15-6$	$20-6$	$18-6$	$22-6$
$prob$	4.3%	45.6%	0.1%	1.6%

Table 9.15: Parameters for background PDFs for $B^0 \to D^- \pi^+$

Table 9.16: Fit components for $B^0 \to D^- \pi^+$ mass fits.

Decay modes	Mass pdf	Configuration
	$\overline{B}^0 \to D^+ \pi^-$ fit	
$B^0 \to D^- \pi^+$	MC	norm floating
$B^0 \to D^- \pi^+ (n\gamma)$	MC	norm floating
$B^0 \to D^- K^+$	MC	$DK/D\pi$ constrained to PDG
$B^0 \to D^- \rho^+$	MC	$D\rho/D\pi$ constrained to PDG
$B^0 \to D^{*-} \pi^+$	MC	$D^*\pi/D\pi$ constrained to PDG
$B^0/B^+ \to D_2^* \pi^+$	MC	fixed to $B^0/B^+ \to D^- X$
$B^0/B^+ \to D^{(*)} K^{(*)}$	MC	fixed to $B^0/B^+ \to D^- X$
$B^0/B^+ \to D^{(*)} e X$	MC	fixed to $B^0/B^+ \to D^- X$
$B^0/B^+ \to D^- X$	MC	norm floating
$B_s \to D_s X$	MC	norm floating
Fake $D+$ track	leakage subtracted D^- sideband	norm fixed
Real $D+$ track	SBS $D^+ \pi^+$ WS [5.00, 6.45] GeV/c^2	norm floating

Decay modes	Number of events	Fraction of total
$B^0 \to D^- \pi^+$	16949.29 ± 161.28	0.276325
$B^0 \to D^- \pi^+ (n\gamma)$	1279.06 ± 396.10	0.020853
$B^0 \to D^- K^+$	1382.43 ± 238.91	0.022538
$B^0 \to D^- \rho^+$	10314.07 ± 834.40	0.168151
$B^0 \to D^{*-} \pi^+$	5535.78 ± 349.01	0.090250
$B^0/B^+ \to D_2^* \pi^+$	1361.60	0.022198
$B^0/B^+ \to D^{(*)} K^{(*)}$	741.11	0.012082
$B^0/B^+ \to D^{(*)} eX$	1672.10	0.027260
$B^0/B^+ \to D^- X$	6877.61 ± 472.43	0.112126
$B_s \to D_s X$	2284.02 ± 326.58	0.037236
Fake $D+$ track	7651.81	0.124748
Real $D+$ track	5289.35 ± 137.20	0.086233

Table 9.17: Results of the mass fit for $B^0 \to D^- \pi^+$ in terms of the number of events in the region [4.85, 6.45] GeV/c^2. Since the fit is extended, the errors on the numbers of events are quoted. The normalization of the fake D component is fixed in the fit. The B^0/B^+ modes without quoted errors have their errors incorporated into mode they are fixed to ($B^0/B^+ \to D^- X$)

Fractions returned by mass fit			
	FR	PR	FR + PR
$D^-\pi^+$	0.807751	0.024551	0.452151
D^-K^+	0.053812	0.011411	0.034561
$D^{*-}\pi^+$	0.000710	0.295018	0.134336
$D^-\rho^+$	0.002388	0.317731	0.145564
B^0 remainder	0.006419	0.117643	0.056876
B^+	0.000000	0.028082	0.012793
B_s	0.036301	0.046463	0.040915
Bkgd - real D	0.036839	0.052600	0.043995
Bkgd - fake D	0.055780	0.106501	0.078809
Real D in upper sideband	0.70		
D leakage	0.364180	0.263989	0.306234
Fractions used by lifetime fit			
	FR	PR	FR + PR
$D^-\pi^+$	0.798589	0.024551	0.447739
D^-K^+	0.053812	0.011411	0.034561
$D^{*-}\pi^+$	0.000710	0.284980	0.129930
$D^-\rho^+$	0.002388	0.307698	0.141150
B^0 remainder	0.006419	0.117640	0.056876
B^+	0.000000	0.028082	0.012793
B_s	0.022557	0.036425	0.027683
Bkgd - D SB	0.062898	0.114070	0.086418
Bkgd - upper SB	0.052627	0.075143	0.062850

Table 9.18: Fractions of each mode reconstructed as $B^0 \to D^-\pi^+$ found in the three mass regions of the full data sample. The fully reconstructed (FR) region includes all events with $m_B \in [5.17, 5.35]$ GeV/c^2. The partially reconstructed (PR) region includes all events with $m_B \in [5.00, 5.17]$ GeV/c^2. The combined (FR+PR) region includes all events with $m_B \in [5.00, 5.35]$ GeV/c^2.

FR	$\tau_{B^0}(\mu\text{m})$	448.6 ± 4.6
	χ^2/ndf	$195.4/(131\text{-}1)$
	prob	1.8E-2%
PR	$\tau_{B^0}(\mu\text{m})$	452.5 ± 5.8
	χ^2/ndf	$169.4/(122\text{-}1)$
	prob	2.5E-1%
FR + PR	$\tau_{B^0}(\mu\text{m})$	449.9 ± 3.6
	χ^2/ndf	$236.0/(139\text{-}1)$
	prob	1.4E-5%

Table 9.19: Results of $B^0 \to D^- \pi^+$ lifetime fit: The lifetime fit is performed in three mass regions. The fully reconstructed (FR) region includes all events with $m_B \in [5.17, 5.35]$ GeV/c^2. The partially reconstructed (PR) region includes all events with $m_B \in [5.00, 5.17]$ GeV/c^2. The combined (FR+PR) region includes all events with $m_B \in [5.00, 5.35]$ GeV/c^2.
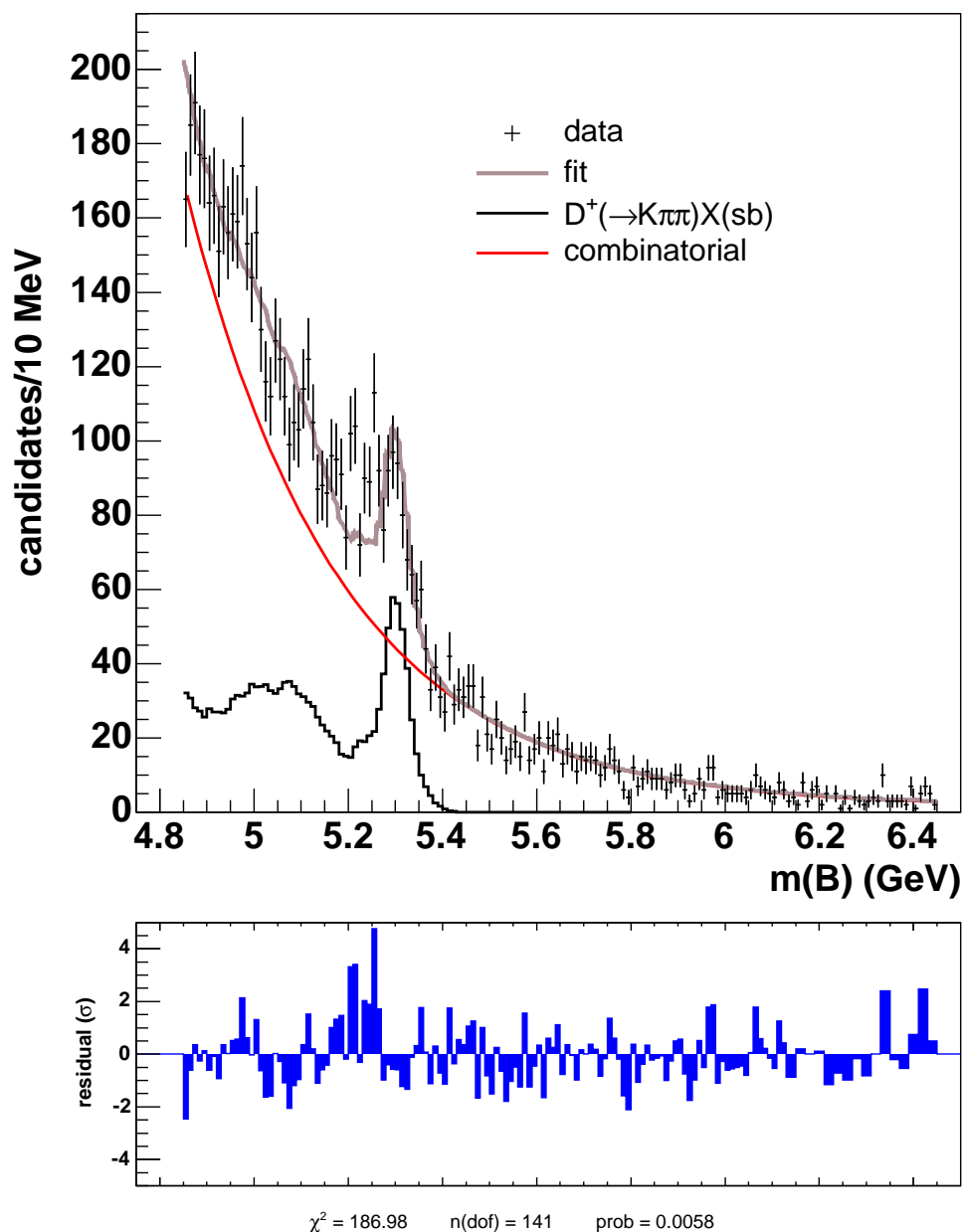
Figure 9.22: This auxiliary fit to the D sidebands with D leakage subtracted is used to determine the shape of the fake-D component for the mass fit. These events are reconstructed as $B^0 \to D^- \pi^+$ in the full 1.3 fb^{-1}.
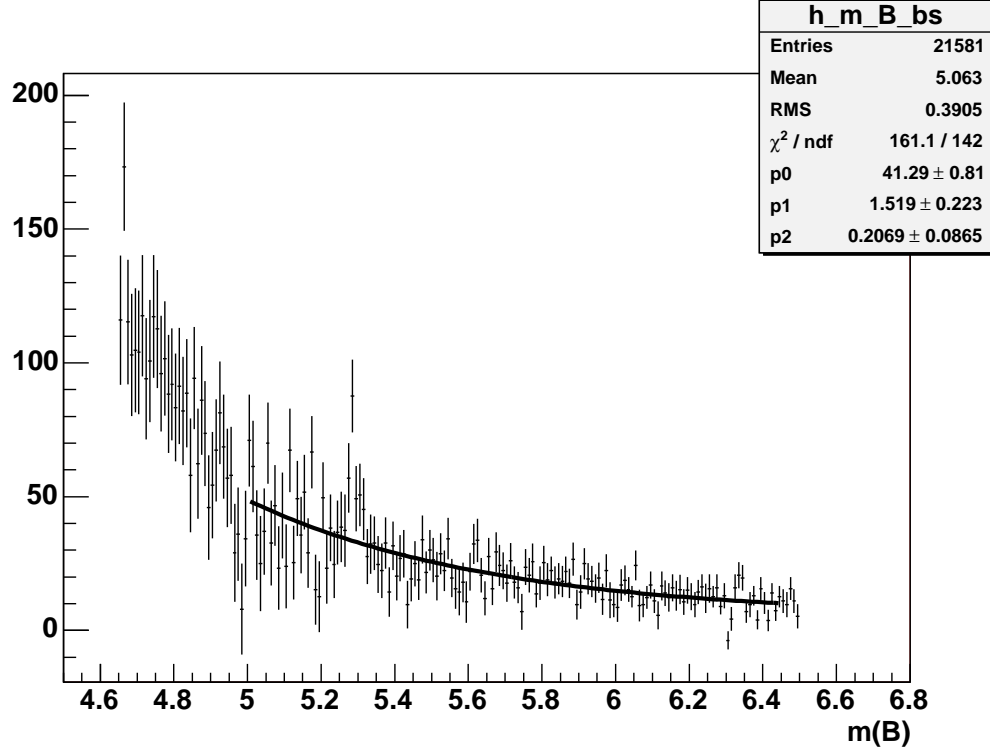
Figure 9.23: This auxiliary fit to the sideband-subtracted WS sample from the full 1.3 fb^{-1} of data. The WS sample is made of events reconstructed as $D^-\pi^-$ that pass the analysis cuts. The functional form employed is an exponential plus a constant in the region $m_B \in$ [5.00, 6.45] GeV/c^2. The resulting shape is in the mass fit as the real-D template.
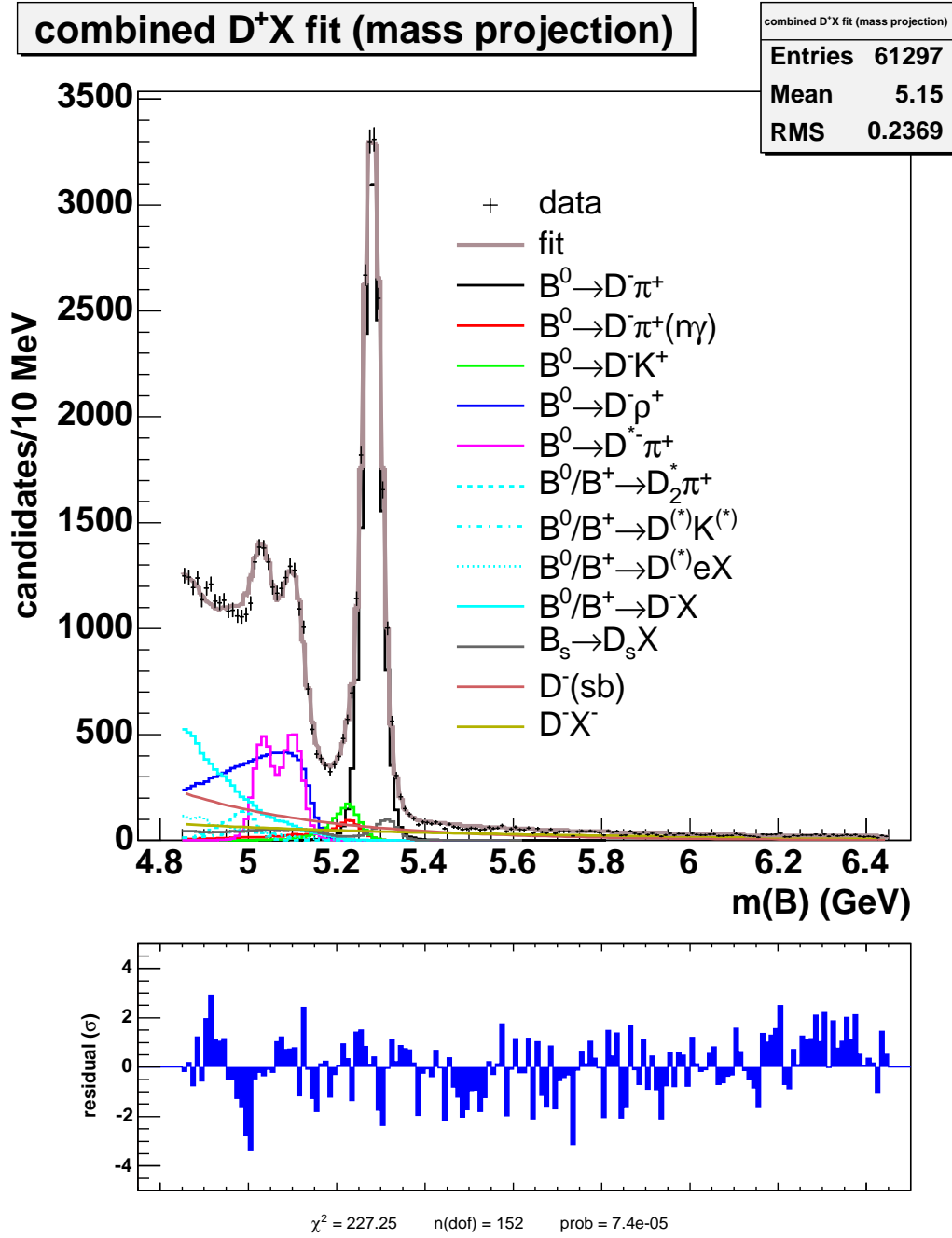
Figure 9.24: Mass fit of events reconstructed as $B^0 \to D^- \pi^+$ in full 1.3 fb^{-1}.
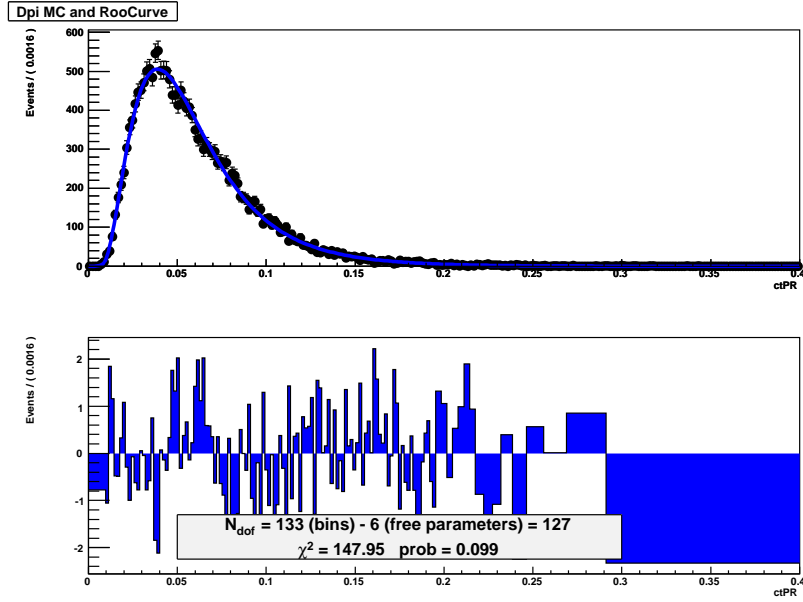
Figure 9.25: PDF fit to Monte Carlo for $B^0 \to D^-\pi^+$ reconstructed as $B^0 \to D^-\pi^+$.
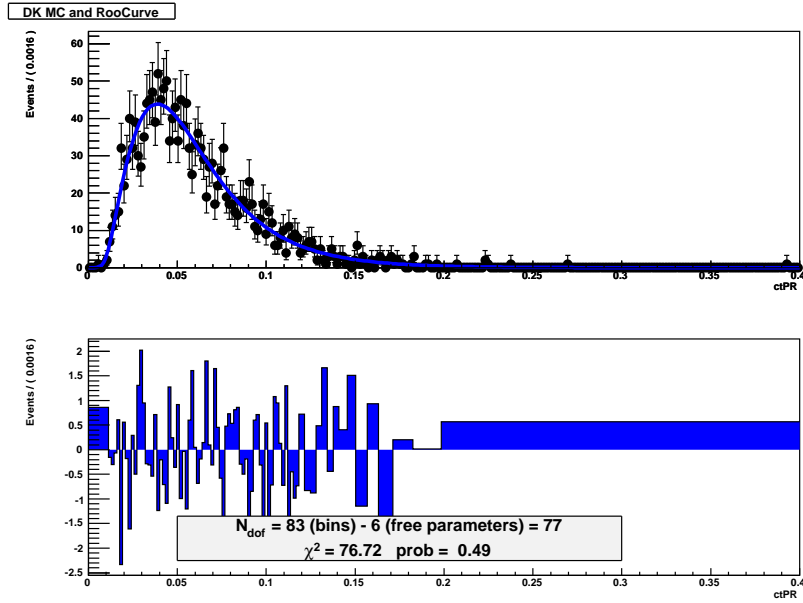
Figure 9.26: PDF fit to Monte Carlo for $B^0 \to D^-K^+$ reconstructed as $B^0 \to D^-\pi^+$.
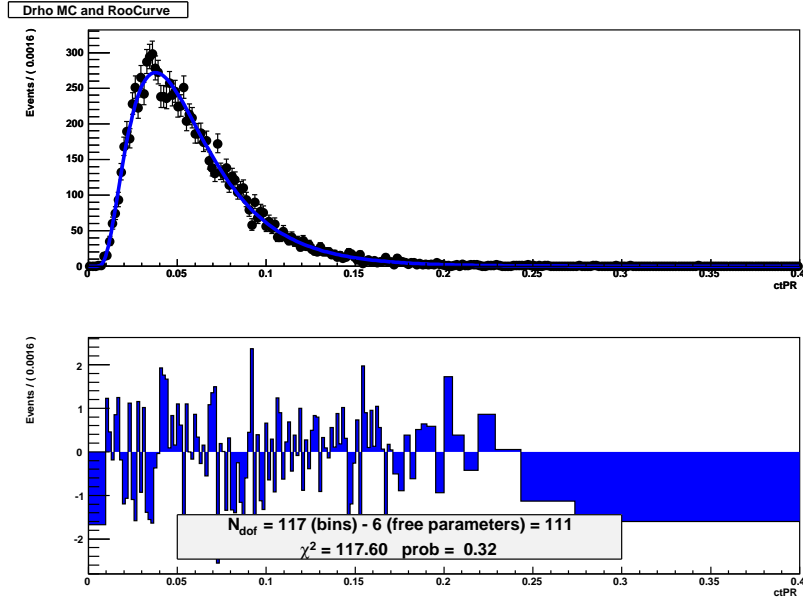
Figure 9.27: PDF fit to Monte Carlo for $B^0 \to D^- \rho^+$ reconstructed as $B^0 \to D^- \pi^+$.
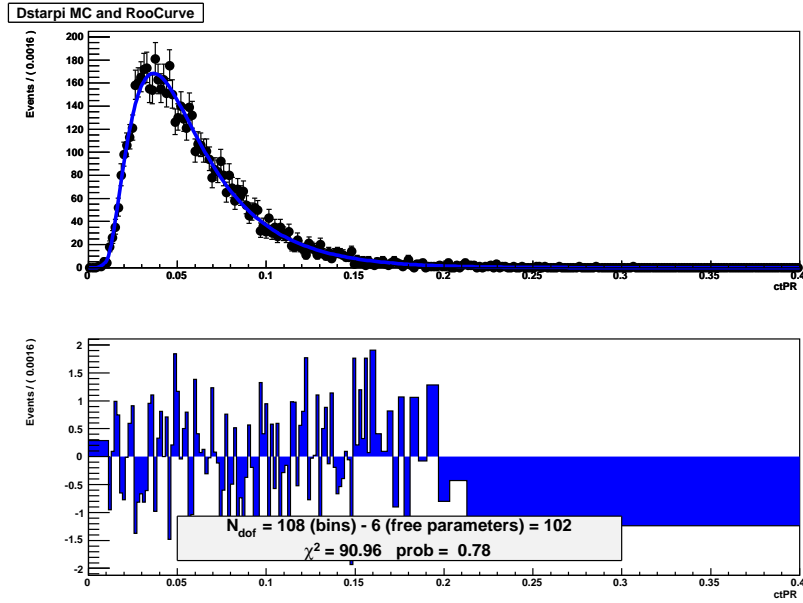
Figure 9.28: PDF fit to Monte Carlo for $B^0 \to D^{*-} \pi^+$ reconstructed as $B^0 \to D^- \pi^+$.
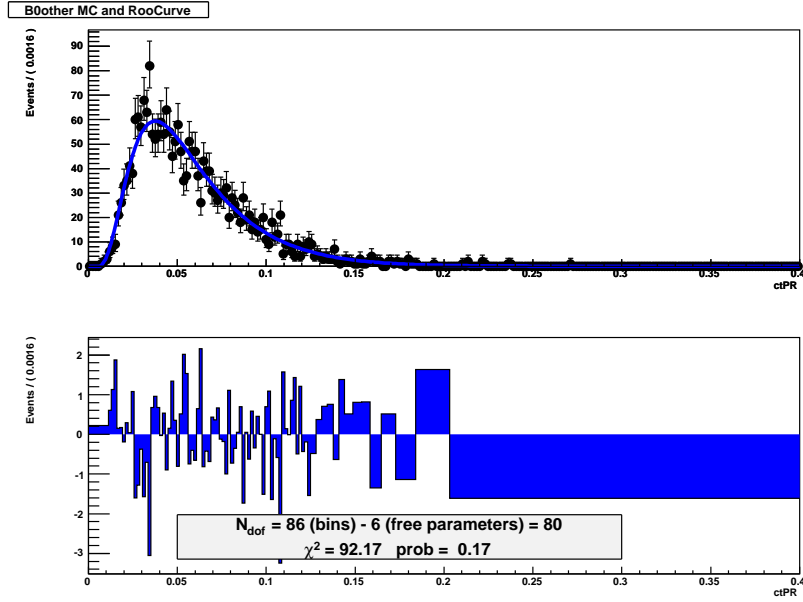
Figure 9.29: PDF fit to Monte Carlo for the remaining $B^0 \to D\pi X$ reconstructed as $B^0 \to D^-\pi^+$.
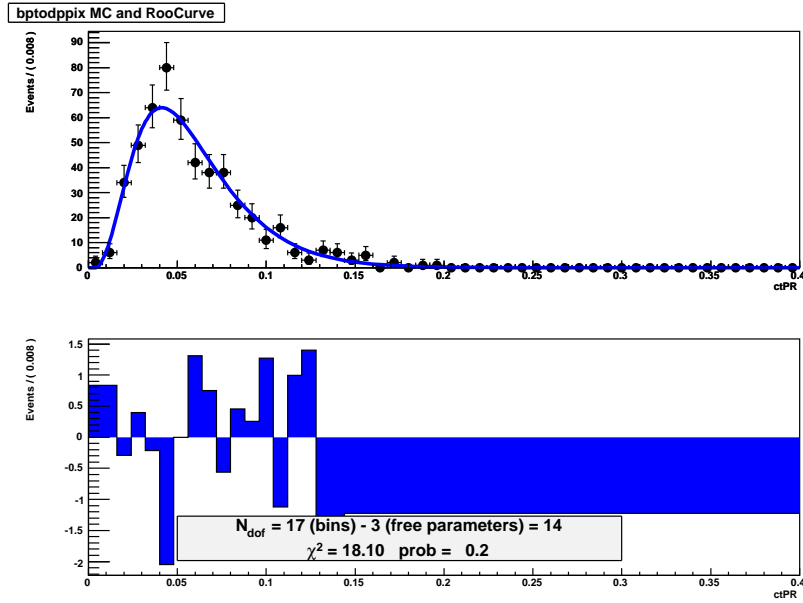
Figure 9.30: PDF fit to Monte Carlo for $B^+ \to D^-\pi^+X$ reconstructed as $B^0 \to D^-\pi^+$.
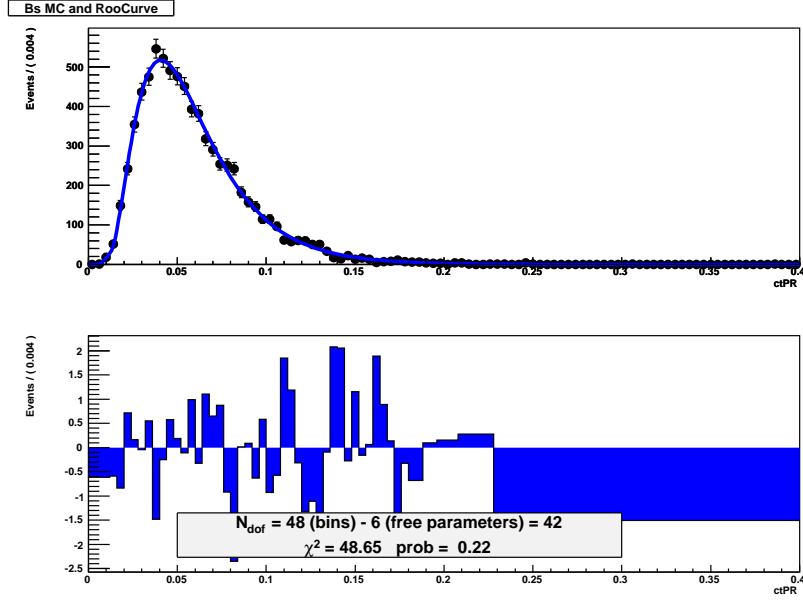
Figure 9.31: PDF fit to Monte Carlo for $B_s \to D_s(\phi\pi)\pi$ and $B_s \to D_s(K^*K)\pi$ reconstructed as $B^0 \to D^-\pi^+$.
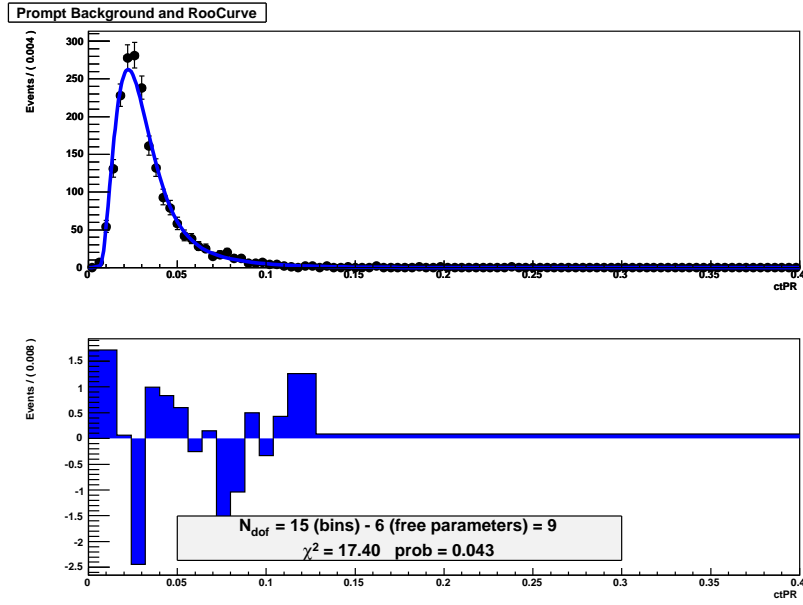
Figure 9.32: Background model for $B^0 \to D^-\pi^+$ from the upper sideband data with $m_B \in [5.7,\ 6.4]\ \mathrm{GeV}/c^2$.
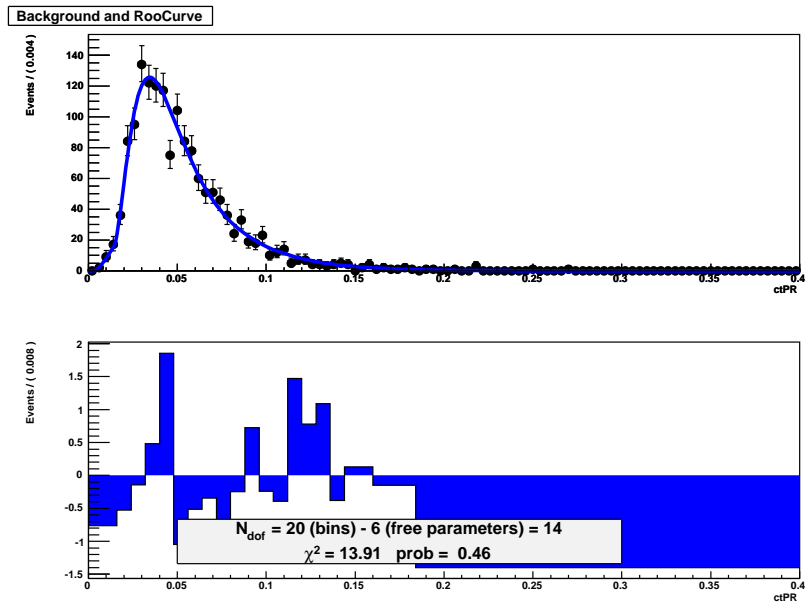
Figure 9.33: Background model for $B^0 \to D^- \pi^+$ from the D sideband in the FR region ($m_B \in [5.17, 5.35]$ GeV/c^2).
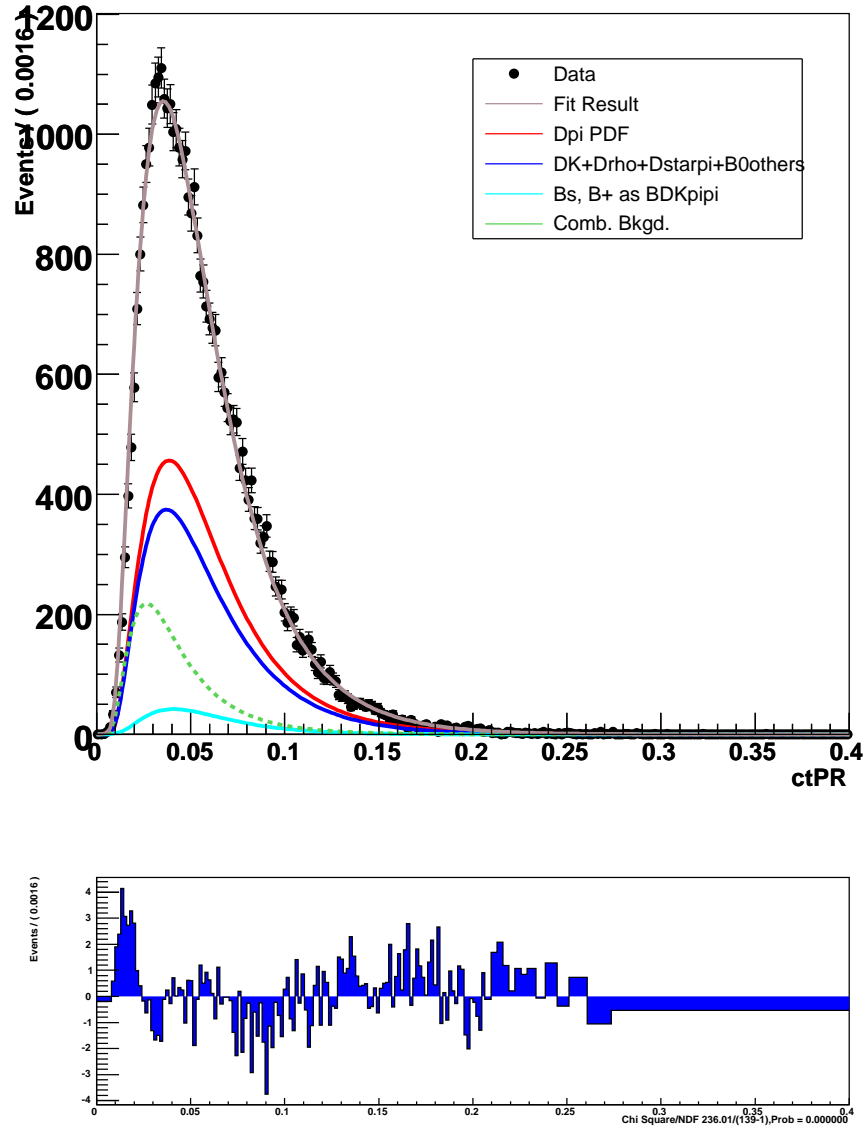
Figure 9.34: ct projection of the lifetime fit to events reconstructed as $B^0 \to D^- \pi^+$ in the combined FR+PR region.

(a) Fully Reconstructed Region

(b) Partially Reconstructed Region

Figure 9.35: ct projection of the lifetime fits to events reconstructed as $B^0 \rightarrow D^- \pi^+$ in the separate FR and PR mass regions.
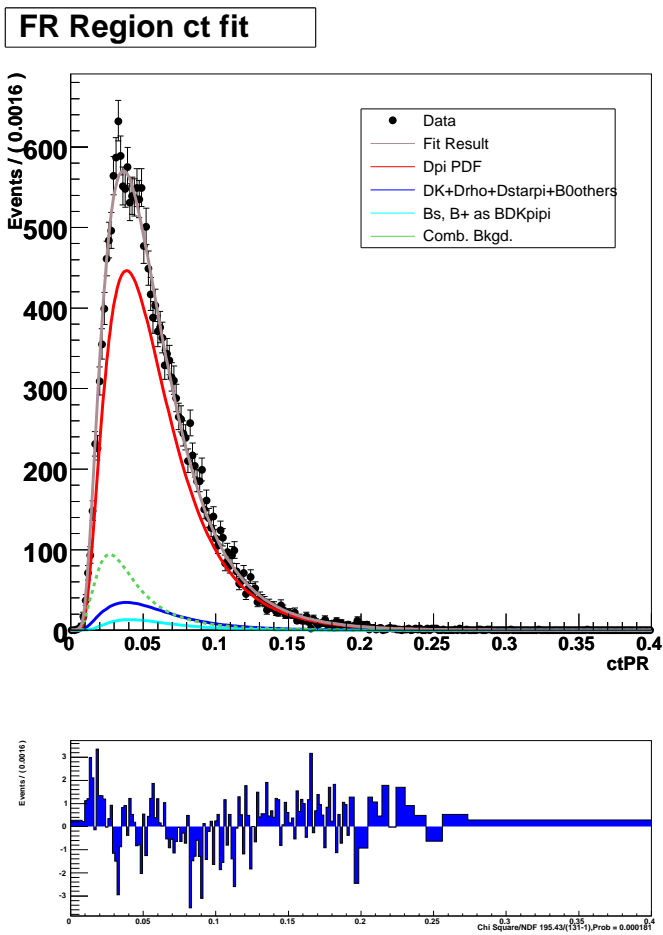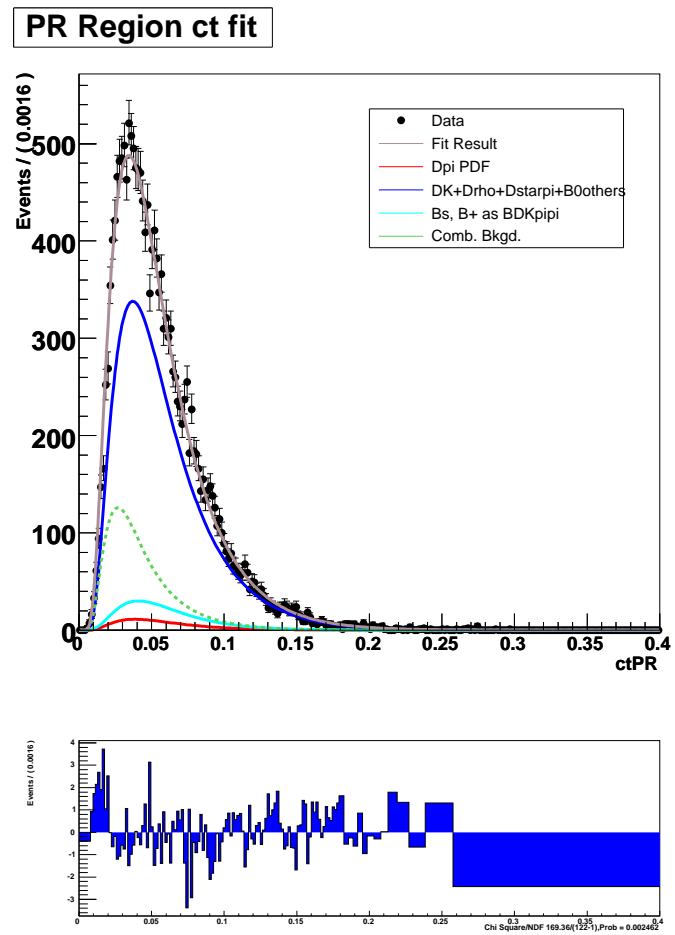
Chapter 10

Signal Sample Results

In this chapter we present the results of the signal sample $B_s \rightarrow D_s^-(\phi\pi^-)\pi^+$ fits. The lifetime of the B_s is determined from two sequential fits. The first fit is to the invariant mass distribution of the candidates, and it is used to determine the fractions of events in the background and signal modes that will be inputs to the second fit. The second fit is to the proper time distribution of the sample. The only variable that is able to float in the second fit is the lifetime of the B_s meson.

As discussed in Chapters 6 and 7, there are auxiliary fits to determine the background PDFs for the mass fit and the efficiency curve shapes for the lifetime fit. The results of these fits are also given.

10.1   Mass Fit Results

Before the final fit to the invariant mass distribution of $B_s \rightarrow D_s^-(\phi\pi^-)\pi^+$ candidates, two auxiliary fits are performed to determine the shapes of the background PDFs that will be used.

10.1.1   Auxiliary Mass Fits

The first auxiliary fit is a fit to the invariant mass distribution of the candidates in the D_s sidebands, those candidates that satisfy $m(D_s) \in [1.924, 1.939] \cup [1.999, 2.014]$ GeV/c^2, to determine the fake D + track shape. The fake D + track shape is assumed to be an exponential on top of a flat line. Since there are some real D's that leak into the D sidebands, the fit to the invariant mass of the candidates in the sidebands includes a histogram PDF taken from D_s sidebands of B_s Monte Carlo. Its normalization floats along with the normalization and shape parameters of the fake D + track PDF. The results of the fake-D + track fit are shown in Fig. 10.2.

The second auxiliary fit is to the invariant mass distribution of the $D_s^-\pi^-$ sample, also called the wrong-sign (WS) sample, to determine the real D + track shape. The sample is first sideband subtracted in the D_s mass, so that only real D_s's remain. The real D + track shape is also assumed to be an exponential on top of a flat line. The results of the real-D + track fit are shown in Fig. 10.3.

10.1.2 Final Mass Fit

The mass fit for the $B_s \to D_s^-(\phi\pi^-)\pi^+$ candidates is non-extended. A few simplifying assumptions are made, employing results from an earlier $B_s \to D_s^-(\phi\pi^-)\pi^+$ fit that used dE/dx information [24]. Most notably, the $D_s^- K^+/D_s^- \pi^+$ fraction is constrained to (0.095 ± 0.021). The $D_s^- \pi^+(n\gamma)/D_s^- \pi^+$ fraction is fixed to 4.2%. The shape of the real-D + track background PDF is fixed, but its normalization is allowed to float. Both the shape and normalization of the fake-D + track background PDF are fixed. The normalization assumes the fake-D shape is flat in the D_s mass distribution. The configuration of the mass fitter is summarized in Table 10.5.

A plot of the mass fit of the full data sample is found in Figure 10.4. The results of the fit in the full mass range $[4.85, 6.45]$ GeV/c^2 are shown in Table 10.6. The fractions of the events found in each decay mode in the FR region ($m(B_s) \in [5.35, 5.45]$ GeV/c^2), the PR region ($m(B_s) \in [5.00, 5.35]$ GeV/c^2), and the combined FR+PR region are listed separately in the upper portion of Table 10.7.

10.2 Lifetime Fit Results

The final fit to the proper time distribution of the $B_s \to D_s^-(\phi\pi^-)\pi^+$ candidates requires two types of inputs: the fractions of events in each mode and the shape parameters of their PDFs. The fractions are derived from the mass fit results. Since the backgrounds in the mass fit are not grouped in the same categories as in the lifetime fit, some translation (described in Chap. 8) is required. The final fractions used by the lifetime fit are shown in the lower portion of Table 10.7. The shape parameters are derived from auxiliary fits performed for each mode. We discuss the results of these fits in greater detail below.

10.2.1 Auxiliary Lifetime Fits

The shape parameters of the PDFs for the fully and partially reconstructed B_s modes are determined in fits to Monte Carlo samples that have been reweighted in

trigger category and $p_T(B_s)$. Since the lifetime used for generation is known, it can be fixed in the auxiliary fits for the parameters that describe the effects of detector smearing and selection requirements on the proper time distribution. In the final fit to data, the shape parameters are fixed, and the lifetime of the B_s is the only variable allowed to float. The results of these auxiliary fits are shown in Figs. 10.5-10.9 and summarized in Tab. 10.3.

For the background PDFs, we fit for the shape parameters of several background samples. Since the backgrounds do not depend on $\tau(B_s)$, all the background shape parameters are frozen in the final fit. The backgrounds included in this fit are $B^{+/0} \to D^+\pi X$ (reconstructed as $D_s\pi$), $B^0 \to D_s\pi X$, $\Lambda_b \to \Lambda_c\pi$ (reconstructed as $D_s\pi$), the D_s sidebands, and the B_s upper sideband ($m_B \in [5.7, 6.4]\ \mathrm{GeV}/c^2$). Since τ_{Bkgd} in these fits is degenerate with other shape parameters and has little physical meaning, we fix it to 500 μm. The results of the background auxiliary fits are shown in Figs. 10.10-10.14 and summarized in Tab. 10.4.

10.2.2   Final Lifetime Fit

Several precautions were taken to protect the $\tau(B_s)$ result from bias. The extensive studies performed on three control samples with a range of background levels, decay structures, and statistical power allowed us to refine the fit procedure without looking at the B_s results. After the procedure was set, the initial fits for $\tau(B_s)$ and the studies of the systematics uncertainties were performed blinded. All results displayed during this period were offset by the same unknown number. The results from the fitter in different mass regions could be compared relative to each other, but the absolute scale was not known. The statistical uncertainties displayed were accurate. However, now that the fit has been unblinded, we will only quote the unblinded result.

Fitting the FR and PR regions separately, we checked for agreement. The results for the FR region ($436.5 \pm 20.0\ \mu$m) and PR region ($463.0 \pm 15.2\ \mu$m) disagree with each other by 1.0σ. In the final fit to the combined FR and PR region, the lifetime of $c\tau_{B_s} = 455.0 \pm 12.2(\mathrm{stat.})\ \mu$m is obtained. The results of the lifetime fit are separated

143

by mass region in Table 10.8. The fit results are plotted in Figures 10.15 and 10.16.

10.3 Systematic Uncertainties

For each systematic uncertainty, 1000 pseudo-experiments are generated with the number of events Poisson-distributed around 3967 (the number of events in the combined fully and partially reconstructed regions). Each set of experiments is generated with a non-standard configuration of the fitter (the one exception is a bootstrapped Monte Carlo described in Sec. 10.3.5); the particular variations are described in detail in the following sections. With one exception, the model used to fit the the pseudo-experiments is the same as was used for the $B_s \to D_s^- \pi^+$ full data sample fit. The mean biases ($c\tau_{\mathrm{returned}} - c\tau_{\mathrm{gen}}$) returned from the toy Monte Carlo are used to set the size of the systematic uncertainties. Where $\pm 1\sigma$ variations are considered, the larger returned bias is used to set the final systematic. The results of all the toy Monte Carlo studies, including those that probe greater than 1σ variations, are summarized in Table 10.1. Table 10.2 contains the final list of systematic uncertainties for this lifetime measurement.

10.3.1 Background Model Choice and Fractions

In the default model, the B upper sideband ($m_B \in [5.7, 6.4]$ GeV/c^2) and the D sideband in the FR + PR regions ($m_B \in [5.00, 5.45]$ GeV/c^2) are combined to form the mixture of real D's and fake D's measured by the mass fit. There are several inputs that go into determining the fractions of B upper sideband and D sideband (see Chap. 8). The uncertainties on these inputs translate into a systematic uncertainty on the final lifetime measurement. We also perform an extreme test (greater than 1σ variation) where we generate with only one type of background, and fit with the default model. The biases returned from the toy Monte Carlo studies are listed below.

The following two situations in which only one background is used for generation are extreme deviations from the default model. These studies probe the size of the

largest possible deviation from the default fit, and a 1σ variation will be well within the bounds established by these two situations.

- We use a background PDF from the B upper sideband only for generation and fit with the default model. The returned bias is -7.7 μm.

- We use a background PDF from the D sideband only for generation and fit with the default model. The returned bias is 11.9 μm.

The following situations are more consistent with $\pm 1\sigma$ variations. The four sources of systematics will be added in quadrature to determine the final systematic for the background fraction.

- The fraction of the B upper sideband that is real D is determined by extrapolating the D sidebands in the B upper sideband under the D peak. The value used in the default fit is 79%. Varying this fraction by +5% and -5% for generation returns biases of 0.8 μm and -0.2 μm, respectively.

- The fraction of the D sidebands in the FR+PR region that is D-signal leakage is determined by an auxiliary fit to the B mass shape of the D sidebands. The value used in by the default fit is 50.7%. Varying this fraction by +7.2% and -7.2% for generation returns biases of -0.8 μm and 1.2 μm, respectively.

- The mass fit measures the fraction of real-D events in the FR+PR region to be 2.8%. Varying this fraction by +0.3% and -0.3% for generation returns biases of -1.5 μm and 2.7 μm, respectively.

- The mass fit measures the fraction of fake-D events in the FR+PR region to be 3.4%. Varying this fraction by +0.3% and -0.3% for generation returns biases of -0.5 μm and 1.8 μm, respectively.

Combining the above errors in quadrature, we find a 3.6 μm uncertainty.

Further studies have indicated that a systematic uncertainty should be assessed for the "choice of background model" in addition to the "background fraction" systematics associated with the default model that have already been discussed in this section. The systematic is estimated using the following procedure:

145

1. We perform a mass fit to full sample using a flat (constant in B mass) real-D shape and the fake-D shape from the auxiliary D-sideband fit. The normalizations of both the real-D and fake-D shapes are allowed to float, but their shapes are fixed.

2. We generate toy Monte Carlo for the FR+PR region using the new fractions from Step 1 and fit the toy Monte Carlo samples with the default fractions.

3. Since this variation is believed to be greater than 1σ and is not completely isolated from the "background fraction" systematics above, we take half the size of the observed toy Monte Carlo bias as the systematic.

Since the returned bias is 9.0μm, the systematic for background modeling is estimated to be 4.5μm. The combined uncertainty for both the choice of background model and the background fraction is then $3.6 \oplus 4.5 = 5.7\mu$m.

10.3.2 Fixed Single-B Background $c\tau$

The PDFs for the single-B backgrounds come from fits to Monte Carlo samples. In the fits, $c\tau_{B^0}$, $c\tau_{B^+}$, and $c\tau_{\Lambda_b}$ are all set to 500 μm, as the other lifetime-like parameters are more than adequate to describe the shape. If a lifetime used by the Monte Carlo generator is different from the true hadron lifetime by a few percent, this would then affect the B_s lifetime measurement. To estimate the size of this effect, we generate toy MC with $c\tau_{B^0}$, $c\tau_{B^+}$, and $c\tau_{\Lambda_b}$ set to 490 μmand fit with the default (500 μm) model. We repeat the toy Monte Carlo study with the lifetimes set to 510 μm. The returned biases for these -2% and +2% variations are -0.6 μm and 1.0 μm, respectively.

10.3.3 Effect of Reweighting for p_T and Trigger Category

Due to the finite statistics of data and Monte Carlo, there is a possibility that a bias is introduced when the Monte Carlo samples are reweighted to match the data p_T and trigger category distributions. The procedure for the reweighting is described

146

in Sec. 7.3. To estimate the systematic uncertainty associated with reweighting to a histogram, we use a functional form fit to the histogram instead. We choose to fit the $p_T(B)$ histogram with a first degree polynomial. The efficiency curves derived from Monte Carlo reweighted to the function are then used for generation of toy Monte Carlo. The toy Monte Carlo is fit with the default model. The mean bias is 3.7 μm.

For an extreme test (much larger than a 1σ variation) to probe the importance of reweighting, we also generate with curves fit to unreweighted Monte Carlo. The returned bias is 13.6 μm.

10.3.4 Lifetime Contribution of the Radiative Tail

In the default configuration, we do not currently separate the radiative tail (modeled by PHOTOS [27]) from the $D_s^-\pi^+$ Monte Carlo before fitting for the P_{FR} efficiency curve parameters. For the mass fit, the PHOTOS tail is treated separately, although its value is fixed to 4.2% of the non-PHOTOS $D_s^-\pi^+$ size.

Here we estimate the systematic uncertainty associated with (1) treating the $D_s\pi(n\gamma)$ as a single, fully reconstructed mode and (2) fixing the size of the PHOTOS tail. When deriving efficiency curves we treat the PHOTOS tail as a PR mode and the non-PHOTOS peak as a FR mode. We use these separate efficiency curves for generation and at the same time vary the relative fraction of PHOTOS to non-PHOTOS events. We perform two toy Monte Carlo studies: one with the fraction set to 8.0% for generation, the other with the fraction set to 0.3%. Since the statistics of the PHOTOS component is low, the divided $D_s\pi$ sample is not reweighted. We then fit with the default model with one modification: the combined $D_s\pi$ (PHOTOS + non-PHOTOS) template is also derived from unreweighted Monte Carlo. The mean biases are -0.4 and 0.6μm for the relative fractions of 8.0% and 0.3%, respectively.

10.3.5 Efficiency Curve Parameterization

To test whether a PDF adequately describes a Monte Carlo ct distribution, one would ideally fit for the efficiency curve parameters on one MC sample and then freeze the parameters and fit for the lifetime on 1000 other MC samples. Since we do not have the extra realistic MC samples, we "make" 1000 samples from the one we have by bootstrapping.

For example, we know the final B_s data has (according to the mass fit) 1128 $D_s\pi$ events in the FR+PR region. We generate the $D_s\pi$ part of a bootstrapped Monte Carlo as follows:

1. The number of $D_s\pi$ events for a particular bootstrapped sample is *Poisson* distributed around 1128.

2. To get the first event, we generate a random number N between 0 and 23159 (the number of events in the original sample) and get the ct from the N-th event.

3. To get the second event, we generate another random number between 0 and 23159 and grab the ct from that event. The same event can be chosen twice; not all events have to be chosen.

4. This process continues until the target number of $D_s\pi$ events is reached.

The process is repeated for all the individual modes, including the real-D, fake-D, and single-B backgrounds, until a complete sample is generated. For the fake-D and real-D backgrounds we bootstrap off the D sideband and B upper sideband data samples. The complete bootstrapped sample is then fit with the default PDFs.

After generating and fitting 1000 bootstrapped samples, we find the mean bias is 0.6 μm.

10.3.6 SVT Modeling

Because the efficiency curve parameters are derived in fits to Monte Carlo and fixed in the final fit to data, the lifetime measurement relies heavily on the agreement

between Monte Carlo and data. The concern addressed by this study is how well the trigger turn-on is modeled in the Monte Carlo. Since the SVT simulation code that is run in the trigger simulation is identical to the SVT code run on data, we expect excellent agreement. However, because the trajectories and hit patterns of real and simulated particles can be different even if they have identical initial conditions, the SVT response can also be different.

To determine whether there is an overall disagreement between the trigger turn-ons in data and Monte Carlo, we study a J/ψ sample collected by the unbiased dimuon trigger. With the methods of [28], we determine the efficiency for Scenario A events as a function of $L_{xy}(J/\psi)$ for J/ψ data and Monte Carlo. Fitting a line to the ratio of data and MC efficiencies, we take the uncertainty on the slope as an estimate of the uncertainty on the level of data-MC agreement. We use $\pm 1\sigma$ variations to reweight the B_s Monte Carlo (after the p_T and trigger reweightings have already been performed) and calculate new efficiency curves. These new efficiency curves are used to generate toy MC which are then fit with the default curves. The $+1\sigma$ and -1σ variations yield mean biases of 4.1 μm and -3.1μm, respectively. We take the larger value as the systematic uncertainty for SVT modeling. More details of the J/ψ studies can be found in Appendix A.

10.3.7   Additional Systematics

We assess 1.0 μm uncertainty for the impact parameter correlation. This value is taken from the previous hadronic lifetime analysis [20]. For the uncertainty due to the internal alignment of the detector, we assess a value of 1.0 μm This value is taken from a previous lifetime analysis [29].

	Pull Width (σ)	Pull Mean (σ)	Mean Bias (μm)
Single background proxy choice			
a) B upper sideband only	1.031±0.024	-0.697±0.034	-7.739±0.374
b) D sideband only	0.959±0.021	0.991±0.030	11.933±0.371
Background rotation inputs			
a) Real D % upper SB = 74%	1.003±0.023	-0.032±0.032	-0.167±0.369
b) Real D % upper SB = 84%	1.000±0.023	0.056±0.033	0.847±0.378
c) D leakage in D SB = 43.5%	0.983±0.023	0.081±0.032	1.152±0.372
d) D leakage in D SB = 57.9%	1.010±0.023	-0.088±0.032	-0.774±0.369
Real D background fraction			
$+1\sigma$	0.991±0.022	-0.147±0.031	-1.474±0.362
-1σ	0.989±0.023	0.210±0.032	2.672±0.374
Fake D background fraction			
$+1\sigma$	0.971±0.022	-0.065±0.031	-0.531±0.362
-1σ	0.998±0.023	0.139±0.033	1.822±0.382
Alternate Background Model	0.994±0.022	0.744±0.031	9.000±0.381
Fixed single-B background $c\tau$			
$+2\%$	1.013±0.023	0.068±0.033	1.040±0.384
-2%	1.029±0.024	-0.071±0.034	-0.556±0.386
Reweighting for p_T and trigger			
no reweight	0.966±0.022	1.139±0.031	13.610±0.376
reweight with function	0.977±0.022	0.297±0.031	3.665±0.367
Contribution of radiative tail			
+ variation	1.023±0.023	-0.053±0.033	-0.374±0.375
− variation	1.049±0.022	0.027±0.031	0.558±0.357
Efficiency curve parameterization	1.022±0.023	0.034±0.033	0.625±0.381
SVT Modeling			
slope = 0 + 1σ	0.985±0.023	0.350±0.032	4.06±0.39
slope = 0 − 1σ	0.999±0.024	-0.286±0.032	-3.11±0.38
alternate central value $+1\sigma$	1.001±0.024	0.684±0.032	8.17±0.40
alternate central value -1σ	0.998±0.024	-0.139±0.032	1.82±0.39

Table 10.1: Summary of toy Monte Carlo studies with the $B_s \to D_s^- \pi^+$ fitter. Note that some of these toy Monte Carlo studies test variations that are greater than 1σ. See text for full explanation. The pull is defined as $(c\tau_{\mathrm{returned}} - c\tau_{\mathrm{gen}})/\sigma_{\mathrm{returned}}$ and is measured in units σ. Gaussian curves were fit to the pull and bias $(c\tau_{\mathrm{returned}} - c\tau_{\mathrm{gen}})$ histograms; the widths and means of the Gaussian curves are quoted in the table.

Description	Value (μm)
Background modeling and fractions	5.7
Fixed single-B background ct	1.0
Reweighting for p_T and trigger	3.7
Lifetime contribution of radiative tail	0.6
Efficiency curve parameterization	0.6
SVT Modeling	4.1
Impact parameter correlation	1.0
Alignment + others	1.0
TOTAL	8.2

Table 10.2: Final systematics for $B_s \to D_s^- \pi^+$ fit. The total is calculated assuming the individual contributions are uncorrelated.

10.4 Effect of Trigger Bias on 50/50 Mixture of $B_{s,L}$ and $B_{s,H}$

The displaced-vertex trigger alters the expected mixture of $B_{s,L}$ and $B_{s,H}$ in flavor-specific decays by preferentially selecting the longer lived $B_{s,H}$. The size of the imbalance depends on the values of $\Delta\Gamma$ and Γ.

At production, a $|\bar{b}s\rangle$ state is an equal mixture of $B_{s,H}$ and $B_{s,L}$. The decay length distribution as a function of time (assuming no trigger bias) is $F(t) \propto e^{-\Gamma_H t} + e^{-\Gamma_L t}$ where $\Gamma_H = 1/\tau_H$, $\Gamma_L = 1/\tau_L$, and $\Gamma = (\Gamma_H + \Gamma_L)/2$. If the PDF is integrated over time, one does not expect equal parts $B_{s,H}$ and $B_{s,L}$. The fraction of $B_{s,H}$ will be

$$f_H = \frac{1/\Gamma_H}{1/\Gamma_H + 1/\Gamma_L} = \frac{\Gamma_L}{\Gamma_H + \Gamma_L} = \frac{\Gamma_L}{2\Gamma}. \tag{10.1}$$

The fraction of $B_{s,L}$ will be

$$f_L = \frac{1/\Gamma_L}{1/\Gamma_H + 1/\Gamma_L} = \frac{\Gamma_H}{\Gamma_H + \Gamma_L} = \frac{\Gamma_H}{2\Gamma}. \tag{10.2}$$

The expected fraction of $B_{s,H}$ in a flavor-specific sample is plotted as a function of $\Delta\Gamma/\Gamma$ as a dashed line in the upper panel of Figure 10.1 assuming the world average $1/\Gamma = 1.47$ ps^{-1} [2]. The mean B_s lifetime measured in such a flavor-specific sample

will be

$$\begin{aligned}
\tau_m(B_s) &= f_L \cdot \tau_L + f_H \cdot \tau_H \\
&= \frac{1}{\Gamma} \cdot \frac{1 + \frac{1}{4}\left(\frac{\Delta\Gamma}{\Gamma}\right)^2}{1 - \frac{1}{4}\left(\frac{\Delta\Gamma}{\Gamma}\right)^2}
\end{aligned} \tag{10.3}$$

Note that $\tau_m(B_s) \neq 1/\Gamma$ and also $\tau_m(B_s) \neq (\tau_H + \tau_L)/2$, since

$$\begin{aligned}
\frac{1}{2}(\tau_H + \tau_L) &= \frac{1}{2}\left(\frac{1}{\Gamma_H} + \frac{1}{\Gamma_H}\right) \\
&= \frac{1}{2}\left(\frac{1}{\Gamma - \frac{1}{2}\Delta\Gamma} + \frac{1}{\Gamma + \frac{1}{2}\Delta\Gamma}\right) \\
&= \frac{1}{\Gamma} \cdot \frac{1}{1 - \frac{1}{4}\left(\frac{\Delta\Gamma}{\Gamma}\right)^2}
\end{aligned} \tag{10.4}$$

As was mentioned earlier, trigger and analysis cuts change the expected decay length distributions from simple exponential decays to the forms found in Equations 7.7 and 7.10. Once the efficiency curve parameters are known, these equations (with an appropriate factor of τ out front) can be integrated with $\tau = \tau_L$ and $\tau = \tau_H$ to determine the f_L^{SVT} and f_H^{SVT} for our SVT-triggered sample. We plot f_H^{SVT} as a function of $\Delta\Gamma/\Gamma$ as a solid line in the upper panel of Figure 10.1, again assuming the world average $1/\Gamma = 1.47$ ps^{-1} [2]. The mean B_s lifetime measured in the SVT-triggered sample will be $\tau_m^{SVT}(B_s) = f_L^{SVT} \cdot \tau_L + f_H^{SVT} \cdot \tau_H$

The lower panel of Fig. 10.1 shows the resulting bias $\tau_m^{SVT}(B_s) - \tau_m(B_s)$ in the flavor-specific lifetime measurement. The yellow band represents the most likely value from the 2008 world average $\Delta\Gamma/\Gamma = 0.069^{+0.058}_{-0.062}$ [2]. The graph indicates the most likely bias is 0-0.5 μm. Because this is much smaller than our current statistical and systematic uncertainties, we do not correct the central value or assess an additional systematic uncertainty. We provide a correction factor of the form $a + b\left(\Delta\Gamma/\Gamma\right) + c\left(\Delta\Gamma/\Gamma\right)^2$ from a fit to the lower panel in Fig. 10.1 where we fix $a = b = 0$ for physical reasons. Our result can be corrected back to a flavor-specific lifetime measurement with $\delta\tau(B_s) = 33.09\left(\Delta\Gamma/\Gamma\right)^2$ μm.
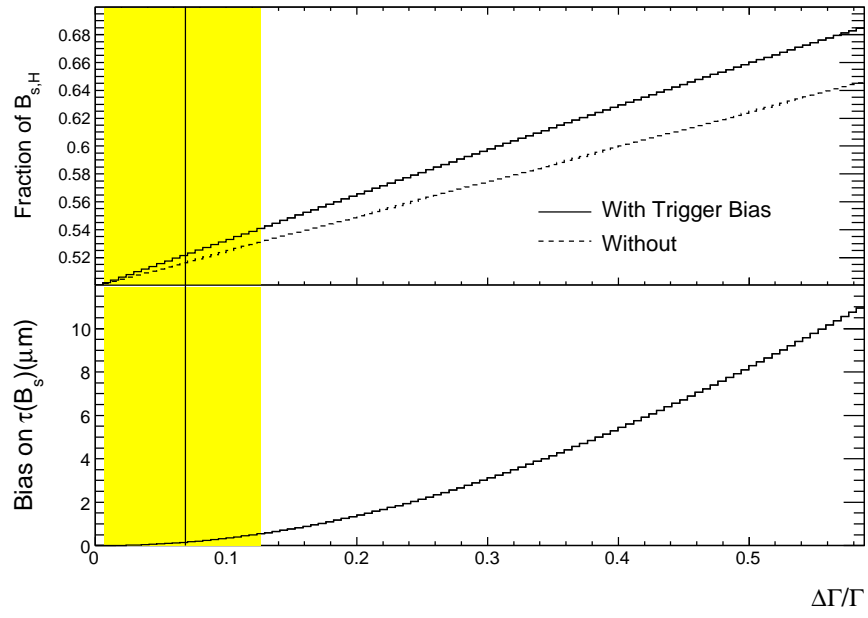
Figure 10.1: Effect of trigger selection on the mixture of $B_{s,L}$ and $B_{s,H}$ in a flavor-specific sample as a function of $\Delta\Gamma/\Gamma$.

	$D_s\pi$	D_sK	$D_s^*\pi$	$D_s\rho$	B_s other
N_1	1.000000	1.000000	1.000000	1.000000	1.000000
β_1	0.005591	0.000502	0.005387	0.006038	0.004694
τ_1	0.040831	0.077081	0.037380	0.038323	0.032765
N_2	8.533206	56.01398	10.90722	9.340490	31.24866
β_2	0.012362	0.010396	0.013920	0.012294	0.012824
τ_2	0.016191	0.022351	0.012984	0.014658	0.008134
τ	τ_{B_s}	τ_{B_s}	τ_{B_s}	τ_{B_s}	τ_{B_s}
σ	0.001986	0.003275	0.005913	0.004542	0.025179
χ^2	148.1	50.6	127.5	117.5	78.3
ndf	$130-6$	$54-6$	$109-6$	$100-6$	$92-6$
$prob$	6.9%	37.2%	5.1%	5.1%	71.0%

Table 10.3: Parameters of FR and PR curves for $B_s \to D_s^-(\phi\pi^-)\pi^+$

	upper sideband (RS)	D sideband (FR+PR)	$B^{0/+} \to D^+\pi X$ $B^{0/+} \to D^+\pi X$	$B^0 \to D_s\pi X$ $B^0 \to D_s\pi X$	Λ_b Λ_b
N_1	1.00000e+00	1.00000e+00	1.000000	1.000000	1.000000
β_1	7.91257e-03	1.04327e-02	0.008679	0.005389	0.012103
τ_1	7.81830e-03	1.13331e-02	0.024731	0.042937	0.012365
N_2	8.25757e-03	9.51127e-02		8.268733	0.065624
β_2	8.49249e-03	1.50003e-02		0.009035	0.019063
τ_2	2.08721e-02	2.80787e-02		0.018384	0.031806
τ_{Bkgd}			0.0500(fixed)		
σ_{Bkgd}	1.30919e-02	1.57849e-02	0.013223	0.014514	0.021456
χ^2	2.9	13.5	6.3	134.3	24.6
ndf	$6-6$	$13-6$	$9-3$	$120-6$	$34-6$
$prob$		6.1%	38.7%	9.5%	64.7%

Table 10.4: Background parameterization for $B_s \to D_s^-(\phi\pi^-)\pi^+$

Table 10.5: Fit components for $B_s \to D_s^-(\phi\pi^-)\pi^+$ mass fits.

Decay modes	Mass pdf	Configuration
	$B_s \to D_s^-(\phi\pi^-)\pi^+$ fit	
$B_s \to D_s\pi$	MC	norm floating
$B_s \to D_s\pi(n\gamma)$	MC	fixed to 4.2% of $D\pi$(non-PHOTOS)
$B_s \to D_sK$	MC	$DK/D\pi$ constrained to 9.531418 %
$B_s \to D_s\rho$	MC	norm floating
$B_s \to D_s^*\pi$	MC	norm floating
$B^0/B^+ \to D^+X$	MC	norm floating
$B_s \to D_s^{(*)}K^{(*)}$	MC	fixed to $B_s \to D_s^{(*)}X$
$B_s \to D_s^{(*)}eX$	MC	fixed to $B_s \to D_s^{(*)}X$
$B_s \to D_s^{(*)}X$	MC	norm floating
$B^0 \to D_s^{(*)}K$	MC	fixed to $B^0 \to D_s^{(*)}\pi$
$B^0 \to D_s^{(*)}\pi$	MC	norm floating
$\Lambda_b \to \Lambda_c X$	MC	norm floating
Fake D_s +track	leakage-subtracted D_s sideband (function)	norm fixed
Real D_s +track	SBS $D_s\pi$ WS [5.00, 6.45] GeV/c^2 (function)	norm floating

Decay modes	Number of events	Fraction of total
$B_s \to D_s\pi$	1127.84	0.202630 ± 0.007557
$B_s \to D_s\pi(n\gamma)$	47.32	0.008501
$B_s \to D_sK$	110.03	0.019769 ± 0.004348
$B_s \to D_s\rho$	1406.90	0.252767 ± 0.035888
$B_s \to D_s^*\pi$	648.21	0.116458 ± 0.030848
$B^0/B^+ \to D^+X$	307.44	0.055236 ± 0.019468
$B_s \to D_s^{(*)}K^{(*)}$	53.25	0.009566
$B_s \to D_s^{(*)}eX$	187.65	0.033713
$B_s \to D_s^{(*)}X$	872.90	0.156826 ± 0.022567
$B^0 \to D_s^{(*)}K$	26.79	0.004813
$B^0 \to D_s^{(*)}\pi$	24.10	0.004330 ± 0.022199
$\Lambda_b \to \Lambda_cX$	175.71	0.031569 ± 0.015183
Fake D_s +track	293.44	0.052720
Real D_s +track	284.44	0.051103 ± 0.005377

Table 10.6: Results of the mass fit for $B_s \to D_s^-(\phi\pi^-)\pi^+$ in terms of the number of events in the region [4.85, 6.45] GeV/c^2. Since the fit is non-extended, the errors on the fractions are quoted. The normalization of the fake D component was fixed in the fit. The other modes without quoted errors have their errors incorporated into modes they are fixed to.

Fractions returned by mass fit			
	FR	PR	FR + PR
$D_s^- \pi^+$	0.904758	0.074750	0.294641
$D_s^- K^+$	0.008656	0.034594	0.027722
$D_s^{*-} \pi^+$	0.000531	0.221297	0.162811
$D_s^- \rho^+$	0.000324	0.349885	0.257277
B_s remainder	0.000337	0.134796	0.099174
$B^{0/+} \to D^+ \pi X$	0.034286	0.063184	0.055528
$B^0 \to D_s \pi X$	0.000059	0.015099	0.011115
Λ_b	0.016414	0.035117	0.030162
Bkgd - real D	0.020019	0.030634	0.027822
Bkgd - fake D	0.014616	0.040644	0.033748
Real D in upper sideband	0.79		
D leakage	0.51		
Fractions used by lifetime fit			
	FR	PR	FR + PR
$D_s^- \pi^+$	0.895186	0.074749	0.281072
$D_s^- K^+$	0.008656	0.034594	0.027722
$D_s^{*-} \pi^+$	0.000531	0.204560	0.156030
$D_s^- \rho^+$	0.000324	0.333150	0.250490
B_s remainder	0.000337	0.134800	0.099174
$B^{0/+} \to D^+ \pi X$	0.034286	0.063184	0.055528
$B^0 \to D_s \pi X$	0.000059	0.015099	0.011115
Λ_c	0.016414	0.035117	0.030162
Bkgd - D SB	0.018866	0.065970	0.053489
Bkgd - upper SB	0.025341	0.038777	0.035218

Table 10.7: Fractions of each mode reconstructed as $B_s \to D_s^-(\phi\pi^-)\pi^+$ found in the three mass regions of the full data sample. The fully reconstructed (FR) region includes all events with $m_B \in [5.35, 5.45]$ GeV/c^2. The partially reconstructed (PR) region includes all events with $m_B \in [5.00, 5.35]$ GeV/c^2. The combined (FR+PR) region includes all events with $m_B \in [5.00, 5.45]$ GeV/c^2.

FR	$\tau_{B_s}(\mu\text{m})$	436.5 ± 20.0
	χ^2/ndf	$68.3/(67\text{-}1)$
	prob	39.9%
PR	$\tau_{B_s}(\mu\text{m})$	463.0 ± 15.2
	χ^2/ndf	$93.5/(89\text{-}1)$
	prob	32.4%
FR + PR	$\tau_{B_s}(\mu\text{m})$	455.0 ± 12.2
	χ^2/ndf	$99.6/(95\text{-}1)$
	prob	32.8%

Table 10.8: Results of $B_s \rightarrow D_s^-(\phi\pi^-)\pi^+$ lifetime fit: The lifetime fit is performed in three mass regions. The fully reconstructed (FR) region includes all events with $m_B \in [5.35, 5.45]$ GeV/c^2. The partially reconstructed (PR) region includes all events with $m_B \in [5.00, 5.35]$ GeV/c^2. The combined (FR+PR) region includes all events with $m_B \in [5.00, 5.45]$ GeV/c^2.
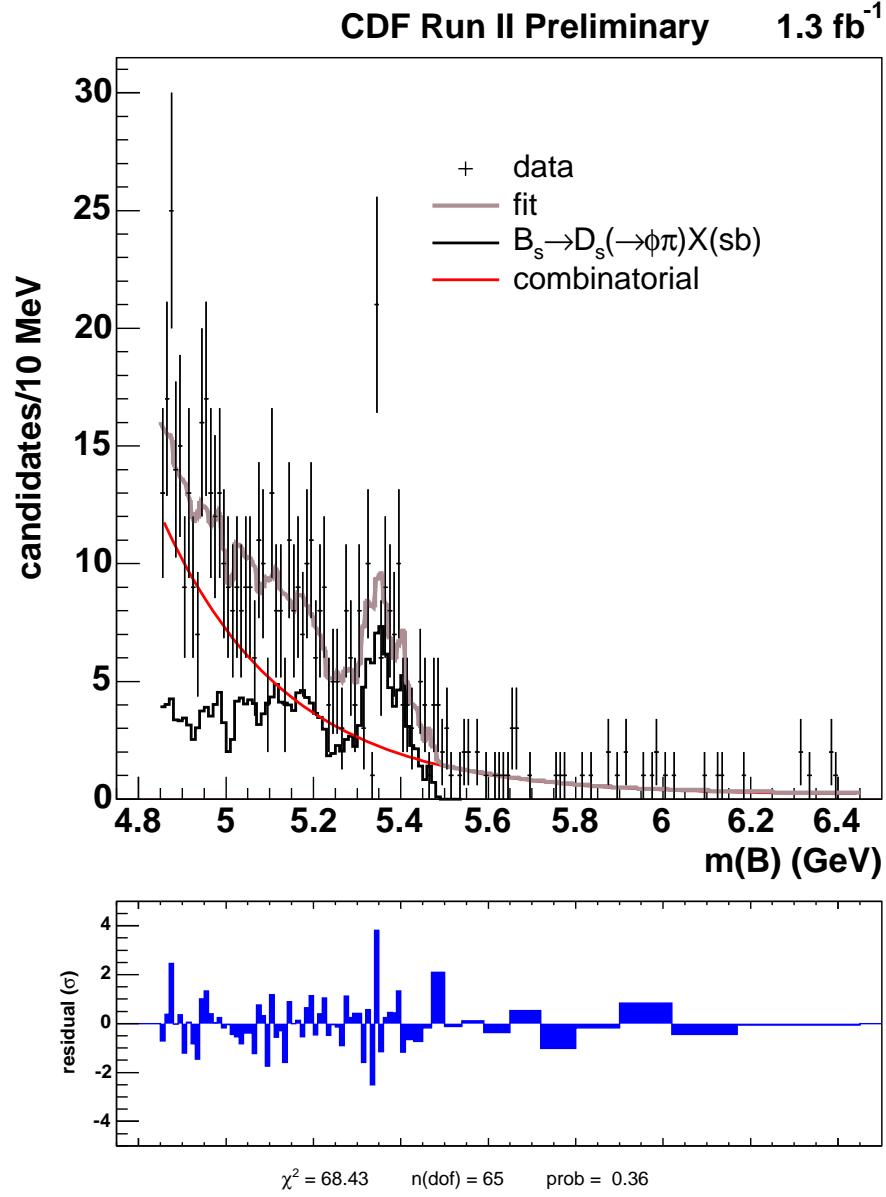
Figure 10.2: This auxiliary fit to the D_s sidebands with D_s leakage subtracted is used to determine the shape of the fake-D component for the mass fit. These events are reconstructed as $B_s \to D_s^-(\phi\pi^-)\pi^+$ in full 1.3 fb^{-1}.
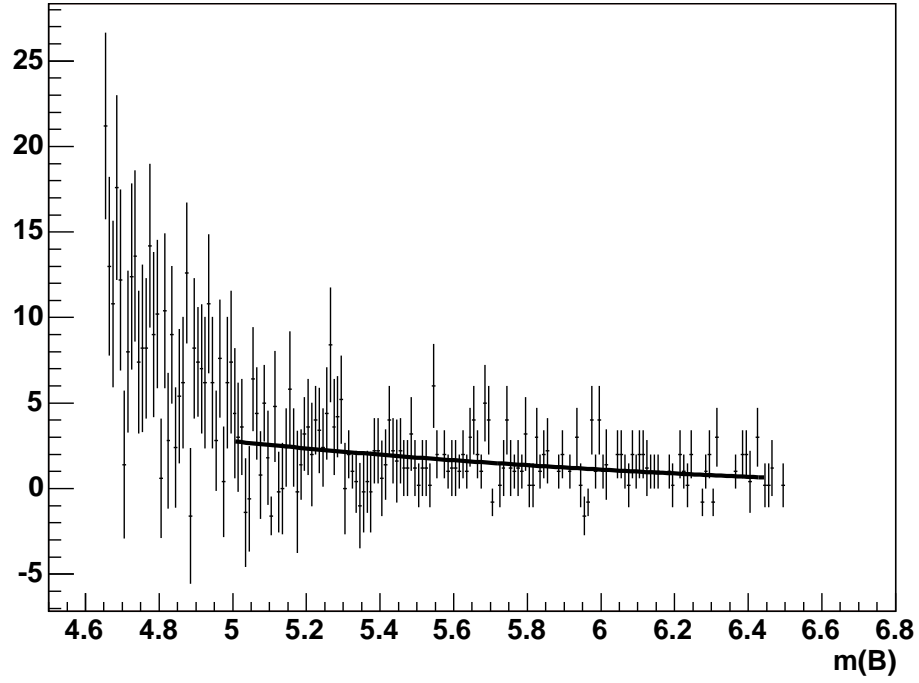
Figure 10.3: This auxiliary fit to the sideband-subtracted WS sample from the full 1.3 fb^{-1} of data. The WS sample is made of events reconstructed as $D_s^- \pi^-$ that pass the analysis cuts. The functional form employed is an exponential plus a constant in the region $m_B \in [5.00, 6.45]$ GeV/c^2.
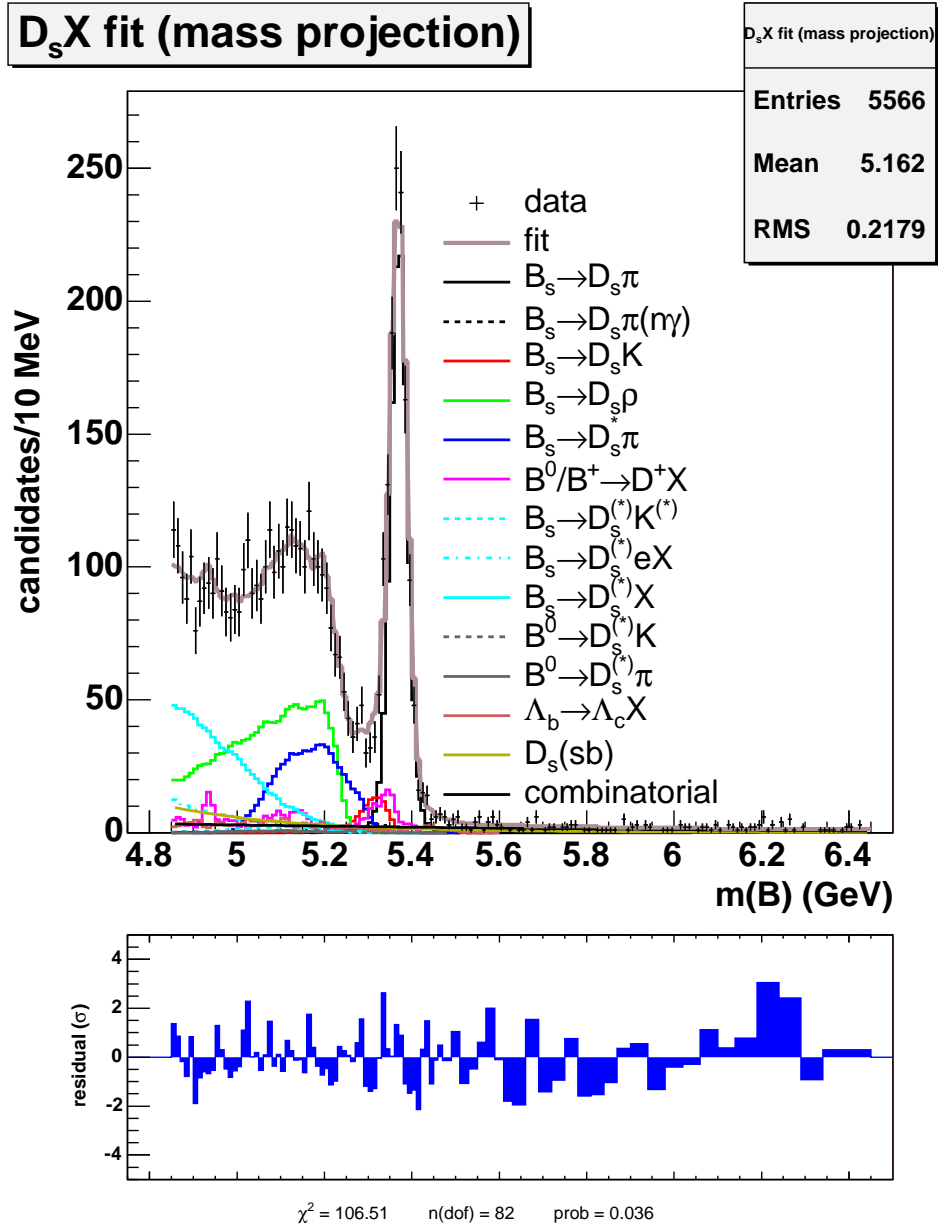
Figure 10.4: Mass fit of events reconstructed as $B_s \rightarrow D_s^-(\phi\pi^-)\pi^+$ in full 1.3 fb^{-1}.
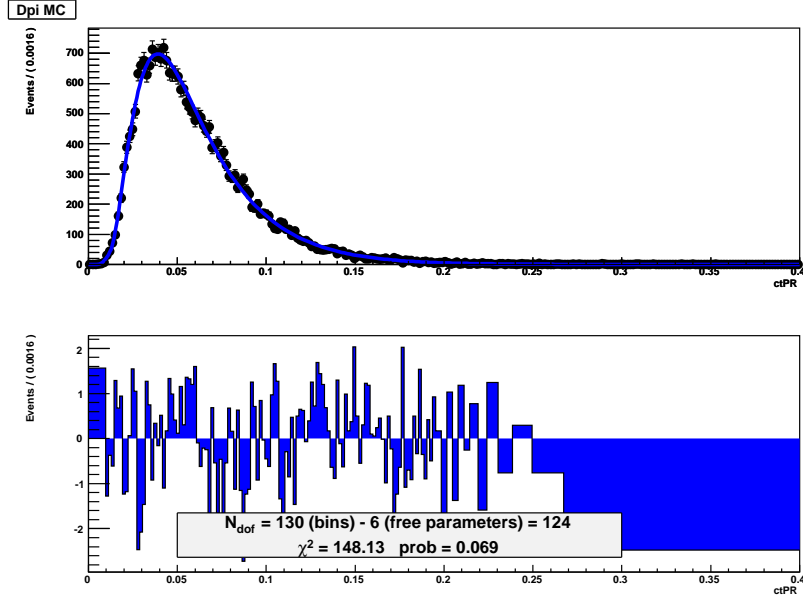
Figure 10.5: PDF fit to Monte Carlo for $B_s \to D_s^-(\phi\pi^-)\pi^+$ reconstructed as $B_s \to D_s^-(\phi\pi^-)\pi^+$.
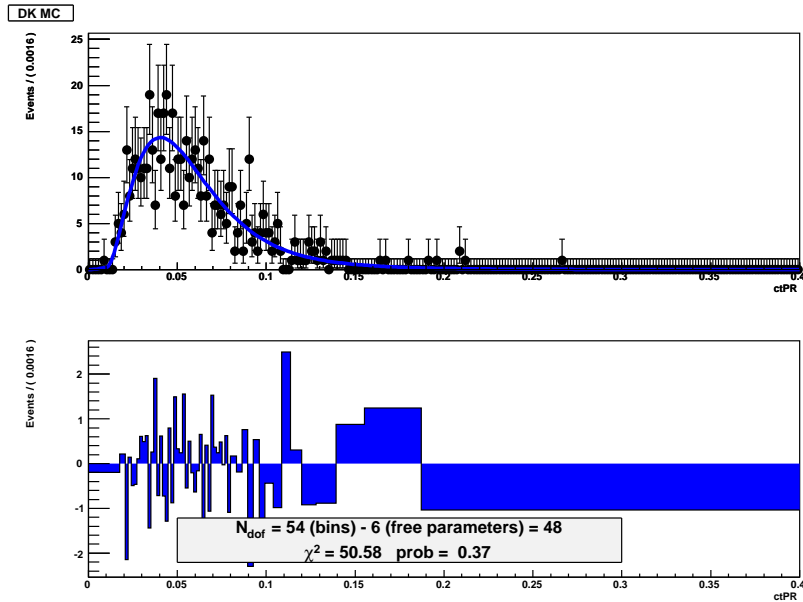
Figure 10.6: PDF fit to Monte Carlo for $B_s \to D_s^-(\phi\pi^-)K^+$ reconstructed as $B_s \to D_s^-(\phi\pi^-)\pi^+$.
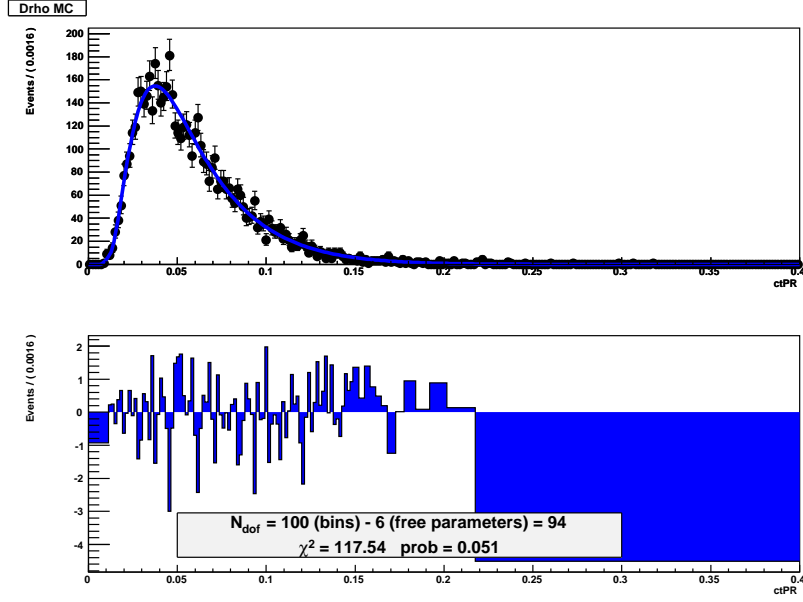
Figure 10.7: PDF fit to Monte Carlo for $B_s \to D_s^-(\phi\pi^-)\rho^+$ reconstructed as $B_s \to D_s^-(\phi\pi^-)\pi^+$.
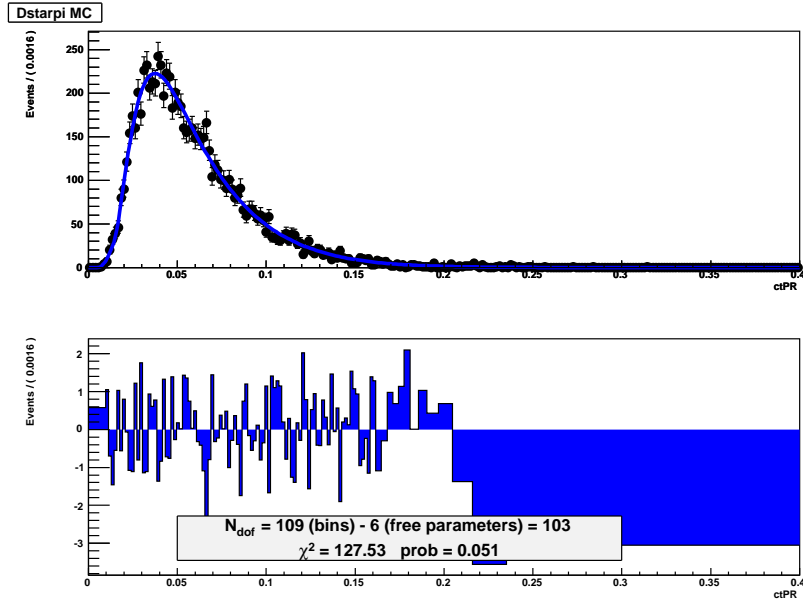
Figure 10.8: PDF fit to Monte Carlo for $B_s \to D_s^{*-}(\phi\pi^-)\pi^+$ reconstructed as $B_s \to D_s^-(\phi\pi^-)\pi^+$.
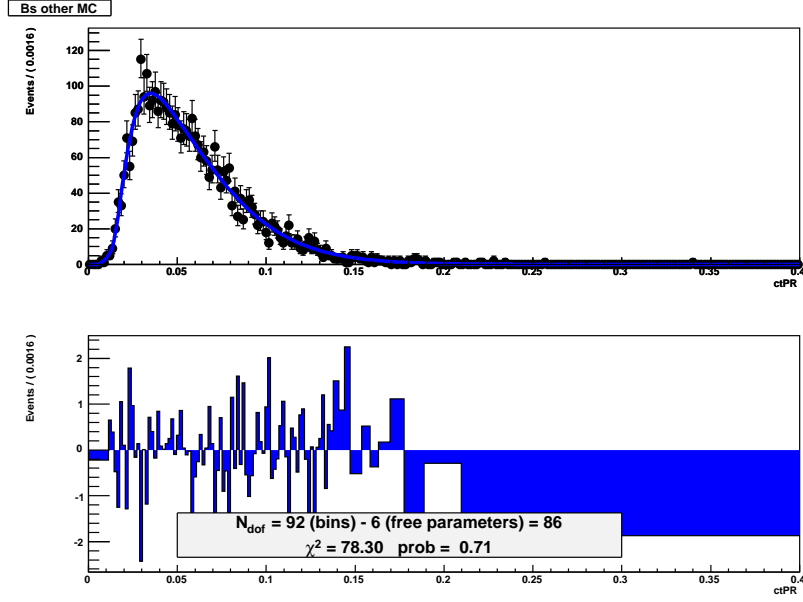
Figure 10.9: PDF fit to Monte Carlo for the remaining $B_s \rightarrow D_s^{*-}(\phi\pi^-)X$ reconstructed as $B_s \rightarrow D_s^-(\phi\pi^-)\pi^+$.
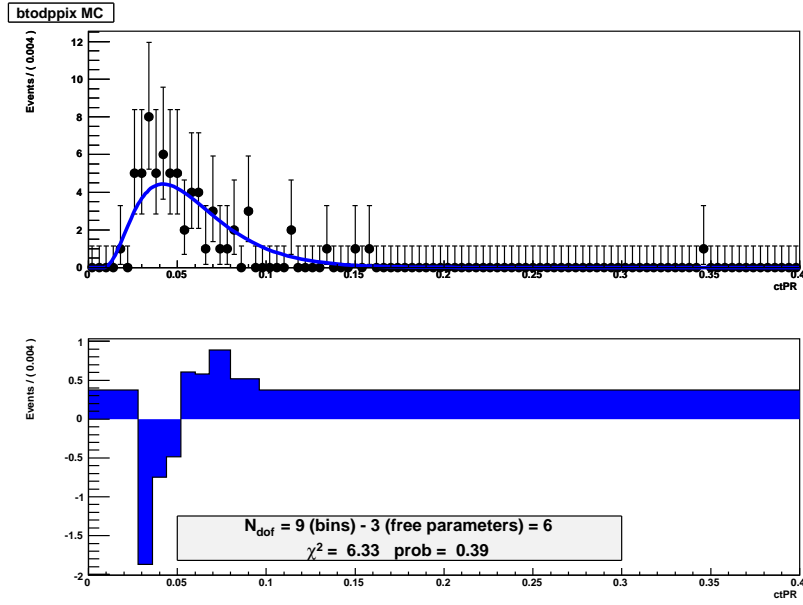
Figure 10.10: PDF fit to Monte Carlo for $B^{0/+} \rightarrow D^+\pi X$ reconstructed as $B_s \rightarrow D_s^-(\phi\pi^-)\pi^+$.
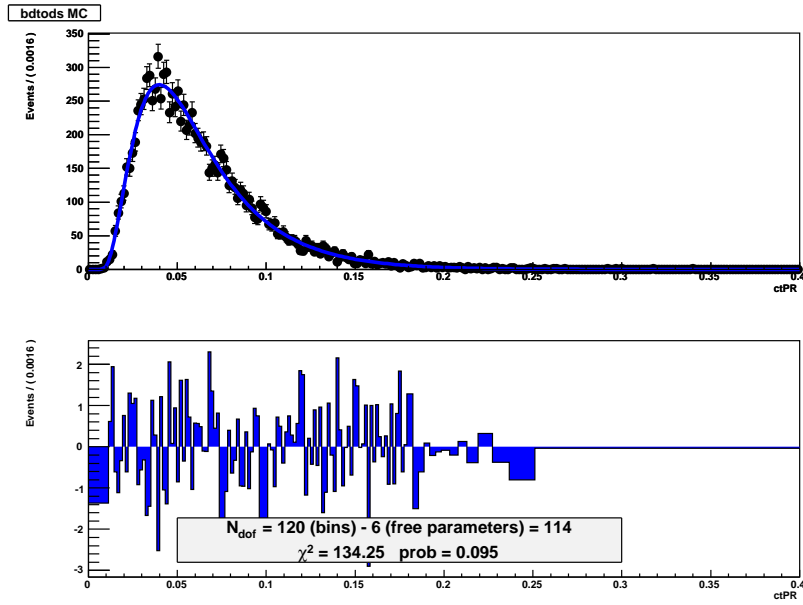
Figure 10.11: PDF fit to Monte Carlo for $B^0 \to D_s \pi X$ reconstructed as $B_s \to D_s^-(\phi\pi^-)\pi^+$.
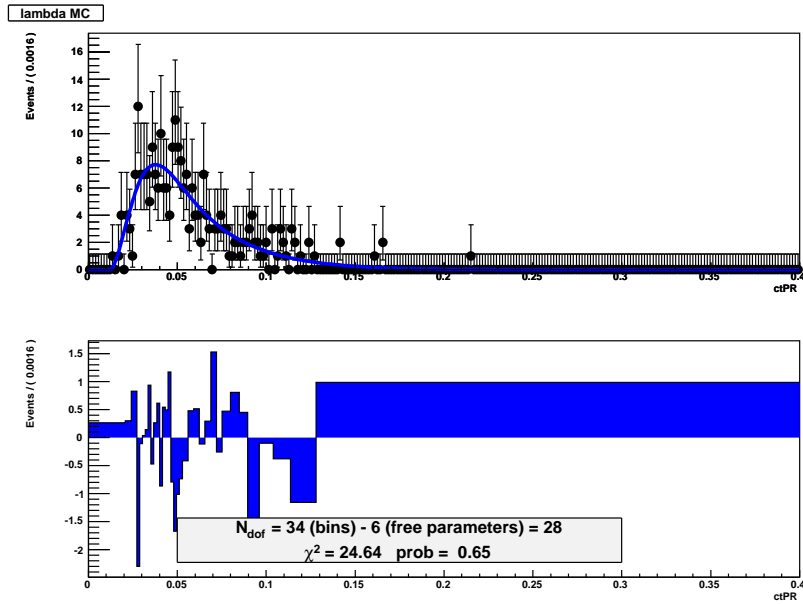
Figure 10.12: PDF fit to Monte Carlo for Λ_b reconstructed as $B_s \to D_s^-(\phi\pi^-)\pi^+$.
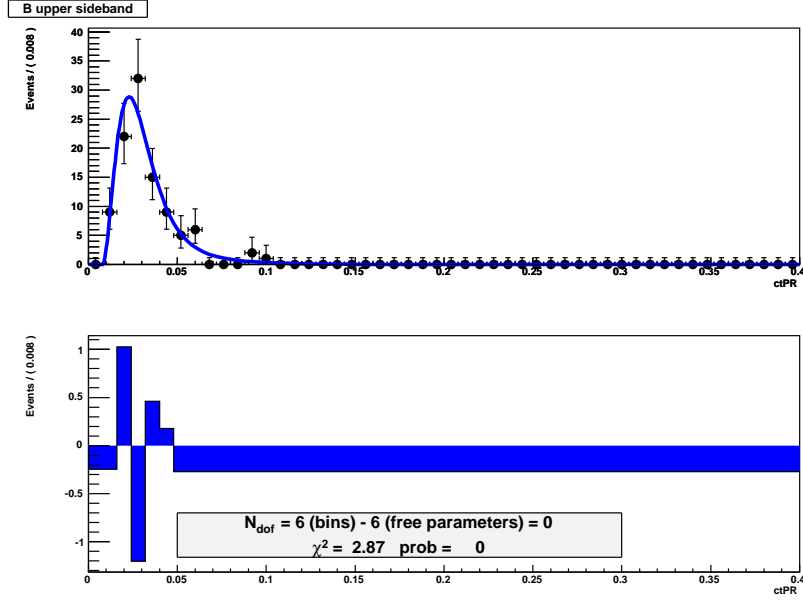
Figure 10.13: Background model for $B_s \to D_s^-(\phi\pi^-)\pi^+$ from the upper sideband data with $m_B \in [5.7, 6.4]$ GeV$/c^2$.
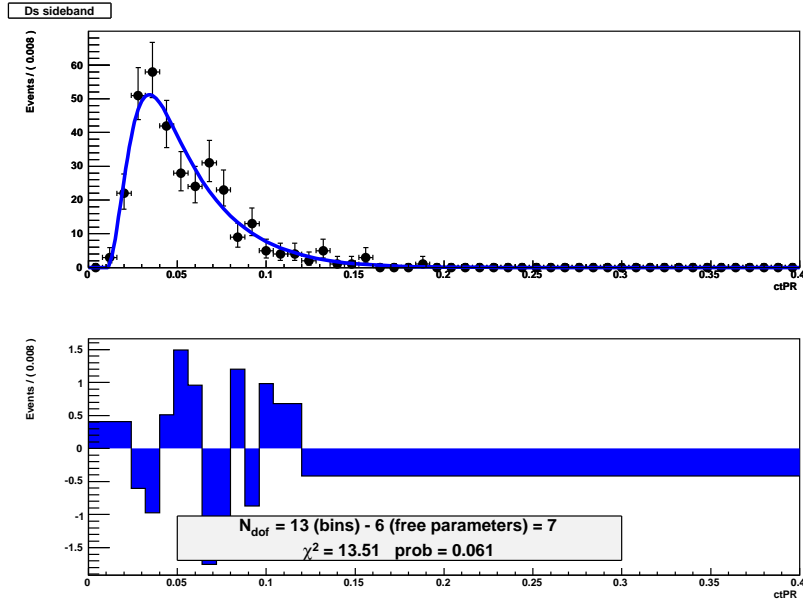
Figure 10.14: Background model for $B_s \to D_s^-(\phi\pi^-)\pi^+$ from the D_s sideband in the FR+PR regions ($m_B \in [5.00, 5.45]$ GeV$/c^2$).
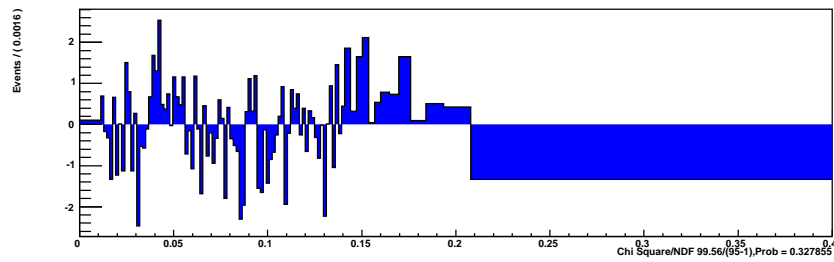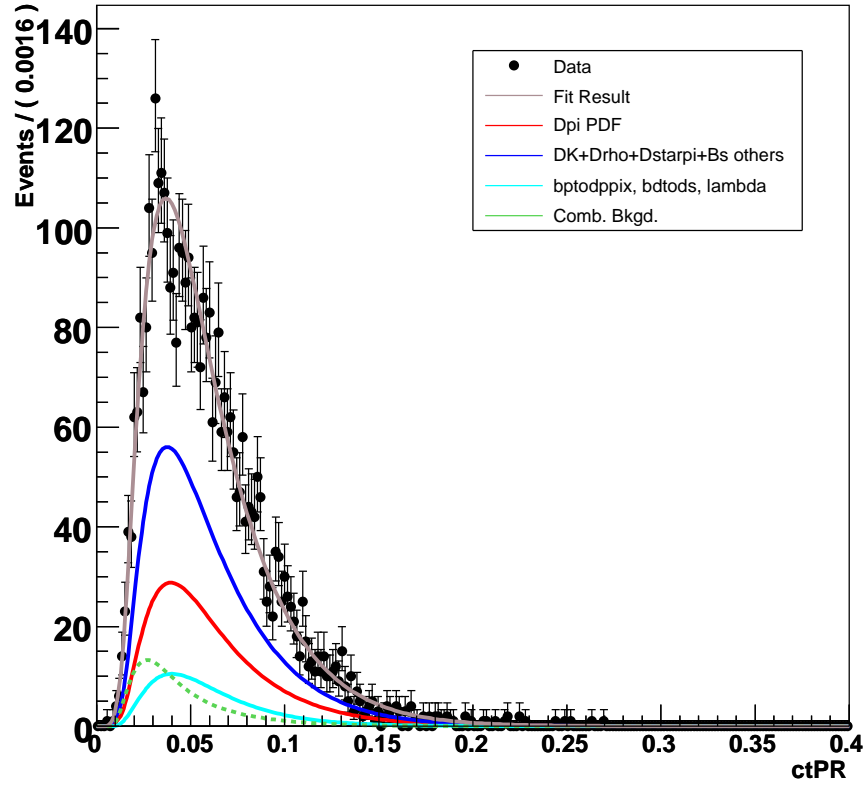
Figure 10.15: ct projection of the lifetime fit to events reconstructed as $B_s \to D_s^-(\phi\pi^-)\pi^+$ in the combined FR+PR region.
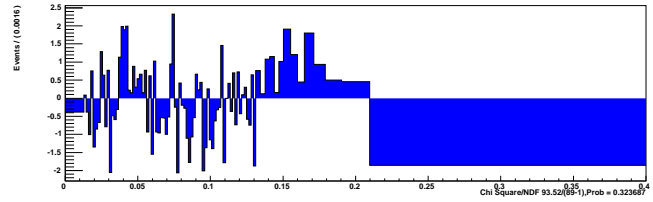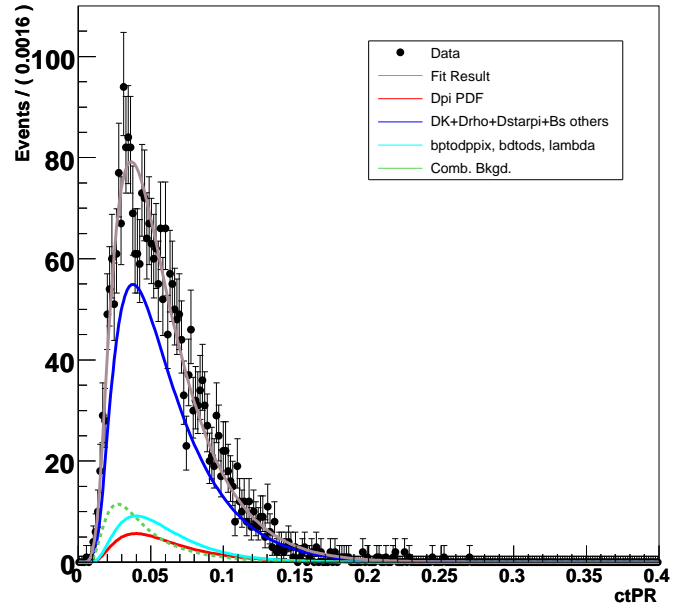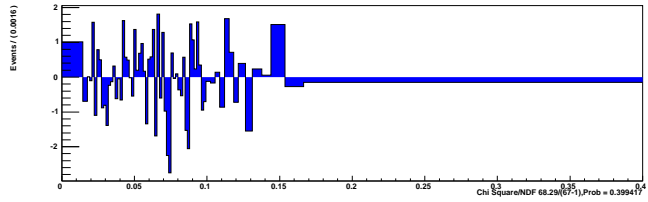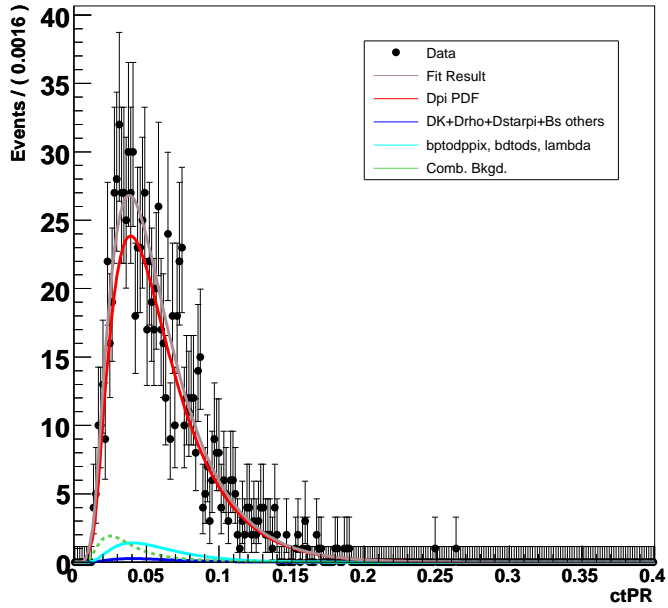
Figure 10.16: ct projection of the lifetime fits to events reconstructed as $B_s \rightarrow D_s^-(\phi\pi^-)\pi^+$ in the separate FR and PR mass regions.

(a) Fully Reconstructed Region

(b) Partially Reconstructed Region

168

Chapter 11

Conclusions

We have presented a procedure for utilizing both fully and partially reconstructed hadronic decays in measurements of B meson lifetimes. We first studied three control samples before performing fits to the signal sample. We also kept the signal results blinded until after the systematic uncertainties had been assessed.

The data come from $\overline{p}p$ collisions at $\sqrt{s} = 1.96$ TeV collected by the CDF II detector at the Fermilab Tevatron. This analysis is based on an integrated luminosity of $\sim$1.3 fb^{-1} collected by the CDF II detector between February 2002 and November 2006.

For our three control samples we measure

$$
\begin{aligned}
c\tau(B^0 \to D^-(K^+\pi^-\pi^-)\pi^+) &= 449.9 \pm 3.6(\text{stat.}) \pm 7.0(\text{syst.}) \ \mu\text{m} \\
c\tau(B^0 \to D^{*-}[\overline{D}^0(K^+\pi^-)\pi^-]\pi^+) &= 452.1 \pm 9.5(\text{stat.}) \ \mu\text{m} \\
c\tau(B^+ \to \overline{D}^0(K^+\pi^-)\pi^+) &= 487.8 \pm 3.3(\text{stat.}) \ \mu\text{m}
\end{aligned}
$$

The results for $B^0 \to D^{*-}[\overline{D}^0(K^+\pi^-)\pi^-]\pi^+$ and $B^+ \to \overline{D}^0(K^+\pi^-)\pi^+$ are consistent within statistical errors with the PDG values $c\tau(B^0) = 458.7 \pm 2.7$ and $c\tau(B^+) = 491.1 \pm 3.3$ [2]. The sample with the largest background contribution, the $B^0 \to D^-(K^+\pi^-\pi^-)\pi^+$ sample, has large systematics associated with the background modeling, but its result is consistent with the PDG value if the systematics are included.

In our signal sample, the $B_s \to D_s^-(\phi\pi^-)\pi^+$ we measure

$$
c\tau(B_s) = 455.0 \pm 12.2 \ (\text{stat.}) \pm 8.2 \ (\text{syst.}) \ \mu\text{m}.
$$

This is the most precise measurement of the B_s lifetime in a flavor-specific decay channel to date. The ratio of this result and the world average B^0 lifetime yields $\tau(B_s)/\tau(B^0) = 0.99 \pm 0.03$, which is in agreement with the theoretical prediction of 1.00 ± 0.01.

Appendix A

Study of SVT Efficiency in $J/\psi \rightarrow \mu^+\mu^-$

Because the efficiency curve parameters are derived in fits to Monte Carlo and fixed in the final fit to data, the lifetime measurement relies heavily on the agreement between Monte Carlo and data. The concern addressed by the studies in this appendix is how well the trigger turn-on seen in data is modeled in the Monte Carlo. Since the SVT simulation code run during the trigger simulation is identical to the SVT code run during data collection, we expect excellent agreement. However, because the trajectories and hit patterns of real and simulated particles can be different even if they have identical initial conditions, the SVT response can also be different.

To determine whether there is an overall disagreement between the trigger turn-ons in data and Monte Carlo, we study a J/ψ sample collected by the unbiased dimuon trigger in the 0d, 0h, and 0i run ranges. To prevent other simulation issues such as momentum spectra from affecting the outcome of our studies, the Monte Carlo is seeded with the muon momentum four vectors from the dimuon data sample. We also input the event's run number. The Monte Carlo simulation includes full detector and trigger simulations. For technical reasons, we assign 0d run numbers to events seeded with 0h and 0i muon momentum four vectors. This run number re-assignment is consistent with our B_s MC generation: we only simulate B_s MC in the 0d run range. The uncertainties associated with reweighting 0d MC to match

171

`0d+0h+0i` data is already covered by another systematic.

The studies presented here are analogous to those performed in [28]. We find the Scenario A two-track trigger efficiency in data (and separately in MC) as functions of $p_T(\mu)$, $d_0(\mu)$, $L_{xy}(J/\psi)$, and $p_T(J/\psi)$ by taking the ratio of histograms:

$$\epsilon = \frac{\text{Events with both muons matched to SVT tracks, pair satisfies Scen A}}{\text{Events with both muons satisfying } p_T > 2.0 \text{ GeV}/c^2}$$

An offline track is matched to an SVT track if $\chi^2 \leq 25$, $\Delta\phi \leq 15$ mrad, and $\Delta curvature \leq 10^{-4}$ cm^{-1}. Before taking the ratio, both the numerator and denominator histograms are first sideband subtracted in the reconstructed J/ψ mass. The signal region is defined as the region $\pm 3\sigma$ around the J/ψ peak, $|m(\mu\mu) - 3.0969| <$ 0.048 GeV$/c^2$. We consider the events 5 to 10σ from the peak to be in the sideband region, $0.080 < |m(\mu\mu) - 3.0969| < 0.16$ GeV$/c^2$. The efficiencies are shown for data in run ranges `0d`, `0h`, `0i`, and `0d+0h+0i` (and the MC seeded by the data) in Figures A.1-A.4 (and Figures A.5-A.8).

To determine the level of agreement between data and MC, we take the ratio of the efficiency histograms $\epsilon^{data}/\epsilon^{MC}$ and fit the resulting histogram with a 1st degree polynomial in the L_{xy} range [0.0450, 0.4] cm. The lower value is set by the $L_{xy}(B_s) > 450$ μm cut applied in this $\tau(B_s)$ analysis. These ratio histograms are shown with their fits in Figures A.9-A.12. The slopes of the lines for the separate run ranges are summarized in Table A.1. The slopes are consistent with statistical fluctuations around zero, indicating good data/MC agreement.

`0d`	-0.1459 $\pm$ 0.1396
`0h`	0.0636 $\pm$ 0.1053
`0i`	-0.0255 $\pm$ 0.0867
`0d+0h+0i`	0.0929 $\pm$ 0.0598

Table A.1: SVT Modeling: Summary of slopes from straight lines fit to $\epsilon^{data}/\epsilon^{MC}$ histograms. The slopes are consistent with statistical fluctuations around zero.

Although the data and MC agree well in this J/ψ cross-check, we choose to set a systematic uncertainty using the statistical errors. We generate alternate configurations by doing the following:

1. Reweight the B_s MC (already reweighted in p_T and trigger category) in $L_{xy}(B_s)$ according to a line with a y-intercept of zero and slope ± 0.0598, the uncertainty of the slope returned by the fit to `0d+0h+0i`. The general reweighting procedure has already been described in Sec. 7.2.5.

2. Derive new efficiency curve parameters from the reweighted MC.

3. Generate toy MC with the new efficiency curves. Fit with the default curves.

Since we believe the fits summarized in Table A.1 show the data and MC are consistent (slope $= 0$) within errors, we choose to fluctuate the slope around a central value of zero. It is also possible to reweight using a slope of 0.0929 ± 0.0598 instead of 0 ± 0.0598. For completeness, we also generated toy MC using the non-zero central value. The results of both studies are summarized in Table A.2. We take the larger bias from the $\pm1\sigma$ variations around zero slope as the SVT modeling systematic uncertainty, 4.1μm.

	Pull Width (σ)	Pull Mean (σ)	Mean Bias (μm)
slope $= 0 + 1\sigma$	0.985 ± 0.023	0.350 ± 0.032	4.06 ± 0.39
slope $= 0 - 1\sigma$	0.999 ± 0.024	-0.286 ± 0.032	-3.11 ± 0.38
alternate central value $+ 1\sigma$	1.001 ± 0.024	0.684 ± 0.032	8.17 ± 0.40
alternate central value $- 1\sigma$	0.998 ± 0.024	-0.139 ± 0.032	1.82 ± 0.39

Table A.2: SVT Modeling: Summary of toy MC based on J/ψ studies

Figure A.1: J/ψ distributions for `0d` data. From left to right: $p_T(\mu)$, $d_0(\mu)$, $L_{xy}(J/\psi)$, and $p_T(J/\psi)$. The top plots show two histograms for each variable: events where both muons are matched to SVT tracks that satisfy Scen A requirements (red) and events where both muons have $p_T > 2.0$ GeV/c (black). Both histograms are sideband subtracted in the J/ψ mass. The lower plots are the results of histogram division (red/black).
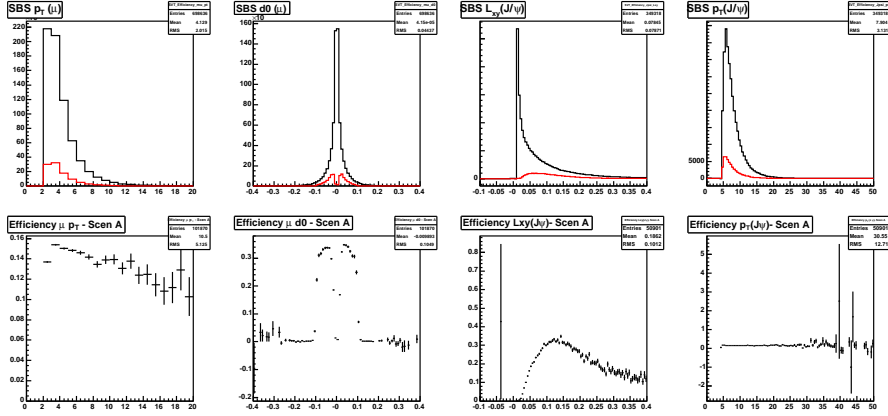
Figure A.2: J/ψ distributions for `0h` data. From left to right: $p_T(\mu)$, $d_0(\mu)$, $L_{xy}(J/\psi)$, and $p_T(J/\psi)$. The top plots show two histograms for each variable: events where both muons are matched to SVT tracks that satisfy Scen A requirements (red) and events where both muons have $p_T > 2.0$ GeV/c (black). Both histograms are sideband subtracted in the J/ψ mass. The lower plots are the results of histogram division (red/black).

174
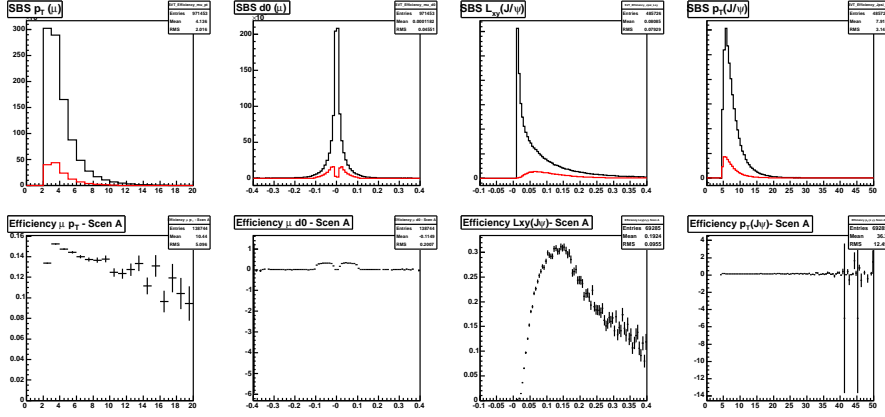
Figure A.3: J/ψ distributions for 0i data. From left to right: $p_T(\mu)$, $d_0(\mu)$, $L_{xy}(J/\psi)$, and $p_T(J/\psi)$. The top plots show two histograms for each variable: events where both muons are matched to SVT tracks that satisfy Scen A requirements (red) and events where both muons have $p_T > 2.0$ GeV/c (black). Both histograms are sideband subtracted in the J/ψ mass. The lower plots are the results of histogram division (red/black).
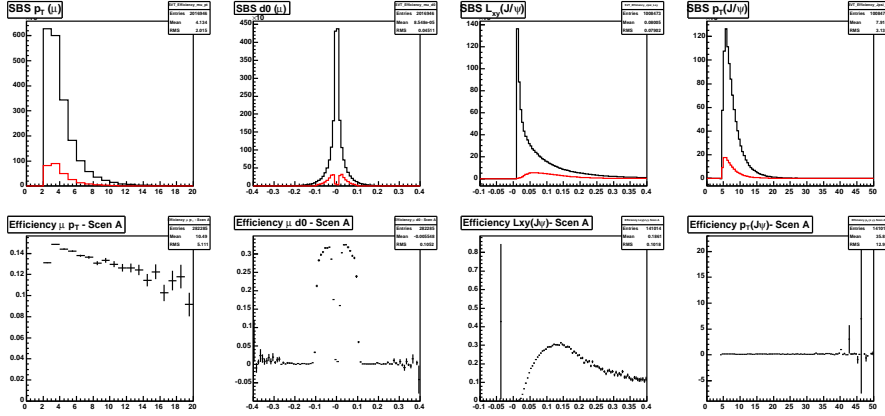
Figure A.4: J/ψ distributions for 0d+0h+0i data. From left to right: $p_T(\mu)$, $d_0(\mu)$, $L_{xy}(J/\psi)$, and $p_T(J/\psi)$. The top plots show two histograms for each variable: events where both muons are matched to SVT tracks that satisfy Scen A requirements (red) and events where both muons have $p_T > 2.0$ GeV/c (black). Both histograms are sideband subtracted in the J/ψ mass. The lower plots are the results of histogram division (red/black).
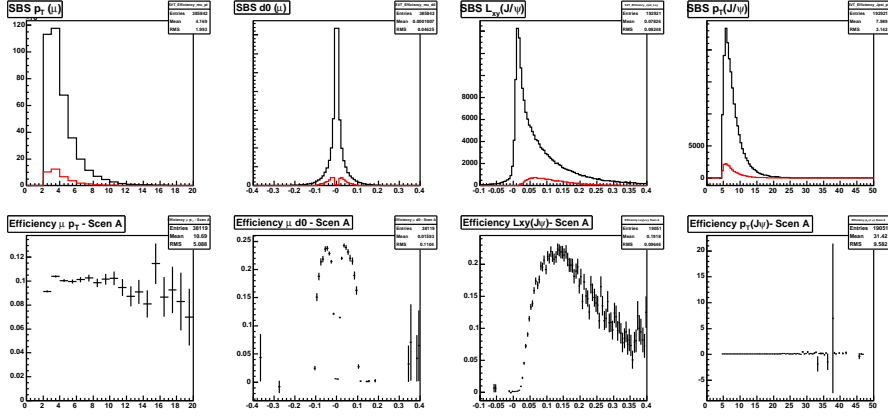
Figure A.5: J/ψ distributions for MC seeded from `0d` data. From left to right: $p_T(\mu)$, $d_0(\mu)$, $L_{xy}(J/\psi)$, and $p_T(J/\psi)$. The top plots show two histograms for each variable: events where both muons are matched to SVT tracks that satisfy Scen A requirements (red) and events where both muons have $p_T > 2.0$ GeV/c (black). Both histograms are sideband subtracted in the J/ψ mass. The lower plots are the results of histogram division (red/black).
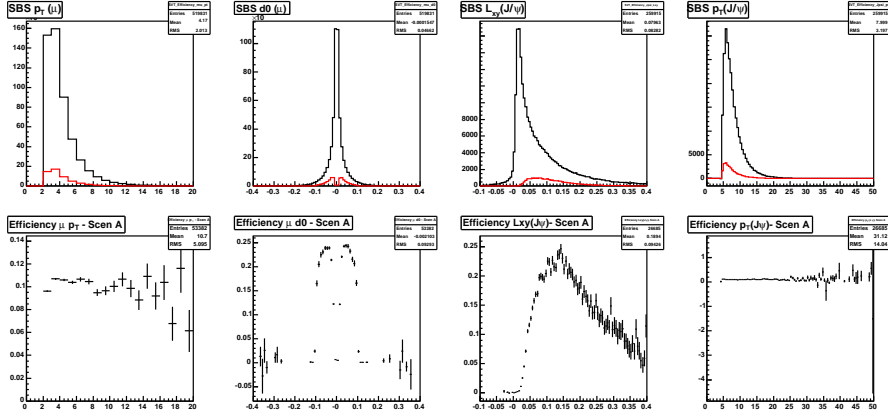
Figure A.6: J/ψ distributions for MC seeded from `0h` data. From left to right: $p_T(\mu)$, $d_0(\mu)$, $L_{xy}(J/\psi)$, and $p_T(J/\psi)$. The top plots show two histograms for each variable: events where both muons are matched to SVT tracks that satisfy Scen A requirements (red) and events where both muons have $p_T > 2.0$ GeV/c (black). Both histograms are sideband subtracted in the J/ψ mass. The lower plots are the results of histogram division (red/black).
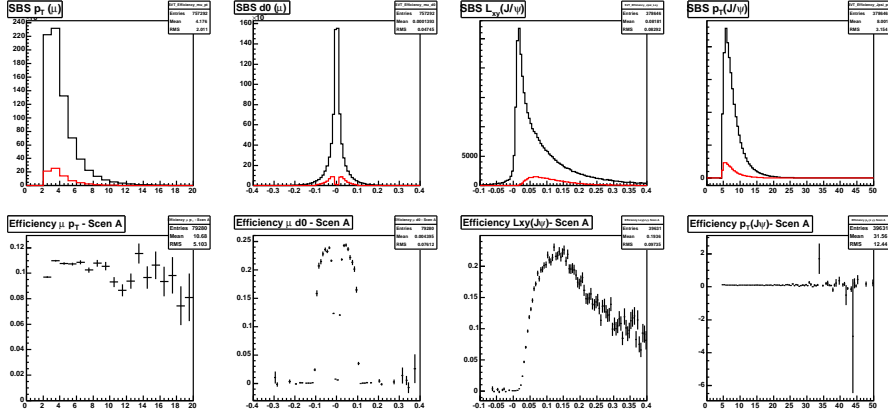
Figure A.7: J/ψ distributions for MC seeded from 0i data. From left to right: $p_T(\mu)$, $d_0(\mu)$, $L_{xy}(J/\psi)$, and $p_T(J/\psi)$. The top plots show two histograms for each variable: events where both muons are matched to SVT tracks that satisfy Scen A requirements (red) and events where both muons have $p_T > 2.0$ GeV/c (black). Both histograms are sideband subtracted in the J/ψ mass. The lower plots are the results of histogram division (red/black).
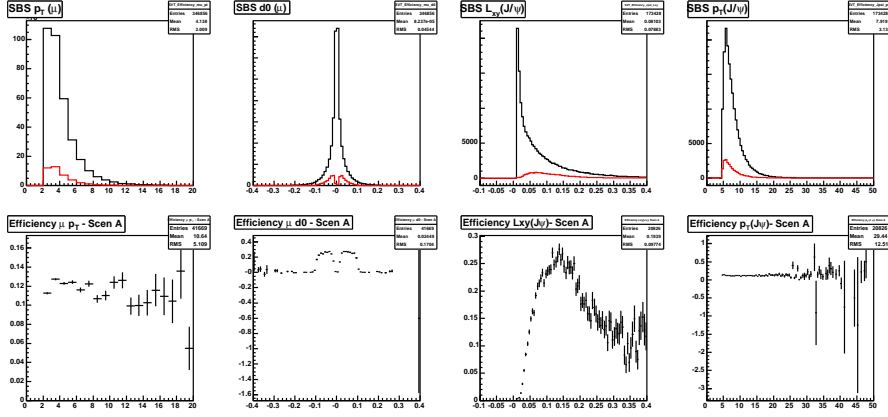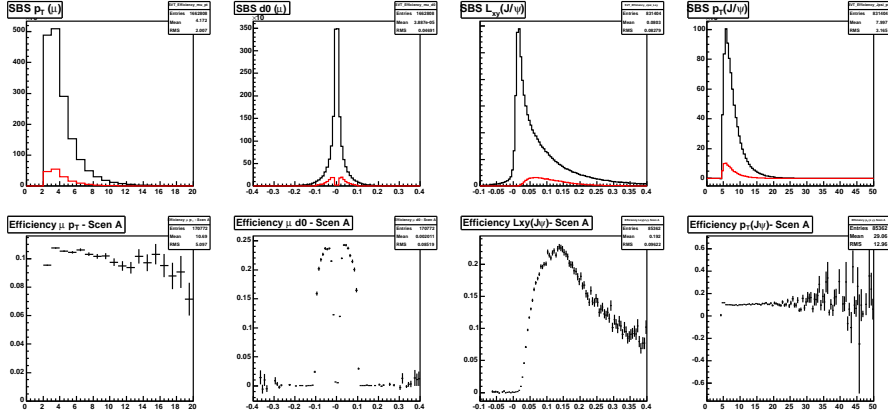

Figure A.8: J/ψ distributions for MC seeded from 0d+0h+0i data. From left to right: $p_T(\mu)$, $d_0(\mu)$, $L_{xy}(J/\psi)$, and $p_T(J/\psi)$. The top plots show two histograms for each variable: events where both muons are matched to SVT tracks that satisfy Scen A requirements (red) and events where both muons have $p_T > 2.0$ GeV/c (black). Both histograms are sideband subtracted in the J/ψ mass. The lower plots are the results of histogram division (red/black).
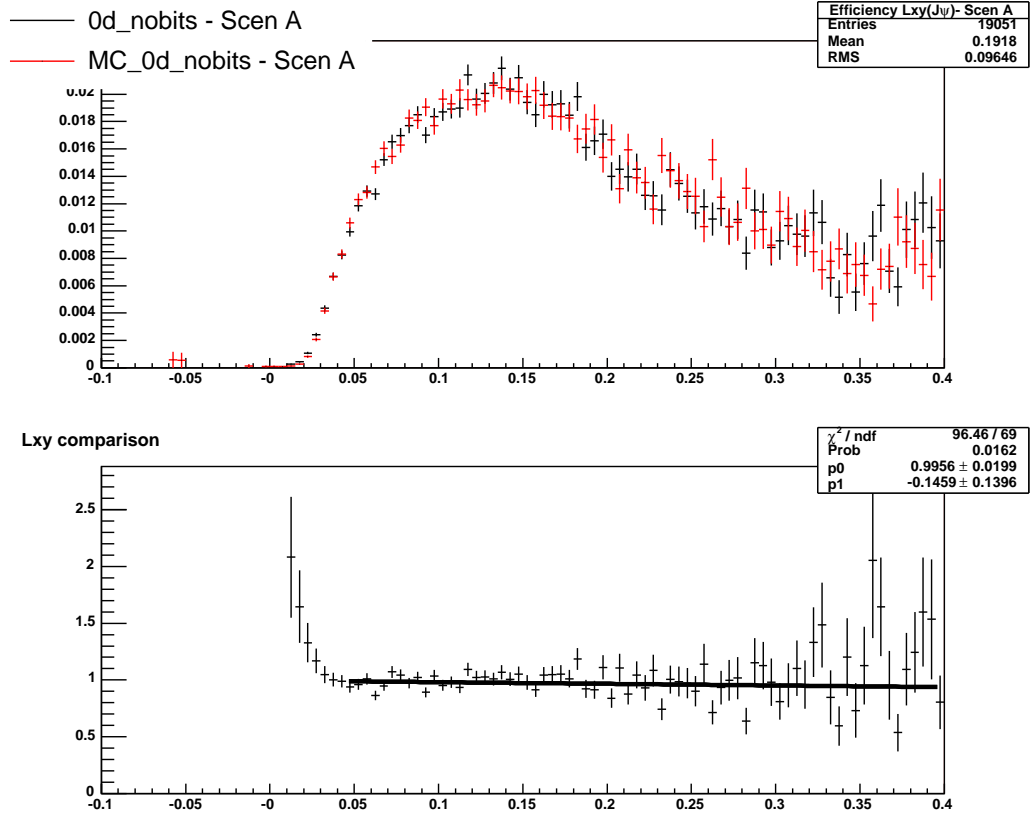
Figure A.9: The top plot shows SVT efficiency for `0d` data (black) and MC (red) as a function of $L_{xy}(J/\psi)$. The lower plot is the result of histogram division (black/red = data/MC).
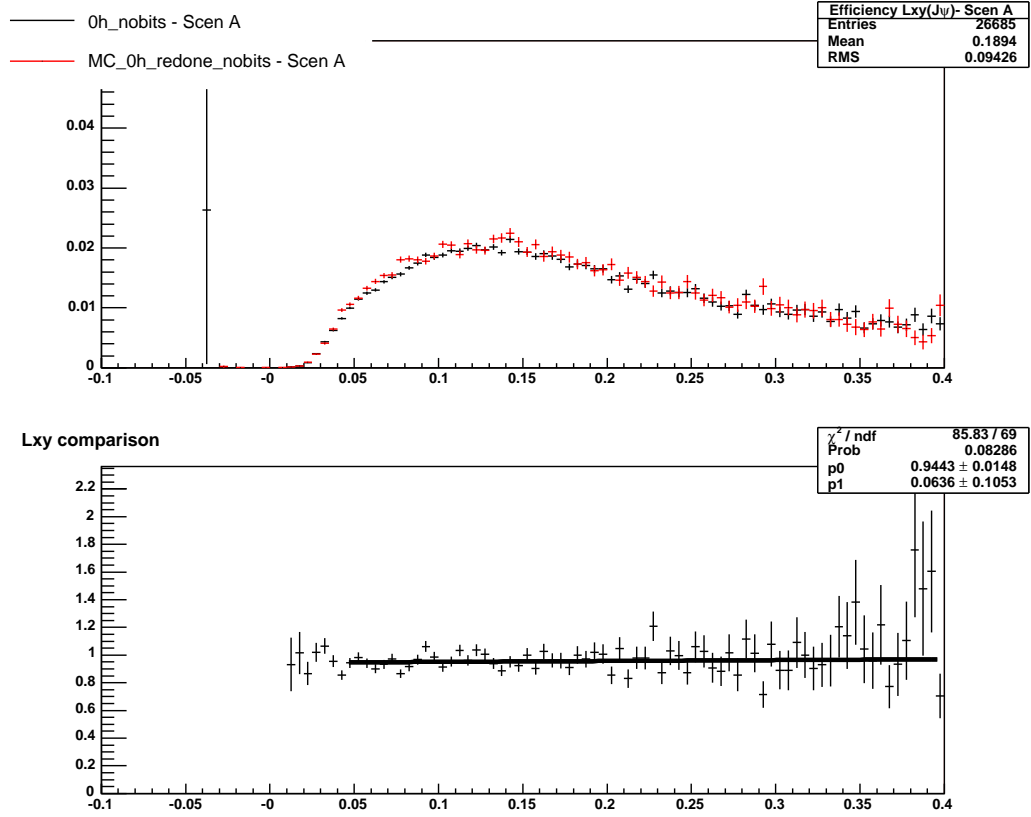
Figure A.10: The top plot shows SVT efficiency for 0h data (black) and MC (red) as a function of $L_{xy}(J/\psi)$. The lower plot is the result of histogram division (black/red = data/MC).
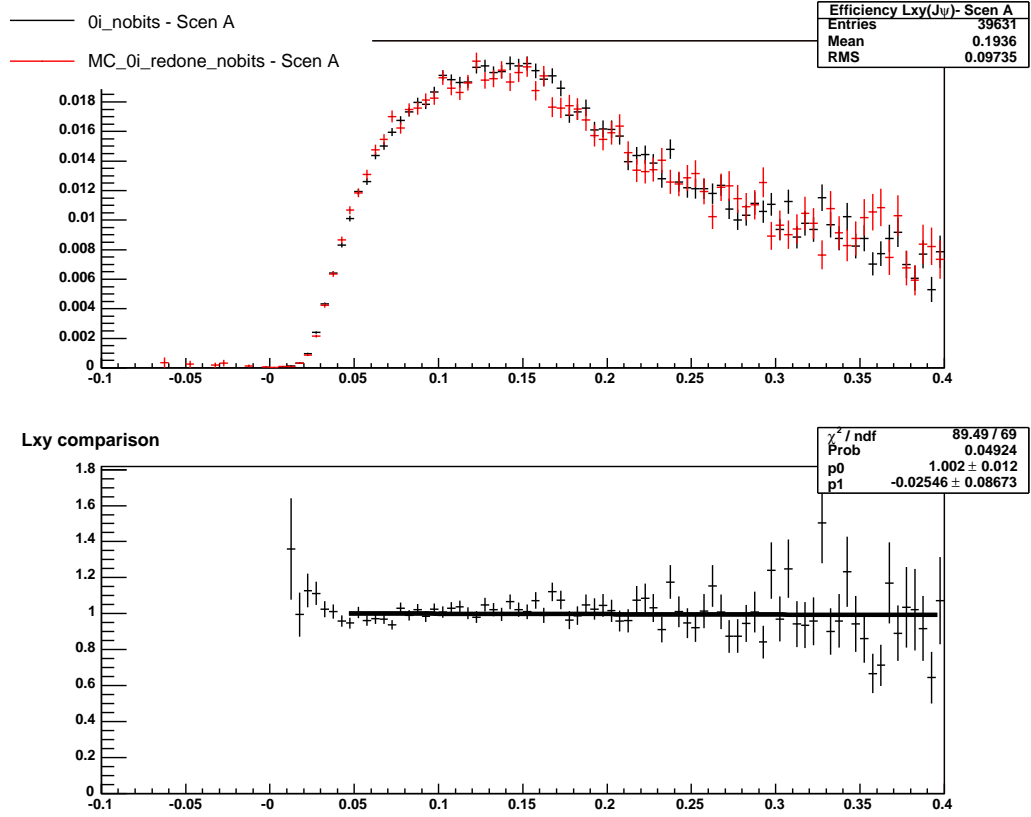
Figure A.11: The top plot shows SVT efficiency for `0i` data (black) and MC (red) as a function of $L_{xy}(J/\psi)$. The lower plot is the result of histogram division (black/red = data/MC).
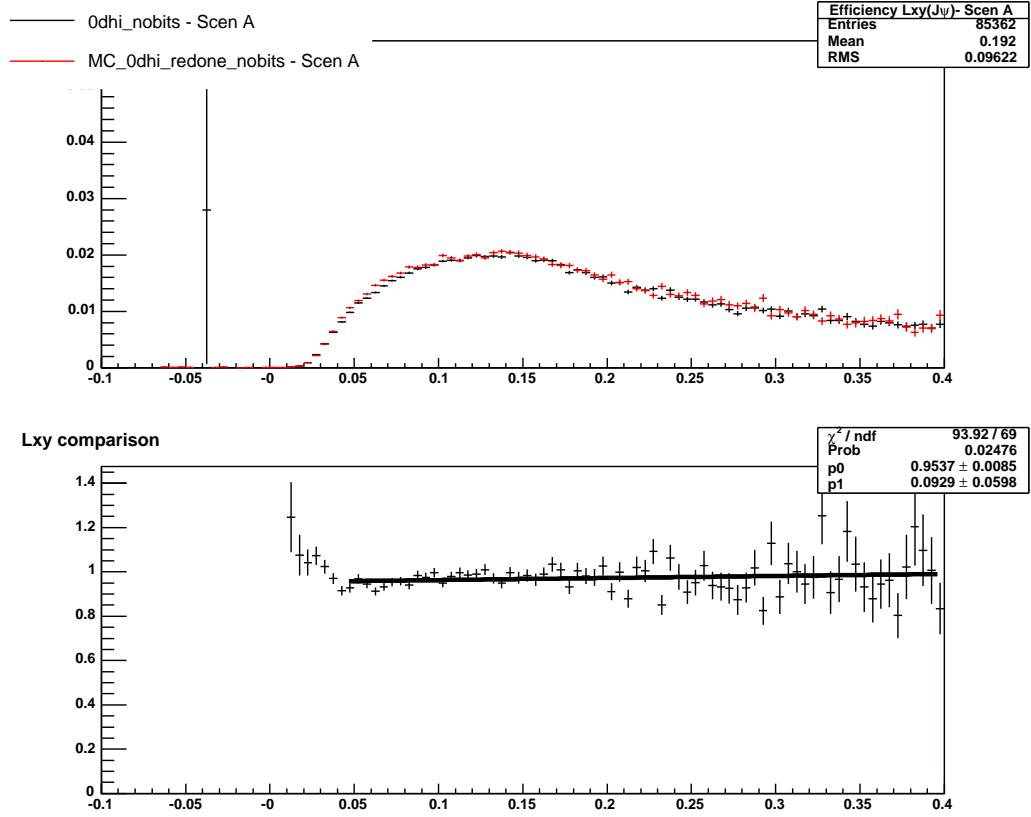
Figure A.12: The top plot shows SVT efficiency for `0d+0h+0i` data (black) and MC (red) as a function of $L_{xy}(J/\psi)$. The lower plot is the result of histogram division (black/red = data/MC).

Appendix B

B^0 Journey

The $B^0 \to D^-(K^+\pi^-\pi^-)\pi^+$ sample was originally intended to be the primary control sample for the $B_s \to D_s^-(\phi\pi^-)\pi^+$ lifetime measurement. In both samples the B meson decays to a pion plus a D meson, which itself has three daughter particles. However, there is a very significant difference between these two four-body decays: the level of background. A narrow mass cut on the reconstructed ϕ gives us a very efficient way to decrease combinatorial background, and the resulting B_s sample has 3% background in the FR region and 7% in the PR region. In contrast, with the default cuts, the $B^0 \to D^-\pi^+$ sample has 9% background in the FR region and 16% in the PR region.

Much work has been devoted to better understanding the $B^0 \to D^-\pi^+$ sample composition and its effect on the lifetime analysis. This work has helped motivate some innovations, the most significant of which was the move from the 2-D fit (ct and event-by-event σ_{ct}) to the 1-D fit (ct only). Experimenting with tightening analysis cuts and different fit configurations first suggested that the uncertainties associated with modeling the background proper time distribution were large. These experiments are presented in detail in Sec. B.1. To confirm the large size of the background systematic, we performed toy Monte Carlo studies that are described in Section B.2. (A refined version of these systematics studies are presented in Sec. 9.4.) We found the associated uncertainty may be as large as 10 μm, demonstrating that with the default cuts, the $B^0 \to D^-\pi^+$ sample is systematically, rather than statistically,

limited.

We can still learn from the B^0, however, and apply its lessons to the B_s sample where the background systematics are expected to be much smaller. The lessons learned from the collected experience with the B^0 sample are summarized in Sec. B.3.

B.1 Three B^0 Fit Configurations

We discuss in this section several $B^0 \to D^-\pi^+$ analysis cut and fit configurations that were tested in order to better understand the sample composition. The default cuts described in Table 5.1 were used in Section B.1.1. An additional requirement that the π from the B be one of the two-track-trigger (TTT) tracks was added to the default cuts for the fits described in Section B.1.2. A draconian cut $L_{xy}(B \to D) > 500 \, \mu$m designed to suppress the background at the expense of signal was added for the fits described in Section B.1.3. These three fit configurations produce results that vary greatly from each other and, at times, from the PDG value.

As we look at the quality of fits in this section, we have three handles for determining the success of the fit procedure.

1. Do the FR and PR results agree when the fits are performed separately?

2. Is there structure visible in the lifetime residuals?

3. (For the control samples only) Is the result consistent with the world average?

B.1.1 Default Cuts

The default $B^0 \to D^-(K^+\pi^-\pi^-)\pi^+$ fit results have already been shown in Chap. 9, but we repeat the relevant details here.

The data and Monte Carlo for this fit were both processed with the cuts described in Table 5.1. The Monte Carlo was reweighted according to the procedure for high statistics samples described in Section 7.3. The fractions of each mode used in the fit are shown in Table B.1. The plots of the results for the FR and PR regions are shown in Figure B.1.

The results for the FR region (448.7 ± 4.6 μm) and PR region (452.5 ± 5.8 μm) are both within two σ of the world average $c\tau(B^0) = 458.7 \pm 2.7$ μm [2], and they disagree with each other by less than one σ. However, both residual plots have a slight wave structure. The fit is slightly higher than the data in the small and large ct regions (positive residuals), but the data is higher than the fit in the region around 0.07 cm (negative residuals). There is also a double-peak structure in the FR ct distribution. Previous studies have shown that the lower-lifetime positive residuals can be removed by requiring the π from the B to be one of the two-track-trigger (TTT) tracks, and this cut was added for the fits in the next section.

(a) $\tau_{\mathrm{FR}} = 448.7 \pm 4.6$ (b) $\tau_{\mathrm{PR}} = 452.5 \pm 5.8$

Figure B.1: Results for the fits to the FR (left) and PR (right) regions of the $B^0 \to D^-(K^+\pi^-\pi^-)\pi^+$ sample with the default cuts.

Fractions returned by mass fit		
	FR region	PR region
DK	0.053812	0.011411
Dstarpi	0.0007100	0.27899
Drho	0.0023880	0.024551
B0other	0.0064190	0.11764
bptodppix	0.0000	0.028082
Bs	0.022557	0.030433
Bkgd - real D	0.036839	0.052600
Bkgd - fake D	0.055780	0.106501
Real D in upper sideband	0.70	
D leakage	0.364180	0.263989
Fractions used by lifetime fit		
	FR region	PR region
Bkgd - D SB	0.062898	0.114070
Bkgd - upper SB	0.052627	0.075143

Table B.1: Fractions of each mode for the fits to the $B^0 \rightarrow D^-(K^+\pi^-\pi^-)\pi^+$ sample with the default cuts.

B.1.2 Default Cuts + Requiring π_B to Be a TTT Track

The data and Monte Carlo for this fit were both processed with the cuts described in Table 5.1 with the additional requirement that the π from the B and one of the D daughters form a TTT pair. We explicitly exclude events where two D daughters also satisfy the TTT requirements. The Monte Carlo was reweighted according to the procedure for high statistics samples described in Section 7.3. The fractions of each mode used in the fit are shown in Table B.2. The plots of the results for the FR and PR regions are shown in Figure B.2.

The results for the FR region (461.8 ± 7.1 μm) and PR region (465.8 ± 8.8 μm) are both within one σ of the world average $c\tau(B^0) = 458.7 \pm 2.7$ μm [2], and they disagree with each other by less than one σ. However, both residual plots have strong wave structures. The fit is now much higher than the data in the small and large ct regions (positive residuals), and the data is higher than the fit in the region around 0.07 cm (negative residuals). This pronounced wave structure (in the absence of the double peak) suggests that the prompt component of the fit model is too large, and the lifetime of the B^0, the only variable that floats in this fit, goes high to compensate for this effect.

The large prompt fraction is better understood if one examines the background fractions found in Table B.2. The mass fit says the PR region is 1.7% real D and 13.9% fake D. Because the B upper sideband, our only source of a real-D lifetime PDF, is only 11% real D, the lifetime fit must use 15.7% upper sideband (1.7% is real D, the other 14% is fake D). The upper sideband is therefore also functioning as the only source of fake-D background, and the D-sideband fraction (in theory, the primary source of fake D's) used by the fit is negligible. The π_B trigger requirement has, in this case, been very effective at eliminating real-D background as well as our only available proxy for the real-D background in the lifetime fit.

186

(a) $\tau_{\text{FR}} = 461.8 \pm 7.1$

(b) $\tau_{\text{PR}} = 465.8 \pm 8.8$
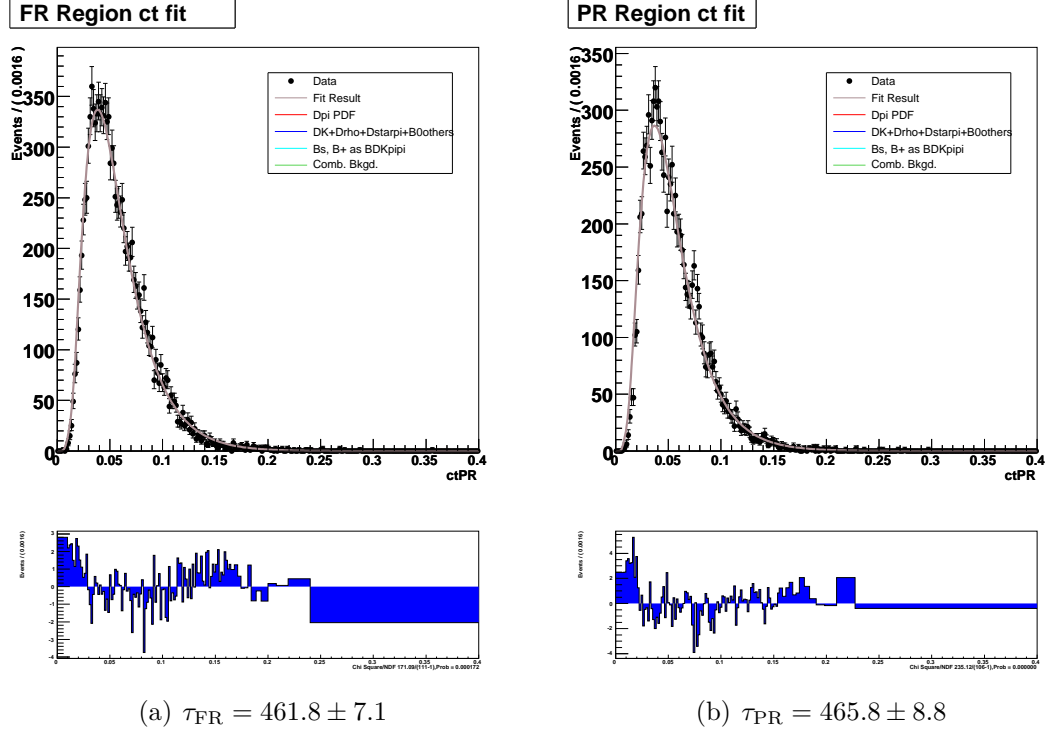
Figure B.2: Results for the fits to the FR (left) and PR (right) regions of the $B^0 \to D^-(K^+\pi^-\pi^-)\pi^+$ sample with the default cuts + π_B trigger requirement

Fractions returned by mass fit		
	FR region	PR region
DK	0.058750	0.0056730
Dstarpi	0.0003710	0.27649
Drho	0.0020510	0.024530
B0other	0.0062620	0.11078
bptodppix	0.0000	0.026184
Bs	0.044286	0.063349
Bkgd - real D	0.006370	0.017215
Bkgd - fake D	0.070628	0.139259
Real D in upper sideband	0.11	
D leakage	0.364180	0.263989
Fractions used by lifetime fit		
	FR region	PR region
Bkgd - D SB	0.029188	-0.000039755
Bkgd - upper SB	0.057909	0.15650

Table B.2: Fractions of each mode for the fits to the $B^0 \to D^-(K^+\pi^-\pi^-)\pi^+$ sample with the default cuts + π_B trigger requirement

B.1.3   Default Cuts + Requiring π_B to Be a TTT Track + $L_{xy}(B \to D) > 500 \ \mu\mathbf{m}$

The data and Monte Carlo for this fit were both processed with the cuts described in Table 5.1 with the additional requirements that the π from the B and one of the D daughters form a TTT pair and $L_{xy}(B \to D) > 500 \ \mu m$. We explicitly exclude events where two D daughters also satisfy the TTT requirements. The Monte Carlo was reweighted according to the procedure for high statistics samples described in Section 7.3. The fractions of each mode used in the fit are shown in Table B.3. The plots of the results for the FR and PR regions are shown in Figure B.3.

The results for the FR region ($472.8 \pm 9.1 \ \mu m$) and PR region ($455.4 \pm 10.3 \ \mu m$) are both within two σ of the world average $c\tau(B^0) = 458.7 \pm 2.7 \ \mu m$ [2] and each other. However, the wave structure of the residuals is still visible.

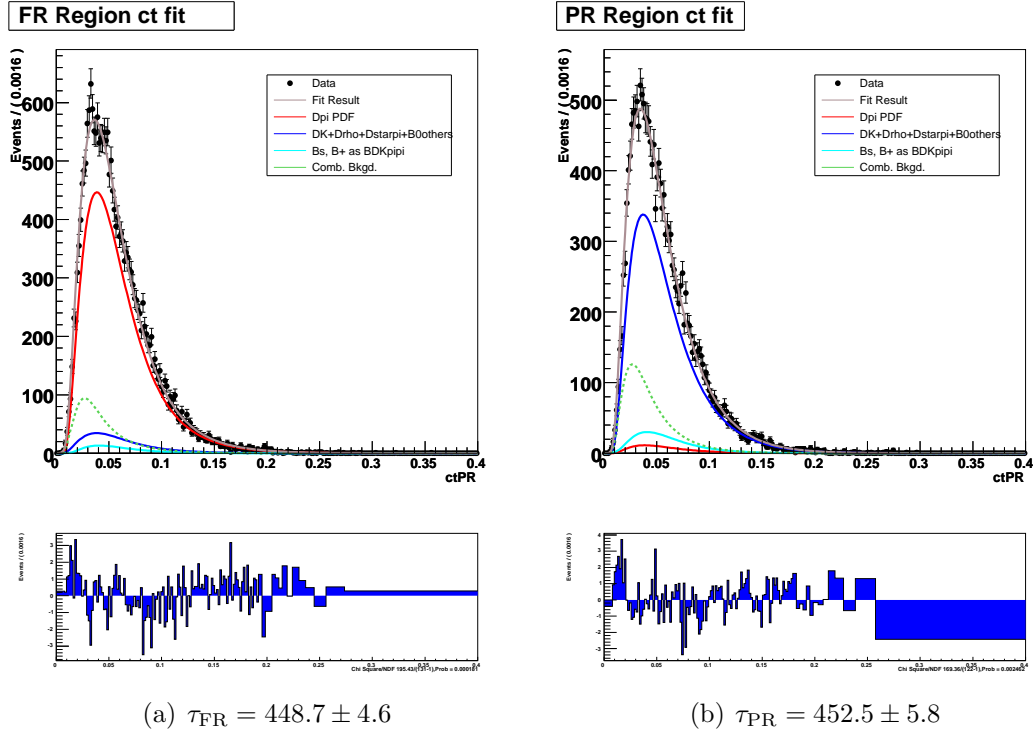(a) $\tau_{\mathrm{FR}} = 472.8 \pm 9.1$ (b) $\tau_{\mathrm{PR}} = 455.4 \pm 10.3$
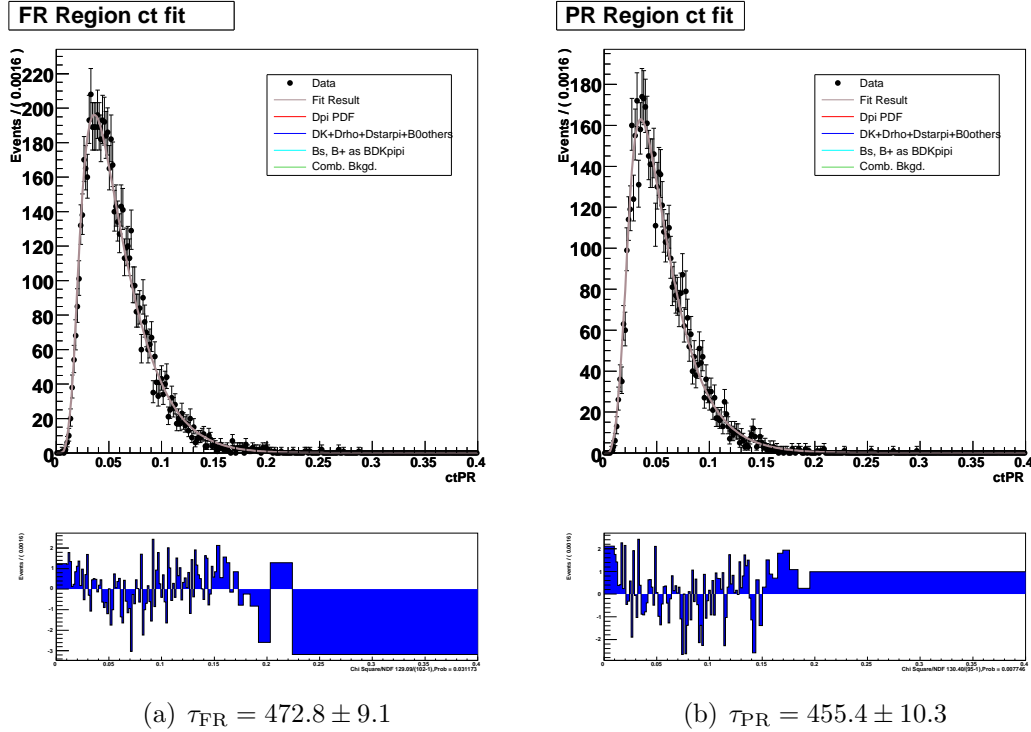
Figure B.3: Results for the fits to the FR(left) and PR(right) regions of the $B^0 \to D^-(K^+\pi^-\pi^-)\pi^+$ sample with the default cuts + π_B trigger requirement + $L_{xy}(B \to D) > 500 \ \mu m$

Fractions returned by mass fit		
	FR region	PR region
DK	0.064031	0.0078760
Dstarpi	0.00039400	0.31725
Drho	0.0021600	0.021231
B0other	0.0075330	0.13750
bptodppix	0.0000	0.031388
Bs	0.018904	0.028435
Bkgd - real D	0.007000	0.017645
Bkgd - fake D	0.033696	0.068000
Real D in upper sideband	0.27	
D leakage	0.364180	0.263989
Fractions used by lifetime fit		
	FR region	PR region
Bkgd - D SB	0.026020	0.029981
Bkgd - upper SB	0.025926	0.065352

Table B.3: Fractions of each mode for the fits to the $B^0 \rightarrow D^-(K^+\pi^-\pi^-)\pi^+$ sample with the default cuts + π_B trigger requirement + $L_{xy}(B \rightarrow D) > 500 \ \mu$m

B.1.4   Summary of Alternate $B^0 \to D^- \pi^+$ Fit Configurations

The fit results for the FR and PR regions and the fractions of real-D and fake-D backgrounds are summarized in Table B.4. We also take away the following points:

- The default cuts for the $B^0 \to D^- \pi^+$ are loose enough that they allow background fractions of order 10-20%.

- When the cuts were tightened by requiring the π_B to be a TTT track, we ran into an additional problem that the cut might be considered too efficient at rejecting real-D background. We found the two-background method for the lifetime fit does not work well if we do not have a reliable way to find a real-D proxy. Recall the B upper sideband is only 11% real D in this scenario.

- When a draconian cut of $L_{xy}(B \to D) > 500 \ \mu$m is imposed, the fake-$D$ background goes down considerably. The B upper sideband in this case is 27% real D, and the two-background method is again effective. However, there is a factor of three reduction in statistics from the default case.

Table B.4: Summary of Alternate $B^0 \rightarrow D^- \pi^+$ fit configurations described in detail in the appendix

	Default	TTT for π_B	TTT plus $L_{xy}(B \rightarrow D)$ cut
FR $c\tau$	448.7 ± 4.6	461.8 ± 7.1	472.8 ± 9.1
PR $c\tau$	452.5 ± 5.8	465.8 ± 8.8	455.4 ± 10.3
FR+PR $c\tau$	449.9 ± 3.6	463.5 ± 5.6	465.6 ± 6.8
FR f_{real-D}	0.036839	0.006370	0.007000
FR f_{fake-D}	0.055780	0.070628	0.033696
PR f_{real-D}	0.052600	0.017215	0.017645
PR f_{fake-D}	0.106501	0.139259	0.068000
FR+PR f_{real-D}	0.043995	0.011299	0.011681
FR+PR f_{fake-D}	0.078809	0.101819	0.048782
Real D % in upper SB	70%	11%	27%
χ^2/NDoF	236.0/(139-1)	290.3/(120-1)	153.4/(110-1)
Quality of Fit	Two peaks in FR region	Strong wave structure fit > data at low ct	Slight wave structure

B.2   Background Studies with Toy Monte Carlo

Six different toy Monte Carlo studies of 1000 pseudo-experiments each are performed to measure the amount of variation that might be possible if the proper time distribution of the background is mismodeled in the $B^0 \to D^- \pi^+$ fit. To make the toy MC as realistic as possible the PDFs used for generation are the same as those used for the default fit to data. The numbers of events per experiment are Poisson distributed around 39600, the number of events in the combined FR+PR region. The lifetime used for toy Monte Carlo generation is 464 μm. The fractions used for generating the toy Monte Carlo are modified in the six ways listed below. The PDFs and fractions used for fitting the toy Monte Carlo data are the same as those used for the default fit to data.

1. Generate using the RS upper sideband as the only background. This effectively makes the generated sample more prompt-like (smaller ct values) than the default fitter expects. The resulting bias is -4.2σ (-15.3 μm).

2. Generate using the D sidebands as the only background. This effectively removes the expected prompt component (the real D's). The resulting bias is $+4.2\sigma$ ($+15.9$ μm).

3. Generate setting the fraction of real D in the upper sideband to 40% (default value 70%). The resulting bias is -3.3σ (-12.1 μm).

4. Generate setting the fraction of real D in the upper sideband to 100% (default value 70%). The resulting bias is $+1.2\sigma$ ($+4.7$ μm).

5. Generate setting the fraction of D leakage in the D sidebands to 0% (default value 31%). The resulting bias is $+1.3\sigma$ ($+4.7$ μm).

6. Generate setting the fraction of D leakage in the D sidebands to 62% (default value 31%). The resulting bias is -3.3σ (-12.5 μm).

The values from toy Monte Carlo studies 1 and 2 bracket the size of possible systematic uncertainties. Studies 3 and 4 are overestimates of the systematic uncer-

tainty, since the fraction of real D in the upper sidebands should be known to at least 10%. From statistical uncertainties alone, one would estimate that the error is approximately 2%. Likewise, the error returned from the auxiliary fit to the D sidebands suggests 2.5% would be a more natural variation to use than 31% in studies 5 and 6.

The intent of these toy studies was to test whether the variations seen between results returned by B^0 fit configurations could be reproduced with toy Monte Carlo with various background fractions. We have seen that variations of 5-10 μm are easy to achieve.

B.3 Lessons Learned from the $B^0 \rightarrow D^-(K^+\pi^-\pi^-)\pi^+$ Explorations

- The modeling of the proper time distribution of the background is the source of a large systematic uncertainty (5-10 μm, which is larger than the statistical uncertainty) for the $B^0 \rightarrow D^-(K^+\pi^-\pi^-)\pi^+$ fit with the default cuts.

- The systematic uncertainty can be bracketed by running toy Monte Carlo studies and changing the background proxy to all D sideband or all RS upper sideband. The results are consistent with variations seen in fits to data.

- These extreme tests are useful to assess if the level of background in the B_s will produce similar uncertainties. In fact, this quick toy Monte Carlo assessment performed on the B_s default fitter lead us to tighten the D_s mass window from ± 20 MeV/c^2 to ± 12 MeV/c^2 as a simple way to reduce the fake D fraction by 40% with less than 8% effect on the signal yield.

- A more reasonable systematic uncertainty can be assessed by varying the fraction of real D's in the upper sideband and the fraction of D leakage in the D sidebands within their returned errors. This is the approach proposed for the B_s.

Appendix C

Cross-Checks Performed before Unblinding the B_s Fit

The purpose of this appendix is to present the cross-checks performed on the *blinded* fit to B_s data. Each cross-check involves dividing the data into two disjoint subsamples of roughly equal size. The different fit configurations used to fit these subsamples are discussed in the appropriate sections. The following three variables are used to divide the sample: run number, event number, and $p_T(B)$.

Note: when the Monte Carlo is reweighted, it is sequentially reweighted in p_T and trigger confirmation category to match the data distributions in these variables for the B_s peak, D_s peak region. Even with the full sample, there are not sufficient data statistics in the fully reconstructed B_s peak to perform the reweightings simultaneously. Dividing the target sample in half further increases the uncertainty associated with the reweighting procedure (already a systematic of 3.7μm). The situation is particularly dire in the case where we divide the sample into low and high p_T. Here, the high p_T subsample has many poorly populated bins in its target p_T histogram.

The results of the *blinded* default fit configuration on the full sample are listed in the left column of Tables C.1-C.4 for comparison. Note that because the fit was *blinded* during these studies, the default results in the tables are offset from the true results.

C.1 Cross-Checks Performed with Default Mass Fit Fractions

C.1.1 Sorting by Run Number

The data is divided into an "early" period (run number < 199030) and a "late" period (run number > 199030). Using the default efficiency curves to fit the sub-samples we find the results shown in Table C.1. The background PDFs (which come from data) are different from the default curves. The default fractions are used.

For another cross-check we reweight the Monte Carlo separately for the two run ranges and re-derive efficiency curves for the B_s Monte Carlo before fitting. The default fractions are used. We find the results shown in Table C.2.

One might ask what the probability is of having such good agreement between statistically independent subsamples (*i.e.*, What is the chance that columns 2 and 3 of row 1 of Table C.2 would agree so well given the large statistical errors? Likewise for row 2.) To answer this question one can do a χ^2 test with one degree of freedom comparing columns 2 and 3 to their mean. For the FR region, the probability is 1.7%; for the PR region, the probability is 5.1%. The probability that both these rows would show such good agreement is $(0.017) \cdot (0.051) = 8.4 \times 10^{-4}$.

C.1.2 Sorting by Event Number

The data is divided into even and odd event numbers and fit with the default efficiency curves and fractions. The background PDFs are different as they are derived from the sample being fit. The default fractions are used. The results are shown in Table C.3.

C.1.3 Sorting by $p_T(B)$

The data is divided into "low p_T" (< 13.3 GeV/c) and "high p_T" (> 13.3 GeV/c) subsamples. We reweight the Monte Carlo separately for the subsamples and re-derive efficiency curves for the B_s Monte Carlo before fitting. The background PDFs

are different as they are derived from the sample being fit. The default fractions are used. We find the results shown in Table C.4.

C.2 Cross-Checks Performed with New Mass Fit Fractions

In the above section, we use the default fractions of events obtained from the mass fit to the full 1.3 fb^{-1} of B_s data. Here we wish to check the effect of using fractions derived from mass fits to lower statistics samples (the even and odd subsamples). As we expect no event number dependence of the $p_T(B)$ and trigger category distributions, we use the default efficiency curves. The background PDFs are different as they are derived from the sample being fit. The results are shown in Table C.5. Table C.3 is included as the first line of Table C.5 for reference. From this table we can draw a few conclusions.

- If one looks in a single row of Table C.5, one can see that the variations between subsamples fit with the same fractions and signal PDFs are statistical and a reasonable size.

- If one looks in a single column and compares the results of fits to the same subsample using various fractions, one can see the variations are consistent with the 3.6 μm systematic uncertainty already assigned for the fit (background) fractions. For example, in the first column, the results for the FR region are 406.2, 407.2, and 405.1 μm; the results for the PR regions are 432.5, 435.8, and 429.5 μm.

- With so many fits, one also notices that $c\tau(PR)$ is consistently greater than $c\tau(FR)$ by a value larger than our current systematic uncertainty for the background fractions. Historical Note: this suggested that there was a systematic uncertainty associated with our choice of background model (in addition to the background fraction uncertainty we had already planned to include) that had to be assessed before unblinding. We discuss this further in the next section.

196

C.3 Alternate Mass Fit Models

The default mass fit for this analysis divides the combinatorial background into two types: fake D and real D. The fake-D shape comes from an auxiliary fit to the D_s sidebands, and its normalization is fixed in the final mass fit. The real-D shape comes from an auxiliary fit to the sideband-subtracted wrong-sign $(D_s^+\pi^+)$ sample, and its normalization is floated in the final mass fit. For the purpose of selecting a reasonable alternate model we have considered two scenarios that both involve using a flat WS shape. In the first, we continue to fix the fake-D shape and normalization. In the second, we fix the fake-D shape but allow its normalization to float. We use the fractions derived from these two mass fits and the default curves as inputs for the lifetime fits to the full 1.3 fb^{-1}, the even subsample, and the odd subsample. The results are shown in Table C.6. Note that the $c\tau(PR)$-$c\tau(FR)$ separation is greatly reduced. Historical Note: we used the alternate mass fit models explored here to generate toy MC to assess an additional background modeling systematic.

C.4 Additional Event Number Cross-Check

We reweight the Monte Carlo separately for the even and odd event numbers and re-derive efficiency curves for the B_s Monte Carlo before fitting. The default fractions are used. We find the results shown in Table C.7.

C.5 Conclusions

The early and late data shown in Table C.2 are in excellent agreement, but the probability for such agreement in the FR and PR modes are 1.7% and 5.1%, respectively. The other cross-checks performed show that there is nothing pathological in the fit. For additional confirmation that the likelihood is not discretized and forcing the fitter to return the same values, one can look at the bootstrapped toy Monte Carlo results. The plot of the returned biases ($c\tau - 438$ μm) is shown in Figure C.1, and there is no unusual grouping visible.

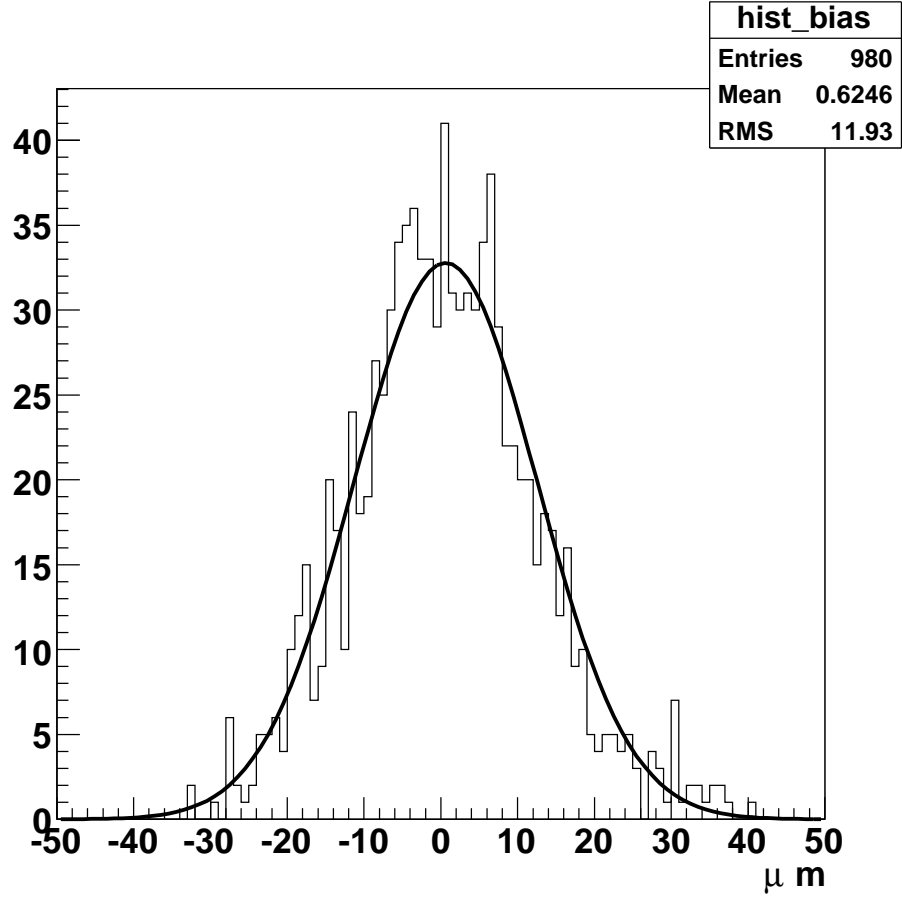**Figure C.1:** Biases returned from 1000 bootstrapped toy MC experiments

	Full 1.3 fb^{-1}	"Early" data	"Late" data
FR	406.2 ± 20.0	411.8 ± 29.2	400.9 ± 27.6
PR	432.5 ± 15.2	440.6 ± 21.9	423.5 ± 20.9
FR + PR	424.7 ± 12.2	432.2 ± 17.6	416.4 ± 16.7

Table C.1: Fits performed on data separated by run number. The default curves derived from Monte Carlo reweighted to the full data sample are used. The background PDFs (which come from data) are different from the default curves. The default fractions are used.

	Full 1.3 fb^{-1}	"Early" data	"Late" data
FR	406.2 ± 20.0	404.9 ± 34.8	404.0 ± 27.7
PR	432.5 ± 15.2	430.3 ± 21.3	432.0 ± 21.4
FR + PR	424.7 ± 12.2	422.2 ± 18.1	423.3 ± 17.1

Table C.2: Fits performed on data separated by run number. New efficiency curves have been derived from Monte Carlo reweighted to the separate subsamples. The background PDFs (which come from data) are different from the default curves. The default fractions are used.

	Full 1.3 fb^{-1}	Even	Odd
FR	406.2 ± 20.0	423.5 ± 29.5	388.8 ± 27.1
PR	432.5 ± 15.2	434.1 ± 21.8	431.5 ± 21.2
FR + PR	424.7 ± 12.2	431.0 ± 17.6	418.9 ± 16.9

Table C.3: Fits performed on data separated by event number. The default efficiency curves are used. The background PDFs (which come from data) are different from the default curves. The default fractions are used.

	Full 1.3 fb^{-1}	$p_T(B) < 13.3$ GeV/c	$p_T(B) > 13.3$ GeV/c
FR	406.2 ± 20.0	411.9 ± 26.6	385.1 ± 28.7
PR	432.5 ± 15.2	461.9 ± 21.9	390.2 ± 20.2
FR + PR	424.7 ± 12.2	446.0 ± 17.0	388.9 ± 16.6

Table C.4: Fits performed on data separated by $p_T(B)$. New efficiency curves have been derived from Monte Carlo reweighted to the separate subsamples. The background PDFs (which come from data) are different from the default curves. The default fractions are used.

Fit Fractions		Full 1.3 fb^{-1}	Even	Odd
	FR	406.2 ± 20.0	423.5 ± 29.5	388.8 ± 27.1
Default	PR	432.5 ± 15.2	434.1 ± 21.8	431.5 ± 21.2
	FR + PR	424.7 ± 12.2	431.0 ± 17.6	418.9 ± 16.9
Refit mass	FR	407.2 ± 20.2	424.6 ± 29.8	389.8 ± 27.4
of even	PR	435.8 ± 15.4	437.3 ± 22.1	434.9 ± 21.6
events	FR + PR	426.7 ± 12.3	433.0 ± 17.8	421.0 ± 17.1
Refit mass	FR	405.1 ± 19.8	422.3 ± 29.2	387.8 ± 26.8
of odd	PR	429.5 ± 14.8	431.1 ± 21.3	428.4 ± 20.7
events	FR + PR	422.5 ± 12.0	428.9 ± 17.3	416.7 ± 16.6

Table C.5: Fits performed on data separated by event number. The default efficiency curves are used. The background PDFs (which come from data) are different from the default curves. A variety of mass fit fractions are used.

Fit Fractions		Full 1.3 fb^{-1}	Even	Odd
Refit mass	FR	401.5 ± 19.8	419.4 ± 29.3	383.5 ± 26.7
-fix fake-D norm	PR	421.2 ± 14.8	423.3 ± 21.3	419.3 ± 20.7
-flat real-D shape	FR + PR	415.4 ± 11.9	422.3 ± 17.3	408.7 ± 16.5
Refit mass	FR	401.9 ± 19.9	419.9 ± 29.5	383.6 ± 26.9
-float fake-D norm	PR	423.8 ± 15.3	426.0 ± 22.0	421.7 ± 21.3
-flat real-D shape	FR + PR	417.3 ± 12.2	424.6 ± 17.7	410.4 ± 16.9

Table C.6: Testing the way we fit the background in the mass fit. Fits performed on data separated by event number. The default efficiency curves are used. The background PDFs (which come from data) are different from the default curves. A variety of mass fit fractions are used.

	Full 1.3 fb^{-1}	Even	Odd
FR	406.2 ± 20.0	414.9 ± 30.9	393.4 ± 25.5
PR	432.5 ± 15.2	432.0 ± 23.0	421.5 ± 20.0
FR + PR	424.7 ± 12.2	427.0 ± 18.5	412.8 ± 15.9

Table C.7: Fits performed on data separated by event number. New efficiency curves have been derived from Monte Carlo reweighted to the separate subsamples. The background PDFs (which come from data) are different from the default curves. The default fractions are used.

References

[1] I. I. Y. Bigi, *Heavy Quark Expansions for Inclusive Heavy-Flavor Decays and the Lifetimes of Charm and Beauty Hadrons*, UND-HEP-96-BIG06 (1996).

[2] C. Amsler, *et al.* (Particle Data Group), Phys. Lett. B667, 1 (2008).

[3] K. Wilson, Phys. Rev. 179 (1969)1499; K. Wilson, J. Kogut, Phys. Rep. 12 (1974) 75.

[4] These calculations have been much discussed. A review with references to the early literature can be found in the following: I.I. Bigi, M. Shifman, N.G. Uraltsev, Annnu. Rev. Nucl. Part. Sci. 47 (1997) 591.

[5] W.-M. Yao, *et al.* (Particle Data Group), J. Phys. G **33**, 1 (2006).

[6] F. Gabbiani, A. I. Onishchenko and A. A. Petrov, Phys. Rev. D **70**, 094031 (2004).

[7] E. Franco *et al.*, Lifetime Ratios of Beuty Hadrons at the Next-to-Leading Order in QCD, arXiv:hep-ph/0203089 (2002).

[8] K. Anikeev *et al.*, *B Physics at the Tevatron Run II and Beyond*, FERMILAB-Pub-01/197 (2001).

[9] Fermilab Beams Division, Accelerator concepts rookie book, http://www-bdnew.fnal.gov/operations/rookie_books/Concepts_v3.1.pdf

[10] D. Acosta, *et al.*, Phys. Rev. D **71**, 032001 (2005).

[11] C.S. Hill, Nucl. Instrum. Methods, A **530**, 1 (2004).

[12] T. K. Nelson (CDF Collaboration), Int. J. Mod. Phys. A **16S1C**, 1091 (2001).

[13] A. Affolder, *et al.*, Nucl. Instrum. Methods, A **453**, 84 (2000).

[14] T. Affolder, *et al.*, Nucl. Instrum. Methods, A **526**, 249 (2004).

[15] E.J. Thomson, *et al.*, IEEE Trans. on Nucl. Science., **49**, 1063 (2002).

[16] W. Ashmanskas, *et al.*, Nucl. Instrum. Methods, A **518**, 532 (2004).

[17] K. Anikeev, P. Murat, C. Paus, *Description of Bgenerator II*, CDF Internal Note 5092 (1999); P. Nason, S. Dawson and R. K. Ellis, Nucl. Phys. B **303**, 607 (1988).

[18] D. J. Lange, Nucl. Instrum. Meth. A **462**, 152 (2001).

[19] Geant Team, *Geant detector description and simulation tool*, CERN Program Library Long Write-up W5013; see also http://consult.cern.ch/writeup/geant/

[20] F. Azfar *et al.*, *B Mesons Lifetime Determination in Fully Hadronic Decays*, CDF Internal Note 7386 (2005).

[21] A. Abulencia *et al.* (CDF Collaboration), Phys. Rev. Lett. **97**, 242003 (2006).

[22] http://roofit.sourceforge.net/ now a part of the ROOT analysis package at http://root.cern.ch.

[23] A. Cerri *et al.*, *Measurement of B^0 Branching Fractions Using Combined Mass and dE/dx Fits*, CDF Internal Note 8705 (2007).

[24] A. Cerri *et al.*, *Measurement of B^0_s Branching Fractions Using Combined Mass and dE/dx Fits*, CDF Internal Note 8776 (2007).

[25] A. Cerri *et al.*, *Measurement of B^- Branching Fractions with a Combined Mass and dE/dx Fit*, CDF Internal Note 8777 (2008).

[26] J. Muelmenstaedt,*First observation of the decay antineutral B(s) meson going to D(+/-) meson-kaon(-/+) and measurement of the relative branching fraction (antineutral B(s) meson going to D(+/-) meson-kaon(-/+))/(antineutral B(s) meson going to D meson-antipion)*. Diss. University of California, Berkeley, 2007. Dissertations & Theses @ University of California. ProQuest. 10 Dec. 2008 http://www.proquest.com/

[27] E. Barberio and Z. Was, Comput. Phys. Commun. **79**, 291 (1994).

[28] A.Cerri *et al.*, *A Measurement of the Relative Branching Fractions: $BR(D^0 \to K\pi/KK/\pi\pi)$*, CDF Internal Note 6018 (2002).

[29] K.Anikeev and C.Paus, *Using Transversity Variable to Disentangle (C)P Eigenstates in $B_s \to J/\psi\phi$ and $B^0 \to J/\psi K^{*0}$*, CDF Internal Note 6551 (2004).